GNSS Precise Point Positioning: The enhancement with GLONASS

Ian Martin

Thesis submitted for the Degree of
Doctor of Philosophy

School of Civil Engineering and Geosciences
Newcastle University

June, 2013

Abstract

Precise Point Positioning (PPP) provides GNSS navigation using a stand-alone receiver with no base station. As a technique PPP suffers from long convergence times and quality degradation during periods of poor satellite visibility or geometry. Many applications require reliable real time centimetre level positioning with worldwide coverage, and a short initialisation time. To achieve these goals, this thesis considers the use of GLONASS in conjunction with GPS in kinematic PPP. This increases the number of satellites visible to the receiver, improving the geometry of the visible satellite constellation.

To assess the impact of using GLONASS with PPP, it was necessary to build a real time mode PPP program. *pppncl* was constructed using a combination of Fortran and Python to be capable of processing GNSS observations with precise satellite ephemeris data in the standardised RINEX and SP3 formats respectively. *pppncl* was validated in GPS mode using both static sites and kinematic datasets. In GPS only mode, one sigma accuracy of 6.4 mm and 13 mm in the horizontal and vertical respectively for 24 h static positioning was seen. Kinematic horizontal and vertical accuracies of 21 mm and 33 mm were demonstrated.

pppncl was extended to assess the impact of using GLONASS observations in addition to GPS in static and kinematic PPP. Using ESA and Veripos Apex G2 satellite orbit and clock products, the average time until 10 cm 1D static accuracy was achieved, over a range of globally distributed sites, was seen to reduce by up to 47%. Kinematic positioning was tested for different modes of transport using real world datasets. GPS/GLONASS PPP reduced the convergence time to decimetre accuracy by up to a factor of three. Positioning was seen to be more robust in comparison to GPS only PPP, primarily due to cycle slips not being present on both satellite systems on the occasions when they occurred, and the reduced impact of undetected outliers.

Acknowledgements

This research was funded by the Engineering and Physical Sciences Research Council, and Veripos/Subsea 7.

I would like to thank my supervisors Professor Phil Moore and Dr Nigel Penna for their help and guidance, as well as their feedback reading this thesis.

In addition, thanks are due to Martin Robertson for his invaluable help during the data collection, and Sam Webb and Matthew Goode for their assistance in fieldwork.

Thanks to Dr Stuart Edwards for his flexibility during the final stages of the thesis write up, in parallel with another research project.

Also I would like to recognise my colleagues in the Geodesy group at Newcastle University for their valuable discussion and advice.

Thanks also to Pieter Toor of Veripos for providing Veripos orbit and clock products, offshore GNSS datasets, as well as an industrial perspective. My thanks to Dr Tim Springer of ESA for the data and information he provided. The data and products from ESA, CODE, the IGS and the NERC BIGF network has been invaluable in completing this research.

Thanks to Captain Neale Smiles, Albemarle Barracks for arranging access to the airfield, and to members of the Lynceus survey vessel for supporting data collection in the River Tyne.

Finally, thanks to Clare for the endless support and encouragement, without whom none of this would have been possible.

Contents

List of Figures

List of Tables

Chapter 1 Introduction

1.1 Research background

Current Global Navigation Satellite Systems (GNSS) methods used to estimate position provide varying levels of accuracy and coverage. There is a demand for reliable real-time centimetre level positioning with worldwide coverage. Relative positioning methods achieve high accuracy with quick start up times using a stream of data transmitted from a nearby base station, or generated from a regional network of GNSS base stations. However, these methods are limited in operational area due to a decrease in accuracy with increasing range from the base station or regional network. In remote locations without accessible base stations, such as offshore, Precise Point Positioning (PPP) provides an alternative (Russell-Cargill, 2010). In place of the data from a reference base station or regional network, PPP uses satellite position and clock data calculated using a global network of GNSS receivers that is considerably more accurate than ephemeris data broadcast by the satellites themselves. The remaining error sources are then mitigated where possible by linear combinations of observables, physical and empirical models and estimated parameters (Zumberge et al., 1997). Although able to provide global coverage, PPP suffers from a convergence period where the attainable positional accuracy progressively improves.

Bisnath and Gao (2008) suggested that integrating the Global Positioning System (GPS) with other navigation systems such as the Russian Globalnaya Navigatsionnaya Sputnikovaya Sistema (GLONASS), European Galileo or Chinese BeiDou could provide more observations and improve the accuracy of positioning and convergence time of the PPP method. This theory was based on having an increased number of visible satellites, and improving the geometry for determining the position. Of these alternative navigation systems, currently only GLONASS contains enough satellites for functional operation, with 23 out of the planned 24 satellites already in operation. As of late 2011, both Galileo and the global segment of BeiDou are at initial testing stage.

There is a range of industrial applications for these highly accurate positioning techniques such as offshore surveying and underwater construction (Barker et al., 2002). Subsea 7 part-funded this research to gain further understanding of the potential areas for future development of their products.

Research is underway in a number of universities and commercial bodies looking at further exploitation and improvement of the PPP method. A first look at combined

GPS/GLONASS was by Cai and Gao (2007); this research showed no significant impact on PPP results with the addition of two to three GLONASS satellites that were visible at any one time in 2007. Since then the number of operational GLONASS satellites has increased from 13 to 23. The importance of high rate clock corrections was shown by Hesselbarth and Wanninger (2008) in 1 Hz PPP positioning. They showed a 1.5 to 2.5 times reduction in time to decimetre accuracy of GPS/GLONASS PPP compared to GPS only PPP when using GPS and GLONASS clock corrections tabulated at 30 s intervals. No such corrections were available, so they used phase interpolation of the low frequency clocks that were available at the time. Recently high rate GLONASS clock products have become available as part of an integrated GNSS navigation product, this allows for combined GPS/GLONASS kinematic PPP processing.

In a recent assessment of GPS/GLONASS PPP Martín et al. (2011) compared the convergence time of GPS and GPS/GLONASS PPP. They used MagicGNSS (Píriz et al., 2009) for processing 8 static IGS sites using the MagicGNSS orbit and clock products. The study is based on the convergence time for the first four hours of the first day of 2010 of the 8 globally distributed sites. Convergence in each of the North, East and Up components of position is defined as time until the estimated coordinate is within 1 cm of the reference position. The mean reduction in time to convergence was 3.1% for North, 12.5% for East and 2.1% for Height. They did not consider the relative accuracy of GPS and GPS/GLONASS PPP, and concluded that there was no significant convergence improvement during static positioning.

However, the increased number of GLONASS satellites now in operation, and the new orbit and clock products available, provide the opportunity for further investigation into the improvement of PPP performance, particularly for kinematic positioning, using GLONASS satellite observations.

1.2 Research motivations and objectives

In both scientific research and industrial activity in remote locations, there is a need for determining accurate positions within a short period of time. Positioning performance can be quantified by the following metrics: accuracy, precision, initialisation time, reliability (in terms of correctly reported accuracy), availability and continuity of positioning solution (Bisnath and Gao, 2008). These metrics are discussed further in Chapter 2.

Whilst PPP solves the availability problem for high accuracy GNSS positioning in remote locations, the initialisation time and reconvergence time following loss of signal tracking are major drawbacks with this technique.

Additional satellites offer the prospect of improved geometry and therefore the potential to reduce both the initialisation time and the reconvergence time. There is also the possibility of improved accuracy dependent on the noise present in the additional observations. Availability can be improved in locations with poor sky view due to the additional satellites present, and also frequency diversity of multiple GNSS operating on different frequencies, providing resilience against interference in a given frequency band. The addition of extra satellites by using GLONASS also brings increased operational diversity through the use of two independent systems. There is also the potential for reliability to be improved by the increase in observations leading to an increased ability to identify erroneous observations.

The recent release of the European Space Agency (ESA) combined GPS/GLONASS ephemeris products (Springer, 2010) is the first publicly available opportunity to assess GPS/GLONASS kinematic PPP. Additionally the almost complete network of GLONASS satellites (23 out of 24 planned) provides increased additional satellite numbers compared to previous studies.

The objective of this thesis is to quantify the benefits of using the GLONASS satellite network in addition to the GPS satellite network. Specifically, this research considers the improvement brought by these additional satellites with respect to the following metrics: positional accuracy, time to a given positional accuracy and reconvergence time following an outage or cycle slip. The choice of these metrics is discussed in Chapter 2.

The novel contributions of this thesis are:

- The assessment of the impact of combined GPS/GLONASS PPP using ESA and Veripos orbit and clock products.
- The comparison of real-time mode GPS only and GPS/GLONASS PPP in kinematic data sets. Previous work has only considered static sites or kinematic receivers with preprocessing to remove cycle slips.
- Quantification of the relative noise of GPS and GLONASS observations using ESA products.

Throughout this work the approach has been to complete the above comparison

for a range of real world datasets from different transport modes in order to draw representative conclusions.

1.3 Research methodology

The initial phase involved writing a program which estimates the position of the moving receiver in real-time mode using the PPP method. Although there are several existing programs, the source code was not available for modification. Therefore a new program, *pppncl*, was written to be used as a platform for the research, using routines from *Track*, a double difference post processing kinematic GPS program (Chen, 1998), as a starting point to build a PPP program. The software had to be capable of:

- Real-time mode processing of GPS datasets giving results in line with or better than existing published work for static and kinematic modes.
- Real-time mode processing of GPS/GLONASS combined satellite observation data.
- Producing outputs such that the convergence time and position accuracy could be compared for different options.

Once developed, *pppncl* output was compared to published results from other academic programs as well as the commercially available Veripos Ultra. Both static and kinematic validations were completed using a range of globally distributed sites and datasets.

The relative magnitudes of GPS and GLONASS observation noise was assessed. The impact of GLONASS on accuracy and convergence time was determined using static and kinematic datasets from several sites. Real world data from global locations was used to verify that the results are applicable on a global scale. Additionally, datasets provided by Veripos allowed testing of the software using data from an environment in which PPP is commercially deployed.

1.4 Thesis layout

Chapter 2 provides background on the types of GNSS positioning available. The basic principles of Single Point Positioning (SPP), relative positioning and PPP methods are explained. This is followed by a comparison of the methods described,

in particular considering the range of convergence times and accuracies achieved. Then follows a more detailed introduction to PPP and a review of existing research literature. An introduction is given to the existing and planned GNSS with particular focus on the GLONASS satellite system and how it compares to GPS. The chapter concludes with a discussion of the relevant metrics to assess the performance of GPS/GLONASS PPP, and the basis for expected improvement.

Chapter 3 considers the possible error sources the PPP method is subject to, and describes the relevant mitigation used in each case to enable accurate positioning. The chapter starts with discussion of satellite ephemeris and clocks, and then follows tropospheric and ionospheric effects. Next, the relativistic effects experienced by satellite clocks and the importance of satellite orientation, antenna phase centres and phase windup are considered. This is followed by an explanation of the deformation effects of the Earth body tides, ocean tide loading, atmospheric pressure loading, differential code biases and multipath errors. Finally, the residual range error budget is calculated.

Chapter 4 goes into more depth on the PPP method, describing the theory and fundamentals as implemented in *pppncl*. The chapter begins with an overview of the Kalman filter, the state vector and the design matrix, moving on to observation and parameter stochastic modelling and finally, the approach taken to observation quality control.

Chapter 5 describes the *pppncl* software created during this investigation. This gives a high level overview of the software design and in particular the considerations needed for including GLONASS in a PPP program. A detailed description of the user interface and input and output formats is given in Appendix A.

Chapter 6 describes the validation of the PPP software, *pppncl*, created. This includes static validation across a range of globally distributed sites. Next, validation of kinematic datasets is described and results compared to published work.

Chapter 7 looks at the effect of incorporating GLONASS observation data into the PPP method. The GLONASS observation noise is evaluated, and the orbit and clock products described. Next, the main research objective, understanding the impact of using GLONASS combined with GPS satellite observation data on positioning quality, is investigated. The chapter steps through this comparison for a range of datasets collected from different transport modes.

Finally, Chapter 8 presents a summary of the conclusions drawn from this research

and introduces some suggestions for further work in this area.

Chapter 2 Types of kinematic GNSS positioning and navigation

At a high level the fundamental performance of a navigation system can be characterised by four essential criteria (ICAO, 2005):

- Accuracy,
- Integrity,
- Continuity,
- Availability.

Accuracy is the difference between the estimated position and the true position, specified with a certain confidence.

The integrity of a system is the level of trust that can be placed in the output of that system. In some applications such as aircraft positioning, integrity includes the ability of the system to alert the user when the accuracy is worse than defined operational limits (Ochieng et al., 2003).

Continuity is the probability that accuracy and integrity will be maintained for a certain period into the future.

For a navigation system to be useful it must achieve a required level of accuracy, integrity and continuity to perform the chosen task. The availability of a system is the proportion of time during which it is able to provide this level of service.

With this framework in mind, this chapter examines the principles of GNSS positioning, and how the error budget defines the performance of a positioning method. The distinct classes of GNSS positioning techniques used to reduce the error budget to achieve improved performance are discussed. Additionally the advantages and disadvantages of each technique are considered, along with further metrics that may be useful in understanding the limitations and strengths of each system.

The final part of this chapter briefly discusses the current and planned GNSS. In particular the differences between GPS and GLONASS are reviewed, followed by the expected effect of combining GPS and GLONASS in PPP. The chapter concludes with an examination of the particular metrics relevant to characterising the impact of combined GPS/GLONASS PPP.

2.1 GNSS positioning, error budget and methods

A position can be determined by measuring the range from the rover receiver point to a set of GNSS satellites in orbit around the Earth, using the signals transmitted from each satellite. A brief introduction to GNSS positioning is given here, for further background information to GNSS the reader is referred to Hofmann-Wellenhof et al. (2008) and Leick (2004).

The satellites contain clocks which are used to control the generation of one or more coded signals which are then transmitted on one or more radio frequencies. A receiver that knows the transmitted code and the time of generation can measure the reception time of that code against its local clock. This allows the receiver to determine the propagation time of the signal from the satellite to the receiver. The observed propagation time can be converted to a range measurement by multiplying by the speed of light in a vacuum.

This measured range is not the geometric range from satellite to receiver, but a measure containing the receiver satellite range in addition to other biases. For this reason the measured ranges are known as pseudoranges. If the satellite positions and clock offsets are known then each pseudorange observation describes the surface of the sphere upon which the receiver may lie. With three or more observations the location of the receiver in 3D space can be determined. In practice four or more observations are needed in order to also account for the receiver clock offset.

The biases in the pseudoranges are often considered as errors, as failing to account for them leads to a reduction in positioning accuracy. There are several classes of error including: errors in the values of the satellite position and clock offset; physical effects that delay or advance the signal compared to a propagation model based on a straight line path moving at the speed of light in a vacuum; and receiver measurement errors. There are a further set of errors introduced by the definition of the coordinate system, both in the accuracy of its definition, and due to Earth deformation effects that are taken into account in the definition of the reference frame. Finally, multiple reflected signals interfering at the receiver introduce a source of noise which is highly dependent on the local environment.

The combination of all these effects gives the error budget for the measurements made by a receiver. This error budget can be related to the accuracy of the estimated position as discussed in Section 4.9.1. To improve the accuracy of positioning, the errors contained within observations must be minimised. There are several methods

of GNSS positioning that aim to correct, or accept the limitations of ignoring, these errors. The key concepts of some common GNSS positioning methods are described in the following sections.

2.2 SPP

Single Point Positioning (SPP) is the simple default form of GNSS positioning. This form only requires a GNSS receiver, no extra infrastructure is required. Satellite navigation information (orbits and clocks) is broadcast by the satellites and updated every 4 hours. The accuracy of this broadcast is low due to limitations of the format and the widely spaced update time. The quality of the orbits is generally the limiting factor in positioning so most other error sources are ignored. An ionospheric model is also broadcast which helps single frequency receivers mitigate approximately 50% of the range bias due to the ionosphere.

The User Equivalent Range Error (UERE) is the combination of the Signal In Space (SIS) User Range Error (URE) (an estimate comprising orbit data, satellite clock, ionospheric and tropospheric delay), errors introduced by the user equipment, as well as local environment errors. Typical values for the UERE are given in Table 2.1. The total column is formed from the root sum of squares of the bias and random quantities. The UERE is an estimate of the standard deviation of the measurement error.

Error source	Bias (m)	Random (m)	Total (m)
Orbit data	2.1	0.0	2.1
Satellite clock	2.0	0.7	2.1
Ionosphere	4.0	0.5	4.0
Troposphere	0.5	0.5	0.7
Multipath	1.0	1.0	1.4
Receiver measurement	0.5	0.2	0.5
UERE	5.1	1.4	5.3

Table 2.1: UERE computation (Hofmann-Wellenhof et al., 2008)

The receivers measure the code observations giving a pseudorange to the satellite. With four or more satellites in view, the 3D position and receiver clock offset may be solved for. This method of GNSS positioning is most commonly used in consumer applications such as in-car navigation and smart phones.

2.3 Relative positioning

Relative positioning makes use of the fact that many of the error sources that bias the receiver to satellite range measurements are spatially correlated. Using one or more reference stations at known positions, the errors affecting measurements at the rover can be corrected for. All relative positioning methods need at least one simultaneously observing reference station, and for real-time applications, a data link. This imposes limitations on operating areas, for example offshore use is not practical as there are no nearby reference stations. Three common forms of relative positioning are described here: Differential GNSS (DGNSS), Real-Time Kinematic (RTK) and Network RTK.

2.3.1 *DGNSS*

The simplest form of relative positioning is DGNSS. As mentioned, this method requires a simultaneously observing reference station at known coordinates near the rover. There are then two methods which can be used to provide corrections for use at the rover. In one case, state space, the current set of observations is used to work out the offset between the current GNSS derived coordinates and the actual coordinates of the base station. This offset can then be used to correct the GNSS derived coordinates of the rover. Alternatively, the code observations from the base station are sent to the rover. The difference between the rover observation and the reference observation is used to position the rover with respect to the base station. This new measurement is free from the common errors affecting measurements at both the rover and reference station. Monteiro et al. (1999) showed the DGNSS horizontal coordinate error (95% confidence) is equal to 0.5 m to 1 m near the reference station plus 0.2 m for each 100 km from the reference station.

2.4 Carrier phase positioning

The methods described so far use the code phase pseudorange as the observable in the position estimation calculation. Even high end geodetic receivers can only measure this with at best decimetre accuracy (Groves, 2008). The code phase is also susceptible to large errors caused by multipath due to the frequency of the code chipping rate (Hofmann-Wellenhof et al., 2008). It is also possible to measure the phase of the carrier wave onto which the code signal is modulated. The carrier phase

can be measured by receivers with an root mean square (RMS) error of 0.5° to 2° depending on the signal to noise ratio which corresponds to millimetre accuracy in range (Braasch and Van Dierendonck, 1999).

The carrier phase is an ambiguous measurement due to the sinusoidal nature of the carrier wave. Pseudoranges can be obtained from the carrier phase by the addition of a time-independent phase bias. Complicating matters is the potential for cycle slips: these are integer discontinuities in the bias caused by the receiver losing lock on the signal. If the bias can be determined or estimated then the more precisely measurable carrier phase may be used in addition or instead of the code phase. The major advantage of the carrier phase compared to the code phase is the increased measurement accuracy and the reduction in the multipath effect (Hofmann-Wellenhof et al., 2008).

The bias b may be split into two parts, $b = b' + N$ where N is the integer part, commonly known as the carrier phase ambiguity or simply ambiguity, and b' is the fractional part. There are two classes of positioning based on how b is determined. If b is estimated directly then it is known as ambiguity float, and the integer and fractional part are estimated as one. If instead the integer and fractional part can be separated, and the integer part N estimated, the technique is referred to as ambiguity fixed. The following sections describe the different techniques that make use of the carrier phase.

2.4.1 *RTK*

RTK positioning involves a base station transmitting its code and carrier phase observations to the rover. Receiver specific errors are removed by differencing observations between two satellites forming a single difference observation. Satellite specific errors are removed by differencing the previously described single differences from the rover and the base station; this is known as a double difference observation. Over short baselines the double difference removes all errors sufficiently that the correct set of carrier phase integer ambiguities can be found. At longer baselines the errors seen at the rover and base station, particularly due to the troposphere and ionosphere, are no longer sufficiently similar for the integer ambiguities to be resolved. RTK has been shown to work effectively up to baseline lengths of approximately 10 km to 20 km.

2.4.2 *Network RTK*

Network RTK (NRTK) extends the concept of RTK to a system with multiple base stations. This allows the spatial variability in the errors to be accounted for based on the rover's location relative to the set of base stations. There are two common forms of NRTK: Virtual Reference Station (VRS) and Master Auxiliary Concept (MAC). Both approaches attempt to reduce the amount of information required to be sent to the rover.

In VRS, the observations are combined in the network processing stage to produce a new set of observations at a virtual reference station at, or very close to the receiver position. This virtual set of observations contains the expected errors at the rover based on the current set of reference station measurements. Standard RTK is then performed using the VRS as the base station. This approach ensures the distance between the rover and the reference station will be short enough for integer ambiguity resolution.

In MAC, the complete set of observations from one master reference station and the atmospheric, orbit and clock errors estimated by the network for the surrounding auxiliary stations, are transmitted to the rover (Euler et al., 2002). Thus the spatial distribution of the errors may be interpolated by the rover relative to the master station, or the observations at the auxiliary stations may be reconstructed allowing for a multi-baseline solution.

The accuracy of NRTK methods is typically (one-sigma) 10 mm to 20 mm in plan and 15 mm to 35 mm in height, similar to RTK, however the range is extended to that covered by the network of reference stations (Edwards et al., 2010).

2.5 PPP

Zumberge et al. (1997) introduced and then Kouba and Héroux (2001) developed the technique of PPP using undifferenced code and carrier phase observations from dual frequency receivers. Rather than using differences between receivers and satellites to reduce the error budget, PPP uses external correction products and models for the error sources.

The starting point for PPP is orbit and clock products accurate to within a few centimetres. These can be produced from a global network of receivers; this then enables positioning of a receiver anywhere in the world. Using ionosphere free linear

combinations of the code and phase observables, along with models for predominant error sources, Zumberge et al. (1997) showed it was possible to reduce the error budget sufficiently to enable centimetre accurate static positioning. A full examination of the error sources and applicable models is given in Chapter 3.

In a review of the status of PPP, Bisnath and Gao (2008) found little in the way of biases in position estimates, so there is little difference between the precision and the accuracy. North and East one sigma level position errors were a few centimetres in static and decimetre level in kinematic mode (Bisnath, 2004; Dixon, 2006; Gao et al., 2005; Muellerschoen et al., 2001).

When using PPP for position estimation there are some key metrics that can be used to evaluate its performance, these include accuracy, integrity and continuity, as introduced at the start of this chapter. There is an additional metric that needs to be evaluated in the case of PPP, known as convergence time. This is the time for the estimated position to reach a given accuracy. Various authors have chosen different metrics for convergence time, so that inter-comparison of results is not straightforward. Metrics proposed have included time to decimetre-level (Bisnath and Gao, 2008) or centimetre level accuracy (Martín et al., 2011), and accuracy after a given time period (Colombo et al., 2004; Zumberge et al., 1997).

Due to the unknown fractional part of the ambiguity at the satellite, the carrier phase ambiguities are estimated as floating. Initially the position accuracy is entirely dependent on the code phase observations. This results in initialisation times of approximately 30 min for decimetre level accuracy and significantly longer for centimetre level accuracy, reflecting the time taken for the ambiguities to be sufficiently determined (Bisnath and Gao, 2008).

Gao and Shen (2002) introduced an alternative observation model that uses combined code and carrier phase observations, in addition to the ionosphere free carrier phase combination. In this model two float ambiguities are estimated for each satellite. Out of 36 one hour static datasets from the Canadian Active Control Station PRDS, three of the datasets that did not converge below the metre level with the standard method described by Héroux et al. (2004), did converge to decimetre accuracy using the alternative observation model.

Colombo et al. (2004) evaluated the performance of kinematic PPP using 30 s clock products. They noted 3D RMS position errors of 4.6 cm to 9.3 cm with typically a 30 min to 40 min or longer convergence period. They proposed using a "stop and go" survey method where the receiver is held fixed at known coordinates in order to

reduce the initial convergence time before kinematic operations continued.

In kinematic positioning there is a need for high rate clock products, ideally at the positioning estimation rate, so that the short term variability in the satellite clocks is captured and corrected for (Colombo et al., 2004). Hesselbarth and Wanninger (2008) examined the stability of the satellite clocks for use with PPP and found that there was minimal change in the kinematic coordinate error RMS when using 30 s tabulated clock corrections as opposed to 10 s tabulated corrections.

There are a range of groups, including the International GNSS Service (IGS) analysis centres and commercial providers, that produce the required precise orbit and clock products at a range of latencies from near real-time to two weeks delayed. The use of additional data in processing means the delayed products are more accurate.

Investigations have focussed on reducing the error budget, this includes more accurate orbits and clocks, as well as improved error source models. In order to reduce the error introduced by the atmosphere, a tropospheric delay parameter is usually estimated and linear combinations of observables are used to reduced the effect of the ionosphere (Kouba, 2009a). Using precision atmospheric products could reduce the number of unknown parameters or remove the need for the linear combinations that increase observation noise, and show the potential to improve positioning performance (Dodd, 2007; Keshin et al., 2006). Whilst steps are being made in this direction, for example the European ionosphere forecast (Belehaki et al., 2006), producing sufficiently accurate range corrections (better than a few centimetres) remains a challenge (Bisnath and Gao, 2008).

The convergence period present in PPP affects the achievable accuracy at a given time since the start of navigation. Therefore for a given accuracy, the length of the convergence period to that accuracy directly affects the availability. Any event which requires the carrier phase biases to be re-estimated, such as temporary obstruction of the sky, high receiver dynamics or interference causing loss of lock, introduces a period of reconvergence. This reconvergence is an interruption in the continuity and reducing the length of this period would improve the overall performance of the system.

In kinematic PPP the interruption of a satellite signal is both much more likely than the static case and is more problematic (Grinter and Roberts, 2011). Therefore there has been significant work on identifying and correcting cycle slips. For real-time applications methods involving curve fitting across discontinuities of carrier-phase observations (Beutler et al., 1984) or of linear combinations of observations (Bisnath,

2000; Blewitt, 1990) are not feasible.

Banville and Langley (2010) demonstrated a method using time-differenced linear combinations of observations and then applying ambiguity fixing techniques developed in relative carrier phase positioning to solve for the cycle slips (Teunissen, 1995). In static positioning they showed 99% success rate in correctly fixing simulated cycle slips. In a kinematic test on a survey vessel the success rate varied from 100% at a 1 s sampling interval, to 7.1% at a 30 s interval. The reduced performance in kinematic mode at longer sampling intervals was attributed to decorrelation of the multipath effect on the code phase, and the effect of unmodelled receiver phase windup (Banville and Langley, 2010).

Multipath, cycle slips, malfunctioning satellites and erroneous navigation data are all mechanisms through which the measurement accuracy could exceed the expected error budget. Including such outliers negatively affects the accuracy, hence detecting these outliers is required to achieve both accuracy and integrity. Bisnath and Gao (2008) highlight the current poor state of PPP integrity checking as compared to relative GNSS methods. There is no external quality reference as in Network RTK where positions can be computed to several of the network base stations.

Teunissen (1990) describes a standalone technique based on the comparison of observation residuals to their expected distribution to detect and identify outliers. Receiver Autonomous Integrity Monitoring (RAIM) is a technique regularly used in code phase navigation based on residual checking against a test statistic. The redundancy available in the system when more than four satellites are visible is used to remove observations to obtain a given protection level. Feng et al. (2009) demonstrate the possibility to extend the RAIM concept to use carrier phase observations, however as yet this has not been extended to the PPP method.

Apart from filter position covariance estimates, quantitative quality measures of the obtained results are limited. The estimation filter covariance estimates tend to be optimistic by comparison with the true error in positional accuracy. This is largely due to the time correlated nature of many of the error sources which is ignored in the filter. Correctly determining the residual observation noise after modelling allows the generation of more realistic uncertainties for the estimated coordinates. Therefore the estimation of the residual error budget, discussed in Chapter 3, is important to achieving integrity.

For real-time PPP the reliability of transport for the correction stream is critical to the availability of the method. For real-time use the IGS real-time working group

are distributing open access real-time orbit and clocks products in NTRIP format over the internet (Weber et al., 2007). Commercial bodies provide real-time clocks distributed by satellite links to ensure global reach (Rocken et al., 2011).

After initialisation, PPP achieves good availability when used in a continuously unobstructed open sky environment. However in an environment where the sky view is regularly obstructed, for example under trees or bridges, the necessary reinitialisation results in a reconvergence period similar to the initialisation period. Equally the reduced satellite number and resulting poor geometry in, for example, urban locations, can significantly increase the convergence time. Despite these shortcomings, PPP has been used in many areas where centimetre static or decimetre accurate kinematic positioning is required, particularly in areas where there is no local network of reference receivers. Some static geodetic applications include crustal deformation monitoring (Zumberge et al., 1997) and glacial isostatic rebound measurements (Thomas et al., 2011); scientific kinematic applications include positioning low earth orbiters (Bisnath, 2004); commercial applications include precision farming (Dixon, 2006), marine sensor positioning, sea floor mapping, marine construction (Arroyo-Suarez et al., 2005; Rocken et al., 2011) and airborne mapping (Gao et al., 2005).

In summary, PPP has a wide range of uses, but convergence time and reconvergence time is still a major issue. Two complementary approaches have been investigated: fixing the ambiguities to integer values is discussed in the following section, and integrating GPS with other navigation systems such as GLONASS, covered in Section 2.8.

2.5.1 *PPP with ambiguity resolution*

The carrier phase ambiguities that must be estimated during PPP positioning can be split into three parts. These are an integer part, and two Fractional Cycle Biases (FCBs), one associated with the transmitting satellite and the other associated with the receiver, $b = b^j + b_i + N$.

If both fractional biases can be determined, then it would be possible to use the same search techniques as employed in relative carrier phase positioning to determine the integer part. Fixing the integer part to the correct value is desirable as it removes the need to estimate the carrier phase ambiguity. The carrier phase can then be used as an unambiguous measurement in the same way as the code phase, but with a measurement accuracy at the millimetre rather than metre level.

Collins (2008), Ge et al. (2008) and Laurichesse et al. (2009) showed that with additional network processing it is possible to separate out the satellite FCBs which can then be used by other receivers, not part of the original network, to fix undifferenced carrier phase ambiguities to integer values.

Ge et al. (2008) decomposed the ambiguity into widelane and narrowlane ambiguities. By taking differences between satellites, they remove the receiver dependant FCB. Then using average values for the Melbourne-Wübbena linear combination of code and carrier phase (Melbourne, 1985; Wübbena, 1985) from complete satellite passes for a set of receivers in a global or regional network, the widelane FCBs can be determined for each satellite. Widelane FCBs are very stable for days or weeks at a time (Gabor, 1999; Gao and Wang, 2008) so daily estimated values can be used. In a similar manner the narrow lane FCBs were determined by averaging the fractional part of estimated narrow lane ambiguities, formed from the combination of the ionosphere-free carrier phase linear combination, and the previously determined widelane ambiguities.

As the narrow lane FCBs are not stable with time, producing a set of average values every 15 minutes was proposed (Ge et al., 2008). Fixing ambiguities in PPP then follows a similar process to the network fixing step, first, the single difference widelane biases are fixed, having corrected for the satellite widelane FCBs using the values previously determined in the network solution. Then the narrow lane ambiguities and their standard deviations are calculated based on the float values from the position estimation process and the fixed widelane biases. The narrow lane ambiguities can now be fixed to integers if the standard deviation is low enough based on a statistical test that the probability of the narrow lane ambiguity be equal to its nearest integer (Dong and Bock, 1989). Alternatively, the LAMBDA decorellation method can be used together with a ratio test between the two best fit sets of narrow lane ambiguities (Teunissen, 1995).

Laurichesse et al. (2009) proposed an approach that determines the widelane FCBs in the same way but does not estimate narrow lane FCBs. Instead, during the network estimation stage, the narrow lane biases are directly fixed to integers and the narrow lane FCB is absorbed into the estimated satellite clock product. Collins (2008) demonstrated a method that decouples the carrier phase and code phase receiver clock estimate by estimating one term for each and then fixing wide and narrow lane ambiguities as in Laurichesse et al. (2009). Both these methods result in the narrow lane FCB being absorbed in the satellite clock estimate and hence the generated clock products have been named Integer Recovery Clocks (IRCs) (Geng

et al., 2010b).

Fixing the PPP narrow lane ambiguities at a single receiver is then simpler than the method proposed by Ge et al. (2008), as the narrow lane satellite FCB correction is already contained in the clock products.

In a comparison of the two approaches Geng et al. (2010b) showed that in static 24 hour positioning both methods performed with equivalent accuracy. The mean RMS position error (compared to the IGS weekly coordinates) of 350 sites for 2008 reduced in the East, North and Up components from 3.4 mm, 2.2 mm and 6.2 mm, to 2.0 mm, 2.1 mm and 5.9 mm, respectively.

Geng et al. (2010c) showed that ambiguity fixed PPP can improve the accuracy of static positioning after one hour, reducing the 3D RMS from 5 cm to 1.6 cm. This is due to the step change in accuracy at the point of fixing ambiguities. However, the time taken until ambiguities are fixed can be lengthy; for example Laurichesse et al. (2009) state this to be around 30 min for static positioning, but around 1.5 h for kinematic positioning with a static initialisation preferred. Such latencies arise from the time taken to sufficiently accurately determine the narrow lane biases as float values to enable them to be reliably fixed to integers, as required by PPP ambiguity resolution.

Li et al. (2011) showed that interpolating the zero difference atmospheric biases found at base stations in a regional network during ambiguity fixing could be used to provide instantaneous PPP ambiguity resolution at a rover within the network. The average baseline used in their test was 60 km and the validity of this approach at larger distances (such as offshore on a survey vessel) is unlikely due to the decorrelation of atmospheric biases with increasing distance.

Geng et al. (2010a) showed the possibility for rapid reconvergence following cycle slips or loss of lock. First the the ionosphere delay is estimated once the ambiguities have been fixed using linear combinations of the carrier phase. Then, following loss of lock instead of using the noisy Melbourne-Wübbena combination to fix the widelane ambiguity, the predicted ionosphere delay is used to correct the widelane combination. It is then possible to estimate the wide lane ambiguity directly by constraining the position using the ionosphere free code phase observation. Using this technique Geng et al. (2010a) showed an improvement in the number of ambiguity fixed epochs during a moving vehicle trial from 7.7% to 93.6%.

CNES produce a GPS orbit and clock product using the IRC method suitable for

ambiguity fixing (Laurichesse, 2011). This is available as a real-time stream or as archived navigation data.

2.6 Comparison of GNSS methods

Table 2.2 summarises the accuracy and initialisation time of the GNSS kinematic methods discussed previously. As shown, PPP is the only option for global stand-alone centimetre positioning. However the method suffers from a long initialisation time and reinitialisation is required after loss of lock, which is particularly a problem for real-time users. Whilst ambiguity fixed PPP offers improved accuracy and the potential for very short reconvergence times, any technique that could improve the float solution convergence time would not only benefit the user position, but also decrease the time to ambiguity fixing, by enabling the faster initial accurate determination of the narrow lane biases.

Method	Range	Accuracy	Initialisation time
SPP	Global	Several metres	None
DGNSS	Local	Metre level	None
RTK	Local	Centimetre	Up to 2 min
NRTK	Regional	Centimetre	Up to 2 min
PPP	Global	Centimetre to decimetre	Up to 90 min
Fixed PPP	Global	Centimetre to decimetre	Up to 90 min

Table 2.2: Comparison of GNSS positioning methods

2.7 Global navigation satellite systems

There are currently four proposed or existing Global Navigation Satellite Systems (GNSS): the American GPS, Russian GLONASS, European Galileo and the Chinese BeiDou. These are all independent systems aiming to provide global coverage for positioning, navigation and time transfer. In this section the differences between these systems are described and the considerations that must be made in combining multiple GNSS are discussed.

Galileo has just reached the In-Orbit Validation (IOV) phase with two satellites launched in mid October 2011. These satellites are designed to validate both the space and ground based components of Galileo; further satellite launches are planned to reach Initial Operational Capability (IOC) by mid-decade, and Full Operational Capability (FOC) by 2020 (ESA, 2011).

The first satellite of the BeiDou system was launched in April 2007, since then further launches have consisted of geostationary and high Earth orbit satellites centred over China. Further satellite launches to medium Earth orbits that will provide global coverage are planned to be completed by 2020 (Beidou, 2011). Galileo and BeiDou do not currently provide a global service and will not be discussed in further detail in this thesis.

The first GPS satellite was launched in 1989 with IOC reached in 1993 when 24 satellites were operational. FOC was achieved in 1995 with 24 satellites once the initial Block I satellites had all been replaced. GPS satellites are arranged in medium Earth orbits in one of 6 orbital planes.

GLONASS initially reached FOC in 1996 with 24 satellites, however due to a lack of funding, the number of available satellites declined to six to eight satellites in 2001 (Hofmann-Wellenhof et al., 2008). Since then the system has been maintained to reach 23 satellites.

	GLONASS	GPS
Constellation		
Number of orbital planes	3	6
Semi-major axis	25 510 km	26 580 km
Orbital height	19 130 km	20 200 km
Orbital period	11 hr 15.8 min	11 hr 58 min
Inclination	64.8°	55°
Distinguishing satellites	FDMA	CDMA
Signal Characteristics		
Carrier frequencies	$1602 + k * 0.5626$ MHz	1575.42 MHz
	$1246 + k * 0.4375$ MHz	1227.60 MHz
Code frequencies	ST code: 0.511 MHz	C/A code: 1.023 MHz
	VT code: 5.11 MHz	P code: 10.23 MHz
Reference System		
Reference frame	PZ-90	WGS-84
System time	GLONASS time	GPS time

Table 2.3: Key differences between GLONASS and GPS

The key characteristics of GPS and GLONASS systems are detailed in Table 2.3. The implications of these characteristics on positioning, and the considerations that must be made in combining both systems in one positioning solution are discussed below.

All GPS satellites use the same set of carrier frequencies and make use of the Code Division Multiple Access (CDMA) method to identify each satellite. This means that each satellite generates a different set of code transmissions with which the receiver can identify each satellite. GLONASS uses Frequency Division Multiple Access (FDMA) to identify the signal from each satellite. This means that all the satellites transmit the same pseudo-random noise code signal, but each on a different frequency. As only half the satellites are ever visible from any point on the Earth, the satellites at opposite points of an orbital plane share the same frequency (ICD GLONASS, 2008).

The two frequencies transmitted by each GLONASS satellite are based around two base frequencies. The nominal values of the L1 and L2 carrier frequencies are defined as follows:

$$f1_k = f1_0 + k\Delta f1 \tag{2.1}$$

$$f2_k = f2_0 + k\Delta f2 \tag{2.2}$$

where k is the channel number of the corresponding satellite. The constants are $f1_0 = 1602\,\text{MHz}$, $\Delta f1 = 562.5\,\text{kHz}$, $f2_0 = 1246\,\text{MHz}$ and $\Delta f2 = 437.5\,\text{kHz}$.

The channel number of each satellite is provided in the almanac which is broadcast as part of the GLONASS navigation message. All satellites launched after 2005 use values of k in the range of -7 to $+6$. The ratio of the two carrier frequencies $f1/f2 = 9/7$ is constant for all k (Leick, 2004, pg. 87) and is very similar to the ratio for GPS of 154/120.

In a CDMA system, any frequency dependent bias introduced by the receiver hardware will be the same for a given signal from all satellites. As this bias is constant across all satellites the effect is inseparable from a bias in the receiver clock. In FDMA systems, such as GLONASS, this bias would be different for each satellite. In an analysis of the effect of this bias on the ionosphere free code phase combination (Equation 4.18), Reussner and Wanninger (2011) conclude that "the effect is mainly frequency dependent but seems to be receiver individual and cannot be modelled with a simple linear function". This effectively reduces the accuracy with which the GLONASS code phase can be observed with biases of up to 6 m measured.

In a network analysis of 133 GPS/GLONASS receivers Wanninger (2011) found large carrier phase bias differences between equipment from different manufacturers. In general, the biases could be modelled by linear functions of frequency and were

similar for both frequencies and for receivers of the same type. The biases appear stable over time and Wanninger (2011) found no temperature dependence when comparing bias estimates produced 6 months apart.

These additional biases complicate the use of GLONASS satellites for precise positioning. If they are ignored then this increases the error budget of the observed pseudoranges. For float PPP any constant bias can be grouped with the ambiguity and considered a single term so the carrier phase biases will not affect the positioning solution.

Due to the wider band of radio spectrum used by the GLONASS FDMA signals, GLONASS is more resistant against narrow-band interference compared to GPS (Hofmann-Wellenhof et al., 2008).

GLONASS satellites have an orbital inclination of 64.8°, compared to the GPS orbital inclination of 55°; this provides better coverage at higher latitudes. Specifically in Arctic and Antarctic regions GLONASS satellites will reach higher elevation angles.

When specifying the location of a satellite, it must be done with reference to some underlying coordinate system. Similarly for the satellite clock offset, it must be specified with respect to a time system. Both GPS and GLONASS satellites broadcast satellite orbit and clock information in their own reference systems and time scales.

The GPS terrestrial reference system is WGS-84 (IS-GPS-200E, 2010). GPS time was set to match UTC in 1980 but is not corrected to match the rotation of the Earth by the addition of leap seconds. GPS time therefore is at a constant offset of $-19\,\mathrm{s}$ compared with International Atomic Time (TAI). The GLONASS reference system is known as PZ-90 and the time system is GLONASS time. GLONASS time is closely related to UTC but has a constant offset of three hours. Apart from this offset, GLONASS time is kept within 1 millisecond of UTC.

If using GPS and GLONASS satellite coordinates and clock offsets, as transmitted in broadcast navigation, a transformation must be made so that both sets of data are in the same time system and referenced to the same time scale. There have been many attempts to derive transformation parameters between WGS-84 and PZ-90, in particular the IGEX campaign produced several solutions that were consistent at the decimetre level (Boucher and Altamimi, 2001). The accuracy with which such a transformation is able to capture the potentially time varying differences has a direct

impact on the accuracy of the used satellite coordinates and clock offsets. This must be taken into consideration when estimating the pseudorange error budget if using broadcast orbits and clocks.

In September 2007 the PZ-90 reference frame was adjusted to align more closely with the International Terrestrial Reference Frame 2000 (ITRF 2000) (Revnivykh, 2007). WGS-84 is regularly adjusted to maintain close alignment with the ITRF and therefore differences in terrestrial coordinates between the two systems are now consistent to within 2 cm (Hegarty and Chatre, 2008).

An alternative to making such a transformation is to directly estimate the GPS and GLONASS ephemeris data and clock offsets in the same reference frame. In ephemeris products produced by ESA the satellite positions for both systems are given in ITRF (Springer, 2010).

There are 23 operational GLONASS satellites as of 18 June 2011 and, as can be seen from Figure 2.1, this provides almost complete global coverage.

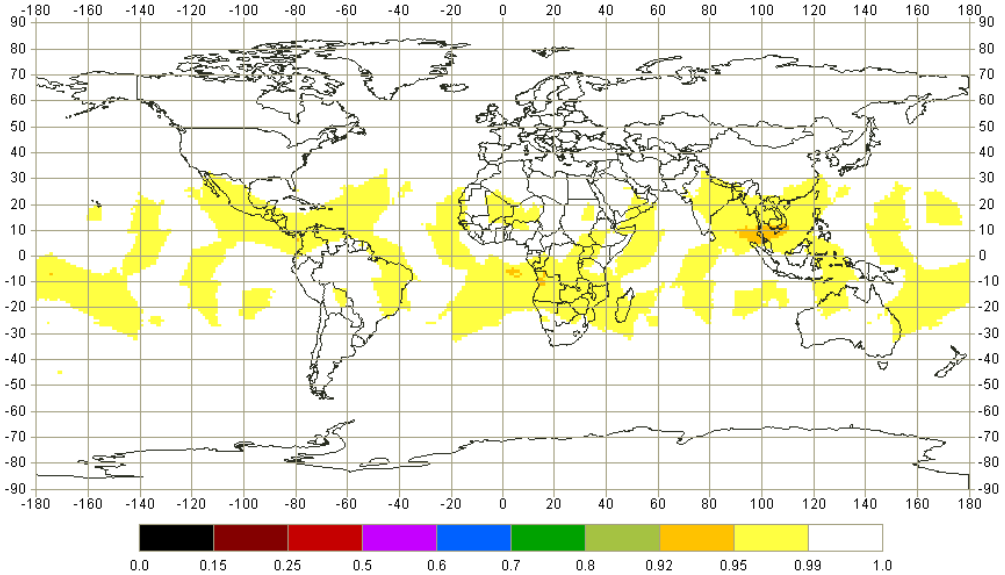

Figure 2.1: GLONASS availability showing the fraction of time during which the dilution of precision is below 6 on 18 June 2011. Source `http://www.glonass-center.ru/en/GLONASS/CumulativeAvailability.php`

The GPS orbital period results in the ground track of a particular GPS satellite repeating once every sidereal day. This causes a resonance between the satellites' orbital periods with variations in the Earth's gravity field. This resonance can create orbital perturbations of up to 4 m (Ferreira and de Moraes, 2009). To counteract this, the satellites must be manoeuvred regularly to keep them close to their nominal

orbit. The ground track of the GLONASS satellites repeats every 8 days, avoiding the resonance experienced by the GPS satellites.

In summary, compared to GPS, GLONASS has additional biases on the code phase and carrier phase due to the FDMA method used. There is a receiver inter-system bias composed of receiver hardware delays and the GPS/GLONASS time system offset. The GPS and GLONASS terrestrial reference systems are different, but using precise orbit and clock products for both systems that are produced in the same reference system eliminates this difference.

2.8 GPS/GLONASS PPP

Bisnath and Gao (2008) suggested that integrating GPS with other navigation systems such as GLONASS, or in the future, Galileo or BeiDou, could provide more observations and improve the accuracy of positioning and convergence time of the PPP method. This conjecture was based on having an increased number of visible satellites, and hence improving the geometry for determining the position. Píriz et al. (2009) undertook a limited test on the accuracy of short-occupation static PPP, by processing 1 hour of data from 20 IGS stations collected on 14 June 2009 using the magicGNSS software (Píriz et al., 2008), and found that the horizontal accuracies of static batch least squares 1 hour PPP solutions improved from around 10 cm for GPS-only, to around 5 cm for GPS/GLONASS. However, a similar analysis by Martín et al. (2011) of 1 hour batch static sessions with the same software, using one day of data from 1 January 2010 for eight IGS stations, showed no improvement for GPS/GLONASS over GPS-only.

A kinematic mode GPS/GLONASS processing of data obtained on 26 April 2007 at three static IGS stations was carried out by Cai and Gao (2007), but they concluded that no significant improvement to position was obtained by also including data from the small number (nine) of GLONASS satellites that were then active. A full kinematic GPS/GLONASS PPP convergence study was reported by Hesselbarth and Wanninger (2008), suggesting improved convergence over GPS-only PPP (using an incomplete GLONASS satellite constellation). However, the roving receiver's data first had to be pre-processed relative to local reference stations, in order to repair cycle slips (the high-rate reference station data were also used to provide high-rate satellite clocks through carrier phase interpolation). Therefore this study only served to demonstrate GPS/GLONASS PPP potential.

Pertinent to the inconclusive outcomes from these previous studies is that during 2010, nine new GLONASS satellites started transmitting data (one was withdrawn) to result in an active satellite constellation of 23, and high-rate (30 second) GLONASS satellite clock values were made freely available by ESA (Springer, 2010). These developments provide motivation for further investigation of the impact of adding GLONASS observations to GPS kinematic PPP, with emphasis on reductions in kinematic convergence time and solution robustness when supplementing GPS with GLONASS tracking.

In principle it is possible to extend PPP ambiguity resolution to include GLONASS satellites. Reussner and Wanninger (2011) showed that by using global ionosphere maps it is possible to fix undifferenced widelane ambiguities in a geometry-dependent way. The GPS method of using the geometry free Melbourne-Wübbena combination was not possible due to receiver specific code phase biases. Reussner and Wanninger (2011) also showed the need to calibrate inter-channel carrier phase biases which are not currently well understood. At this stage there is currently no publicly available GPS/GLONASS product suitable for use in ambiguity fixed PPP, and as such ambiguity fixed PPP is not considered further in this thesis.

2.9 Metrics relevant to GPS/GLONASS PPP

In order to assess the impact of combining GLONASS with GPS on the performance of PPP it was necessary to select relevant performance metrics. The following metrics were chosen with reasons for their selection also provided.

The convergence time is the time for the positional accuracy to reach a minimum required level from the start of positioning. The convergence time was expected to improve due to the increased number and improved geometry of the combined satellite constellation.

Accuracy is a fundamental aspect of any navigation system. The accuracy of the estimated positions is considered both in terms of the contribution of the improved satellite geometry and as a measure of the convergence time. The additional satellites with GLONASS serve to improve the geometry of the satellite observations, as described in Section 4.9.1, this geometry links the error budget to the positional accuracy, and therefore accuracy is a relevant metric to assess in the context of GPS/GLONASS PPP.

Sturza and Brown (1990) showed that the combination of GPS and GLONASS im-

proved RAIM availability at a given protection level. Additionally the increased number of satellite observations available reduces the impact of any outliers on the estimated position. Therefore it is relevant to assess the impact of the additional satellites on outlier detection and performance of GPS/GLONASS PPP in the presence of outliers.

The addition of GLONASS would be expected to bring improved reliability due to the use of a second independent system. Further, obstructions and cycle slips that reduce the usable number of satellites would have a smaller effect when GLONASS is used, thus improving the continuity because the critical number of satellites is more likely to be maintained.

The metrics described here form the framework for the tests used in the analysis of the performance of combined GPS with GLONASS, presented in Chapter 7.

2.10 Summary

This chapter has outlined the principles of several GNSS methods, and the different approaches to minimising the error sources in order to achieve the required level of accuracy, depending on application and environment. This shows the value of PPP, the only method able to provide global centimetre accurate positioning. An overview of the research into PPP has been given, as well as examining the recent developments including ambiguity fixed PPP. Whilst this method offers improved accuracy, PPP still suffers from long convergence times.

A comparison of GLONASS and GPS systems highlights the differences between them, and the considerations that must be made when the systems are used in combination. This forms the basis for the GPS/GLONASS PPP functional model described in Chapter 4. A review of the initial investigations into GPS/GLONASS PPP, together with the increased number of GLONASS satellites now available, provided the motivation to combine these systems in PPP, in an attempt to improve the performance of this method. In order to evaluate the impact on performance, the relevant metrics were selected, and an explanation given of the basis for expected improvement with GLONASS.

Having identified the importance of minimising the error budget in PPP, a detailed description of the error sources, relevant models and mitigation strategies is given in Chapter 3.

Chapter 3 Error sources and mitigation in PPP

As discussed in Chapter 2, satellite signals are subject to a range of error sources. In order to achieve accurate positioning, it is important to understand these sources and identify relevant models or estimates. The key error sources and how to deal with them during processing are considered in the following sections.

3.1 Satellite ephemeris and clocks

The details of the position and clock offset of the satellites are central to all GNSS positioning. For GPS, the satellites transmit Keplerian orbit elements and the clock offset, rate and drift parameters (IS-GPS-200E, 2010). These are calculated by the GPS ground segment and uploaded to the satellites periodically. The accuracy and precision of the data sent from satellites is limited by the satellite storage, downlink bandwidth and ground control processing strategy. For accurate positioning a better quality of satellite information is required.

Using a global network of receivers, accurate satellite orbits and clock offsets can be calculated and distributed to users via the internet or a communications satellite. This information is available commercially or from the IGS analysis centres which produce orbit and clock products at a range of latencies and corresponding accuracies (Dow et al., 2009).

IGS final orbits are calculated in 24 hour periods. In an analysis of discontinuities at day boundaries, Griffiths and Ray (2009) found the 1-D precision and accuracy was on average 15 mm. They found this to be consistent with Satellite Laser Ranging (SLR) residuals of 19 mm to 25 mm.

Real-time products are created by predicting the satellite orbits and clock offsets forwards for a short period. This reduces the accuracy achievable as the prediction is an extrapolation; this is shown in Table 3.1.

In this thesis, commercially available products were used, the real-time Veripos Apex GPS-only and GPS/GLONASS (Rocken et al., 2011).

Table 3.1 shows the accuracy and tabulation interval of the various IGS orbit and clock products, as well as the ESA Final and Veripos Apex products. Both the IGS Ultra Rapid and Veripos Apex G2 products can be used for real time positioning. The Ultra Rapid orbits and clocks are produced with a latency of 3 h but include 6 h of predicted data. The Veripos Apex G2 product is delivered to users via a

continuous satellite link, rather than using batch processing as is done for the IGS Ultra Rapid product, they are continuously updated and transmitted to the user with a 2 s latency.

The remaining residual error in the orbit and clock products is given in the equivalent range error column in Table 3.1. ESA and Veripos do not publish accuracies for their products. In comparison between the ESA Final orbit and clock products, and the IGS Final product, the RMS difference in orbit and clocks was between 1 cm to 2 cm RMS (Kouba, 2009a).

Satellite positions from the IGS analysis centres are produced at 15 min intervals, and must therefore be interpolated to determine the satellite position at transmission time (Schenewerk, 2003). By comparing satellite positions interpolated from 15 min intervals to those produced at a 5 min interval, Yousif and El-Rabbany (2007) showed the standard deviation of the error introduced by a 9 point Lagrange interpolation was below the mm level.

Satellite clocks, however, contain high frequency noise that is not captured by such a long interpolation interval. Therefore the clock product should ideally be tabulated at the same interval as the required positioning interval. When performing high-rate positioning (1 Hz or higher) this is not possible due to the computational requirements of generating such high rate clock estimates in the network solution. Bock et al. (2009) showed the deterioration in 3D coordinate RMS for 1 Hz static positioning was only 2% using 5 s clock products, but up to 30% using 30 s clock products. Therefore, to avoid degradation of potential accuracy, the highest rate clock products up to the sampling rate of the positioning should be used.

The IGS produces a combined GLONASS orbit product using the solutions provided by the Center for Orbit Determination in Europe (CODE) and the ESA. However, there is not an IGS combined GLONASS clock product. GMV produce GLONASS orbit and clock products but they are only available for use within their online positioning service, *magicGNSS* (Príiz et al., 2009). Currently, free of charge GLONASS clock products can only be obtained from ESA (Springer, 2009). CODE orbits and clocks are used for kinematic GPS PPP validation due to their high clock tabulation rate (5 s). ESA orbits provide an integrated GPS/GLONASS product.

Provider	Latency	Clock RMS (ns)	Clock interval (s)	Orbit RMS (cm)	Orbit interval (s)	Equivalent range error (cm)	GLONASS clock product
IGS Ultra Rapid	predicted	3	900	5	900	90	No
IGS Rapid	17 h to 41 h	0.15	300	2.5	900	5	No
IGS Final	12 d to 18 d	0.075	30	2.5	900	3	No
ESA Final	12 d to 18 d	-	30	-	900	-	Yes
CODE Final	12 d	-	5	-	900	-	No
Veripos Apex G2	2 s	-	30	-	30	-	Yes

Table 3.1: Orbit and clock products

3.2 Receiver clock

As discussed in Chapter 2, any bias in the receiver clock introduces a common range error on all received signals. The clock in most receivers is usually a quartz crystal oscillator due to their low cost. These are affected by changes in temperature and do not have the long term stability of the atomic clocks used in GNSS satellites, so often drift compared to the satellite network time scale. Most GPS receivers maintain their internal clock to within 1 ms of GPS time, either by introducing receiver clock jumps or steering the internal clock (Hofmann-Wellenhof et al., 2008).

Additionally, any delay introduced to the signal processing, such as a length of antenna cable, will add a similar bias to all observations. As the common hardware biases and receiver clock offset are inseparable, they are often treated as a single term.

The clock offset can be removed by differencing between satellites or, as is the standard approach in PPP, estimated as a stochastic parameter along with the receiver position (Kouba, 2009a).

In a GNSS receiver the internal components responsible for GPS and GLONASS signal measurement can produce different delays for each network. Therefore a system time difference parameter is needed to account for this (Cai and Gao, 2007), and for GPS/GLONASS PPP, two unknown receiver clock parameters are estimated.

3.3 Troposphere

As electromagnetic signals pass through the troposphere they travel slower than they would in a vacuum. This is due to the refractive index of the neutral atmosphere, and manifests itself as a range bias compared to the assumption of the signals travelling at the speed of light in a vacuum. Over the range of frequencies that GNSS satellites transmit on, this delay is a frequency independent effect. In terms of the refractive index n the tropospheric path delay is defined as:

$$\delta_{\text{trop}} = \int (n(s) - 1) ds \tag{3.1}$$

integrated along the signal path.

The delay can be split into two parts: the hydrostatic part that follows the laws of ideal gases, often known as the “dry” delay; and a more variable part that is harder

to model. The latter is known as the non-hydrostatic or "wet" delay and is related to water vapour present in the troposphere (Hopfield, 1969). Due to the increase in the distance that signals at low elevation angles travel through the atmosphere, the magnitude of this effect is larger at lower elevation angles. The dry part is responsible for a zenith delay of approximately 230 cm at sea level. The wet delay is responsible for up to 40 cm in the zenith direction (Leick, 2004).

It has been shown that the tropospheric delay may be approximated for a given angle by a zenith delay and a corresponding mapping function such that, for a given elevation angle E, the tropospheric path delay can be written as:

$$d_{\text{trop}}(E) = m_{\text{wet}}(E)Z_{\text{wet}} + m_{\text{dry}}(E)Z_{\text{dry}} \tag{3.2}$$

where Z_{wet} and Z_{dry} are the wet and dry zenith delay, and m_{wet} and m_{dry} are the wet and dry mapping functions (Hopfield, 1969).

The zenith delay can be modelled as follows using the method of Saastamoinen (1973) as given by Davis et al. (1985).

Dry zenith delay (m):

$$Z_{\text{dry}} = \frac{0.002277p}{1 - 0.00266\cos 2\phi - 0.0028 \times 10^{-3}h} \tag{3.3}$$

Wet zenith delay (m):

$$Z_{\text{wet}} = \left(\frac{1255}{T} + 0.05\right) \frac{0.002277e}{1 - 0.00266\cos 2\phi - 0.0028 \times 10^{-3}h} \tag{3.4}$$

given the atmospheric pressure p, partial pressure of water vapour e, both in millibars, temperature T in Kelvin, latitude ϕ and height h in km.

The meteorological measurements required as inputs to the Saastamoinen model can either be obtained from local measurements made at the receiver, or if not available, from a global seasonal temperature and pressure model such as the Global Pressure and Temperature (GPT) model (Böhm et al., 2007).

There are many mapping functions to project the zenith delay to a delay at a given elevation angle. A commonly used example is the Niell Mapping Function (NMF) which uses a continued fraction with tabulated seasonal and latitude dependent coefficients (Niell, 1996). More recently the Vienna Mapping Functions 1 (VMF1) were produced by ray tracing through numerical weather models such as the European

Centre for Medium-Range Weather Forecasts (ECMWF) global weather model. The required coefficients of VMF1 are provided for IGS, International VLBI Service (IVS) and International DORIS Service (IDS) stations, as well as on a global grid (2.5 x 2.0 degrees) with a latency of less than 24 hours. The Global Mapping Function (GMF) is a spherical harmonic fit to seasonal average VMF1 parameters. It requires only station coordinates and day of year as inputs, making it suitable for use in real-time global PPP (Böhm et al., 2006a). Compared to the NMF, the GMF significantly reduces regional height biases and annual errors. Both the wet and dry mapping functions take the following form:

$$m(E) = \frac{1 + \dfrac{a}{1 + \dfrac{b}{1+c}}}{\sin E + \dfrac{a}{\sin E + \dfrac{b}{\sin E + c}}} \tag{3.5}$$

where E is the satellite elevation angle. The dry and wet mapping functions are formed from corresponding sets of parameters for a, b and c designated with indices h and w. The coefficients a_h and a_w for any site coordinates and day of year (doy) can be determined from a mean value a_0 and an annual amplitude A of a sinusoidal function using Equation 3.6.

$$a = a_0 + A\cos\left(2\pi\frac{\text{doy} - 28}{365}\right) \tag{3.6}$$

where the mean value and seasonal value are determined from the tabulated spatial spherical harmonic coefficients A_{nm} and B_{nm} up to degree and order 9 as given in:

$$\sum_{n=0}^{9}\sum_{m=0}^{n} P_{nm}(\sin\phi)\left[A_{nm}\cos(m\lambda) + B_{nm}\sin(m\lambda)\right] \tag{3.7}$$

where P_{nm} are the Legendre polynomials, ϕ and λ, the site latitude and longitude. Parameters b and c in Equation 3.5 were estimated by least squares fit to ray traced values produced from monthly mean atmosphere profiles for 2001 (Böhm et al., 2006b):

Hemisphere	c_0	c_{10}	c_{11}	Ψ
Northern	0.062	0.000	0.006	0
Southern	0.062	0.001	0.006	π

Table 3.2: Parameters needed for computing coefficient c of the GMF dry mapping function

$$b_h = 0.0029 \tag{3.8}$$

$$b_w = 0.00146 \tag{3.9}$$

$$c_h = c_0 + \left[\left(\cos\left(\frac{doy - 28}{365}2\pi + \Psi\right) + 1\right)\frac{c_{11}}{2} + c_{10}\right](1 - \cos\phi) \tag{3.10}$$

$$c_w = 0.04391 \tag{3.11}$$

Where Ψ specifies the Northern or Southern Hemisphere, the parameters are given in Table 3.2.

As the wet zenith delay is highly dependent on local conditions, a correction to the modelled wet delay may be estimated as part of the solution, giving the total tropospheric delay

$$d_{\text{trop}}(E) = m_{\text{wet}}(E)(Z_{\text{wet}} + dZ_{\text{wet}}) + m_{\text{dry}}(E)Z_{\text{dry}} \tag{3.12}$$

In this thesis the Saastamoinen wet dry zenith troposphere delay model is used with input meteorological data generated using the GPT model. This accounts for the dry delay to sub-millimetre RMS (Mendes and Langley, 1998). Most of the residual error due to the troposphere is caused by the wet delay. Based on comparisons with radiosondes and water vapour radiometers, Rocken (2005) suggest the wet zenith delay can be estimated as a parameter using kinematic GPS to approximately 13 mm RMS. The residual range error contribution to the error budget is then a combination both of errors in the estimation of the wet trophospheric delay and in the mapping function.

A correction to the wet delay is estimated as this is highly variable and hard to model. The zenith values are mapped to a satellite elevation angle using the GMF. The effect of the troposphere delays is increased at low elevations so any mismodelling in the zenith delay will be increased at low elevations. Therefore, as is done in

this thesis, it is common in PPP to use an elevation dependent weighting function to account for the increased range error at low elevations (Bisnath and Gao, 2008).

3.4 Ionosphere

The ionosphere consists of charged particles that affect radio signals in a frequency dependent way. The Total Electron Content (TEC) is equal to the number of free electrons in a column of unit area along which the signal travels between satellite and receiver. The free electrons delay the pseudoranges, known as group delay, and advance the carrier phases, known as phase advance, by an equal amount. Coronal mass ejections and extreme ultraviolet solar radiation are the main causes of the ionisation, however the relationship between TEC and solar flux is irregular, sometimes showing very poor correlation (Doherty et al., 2000). The spatial and temporal variability of the TEC rules out the option of eliminating the ionospheric delay through modelling.

The ionospheric range delay for the code signal transmitted on a carrier frequency f is given to first order by Leick (2004):

$$I_{f,P} = \frac{40.30}{f^2}\text{TEC} \tag{3.13}$$

leading to the following relationships between code (P) and phase (Φ) observations and frequency:

$$I_{i,P} = -I_{i,\Phi} \tag{3.14}$$

$$\frac{I_{1,P}}{I_{2,P}} = \frac{I_{1,\Phi}}{I_{2,\Phi}} = \frac{f_{\text{L2}}^2}{f_{\text{L1}}^2} \tag{3.15}$$

with f_{L1} the L1 carrier frequency, and f_{L2} the L2 carrier frequency, as given in Table 2.3.

As the ionospheric range delay is proportional to the TEC, signals at lower elevation are affected more than signals at higher elevations, due to the slant angle through the atmosphere. The several metre-level effect this has on measured pseudoranges requires elimination to achieve centimetre or decimetre accurate positioning in PPP.

The ionosphere-free combination, sometimes also referred to as P_3 and Φ_3, can be

formed to eliminate the first order ionospheric effects for both the code:

$$P_{\mathrm{LC}} = \frac{f_{\mathrm{L1}}^2 P_{\mathrm{L1}} - f_{\mathrm{L2}}^2 P_{\mathrm{L2}}}{f_{\mathrm{L1}}^2 - f_{\mathrm{L2}}^2} \tag{3.16}$$

and the carrier phase:

$$\Phi_{\mathrm{LC}} = \frac{f_{\mathrm{L1}}^2 \Phi_{\mathrm{L1}} - f_{\mathrm{L2}}^2 \Phi_{\mathrm{L2}}}{f_{\mathrm{L1}}^2 - f_{\mathrm{L2}}^2} \tag{3.17}$$

The normalisation by $f_{\mathrm{L1}}^2 - f_{\mathrm{L2}}^2$ is performed so that P_{LC} and Φ_{LC} are also measurements of the satellite to receiver range.

Higher order ionospheric effects are generally ignored in kinematic PPP. Although the maximum effect on the "ionosphere free" phase combination is of the order 40 mm, the majority of the second order effect is absorbed by the satellite clock corrections (Petrie et al., 2011). Solar activity rises and falls in cycles, with a recent low activity period from 2006–2010, as shown in Figure 3.1. The period of data analysed in this thesis (2006–2011) covers low to medium solar activity; this corresponds to reduced ionospheric activity and therefore a considerably lower effect on GNSS signals than the worst case. In the near future the impact of higher order ionospheric effects on PPP will have a greater impact.

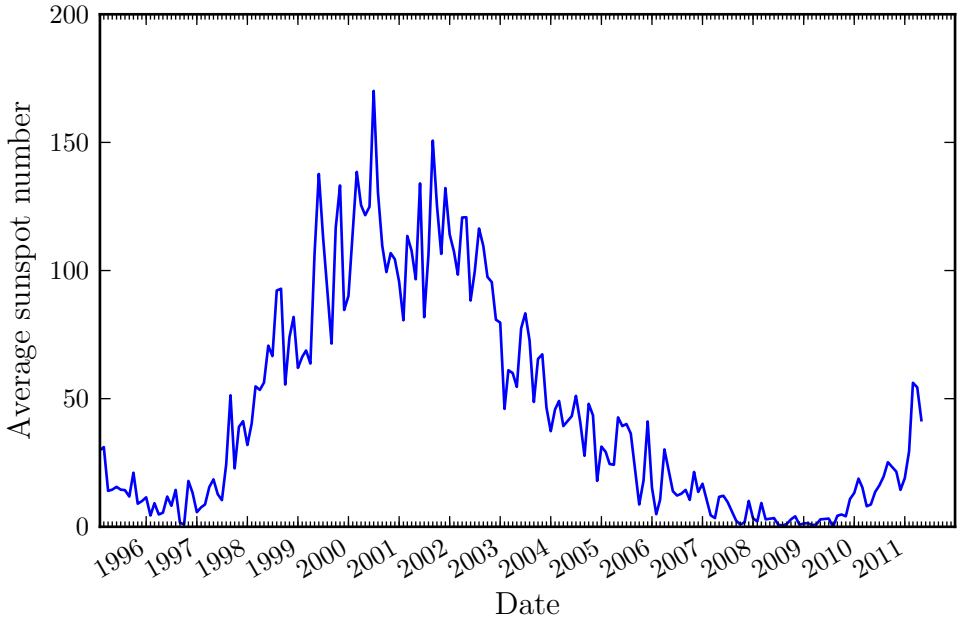

Figure 3.1: Solar activity cycle showing a minimum during the period 2006-2011. Data from `http://solarscience.msfc.nasa.gov/SunspotCycle.shtml`

In this thesis the first order ionospheric range error is removed using the ionosphere free measurement combination described above (Equations 3.16 and 3.17). Higher order terms are ignored due to their relatively small effect on the range error.

3.5 Relativistic effects

The Sagnac effect occurs due to the time dilation experienced by a clock rotating in a non inertial frame (Ashby, 2003). The magnitude of the effect on a satellite clock due to orbital eccentricity, Δt_r, is given by:

$$\Delta t_r = \frac{r_r^s \cdot \dot{r}_r^s}{c^2} \tag{3.18}$$

where r_r^s is the receiver to satellite position vector, $\dot{r}_r^s$ the receiver to satellite velocity vector, and c the speed of light. This is applicable to the satellite clocks, and as the effect is corrected for in the generation of orbit and clock products, observations must be corrected during PPP processing to remain consistent with those products (Kouba, 2009a).

The Earth's gravitational field causes a space-time curvature of the satellite signal, this curvature must be accounted for as the range is modelled as a Euclidean range. This correction may be represented in the following form (Hofmann-Wellenhof et al., 2008, p. 123):

$$\delta^{\text{rel}} = \frac{2\mu}{c^2} \log \frac{\rho^j + \rho_i + \rho_i^j}{\rho^j + \rho_i - \rho_i^j} \tag{3.19}$$

where μ is the Earth's gravitational constant. The geocentric distances of satellite j and receiver i are denoted as ρ^j and ρ_i, and ρ_i^j is the distance between satellite and receiver.

3.6 Satellite orientation

In order to achieve accurate positioning, it is important to know the orientation of the GNSS satellites. The orientation affects phase centre offsets, phase windup and noon and midnight turns; a brief description is given here.

The satellite body frame

$$x' = (i\ j\ k) \tag{3.20}$$

is a coordinate system with its origin at the satellite centre of mass that rotates

with the satellite. The orientation of GPS and GLONASS satellites is maintained so that the antenna is pointing at the centre of the Earth; k is the unit vector in this direction. The solar panels are maintained orientated towards the Sun, so given the satellite to Sun unit vector $\hat{e}$, then j, defined along the solar panel axis is given by $j = k \times \hat{e}$. The unit vector i, located in the Sun-satellite-Earth plane, completes the right-handed coordinate system. This orientation is also known as the "nominal yaw attitude" (Bar-Sever, 1996).

3.7 Antenna phase centres

The effective reception point, the phase centre, of an antenna varies depending on the angle of incidence and frequency of the received signal. This also applies to the phase centre of transmission. As the phase centre is an electromagnetic rather than physical property of an antenna, and may be inside or outside the antenna, a mark is put on the outside of the antenna to allow the location of the phase centre to be measured relative to this point. This mark is known as the Antenna Reference Point (ARP). Several methods exist for calibration — relative, robot and chamber calibrations (Görres et al., 2006). In order to maintain consistency with the orbit and clock products used, the same set of antenna descriptions should be used in processing as are used in the generation of the products.

For each of the two GPS carrier frequencies, the description of the position of the phase centre can be split into two parts: a constant per frequency Phase Centre Offset (PCO), and an azimuth and elevation dependent Phase Centre Variation (PCV). The IGS maintains a consistent set of calibrations tabulated at 5° intervals for receivers and 1° for satellites; by interpolating these values corrections can be applied to GNSS observations at any elevation angle.

For the offsets provided by the IGS the following sign conventions are used:

For the receiver antenna:

$$\bar{x}_{\mathrm{pc}} = x_{\mathrm{ARP}} + x_{\mathrm{pco}} \tag{3.21}$$

$$\rho_{\mathrm{obs}} = \rho_{\mathrm{geom}} + \mathrm{PCV}(\mathrm{elevation}, \mathrm{azimuth}) \tag{3.22}$$

where $\bar{x}_{\mathrm{pc}}$ is the mean phase centre position, x_{ARP} is the location of the antenna reference point, and x_{pco} is the phase center offset vector (given in a topocentric left-handed system: north, east and up component). Ignoring all other propagation

effects, the observed distance ρ_{obs} is then the sum of the geometric range ρ_{geom} and the phase centre variation PCV(elevation, azimuth). Here the azimuth counts clockwise from the North towards the East.

Given an offset x_{pco} in the satellite body frame, the conversion from satellite centre of mass x_{com} calculated using precise orbits, to antenna transmission point in the Earth Centred Earth Fixed (ECEF) can be performed:

$$x_{\text{ant}} = x_{\text{com}} + (i\ j\ k)^{-1} x_{\text{pco}} \tag{3.23}$$

with i, j, k the body frame unit vectors in Equation 3.20.

Similar to the receiver antenna, the phase centre variation is applied as a correction to the geometric range to give the observed range

$$\rho_{\text{obs}} = \rho_{\text{geom}} + \text{PCV}(\text{nadir}, \text{azimuth}) \tag{3.24}$$

Here the azimuth counts clockwise from the j-axis towards the i-axis when looking in the direction of the negative k-axis or towards deep space (Rothacher and Schmid, 2010).

In the set of antenna offsets used with the the IGS realisation of the ITRF2005 reference frame (IGS05), there are only published receiver antenna offsets and variations at the two GPS carrier frequencies, L1 and L2. There are no offsets and variations given for the GLONASS L1 and L2 frequencies, therefore the calibrated values for the nearest GPS frequency are used, both in orbit and clock generation and subsequent PPP coordinate estimation, for GLONASS observations. The difference between the GPS and GLONASS specific corrections are in the range of a few millimetres but may reach 10 mm when combined in the ionosphere-free combination as shown in Figure 3.2. However when estimating float ambiguities the average difference between the GPS and GLONASS corrections will be absorbed by the ambiguity, reducing the 24 h static positioning error to 1 mm or less (Dach et al., 2011b).

The increase in robot calibrations has increased the number of antennas for which GLONASS specific phase centre offsets exist. With the change to the IGS realisation of the ITRF2008 reference frame (IGS08) by IGS analysis centres on 17 April 2011, an updated set of antenna calibrations has been introduced that include GLONASS specific offsets.

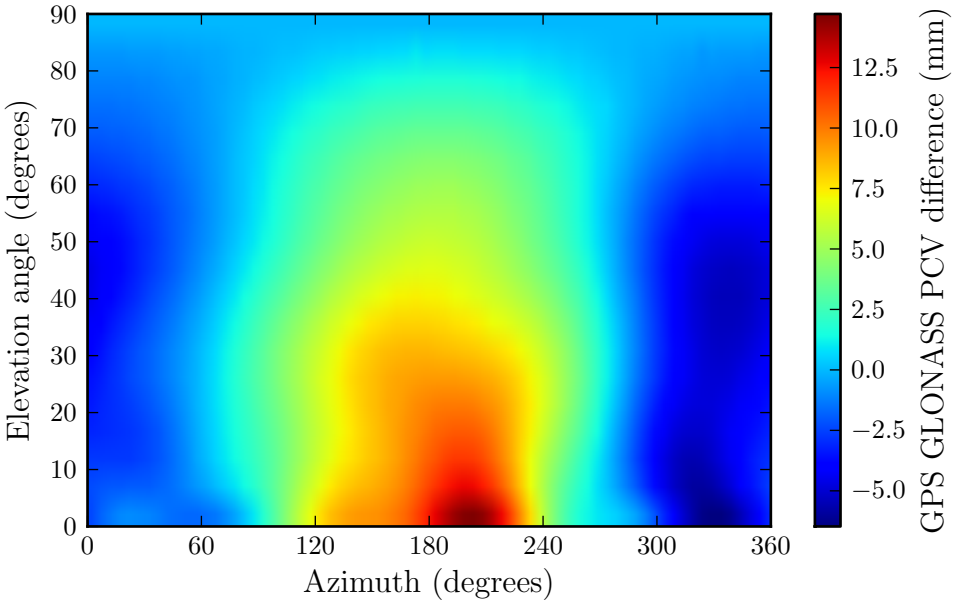

Figure 3.2: Difference between the ionosphere free PCV for GLONASS and GPS from GNSS specific calibrations as a function of azimuth and elevation for the antenna JAV_RINGANT_G3T NONE using the robot calibration values from `http://igs.org/igscb/station/general/igs08.atx`

3.8 Phase windup

GPS satellites transmit right-hand circularly polarised radio waves. Therefore, a rotation of either the satellite or receiver antenna, with respect to the other, about its bore axis, causes a change of phase to be measured at the receiver. This effect is called "phase windup" (Wu et al., 1993). For precise point positioning it is essential to account for phase windup to enable positioning accuracy at the decimetre level.

For a fixed receiver the antenna orientation does not change, however, the satellites rotate about their z axis in order to keep their solar panels directed at the Sun. As the geometry changes due to the satellite's orbit, there is also an apparent rotation of the satellite with respect to the receiver.

The correction (in radians) is given by:

$$\Delta\phi = \text{sign}(\zeta)\cos^{-1}\left(\frac{\vec{D}' \cdot \vec{D}}{|\vec{D}'||\vec{D}|}\right) \tag{3.25}$$

where $\zeta = \hat{r} \cdot (\vec{D}' \times \vec{D})$, $\hat{r}$ is the satellite to receiver unit vector and $\vec{D}'$, $\vec{D}$ are the effective dipole vectors of the satellite and receiver determined by the current

satellite body coordinate unit vectors $(\hat{x}', \hat{y}', \hat{z}')$ and the local receiver unit vectors (i.e. North, East, Up) denoted by $(\hat{x}, \hat{y}, \hat{z})$:

$$\vec{D}' = \hat{x}' - \hat{r}(\hat{r} \cdot \hat{x}') - \hat{r} \times \hat{y}' \tag{3.26}$$

$$\vec{D} = \hat{x} - \hat{r}(\hat{r} \cdot \hat{x}) - \hat{r} \times \hat{y} \tag{3.27}$$

As the satellite completes a full rotation, this must be recognised and the accumulated rotations corrected for by adding full cycle terms of $\pm 2\pi$ to the correction term (Equation 3.25).

For mobile receivers the effect of the receiver antenna rotation is to change all the measured carrier phase observables by the same angular amount. For GPS only positioning using only one linear combination of carrier phase observables, this will add the same range bias to the used linear combination for all satellites. Such a bias is indistiguishable from a receiver clock bias, and will therefore add a bias to the estimated receiver clock offset but will not affect positioning accuracy (Kouba, 2009a).

For multi constellation GNSS positioning where the used linear combinations of observables do not have the same wavelength, a different magnitude bias will be added to each observable type, depending on the wavelength. In the case of GLONASS carrier phase observables, where each satellite is on a different frequency, then the bias added to each satellite's carrier phase observable will differ.

A complete receiver antenna rotation would add a one cycle bias on both carrier phase observables. The range effect of this on the ionosphere free combination used in this thesis is

$$\Delta\Phi = \frac{f_1^2\lambda_1 - f_2^2\lambda_2}{f_1^2 - f_2^2} \tag{3.28}$$

Comparing the effect at GPS frequencies to the effect at the furthest GLONASS frequency ($k = 7$ in Equations 2.1 and 2.2) gives a difference of 1.9 mm and less than 0.5 mm over the range of GLONASS frequencies. The difference between the effect for GPS satellites and the mean effect for an observed set of GLONASS satellites can be considered as an addition to the GLONASS receiver clock bias, leaving only the effect between GLONASS satellites biasing the observed range. For a spinning receiver this difference would accumulate with every rotation but this is not a typical user scenario. The use of a gyroscope or compass to track receiver rotations could allow the receiver orientation to be determined and used in Equation 3.25 to correct this effect. In this thesis, however, whilst satellite phase windup is modelled, the

error due to receiver rotation is not accounted for.

3.9 Noon and midnight turns

There are two situations when satellite orientation does not agree with the model described in Section 3.6. If a satellite crosses between the Earth and the Sun, the definition of its body frame requires it to rotate very rapidly; this is called a "noon turn". The satellites have a limited rotational speed, so during this rotation period the true orientation of the satellite lags the modelled orientation. For Block IIR GPS satellites a similar effect is seen when the Earth is between the Sun and the satellite, known as a "midnight turn".

The other case is when the satellite enters the Earth's shadow. GPS satellites use a solar sensor to orientate themselves towards the Sun. As the satellite enters the Earth's shadow the light sensor can no longer track the Sun. In the shadow, Block II/IIA GPS satellites start yawing with a maximal hardware yaw rate of approximately $0.10\,^\circ\,\mathrm{s}^{-1}$ to $0.13\,^\circ\,\mathrm{s}^{-1}$. The behaviour during the post-shadow recovery period, which lasts about 30 min, is undefined and cannot be properly modelled. More recent GPS satellites from Block IIR maintain the nominal yaw attitude during a shadow crossing. The complete details of this behaviour are described by Bar-Sever (1996) and a simplified model suitable for network solutions and PPP is given by Kouba (2009b).

Dilssner et al. (2011) used the j component of the antenna offset of the GLONASS-M satellites to determine their behaviour during Earth shadow crossing. They found that using the nominal yaw attitude model can introduce range errors of up to ± 19 cm and ± 27 cm during noon and midnight turns respectively.

This special behaviour, during turns and shadow crossing, must either be correctly modelled or observations from satellites during these periods must be removed. In the case of early GPS and all GLONASS satellites, for which the behaviour during Earth shadow crossings is undefined or unknown, there is no option but to remove the observations.

In this thesis the satellites for which the behaviour during shadow crossings is unknown or poorly defined are removed from the solution. Therefore this effect does not contribute to the error budget but does reduce the number of useable satellites when a satellite is performing a noon or midnight turn.

3.10 Earth body tide

The solid Earth is deformed by changing gravitational forces due to the movement of the Sun, Moon and other planets. This is a periodic effect, the magnitude of which depends on latitude. The Earth body tide deformation tidal variation can be as large as 30 cm in the vertical and 5 cm in the horizontal (Kouba, 2009a). Site displacements caused by tides of spherical harmonic degree and order (nm) are characterised by the Love number h_{nm} and the Shida number l_{nm}. The values of these numbers depend on latitude and tidal frequency (Wahr, 1981). The periodic tidal effect is dominated by diurnal and semi-diurnal tides so can be largely averaged out when performing static positioning over an entire day (Kouba and Héroux, 2001).

There is also a permanent displacement, according to adopted International Terrestrial Reference Frame (ITRF) convention used by the IGS in the generation of their orbit and clock products. Thus to be consistent with the ITRF "Tide-free" reference system convention, the permanent part must also be corrected for. The permanent part of the tide can reach 12.5 cm in the radial component in the middle latitude region so must be considered.

For 5 mm precision, only the second-degree tides and a height correction term are necessary (Kouba, 2009a; McCarthy et al., 1989). This gives a site displacement vector Δr, in Cartesian coordinates of:

$$\begin{aligned}\Delta r = \sum_{j=2}^{3} \frac{GM_j}{GM} \frac{r^4}{R_j^3} \left\{ \left[3l_2(\hat{R}_j \cdot \hat{r}) \right] \hat{R}_j + \left[3\left(\frac{h_2}{2} - l_2 \right) (\hat{R}_j \cdot \hat{r})^2 - \frac{h_2}{2} \right] \hat{r} \right\} \\ + \left[-0.025m \sin\phi \cos\phi \sin\theta_g + \lambda \right] \hat{r}\end{aligned} \tag{3.29}$$

where GM, GM_j are the gravitational parameters of the Earth, the Moon $(j = 2)$ and the Sun $(j = 3)$; r, R_j are the geocentric state vectors of the station, the Moon and the Sun with corresponding unit vectors $\hat{r}$ and $\hat{R}_j$, respectively; l_2 and h_2 are the nominal second degree Love and Shida dimensionless numbers (nominal values 0.6078 and 0.0847); ϕ, λ are the site latitude and longitude (positive east) and θ_g is Greenwich Mean Sidereal Time.

A more complete model which takes into account the variability of the Love and Shida numbers due to effects such as the Earth's ellipticity, the Coriolis force due to Earth rotation, and mantle anelasticity is given by McCarthy and Petit (2003). This model is recommended when a positional precision of 1 mm is desired (Kouba, 2009a). A standard implementation of this model is given in the Fortran subroutine

dehanttideinel.f (McCarthy and Petit, 2003, chap. 7), which is used in this thesis.

3.11 Ocean tide loading

Ocean tide loading (OTL) has a similar deformation effect to the solid Earth tides but is caused by the load of the ocean tides. The deformation caused by ocean tide loading is almost an order of magnitude less than that caused by Earth body tides (Kouba, 2009a). These tidal effects are much more localised, largely confined to coastal regions. By convention there is no permanent part of tide loading. The vertical site displacements due to OTL may reach values of several centimetres for coastal sites and reduce with distance from the coast (Urschl et al., 2005). For single epoch positioning to 5 cm accuracy, or sites more than 1000 km from the coast, OTL may be largely discounted (Kouba, 2009a). The OTL effect is not modelled in this thesis, in common with several PPP implementations (Abdel-Salam, 2005; Leandro et al., 2011)

3.12 Atmospheric pressure loading

The weight of the atmosphere causes a load on the Earth's surface. This load varies with changes in atmospheric pressure causing both vertical and horizontal displacements of the Earth's surface. These displacements on average have an RMS of 2.6 mm for the vertical component and 0.6 mm for the horizontal component, with peak to peak variations as large as 20 mm in the vertical component and 3 mm in the horizontal component (Petrov, 2004).

Petrov (2004) provides a model based on using input pressure field data from a numerical weather model. In an analysis of the model performance based on Very-Long-Baseline Interferometry (VLBI), the vertical and horizontal displacements could be computed with errors less than 15%. Dach et al. (2011a) investigated the impact of this model on the generation of orbit and clock products from a global network. They found the effect of Atmospheric Pressure Loading (APL) to be clearly visible and improvement in station repeatabilities of up to 20% when including the Petrov (2004) correction at an observation level. Dach et al. (2011a) also found a change in estimated satellite positions when including the APL correction. This implies that if APL is ignored in the orbit generation then some of the effect is absorbed into the estimated satellite orbits.

Currently the IGS analysis centres do not correct for APL when generating orbits. Therefore when using these products in PPP some of the effect of APL is already included in the orbit product.

Urquhart (2009) showed that including APL corrections did not have a significant effect on positioning given the current accuracy of PPP. Due to the small effect and the lack of appropriate pressure data, this effect is ignored in this thesis. As APL affects the receiver coordinates rather than biasing the satellite pseudoranges, then ignoring APL will not add to the observation error budget, but will reduce the resulting position accuracy by a few millimetres as given above.

3.13 Differential code biases

The different code signals transmitted from a satellite all take different paths through the satellite on their way to the antenna. This causes a slight bias between different code signals such as C1 and P1. Such a bias is known as a Differential Code Bias (DCB).

IGS products are aligned to the ionosphere free combination of P1 and P2, therefore if using a different set of observations they must be corrected. For example, the Leica 1200 receiver records C1 and P2 observables, so for use with orbit and clock products aligned to the ionosphere free combination of P1 and P2 (such as IGS products), the C1 observations must be corrected to a P1 equivalent observation using P1-C1 bias values. The magnitude of the GPS P1-C1 bias can reach up to 0.6 m (Kouba, 2009a).

To convert a C1 observation to a P1 like observation, P1′, the following equation is used:

$$\mathrm{P1}' = \mathrm{C1} + \Delta_{\mathrm{P1-C1}} \tag{3.30}$$

Gao et al. (2001) investigated the nature of the P1-C1 biases using a single antenna split to multiple receivers. This allowed the estimation of constant satellite and receiver dependent DCBs and a satellite independent time varying DCB. They showed the constant satellite dependent P1-C1 biases can be estimated with accuracy at the level of a few centimetres. CODE produces a monthly set of GPS DCBs for P1-C1 that can be used to correct for the bias in receivers observing C1 (Schaer and Steigenberger, 2006).

The case for GLONASS is more complicated as each signal is on a different frequency

and so takes a different route through both the satellite and the receiver. This makes GLONASS DCBs specific to each satellite-receiver pair so corrections cannot be distributed in the same way as for GPS. Using GLONASS code observations requires estimating the DCB for each channel.

3.14 Multipath

The signal received at an antenna may have taken more than one path from the satellite. Objects such as buildings, trees and even the ground can block or reflect a signal so that the path travelled is increased; this is particularly true in urban environments.

For code observations the magnitude of this effect is essentially unlimited. The effect of multipath on carrier phases can be estimated by considering the interference between a direct and indirect signal at the receiver. The two signals may be represented by

$$A_D = a\cos\phi, \quad A_R = \beta A\cos\phi + \delta\phi \tag{3.31}$$

with a the amplitude and ϕ the phase of the direct signal. The amplitude of the reflected signal is affected by the damping factor β and the phase is delayed by the base shift $\delta\phi$ due to the increased geometrical path. Then A_D and A_R are then the instantaneous amplitude of the direct signal and the reflected signal respectively.

The resultant signal can be represented (Hofmann-Wellenhof et al., 2008) in the form

$$\beta_M a\cos\phi + \delta_M \tag{3.32}$$

where the subscript M indicates multipath. By application of the cosine theorem, it can be shown that in the case of $\beta_M = 1$ that:

$$\beta_M = 2\cos\frac{\delta\phi}{2} \tag{3.33}$$

$$\delta\phi_M = \frac{1}{2}\delta\phi \tag{3.34}$$

The maximum effect of multipath on phase measurements therefore occurs at $\delta\phi_M = 90\circ = 1/4$ cycle (Hofmann-Wellenhof et al., 2008). Expressing this phase shift in terms of ranges on L1 and L2 gives a worst case maximum change in range of 4.8 cm and 6.1 cm respectively, though it rarely reaches this size (Lau and Cross, 2007).

There is no simple model for multipath as it is highly dependent on the local environment. Choke ring or multiple antennas can be used to reduce the effect of signals from the ground (Ray, 1999). For a static site the observation errors can be tracked over time and due to the repeating nature of current GNSS satellite orbits, a map of the multipath seen at the site can be generated and then used to correct for permanent errors due to fixed objects (Ragheb et al., 2007; Wanninger and May, 2001).

Lau and Cross (2007) created a multipath model based on ray tracing signals in a model of the local environment. Even for simple environments with one large reflector they found the accuracy of the model highly dependent on the exact specification of the reflection source. For a moving receiver in an ever changing environment this kind of correction is not possible.

An alternative approach is to attempt to determine the current level of multipath for a given signal and weight it appropriately in the position estimation. From a pure geometry point of view, low elevation signals are more likely to suffer from multipath due to the increase in potential reflectors. Vermeer (1997) for example suggests an observation weighting of $1/cos^2(z)$ with z the zenith angle of the satellite.

The carrier to noise ratio is commonly used to describe the quality of a received GNSS signal (Rost and Wanninger, 2009). This measure is a ratio of the received signal power to the noise power. Collins and Langley (1999) compared the effect of even weighting, elevation dependent weighting, and carrier to noise weighting. They found both elevation dependent weighting and carrier to noise weighting improved positioning accuracy compared to even weighting. In general there was little (less than 1 mm) difference between the elevation weighting and carrier to noise weighting coordinate estimates. This is largely due to the similarity of the two weighting functions in a low multipath environment.

Additional protection against positioning accuracy degradation due to multipath is to monitor observations and remove suspected outliers. The weighting and outlier detection and removal strategy used in this thesis is covered in Chapter 4.

3.15 Cycle slips

A cycle slip is the failure of the GNSS receiver to maintain lock on the carrier phase, causing the number of elapsed cycles of the carrier wave to be miscounted (Blewitt, 1990). This can arise due to high receiver dynamics, ionospheric scintillation, or

weak or obstructed signals. The loss of lock causes an apparent jump in the carrier phase ambiguity of a whole number of cycles. Cycle slips may occur for just one satellite or all visible satellites, known as total loss of lock.

If undetected, a cycle slip adds a constant bias to all subsequent carrier phase observations for that satellite. Therefore cycle slip detection is essential if accurate positioning is to be achieved. Ideally the integer value of the cycle slip is determined and subsequent observations are corrected to remove this bias, known as cycle slip fixing. If cycle slip fixing is not possible then the carrier phase ambiguity must be re-estimated to include the new bias.

3.16 Error budget

In assessments of the models used to account for the above error sources, the most common practice in the literature is to report results in terms of quantifying the effect on the GNSS estimated coordinates. This is due to the difficulty in identifying the true value of the effect that is being modelled. Analysing the estimated coordinates for biases, RMS scatter and seasonal variation is both simpler to achieve and directly quantifies the development in terms of improved coordinates for potential users of the model.

The magnitude of some of the error sources, such as atmospheric delays and multipath, are also time and location dependent. The variation can be large, for example the difference in ionospheric activity during the day and at night. Multipath is highly location dependent, and also affected by variations in receiver tracking bandwidth at static or kinematic receivers.

Table 3.3 summarises the average contributions to the range error of the residual error sources following modelling, elimination and reduction methods as described above. The total error budget is calculated as the root sum of squares of the individual contributing factors. The effect of multipath on code phase and carrier phase observations has been omitted as it is so dependent on the local environment, however we can note that carrier phase multipath is at the centimetre level, whereas code phase multipath is at the metre level. Atmospheric effects and multipath both increase at lower elevation, this is often accounted for by elevation dependent observation weighting and an elevation cutoff threshold.

	GPS		GLONASS	
	code	phase	code	phase
Satellite orbit	2.5			
Satellite clocks	2.5	2.5	> 2.5	> 2.5
Higher order ionosphere	4			
Residual troposphere	5			
Tracking noise	60	3	60	3
Multipath	-	-	-	-
Ocean tide loading	1.5			
GLONASS receiver PCV			0.5	
Other	2			
Total	60	8.3	60	8.3

Table 3.3: Contributions to the PPP ionosphere-free range error standard deviation, all values in centimetres. (Braasch and Van Dierendonck, 1999; Groves, 2008; IGS, 2011; Kouba, 2009a; Petrie et al., 2011)

3.17 Summary

This chapter has considered the error sources that affect positioning accuracy in PPP. Suitable corrections, models and mitigation strategies to address these error sources have been identified.

The several metre range bias introduced by the ionosphere, and the lack of a suitably accurate model, leads to the selection of the ionosphere free linear combinations of code and phase observations to remove first order ionosphere effects. Models are identified to account for solid Earth tides, phase centre variation and offset, phase windup and relativistic effects. Given it is not possible to model multipath for a moving receiver, observation weighting is used to account for the likely effect of multipath at different elevations, and signal reception quality. This is also consistent with the expected increase in unmodelled tropospheric and ionospheric delays at low elevations.

Estimated parameters are required for the receiver clock offset (including hardware bias), one for GPS and one for GLONASS. An estimated residual wet troposphere zenith delay is required.

Finally, the remaining residual errors not accounted for by these methods, and their contribution to the error budget have been considered. The models, estimated parameters and residual range error budget form the basis for the PPP algorithm laid out in the next Chapter.

Chapter 4 PPP method

This chapter presents the justification for the use of Kalman filtering as the estimation technique used in this thesis, as well as describing the theoretical model of Kalman filtering and how it is implemented in PPP.

In calculating a position using GNSS the aim is to estimate a set of parameters (including the position) based on a set of measurements. Due to the error sources described in Chapter 3, the measurements contain errors. Estimation is the process of taking measured data as input and producing an estimate of some parameters. For a linear system subject to uncorrelated Gaussian white noise of equal variance, the method of least squares provides the optimal estimate of the estimated parameters (Le and Teunissen, 2008).

Weighted least squares can be used to extend the least squares technique to measurements with differing observational noise. In GNSS navigation, measurements are at intervals and it is desirable to estimate a new position with each new set of measurements. In classical least squares each set of observations creates a new estimated position independent of all previous position estimates.

Multiple sets of measurements can be combined to reduce the effect of the observational noise. In batch least squares this is achieved by combining all the sets of observations in the estimation process; each new set of observations adds to the size of the set of equations to be solved.

The Kalman filter is a set of mathematical equations that provides an efficient computational (recursive) means to estimate the state of a process, in a way that minimises the mean of the squared error (Welch and Bishop, 1995). For a linear system with Gaussian white noise, the Kalman filter is optimal in that it minimises the mean square error over all unbiased estimators. Kalman filtering is the standard estimation technique used for PPP in published investigations (Bisnath and Gao, 2008; Geng et al., 2010c; Kouba, 2009a; Kouba and Héroux, 2001).

The recursive nature of the Kalman filter means that the contribution of past observations is contained in the covariance estimates of the estimated parameters. This makes the addition of a new set of observations numerically efficient compared to the batch least squares method. In batch least squares the addition of a new set of measurements increases the number of observations, and hence the size of the set of linear equations that need to be solved.

The PPP observation model discussed is non-linear, therefore the Kalman filter must

be adapted. There are two approaches to linearising the Kalman filter, the linearised Kalman filter and the Extended Kalman Filter (EKF). The linearised Kalman filter starts from a nominal trajectory about which the Kalman filter equations are linearised using a truncated Taylor series expansion evaluated at the nominal trajectory (Grewal and Andrews, 2001). The EKF, sometimes known as the Schmidt-Kalman filter (Schmidt, 1976), performs the linearisation about the estimated trajectory. The linearised Kalman filter can reduce the real time computational burden as the linearisation can be performed offline, whereas for the EKF it can only be computed once the estimated position is known. The disadvantage of the linearised Kalman filter is that the deviation of the actual trajectory from the nominal trajectory tends to grow with time leading to increasing linearisation errors (Grewal and Andrews, 2001). The EKF is therefore more robust against nonlinear approximation errors, as the filter only assumes linearity over the range of state estimation errors. Additionally, for kinematic positioning the nominal trajectory is often not known.

An alternative to the EKF is the Unscented Kalman Filter (UKF), which uses a deterministic sampling approach to capture the effects of the nonlinear system on the mean and covariance of the state (Wan and Van Der Merwe, 2000). The carefully chosen sample points completely capture the true mean and covariance of the Gaussian Random Variable, and when propagated through the true nonlinear system, capture the posterior mean and covariance accurately to the 3rd order (Taylor series expansion) for any nonlinearity. The EKF, in contrast, only achieves first-order accuracy.

Other nonlinear filtering algorithms include particle filters and the numerical solution of the Fokker-Planck Equation (Daum, 2005). Whilst these can lead to improved performance of estimation in nonlinear systems, this is often at the cost of computational complexity.

Due to the ease of implementation, efficient run time and wide use within the literature the EKF was used in this thesis. The principles of the EKF together with the implementation equations are described in detail below.

4.1 Extended Kalman filter

In simple terms, at a given observation epoch, the expected values of the measurements are estimated based on the predicted state (position, receiver clock offset, troposphere correction and ambiguities) using the precise orbit and clock products

and applying the models outlined in Chapter 3. The actual measurements and the modelled measurements, together with the state and measurement covariances, are combined in the Kalman filter to produce an updated state based on the new information contained in the current set of observations (Figure 4.1).

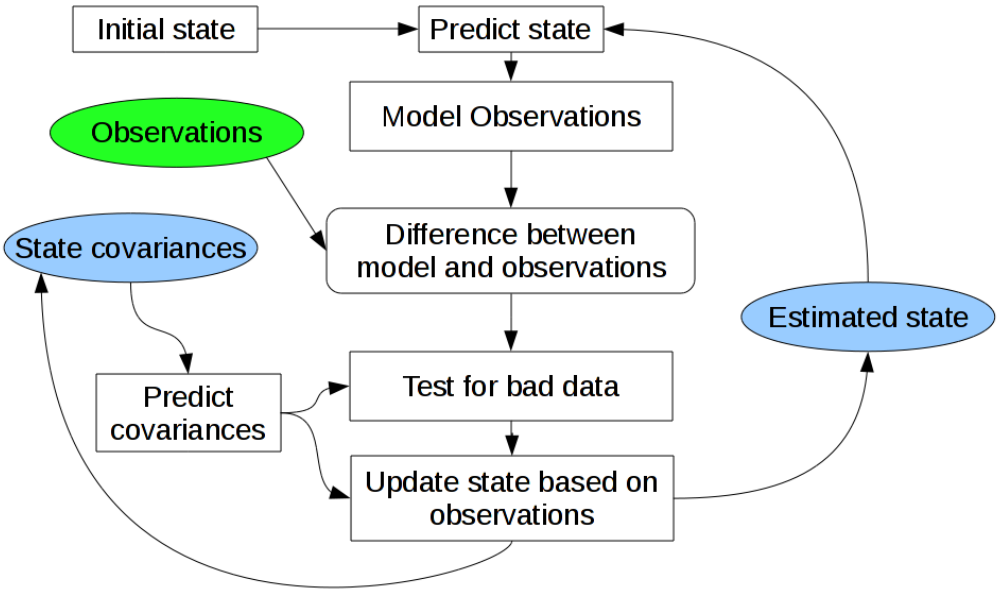

Figure 4.1: PPP Kalman filter flow diagram

The state of a system is the value of a set of parameters that are of interest at a given time. Often these parameters may not be directly measurable but are linked to variables that are observable through a measurement model. The dynamic model of a system describes how the state at one time is related to the state at a subsequent time. The EKF estimates the state of a system based on the predicted state generated by the dynamic model and a set of measurements.

The EKF is comprised of two main stages:

1) the Prediction Step where the time dependent state vector and its associated covariances are updated based on the system dynamic model,

2) the Update Step where the predicted state is updated based on the measurements at that point.

Full derivation is not given here as there are many examples in texts such as Grewal and Andrews (2001) and Anderson and Moore (1979). Details of the models making up the Kalman filter are given; the PPP specific versions of these models are discussed later.

Whilst the movement of a receiver is a continuous process, the models described are based on the sampling of observations and the estimation of state at discrete time intervals. The value of a time dependent variable or function $x(t)$ at time t_k is abbreviated by $x_k \equiv x(t_k)$.

Starting with a system described by a nonlinear dynamic model given by:

$$x_k = f_{k-1}(x_{k-1}) + w_{k-1}, \quad w_{k-1} \sim N(0, Q_{k-1}) \tag{4.1}$$

where x_k is the state vector at epoch k, f_{k-1} the state transition function describing the dynamic model, w_{k-1} the zero mean process noise which describes unmodelled changes in x not contained in f that can be described as a normally distributed random vector with associated covariance matrix Q_{k-1}.

The nonlinear measurement model relating the state x to a set of observations is given by:

$$z_k = h_k(x_k) + v_k, \quad v_k \sim N(0, R_k) \tag{4.2}$$

where h_k is the measurement model and v_k the zero mean, normally distributed measurement noise with covariance matrix R_k.

The estimated state of x_k is represented as $\hat{x}_k$ with associated covariance matrix, P_k, of the elements of $\hat{x}_k$. The two stages of the Kalman filter are represented by $\hat{x}_k(-)$ the predicted state based on the previous estimate, and $\hat{x}_k(+)$ the estimated state after adjustment of the predicted state by the measurements at time t_k. Similarly there is the *a priori* covariance matrix $P_k(-)$ associated with $\hat{x}_k(-)$ and the *a posteriori* covariance matrix $P_k(+)$ associated with $\hat{x}_k(+)$.

Given the dynamic model (Equation 4.1) and measurement model (Equation 4.2), the predicted state and modelled set of observations (given that state) are defined by the following nonlinear implementation equations:

- Computing the predicted state:

$$\hat{x}_k(-) = f_{k-1}(\hat{x}_{k-1}(+)) \tag{4.3}$$

- Computing the predicted observations:

$$\hat{z}_k = h_k(\hat{x}_k(-)) \tag{4.4}$$

The estimated state based on the predicted state and the measured observations is calculated using the following steps:

- Using a linearisation of the dynamic model about the predicted state:

$$F_{k-1}^{[1]} \approx \left.\frac{\partial f_k}{\partial x}\right|_{x=\hat{x}_{k-1}(-)} \tag{4.5}$$

  the covariance matrix can be propagated forwards in time to give the *a priori* covariance matrix:

$$P_k(-) = F_{k-1}^{[1]} P_{k-1}(+) F_{k-1}^{[1]\mathrm{T}} + Q_{k-1} \tag{4.6}$$

- The system dynamic model is linearised about the predicted state to give the design matrix:

$$H_k^{[1]} \approx \left.\frac{\partial h_k(x)}{\partial x}\right|_{x=\hat{x}_k^-} \tag{4.7}$$

- The predicted state can then be conditioned on the measurement

$$\hat{x}_k(+) = \hat{x}_k(-) + K_k(z_k - \hat{z}_k) \tag{4.8}$$

  using the Kalman gain matrix:

$$K_k = P_k(-) H_k^{[1]\mathrm{T}} \left[H_k^{[1]} P_k(-) H_k^{[1]\mathrm{T}} + R_k \right]^{-1} \tag{4.9}$$

  which weights the influence of the observations on the state based on the combined statistics of the predicted state and the observations.

- Finally the *a posteriori* covariance matrix of the estimated state can be computed:

$$P_k(+) = \left[I - K_k H_k^{[1]} \right] P_k(-) \tag{4.10}$$

The derivation of the Kalman filter requires that the random noise vectors v and w

must be uncorrelated with each other and in time i.e.

$$E(w_k v_j^{\mathrm{T}}) = 0 \quad \text{for all } j,\ k \tag{4.11}$$

$$E(w_k w_j^{\mathrm{T}}) = \begin{cases} Q_k & j = k \\ 0 & j \neq k \end{cases} \tag{4.12}$$

$$E(v_k v_j^{\mathrm{T}}) = \begin{cases} R_k & j = k \\ 0 & j \neq k \end{cases} \tag{4.13}$$

where E is the expectation operator. The implication is that any unmodelled biases in the system noise or observation noise will propagate into the solution. Hence the requirement for the precise models and corrections detailed in Chapter 3.

Due to errors introduced by numerical round-off caused by the limited precision of floating point computations commonly used in computers, the *a posteriori* covariance matrix can fail to be both symmetric and positive definite. The underlying cause is an ill-conditioned implementation; for example hugely different process noise values for different estimated parameters. To overcome the ill-conditioning an alternative expression for $P_k(+)$ known as the "Joseph form" may be used:

$$P_k(+) = \left[I - K_k H_k^{[1]}\right] P_k(-) \left[I - K_k H_k^{[1]}\right]^{\mathrm{T}} + K_k R_k K_k^{\mathrm{T}} \tag{4.14}$$

This is the sum of a symmetric positive definite matrix and a symmetric non-negative definite matrix, ensuring $P_k(+)$ is symmetric positive definite (Bucy and Joseph, 1968).

4.2 Kinematic PPP measurement models

This section describes the specifics and mathematical equations of the measurement model used in this GPS/GLONASS positioning software.

The model for code phase P_i and carrier phase Φ_i GPS pseudorange observations is:

$$P_i = \rho + d_{\mathrm{trop}} + cdt + \frac{I}{f_i^2} + \epsilon_{P_i} \tag{4.15}$$

$$\Phi_i = \lambda_i \phi_i = \rho + d_{\mathrm{trop}} + cdt - \frac{I}{f_i^2} + \lambda_i b_i + \epsilon_{\Phi_i} \tag{4.16}$$

for each of the two frequencies $i = 1,\ 2$.

In Equation 4.15 and 4.16:

- ϕ_i is the raw carrier phase observable in cycles,
- ρ the satellite to receiver range corrected for earth deformation and antenna effects,
- d_{trop} the tropospheric delay,
- c the speed of light,
- dt the receiver clock offset,
- I the dispersive ionospheric delay,
- ϵ_{P_i} and ϵ_{Φ_i} respectively, the code and carrier phase noise including multipath and receiver measurement error,
- f_i and λ_i the carrier frequency and wavelength on channel i,
- b_i the carrier phase bias.

Here the satellite and receiver FCB discussed in Section 2.5.1 have been included in the carrier phase bias b_i.

If the receiver records C1 instead of P1, the code observation is adjusted to a P1 equivalent observation using tabulated P1-C1 values, as described in Section 3.13.

The ionosphere free combination is formed for both code and phase observations to eliminate the ionospheric delay:

$$\begin{aligned} P_c &= \frac{f_1^2 P_1 - f_2^2 P_2}{f_1^2 - f_2^2} \\ &= \rho + d_{\text{trop}} + cdt + \frac{f_1^2 \epsilon_{P_1} - f_2^2 \epsilon_{P_2}}{f_1^2 - f_2^2} \end{aligned} \tag{4.17}$$

$$\begin{aligned} \Phi_c &= \frac{f_1^2 \Phi_1 - f_2^2 \Phi_2}{f_1^2 - f_2^2} \\ &= \rho + d_{\text{trop}} + cdt + \frac{f_1^2 \lambda_1 b_1 - f_2^2 \lambda_2 b_2}{f_1^2 - f_2^2} + \frac{f_1^2 \epsilon_{\Phi_1} - f_2^2 \epsilon_{\Phi_2}}{f_1^2 - f_2^2} \\ &= \rho + d_{\text{trop}} + cdt + b_c + \epsilon_{\Phi_c} \end{aligned} \tag{4.18}$$

where b_c is introduced as the ionosphere free carrier phase bias.

The model for GLONASS is similar, with the addition of an extra two terms to account for the difference between GPS and GLONASS time (dt_R), and the frequency

dependent differential code biases ($B^k_{c,R}$) (Cai and Gao, 2007). The time difference includes any offset between the time the receiver samples the GPS observations, and the time the receiver samples the GLONASS observations. Only applicable to the code observations is the differential code bias for each observation frequency. Equations 4.19 and 4.20 are respectively the ionosphere free code and carrier phase observation equations for GLONASS. The index k, used as both a subscript and a superscript denotes the frequency dependence of the denoted terms. The subscript R used to denote GLONASS specific observations and parameters is chosen to match the use of the character `R` in RINEX observation format files to identify GLONASS satellites.

$$\begin{aligned} P^k_{c,R} &= \frac{f^2_{1,k}P_1 - f^2_{2,k}P_2}{f^2_{1,k} - f^2_{2,k}} \\ &= \rho + d_{trop} + cdt + cdt_R + \frac{f^2_{1,k}\epsilon_{P_1} - f^2_{2,k}\epsilon_{P_2}}{f^2_{1,k} - f^2_{2,k}} + \mathrm{B}^k_{c,R} \end{aligned} \tag{4.19}$$

$$\begin{aligned} \Phi^k_{c,R} &= \frac{f^2_{1,k}\Phi_1 - f^2_{2,k}\Phi_2}{f^2_{1,k} - f^2_{2,k}} \\ &= \rho + d_{trop} + cdt + cdt_R + \frac{f^2_{1,k}\lambda_{1,k}b_1 - f^2_{2,k}\lambda_{2,k}b_2}{f^2_{1,k} - f^2_{2,k}} + \frac{f^2_{1,k}\epsilon_{P_1} - f^2_{2,k}\epsilon_{P_2}}{f^2_{1,k} - f^2_{2,k}} \end{aligned} \tag{4.20}$$

If using precise orbits referenced to a single time frame, the difference between GPS time and GLONASS time is contained within the individual satellite clock corrections so requires no further consideration. For example the ESA final GLONASS clock product is aligned to GPS time (Springer, 2010). This does not however imply that $dt_R \equiv 0$ as there is no guarantee that the receiver clock offset between GPS and GLONASS sampling time is zero, either due to sampling timing or different signal propagation paths within the receiver. What it does mean is that the satellite clock offsets correct both GPS and GLONASS satellite clocks to the same timescale and that the ECEF satellite coordinates for both systems are referenced to the same epoch.

4.3 The state vector

From the measurement model the unknown parameters that are either of direct interest or cannot be accurately modelled are:

$$x = [(x_r)_1,\ (x_r)_2,\ (x_r)_3,\ dZ_{\mathrm{wet}},\ cdt,\ cdt_R,\ b_1,\ b_2,\ \ldots,\ b_{1,R},\ b_{2,R}, \ldots]^{\mathrm{T}} \tag{4.21}$$

where $(x_r)_i$ are the three Cartesian coordinates of the receiver position within the reference frame defined by the precise orbit products used, dZ_{wet} the wet tropospheric zenith delay correction, cdt the receiver clock offset with respect to the time frame of the precise clock products, cdt_R the receiver GLONASS sampling time offset with respect to its GPS sampling time, b_i and $b_{i,R}$ respectively the GPS and GLONASS carrier phase biases for the visible set of satellites. Here b_i refers to the ionosphere free bias b_C (introduced in Equation 4.18) for GPS satellite i; similarly for the GLONASS biases $b_{i,R}$.

The exact order of the elements in the state vector is not important but for the following description of design and noise matrices, and in the software produced, the above order is used.

4.4 Calculating the expected observations

For each epoch the modelled value of all GNSS observations made at that epoch is calculated based on the predicted state (Equation 4.3). First the predicted position is adjusted for all Earth deformation effects, antenna offset and antenna phase centre offset.

The range ρ_r^s from receiver r to satellite s depends on the location of the satellite at the time of transmission. The time of transmission is itself dependent on the time of signal travel i.e. the range. Both precise and broadcast orbits are given in an ECEF frame so the rotation of the frame between time of transmission t_{trans} and time of reception t_{rec} must be taken into account. Combined, these effects give the simultaneous equations:

$$\rho_r^s = |R(t_{\text{rec}} - t_{\text{trans}})x^s(t_{\text{trans}}) - x_r| \tag{4.22}$$

$$t_{\text{trans}} = t_{\text{rec}} - \frac{\rho_r^s}{c} \tag{4.23}$$

where $R(t_{\text{rec}} - t_{\text{trans}})$ is the rotation matrix that maps points in ECEF at time t_{trans} to points in ECEF at time t_{rec}. There are two possible approaches to solving Equations 4.22 and 4.23. Either the pseudorange may be used as ρ in Equation 4.23, or the two equations may be iterated starting from a nominal value of ρ (e.g. 20 000 km) which converges rapidly. In this thesis the second method has been used as it enables modelling of satellite observations without the corresponding observation data.

The satellite antenna offset, phase centre offset and variations are then applied

to determine the effective transmission point given the calculated centre of mass. The additional corrections due to satellite and receiver clock offsets, phase windup, tropospheric delay, and the relativistic correction are added to the range having been calculated as described in Chapter 3. The ionosphere free combination is then formed for both the code and carrier phase observations.

4.5 Design matrix

The design matrix is the Jacobian of the measurement model (Equation 4.7). The full matrix form is shown:

$$\begin{pmatrix} \frac{\partial h}{\partial (x_r)_1} & \frac{\partial h}{\partial (x_r)_2} & \frac{\partial h}{\partial (x_r)_3} & \frac{\partial h}{\partial dZ_{\text{wet}}} & \frac{\partial h}{\partial dt} & \frac{\partial h}{\partial dt_R} & \frac{\partial h}{\partial b_1} & \cdots & \frac{\partial h}{\partial b_{1,R}} & \cdots \\ \vdots & & & & & & \vdots & & \vdots & \end{pmatrix} \tag{4.24}$$

with each row being a first order differentiation of the observation equation for each measurement, h, with respect to each element in the state vector. For the three position elements:

$$\frac{\partial h}{\partial (x_r)_i} = \frac{\partial}{\partial (x_r)_i} \left(\sum_j ((x^s)_j - (x_r)_j)^2 \right)^{\frac{1}{2}} = \frac{(x_r - x^s)_i}{\rho} \tag{4.25}$$

where x^s is the satellite transmission point, x_r the receiver reception point and $(\ )_i$ denotes the ith component of a vector.

For the estimated correction to the ZTD, differentiating the wet tropospheric delay from Equation 3.12 with respect to the estimated correction gives:

$$\frac{\partial h}{\partial dZ_{\text{trop}}} = m_{\text{wet}} \tag{4.26}$$

To avoid large differences in the magnitude of the values of $H^{[1]}$ which can lead to problems due to numerical round off (Grewal and Andrews, 2001), the receiver clock corrections and carrier phase biases are chosen to be estimated in metres, i.e. the

state vector contains cdt, cdt_R, $\lambda_c b_i$ and $\lambda_{c,k(i)} b_{i,R}$. This gives partial derivatives of:

$$\frac{\partial h}{\partial dct} = 1 \tag{4.27}$$

$$\frac{\partial h}{\partial dct_R} = \begin{cases} 0 & \text{GPS satellites} \\ 1 & \text{GLONASS satellites} \end{cases} \tag{4.28}$$

$$\frac{\partial h}{\partial \lambda_c b_i} = \begin{cases} 1 & \text{GPS satellite } i \text{ carrier phase observations} \\ 0 & \text{code and other carrier phase observations} \end{cases} \tag{4.29}$$

$$\frac{\partial h}{\partial \lambda_{c,k(i)} b_{i,R}} = \begin{cases} 1 & \text{GLONASS satellite } i \text{ carrier phase observations} \\ 0 & \text{code and other carrier phase observations} \end{cases} \tag{4.30}$$

4.6 Observation stochastic modelling

For each set of observations, the observation covariance matrix R in Equation 4.9 must be constructed. The ionosphere free observations are modelled as independent so off diagonal elements of R are zero. The code phase and carrier phase observations are assumed to be uncorrelated.

The described set of GNSS observations are heterogeneous in nature, mixed code and carrier phase, two GNSS systems, and have quite different measurement noise. To optimally combine a mixed set of observations the stochastic properties of each must be known so each observation is given the correct weighting in the filter.

Due to the wavelength of the pseudo-random noise signal that forms the code observation, there is a limit to how accurately a receiver is able to measure the code pseudorange. A static receiver can use a narrow correlator when tracking the code whereas, due to changing receiver dynamics, a kinematic receiver may have to use a wide correlator reducing the accuracy of the measurements made. Due to the considerably shorter wavelength of carrier phase observables and the frequency dependency of multipath (Lachapelle, 1991), the carrier phase noise is considerably lower than the code noise. Typical noise values for GPS are summarised in Table 4.1.

Elevation dependent weighting of the observations can be used to account for the increased noise due to the higher level of multipath, tropospheric and ionospheric delays experienced at lower elevations. Collins and Langley (1999) showed the most appropriate model was based on the signal to noise ratio. Modelling the observations as independent gives the following equation for the diagonal elements of the

Measurement	Noise
C code	10 cm to 300 cm
P code	10 cm to 30 cm
Carrier Phase	0.2 mm to 5 mm

Table 4.1: GPS observation noise (Hofmann-Wellenhof et al., 2008)

observation noise matrix R (Equation 4.9):

$$R_{ii} = C_i \times 10^{-\frac{\mathrm{SNR}}{10}} \tag{4.31}$$

where SNR is the signal to noise ratio and C_i a constant factor specific to the receiver carrier loop tracking bandwidth. However, much archived RINEX data does not include detailed signal to noise measurements; in this case the following elevation dependant weighting is used

$$R_{ii} = (\sigma_i \sin E)^2 \tag{4.32}$$

The off diagonal elements of R in the standard PPP model are zero.

Lau and Cross (2006) noted the orthogonal nature of the SNR and the carrier phase multipath. Using linear combinations of the observations to determine the pseudorange multipath, each set of observations from a satellite can be classified as containing a multipath error or not. By modifying the SNR based stochastic model when a multipath error is detected, up to 10% improvement in 3D RMS over the unmodified SNR model was found in high multipath environments.

Hesselbarth and Wanninger (2008) phase interpolated ESA GNSS clock products tabulated at 5 min intervals to a 1 Hz frequency and measured the GLONASS carrier phase residuals during PPP. They found the noise of GLONASS carrier phase observations to be comparable to GPS observations. In light of the high-rate GLONASS clock products now available from ESA, the relative noise of GPS and GLONASS carrier phase is compared in Chapter 7.

As the ionosphere free linear combination is used, variance propagation must be applied to determine the variance of the linear-combination given the variance of the observations on each frequency. Assuming no correlation between L1 and L2 the noise on the ionosphere free combination (Equation 4.18) is given by:

$$\sigma^2_{\Phi_c} = (\frac{f_1^2}{f_1^2 - f_2^2})^2 \sigma^2_{\Phi_1} + (\frac{f_2^2}{f_1^2 - f_2^2})^2 \sigma^2_{\Phi_2} \tag{4.33}$$

where $\sigma^2_{\Phi_1}$ and $\sigma^2_{\Phi_2}$ are the carrier phase variances on L1 and L2 respectively.

In the software produced the elevation dependent model in Equation 4.32 is used.

4.7 Parameter stochastic modelling

The stochastic model of the estimated parameters is needed for Kalman filtering. There are two things to consider: first the initial uncertainty which describes the accuracy with which the initial parameters are known, and second the epoch to epoch stochastics.

The initial covariance P_0 that describes the initial state vector $\hat{x}_0$ is set depending on the source of the initial state. Initially one may assume no correlation between elements of the state vector, requiring only diagonal elements of P_0 that represent the variance of each element of $\hat{x}_0$. If certain components of the initial state are known, for example starting the processing from known coordinates then the initial covariance may be provided. Another alternative is to use the method of Bancroft (1985) to solve directly for an initial position with an accuracy of at least 20 m. An initial value for the carrier phase biases may be found by differencing the carrier phase observations with the pseudorange observations:

$$\lambda_c b_i = \Phi_c - P_c \tag{4.34}$$

with initial variance given by the pseudorange observation noise stochastic model.

In the absence of a known dynamic model for the receiver coordinates, the unknown parameters of the state vector may be modelled as random walk processes with sufficient process noise to capture the epoch to epoch dynamics (Kouba and Héroux, 2001; Zumberge et al., 1997). The carrier phase bias parameters are, in the absence of cycle slips, assumed to be constant over time.

Consider a first order model of the state vector rate of change:

$$\dot{x}(t) = g(t)x(t) + w(t), \quad w(t) \approx q(t) \tag{4.35}$$

where $g(t)$ is the system rate dynamic model and $w(t)$ the random white noise defined by the spectral density matrix $q(t)$. The values of the process noise matrix Q_k can be found, to a first order approximation, by the propagation of the system

dynamic model spectral noise (Abdel-Salam, 2005):

$$Q_k = \int_0^{\Delta t_k} F_k^{[1]} q(t) F_k^{[1],\mathrm{T}} dt \tag{4.36}$$

where $\Delta t_k = t_k - t_{k-1}$ and $q(t)$ is the spectral noise.

A random walk process is well suited to receiver coordinate, troposphere delay and clock offset estimation as the rate of change is independent of the current value. For a random walk process, Equation 4.35 becomes:

$$\dot{x}(t) = w(t) \tag{4.37}$$

and the state transition matrix (Equation 4.5) is:

$$F_k^{[1]} = I \tag{4.38}$$

where I is the identity matrix.

With the use of a random walk stochastic model Equation 4.36 simplifies to:

$$Q_k = \int_0^{\Delta t_k} q(t) dt \tag{4.39}$$

The values of the vector $q(t)$ are highly dependent on the characteristics and dynamics of a particular receiver. Whilst the correct values may not be known the spectral density may be chosen to reflect the expected rate of change of a parameter. For example, at a static site the position is constant so q_{x_i} is chosen to be zero. In a survey vessel operating at speeds of up to $10\,\mathrm{m\,s^{-1}}$ the spectral density can be chosen as $q_{x_i} = 10^2 \mathrm{m}^2\,\mathrm{s}^{-2}$.

Tuning the spectral density to a particular application can improve the accuracy of the resulting estimated positions. Over constraining by specifying too low a spectral density results in a reduction in sensitivity to high rate changes in state whereas under constraining leads to excessive noise in the estimated state.

Table 4.2 shows the stochastic model used for the estimated parameters in the EKF. Obtaining a consistent stochastic model is critical to the estimation process but is not straight forward (El-Mowafy, 2011). If there is too much process noise, the estimated parameters will be less accurate due to the influence of observation noise. If there is too little process noise for the estimated parameters, then the filter will be very slow to converge and may not respond to the true dynamics of the system

Component	Stochastic model	Process noise standard deviation
Position	random-walk process	static 0, kinematic speed specific
Receiver clock error GPS	random-walk process	$100\,\mathrm{m\,s^{-0.5}}$
GPS-GLONASS system time offset	random-walk	$100\,\mathrm{m\,s^{-0.5}}$
Troposphere wet delay correction	random-walk	$10^{-3}\,\mathrm{m\,s^{-0.5}}$
Carrier phase ambiguities	constant	0

Table 4.2: Stochastic model of the extended Kalman filter parameters

(Grewal and Andrews, 2001).

The correct process noise depends on the receiver dynamics, the variability of the receiver clock and the variation in the troposphere delay at a given time. Therefore standard values will not be correct all of the time, but the aim is that they are relevant values for the majority of the time considered.

4.8 Quality control

Due to the recursive nature of the Kalman filter, any error in the measurements used not only corrupts the solution for that epoch but also future epochs. It is therefore very important to identify any such errors and correct for or remove them. The methods for dealing with uncorrectable outliers and potentially correctable cycle-slips are described in the next section.

4.8.1 *Outlier detection / blunder detection*

Due to multipath (see Section 3.14), undetected cycle slips and modelling errors, some observations will contain erroneous data. To check if a set of observations is consistent with the stochastic model associated with them, the Local Overall Model test may be used (El-Mowafy, 2010; Teunissen, 1990). The prefit residuals v_k are defined as the difference between the modelled observations and the measured observations:

$$v_k = z_k - H_k x_k(-) \tag{4.40}$$

where z_k are the measured observations, H_k the design matrix and $x_k(-)$ the predicted state.

As the Kalman filter is based on the prefit residuals being normally distributed, a Chi Squared test can be used to test if the prefit residuals are normally distributed.

The global test statistic:

$$T = v_k^{\mathrm{T}} C_{v_k} v_k \tag{4.41}$$

where the prefit residual covariance:

$$C_{v_k} = R_k + H_k P_k(-) H_k^{\mathrm{T}} \tag{4.42}$$

describes the expected variance and correlation between residuals based on the com-

bination of each observation uncertainty and the uncertainty in the predicted state.

An outlier is detected if:

$$T > \chi^2_\alpha(m_k, 0) \tag{4.43}$$

where m_k is the power of the test and α the level of significance.

If the global test statistic detects an outlier then a local test is performed to identify which observation is most likely to be the outlier. Each prefit residual $(v_k)_i$ is normalised:

$$w_i = \frac{(v_k)_i}{\sqrt{(C_{v_k})_{ii}}} \tag{4.44}$$

The index of the most likely outlier is given by $w_{\max}$ the largest absolute normalised residual:

$$w_{\max} = \max |w_i| \tag{4.45}$$

and is considered an outlier and rejected if it fails a normal test:

$$w_{\max} > Z_\alpha(0, 1) \tag{4.46}$$

where α is the power of the test.

The whole process is then repeated on the reduced set of observations until the global model test passes. If no observation fails the local test then the set of observations is inconsistent with the current state and the stochastic model. This could be due to the measurement variances used in the filter being too small or the state being over constrained through not adding enough process noise to describe the state dynamics. Adding additional process noise to the state covariance, $P_k = P_{k-1} + cI$ for some large c, effectively resets the filter, allowing it to re-converge.

4.8.2 *Cycle slips*

If using a positioning algorithm such as the Kalman filter, for which each carrier phase bias term is estimated over more than one epoch, cycle slips need to be identified and ideally corrected for (see Section 3.15). There are several methods to detect cycle slips:

- differencing two carrier phase measurements,
- comparing code and phase measurements,

- differencing the expected cycle count found by integrating the Doppler measurement from the observation,
- monitoring the time difference of wide and carrier phase combinations.

A detection scheme based on a real-time implementation of Blewitt (1990) as adapted by Bisnath (2000) was implemented as described below.

For a dual frequency receiver, a cycle slip is an integer change in one or both of the carrier phase biases:

$$(\Delta n_1,\ \Delta n_2) = (b_1' - b_1,\ b_2' - b_2) \tag{4.47}$$

where b_1' and b_2' are the new values of the phase biases after a cycle slip. A cycle slip can happen on one or both of the carrier frequencies at once, so any detection and repair scheme must be sensitive to both cases, and able to separate out the effect of the slip on each of the frequencies.

The wide-lane phase combination of the two carrier frequencies is given by:

$$\Phi_\delta \equiv \frac{f_1\Phi_1 - f_2\Phi_2}{f_1 - f_2} \tag{4.48}$$

$$= \rho + I\frac{f_1 f_2}{f_1^2 - f_2^2} + \lambda_\delta b_\delta + M \tag{4.49}$$

where $\lambda_\delta = c/(f_1 - f_2)$ is the wavelength of the combination and $b_\delta = b_1 - b_2$ the wide-lane bias. I is the ionospheric delay and M the non-dispersive delays i.e. tropospheric and tidal effects.

To isolate the wide-lane bias, the following pseudorange combination may be subtracted from Φ_δ:

$$P_\delta \equiv \frac{f_1 P_1 + f_2 P_2}{f_1 + f_2} \tag{4.50}$$

$$= \rho + I\frac{f_1 f_2}{f_1^2 - f_2^2} + M \tag{4.51}$$

Then subtracting Equation 4.48 from Equation 4.50, the wide-lane bias, also known as the Melbourne-Wübbena combination, is given by

$$b_\delta = \frac{1}{\lambda_\delta}(\Phi_\delta - P_\delta) \tag{4.52}$$

The wide-lane wavelength , λ_δ, is approximately 86.2 cm so any integer change in b_δ produces a large change in Φ_δ. The long wavelength of the wide-lane means the jump

introduced by a cycle slip is considerably larger than the expected measurement noise. This makes it possible to distinguish any cycle slips from noise in the code observations. However, cycle slips where $\Delta n_1 = \Delta n_2$ are undetectable using this method.

Determining the value of b_δ can be done by forming a running or windowed average. This reduces the effect of pseudorange noise and gives a value against which successive wide-lane biases may be compared. A cycle slip is identified when the value of b_δ differs from the running mean $\langle b_\delta \rangle$ by more than a chosen multiple of the running mean RMS scatter. The running mean and variance can be recursively computed at each epoch as:

$$\langle b_\delta \rangle_i = \langle b_\delta \rangle_{i-1} + \frac{1}{i}(b_{\delta i} - \langle b_\delta \rangle_{i-1}) \tag{4.53}$$

$$\sigma_i^2 = \sigma_{i-1}^2 + \frac{1}{i}\left\{(b_{\delta i} - \langle b_\delta \rangle_{i-1})^2 - \sigma_{i-1}^2\right\} \tag{4.54}$$

with the calculation of the variance being an approximation with error of $O(1/i^2)$, where i is the number of epochs since the last cycle slip.

The wide-lane combination is insensitive to cycle slips of equal magnitude on both frequencies, so a second measure is needed that is sensitive to such slips. The ionospheric phase combination, sometimes called the geometry free combination is commonly used for this purpose.

The ionospheric phase combination is formed from Φ_1 and Φ_2:

$$\begin{aligned} \Phi_I &\equiv \Phi_1 - \Phi_2 \\ &= I + \lambda_1 b_1 - \lambda_2 b_2 \\ &= I + \lambda_1(b_1 - b_2) + (\lambda_1 - \lambda_2) b_2 \\ &= I + \lambda_1 b_\delta - \lambda_I b_2 \end{aligned} \tag{4.55}$$

where the ionospheric wavelength $\lambda_I \equiv (\lambda_2 - \lambda_1) \approx 5.4\,\text{cm}$. Due to the short wavelength of the ionospheric phase combination, the pseudorange cannot be used to remove the ionospheric delay as the noise level of pseudorange observations is too high. Instead the ionospheric combination is time differenced, removing many of the highly time correlated errors. As the ionospheric combination is free from the receiver–satellite geometry, what remains in the time difference is the rate of change

of the ionospheric delay:

$$\Delta\Phi_I = \frac{\Phi_I(t_k) - \Phi_I(t_{k-1})}{t_k - t_{k-1}} \tag{4.56}$$

The theory is that the rate of change of the ionosphere is limited to some bounding value. If $|\Delta I_\Phi|$ is greater than some threshold value then a cycle slip is detected.

Having detected a cycle slip, the next step is to find the integer values of the slip allowing the estimated cycle slip to be corrected to match the current state of the receiver. If the data is being post processed then the sections of cycle slip free carrier phase observations, commonly know as "phase connected arcs", may be identified. For each pair of arcs, interrupted by a cycle slip, the two values of $\langle b_\delta \rangle$ are known. The wide-lane cycle slip is then determined by subtracting the two $\langle b_\delta \rangle$. How close this value is to an integer, combined with the uncertainty in the two values of $\langle b_\delta \rangle$, allow the integer discontinuities to be identified with a high level of statistical confidence. Similarly for the ionospheric combination, as the arc before and after the slip are known, polynomial fitting may be performed. The polynomial may then be extrapolated forwards and backwards across the disconnect allowing the cycle slip to be reliably determined.

For processing in real-time mode these options are not available, so an instantaneous method to fix the slips is required. Banville and Langley (2010) proposed a method based on the techniques used in relative positioning ambiguity fixing but using time differenced measurements. Most of the errors affecting GNSS signals are highly time correlated so over a short time period they may be mostly removed by time differencing. The time difference is composed of the relative receiver/satellite velocity, clock drift and any cycle slips:

$$\Delta\Phi_i = \Delta\rho_r^s + \Delta dt + \lambda_i \Delta n_i \tag{4.57}$$

The cycle slips detected, as well as the receiver velocity and clock drift, are solved for in a least squares adjustment. In comparison to the real valued bias term in the PPP observation model (Equation 4.16), the cycle slip bias term, Δn_i, is integer valued. The techniques of integer least squares, such as the LAMBDA method (Teunissen, 1995) may now be applied to determining the cycle slips. The success rate of this technique is dependent on the number of simultaneous cycle slips. In the case of total loss of lock where there is a cycle slip on all channels, the pseudorange is used to constrain the least squares solution. Thus, in this extreme case the success of the

technique is highly dependent on the current level of pseudorange noise. Banville and Langley (2010) reported cycle slip fixing success rates of greater than 95% for static and kinematic sites with 1 Hz observations, with a rapid drop off in success rate for kinematic positioning with observation intervals greater than 10 s. Thus whilst the method was shown to be very effective for fixing cycle slips with no associated data gap, cycle slips where tracking of the signal is lost for 10 s or longer still prove problematic.

If it is not possible to fix a cycle slip then the row and column in the covariance matrix $P_k(-)$ corresponding to the bias can be zeroed and then reinitialised from the carrier phase - pseudorange difference (Equation 4.34).

4.9 Feasibility of PPP

4.9.1 *Dilution of precision and the effect of observation error budget on estimated position*

Observations contain the range from satellite to receiver, path delays and advances due to atmospheric effects, the error due to inaccurate values for satellite position and clock offset, as well as relativistic effects. Also there are deformation effects where a given location on the Earth moves with respect to the chosen reference frame due to Earth body tides, ocean tide loading and atmospheric pressure loading. Finally there is the accuracy with which the receiver is able to measure the received signals and the effect of multipath. The combined residual effect of these phenomena on the range after modelling and mitigation comprises the error budget (Chapter 3).

The effect of range errors on the estimated parameters is captured by a measure known as Dilution Of Precision (DOP). The DOP factor is a measure of the instantaneous geometry of the visible satellites with respect to a receiver (Hofmann-Wellenhof et al., 2008).

The DOP can be calculated from the cofactor matrix Q_X

$$Q_X = (H^{[1]T} P H^{[1]})^{-1} \tag{4.58}$$

where $H^{[1]}$ is the linearised observation equation and P is the weight matrix.

The subscript capital X denotes that the coordinates are in an ECEF reference frame.

Writing the elements of Q_X as:

$$Q_X = \begin{bmatrix} q_{XX} & q_{XY} & q_{XZ} & q_{Xt} \\ q_{XY} & q_{YY} & q_{YZ} & q_{Yt} \\ q_{XZ} & q_{YZ} & q_{ZZ} & q_{Zt} \\ q_{Xt} & q_{Yt} & q_{Zt} & q_{tt} \end{bmatrix} \tag{4.59}$$

the diagonal elements are used for the following DOP definitions for Geometric Dilution Of Precision (GDOP), Positional Dilution Of Precision (PDOP) and Time Dilution Of Precision (TDOP):

$$\text{GDOP} = \sqrt{q_{XX} + q_{YY} + q_{ZZ} + q_{tt}} \tag{4.60}$$

$$\text{PDOP} = \sqrt{q_{XX} + q_{YY} + q_{ZZ}} \tag{4.61}$$

$$\text{TDOP} = \sqrt{q_{tt}} \tag{4.62}$$

The positional elements of the global cofactor matrix Q_X can be transformed into the local cofactor matrix Q_x in the topocentric local coordinate system with axes along the local north, east and up directions as:

$$Q_x = RQ_xR^T = \begin{bmatrix} q_{nn} & q_{ne} & q_{nu} \\ q_{ne} & q_{ee} & q_{eu} \\ q_{nu} & q_{eu} & q_{uu} \end{bmatrix} \tag{4.63}$$

where the rotation matrix $R^T = [neu]$ contains the axes of the local coordinate system. Due to the invariance of the trace of a matrix with respect to rotation, the PDOP value in the local system is identical to the value in the global system.

Two further DOP definitions that capture the dilution of precision in the local horizontal and vertical, Horizontal Dilution Of Precision (HDOP) and Vertical Dilution Of Precision (VDOP) are defined as:

$$\text{HDOP} = \sqrt{q_{nn} + q_{ee}} \tag{4.64}$$

$$\text{VDOP} = \sqrt{q_{uu}} \tag{4.65}$$

It is then possible to map the expected range error due to the error budget discussed in Section 3.16, to a theoretically achievable positional accuracy, as the product of DOP and measurement accuracy.

Therefore given an error budget with standard deviation σ_{range}, the positional accuracy would be PDOPσ_{range}.

4.9.2 *Expected positional accuracy*

Many studies have shown the feasibility of PPP in achieving centimetre accurate static PPP and decimetre level in kinematic mode (Bisnath, 2004; Bisnath and Gao, 2008; Dixon, 2006; Gao et al., 2005; Kouba, 2009a; Muellerschoen et al., 2001).

Using the DOP to project the expected error from the measurement domain to the position domain, it is possible to obtain a simplistic view of the expected positional accuracy. The simplified calculation using DOP assumes that the UERE is the same for every satellite and there is no correlation between the range errors. Multipath, ionosphere, and troposphere delays all increase at low elevations, and are accounted for using elevation dependent weighting. Errors in the satellite clock and orbit products are correlated; Zumberge et al. (1997) note that combining orbit and clock products from different sources results in degraded position repeatabilities, showing the two not to be independent, so that the absolute measures of accuracy in both orbits and clocks are reduced when combined to produce a range error bias.

Figure 4.2 shows the DOP values for a receiver in Newcastle upon Tyne, UK on 14/04/2011 using a 10° elevation cutoff. As is expected from the increased number of satellites the DOP values when including GLONASS are reduced. Additionally the DOP spikes present when only considering GPS are greatly reduced with a more consistent DOP.

Using the average values from the above example and the residual error budget for carrier phase observations from Chapter 3, gives the one sigma horizontal and vertical positioning accuracy shown in Table 4.3.

GPS
HDOP 1.0 x 8.3 = 8.3 cm
VDOP 1.6 x 8.3 = 13.3 cm

GPS/GLONASS
HDOP 0.75 x 8.3 = 6.2 cm
VDOP 1.1 x 8.3 = 9.1 cm

Table 4.3: Expected Horizontal and Vertical PPP accuracy

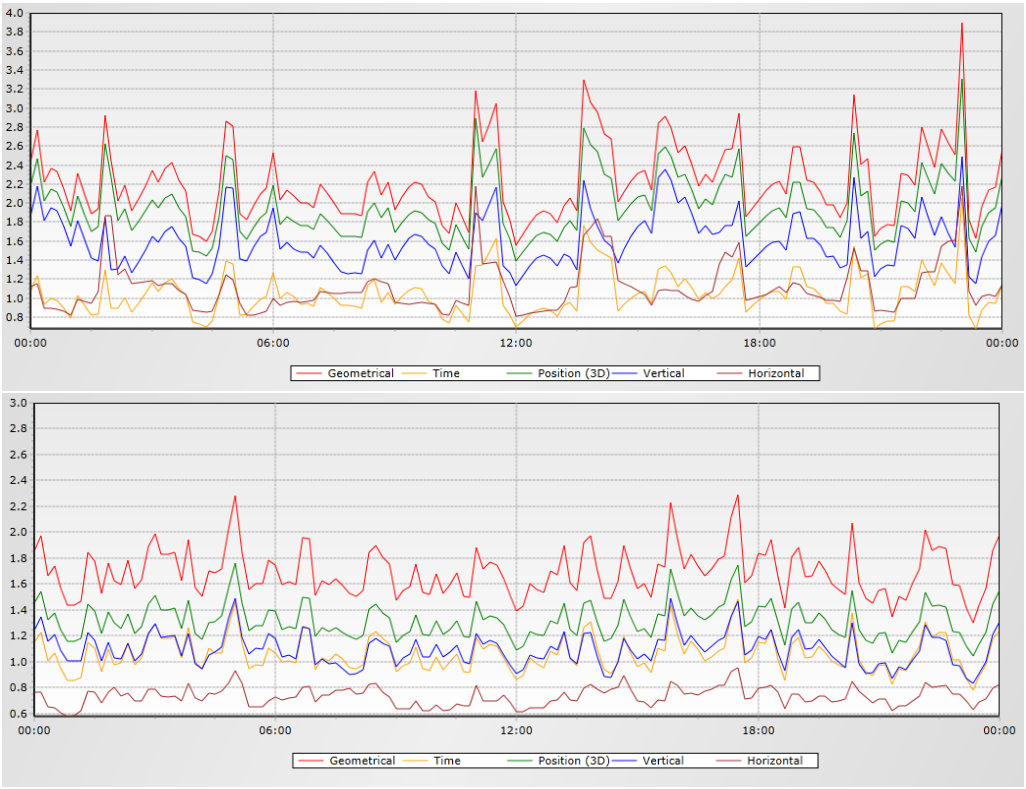

Figure 4.2: GPS (top) and GPS/GLONASS (bottom) DOP values for 14/04/2011 (Data from Trimble GNSS Planning Online `http://www.trimble.com/GNSSPlanningOnline`)

The values in Table 4.3 are instantaneous accuracies assuming the ionosphere free carrier phase ambiguity has been estimated with sufficient accuracy to not affect the error budget (centimetre accuracy) i.e. after convergence. For static positioning the accumulated average of many observations will remove the effect of any zero mean biases on the estimated coordinates resulting in the higher accuracy seen in the literature (Geng et al., 2010c).

Initially, the ambiguities are unknown and the accuracy is determined by the pseudorange error budget and the dilution of precision. Most of the pseudorange noise is due to tracking noise and multipath. As these are not constant bias parameters, time averaging reduces the impact of the errors on the range error. This is the mechanism behind convergence whereby sufficient observations are built up in the estimation filter to reduce the uncertainty in the value of the carrier phase ambiguities, and therefore increase the weight of the carrier phase observations in the position estimation. Therefore the convergence time is largely defined by the pseudorange noise and geometry.

4.10 Summary

This chapter has explained the principles of the Extended Kalman filter, as well as the basis for choosing this technique by comparison with alternative estimation methods. The implementation of the PPP method is described, including definition of the observation model. The mathematical basis of the estimation process, as well as the detailed methods for detecting outliers and cycle slips, are taken forwards into the next chapter which describes the software developed to implement these models.

Chapter 5 Software development

In order to achieve the research objectives, and investigate the impact of combining GLONASS with GPS data on the performance of PPP as a navigation method, a software package *pppncl* was created. This software was capable of performing PPP in real time mode, with the ability to process data from GLONASS as well as GPS.

This software was created based on the theory described in the preceding two chapters. The source code for *Track* (Chen, 1998) was used as a starting point, providing some of the signal propagation delay models, planetary locations, Earth tide routines and GPS-only RINEX file reading.

The following sections provide a brief description of the software design and architecture used, as well as reflecting on the approach to developing this software package.

5.1 Creating a PPP navigation program

Following definition of the research problem and consideration of the proposed experiments to be undertaken, it was determined that *pppncl* needed the following functionality in its design:

- Operate in real time mode
- Process kinematic datasets
- Read standard format observation and ephemeris data
- Process multi-day observation files.

For the software to operate in real-time mode, and function as if it were operating in real-time, there cannot be multiple passes through the input data. Therefore the Kalman filter must operate in filtering mode, where the estimated state at a given time is based only on observations available at or before that time. Additionally, the cycle slip detection algorithms are designed such that they do not require future data.

To allow processing of kinematic datasets the software was designed with no constraint, or assumption, that the predicted position is close to the previous position, therefore all modelled parameters that depend on the receiver position are recalculated with every new observation epoch.

The real-time mode operation forms the design for the high level architecture, which is discussed in Section 5.3.

As navigation data is often distributed as distinct daily files, to analyse continuous receiver observation data spanning more than one day, it is necessary to be able to read multiple navigation files; the approach taken to address this in *pppncl* is discussed in Section 5.4.

In Chapter 3 the models required to minimise the PPP error budget are described, as not all of these existed in *Track* the following needed to be implemented:

- ANTEX format file parsing to read phase centre offsets and variations
- The relativity correction, as given in Section 3.5.
- The phase windup correction as described in Section 3.7
- The GMF troposphere mapping function as given in Equation 3.5
- Real-time mode cycle slip detection
- Real-time mode outlier detection and removal

5.2 Adding GLONASS processing

Having made a software program capable of processing GPS data using the PPP method, extending this software to include additional GLONASS observation data did not require significant changes to the high level software design. GLONASS is very similar to GPS; both systems are dual frequency with the two base carrier frequencies at a similar frequency. As the same theory applies to both systems for many of the physical effects that are modelled, the same processing strategy can be applied.

There are however widespread implementation details that require alteration to accommodate a second satellite network. In *Track* each GPS satellite was uniquely identified by its number. However for a multi-GNSS software each satellite needs to be identified by its network and number. In *pppncl* the choice was made to represent this as a pair of numbers, one to represent the satellite network and one to represent the satellite id. The use of Fortran 90 derived types (Metcalf and Reid, 1999) allows for the definition of a satellite type that is used throughout the program and encapsulates this information.

Another modification required was to update the RINEX reading routines to parse GLONASS observation and navigation data, as well as GPS data.

A function to calculate the carrier frequencies of a GLONASS satellite was created that uses lookup data from the RINEX GLONASS navigation file. The lookup data is required as GLONASS satellites are identified by their slot number based on their position in the satellite grid. Determining the carrier frequency of a given satellite requires the frequency number of that slot number at the given time. This information is included in the RINEX GLONASS navigation file.

The increased satellite numbers due to the inclusion of GLONASS require many of the data storage arrays and matrices to be increased in size. Specifying the array size parameters as a constant allows the same value to be reused in the many places it is required whilst providing the ability to easily change all such instances by only modifying the value in one place. The code was written such that the dimensions of the storage arrays are calculated based upon the number of satellite systems and the number of satellites within each system. This approach offers a simple solution to updating this area of the software to include additional satellite networks in future.

5.3 Source code

The software program *pppncl* developed as part of this thesis is written largely in Fortran 90, with certain reused components in Fortran 77. Fortran was chosen due to the ease of reusing existing code from *Track* that contained many relevant subroutines. Fortran 90 is a superset of the language specified in Fortran 77; the additions include modules, array syntax and derived types.

Modules allow for grouping of functions, subroutines, data types and variables. Grouping sections of code that are conceptually related helps to organise the code during creation and further development. Additionally module interfaces allow the compiler to check that functions and subroutines are being called with the correct number and type of input and output variables passed; this helps catch a common cause of programming error.

In *pppncl*, each set of functionality is packed in a Fortran module. Other modules or functions that make use of a particular module must explicitly state this with the `use` statement. This allows inter-module dependencies to be easily discovered when reading the source code.

Array syntax provides native language support for simple vector mathematics. This allows for elimination of many loops that would be required in Fortran 77.

Derived types allow for the representation of abstract quantities in a single variable. *pppncl* makes use of this to enable the use of object-oriented concepts in Fortran 90 as described by Decyk et al. (1997). For example the Melbourne-Wübenna cycle slip detector described in Section 4.8.2 is implemented in this way. The running averages and standard deviations, along with the required book-keeping, are encapsulated within one variable.

Whilst Fortran provides good syntax for mathematical operations and produces fast numerical code it was found during development of *pppncl* to be less suited to experimentation than higher level more dynamic languages such as Python. Indeed the absence of more complex data types and only a minimal standard library in Fortran often lead to slower implementations due to the laborious nature of implementing basic functionality from scratch.

The majority of variables in *Track* are shared through Fortran common blocks. The use of such global variables is often considered to make programs more difficult to understand (Wulf and Shaw, 1973). An attempt was therefore made to create *pppncl* such that subroutines were made smaller and operated only on those variables that were passed in.

An attempt was made to create an interface to the modelling and linear combination of measurements, as outlined below, as a single function. Initially this seemed to work well but as the software grew as additional models and GLONASS observations were added, issues began to arise. As the modelling was separate from the code that dealt with the estimated state vector, this resulted in many values being copied into and out of the Kalman filter matrices and state vector. Had the modelling been carried out as a distinct step, the prefit residuals and observation process noise could have been calculated directly in the Kalman filter.

Due to the experimental nature of the developed software, it was sometimes found that a calculated value that had been encapsulated within a function was needed at a higher level in the call stack. The advantage of widespread use of shared variables such as used in *Track* is that there is no need to predict this requirement in advance.

The structure of the program is described below with details of the implementation given in Appendix A. During the design phase the potential future conversion to a true real-time PPP positioning engine was considered, hence each loop starts with

the reading in of a new observation.

The structure of *pppncl* is as follows:

- Read in command file to configure program
- Read navigation data
- Read observation file header
- Read in antenna phase centre offsets and variations
- If required read P1C1 bias file
- For each observation in the input file
  - Perform Kalman filter time update step
  - Get satellite frequencies
  - Apply P1C1 biases if required
  - Modelling and linear combination of measurements:
    - Model carrier phase and code phase pseudoranges for each satellite
    - Form partial derivatives of observations with respect to the estimated state
    - Form observed minus computed prefit residuals
    - Model observation stochastics
  - Check for millisecond jumps in the receiver clock
  - Perform cycle slip detection
  - Attempt to repair any detected cycle slips
  - Perform outlier detection and removal
  - Estimate new state based on the current set of measurements
  - Output estimated state and other output files

5.4 Input formats

There are several file formats designed and used by the wider GNSS community to allow exchange of information. The use of open standards allows the use of observation data from the many receivers, and navigation data produced by analysis centres which is freely available on the Internet. By implementing these input formats in *pppncl*, this research was able to benefit from the work of the wider GNSS community.

This section describes the types of input file that can be read by *pppncl* when performing PPP. The different formats that can be used for each type of input data are explained.

pppncl can read the RINEX 2 format for observation data and navigation data (orbits and clocks). RINEX 2 was designed with only GPS in mind, and later adapted to allow mixed data from GPS and GLONASS satellites in the same file. It has become apparent that it has shortcomings as a receiver observation exchange format for files containing observation data of more than one satellite system, each one with different observation types. To address this Gurtner and Estey (2007a) proposed the RINEX 3 standard. Whilst it seems logical that RINEX 3 will replace RINEX 2 as the standard data exchange format, the not inconsiderable effort required to update all the tools used by the wider GNSS community has meant that RINEX 3 adoption has been very slow. For that reason only a RINEX 2 reader has been implemented in *pppncl* currently.

The common format for precise navigation data is the SP3 revision c format (Hilla, 2002). The precise navigation data produced by IGS analysis centres is distributed in SP3 format, in daily (24 hour) files. For observation windows of longer than a day, multiple SP3 files are required to span the observation interval. There are known discontinuities at the day boundary in the generated precise orbits (Griffiths and Ray, 2009), in *pppncl* interpolation is performed across this discontinuity. As there is not a commonly used tool to concatenate multiple SP3 files together, the facility to read directly concatenated SP3 files was added to *pppncl*. Multiple header blocks are therefore allowed in *pppncl* SP3 input files.

High rate clock data, essential to high rate PPP can be read in RINEX 2 or 3 clock format (Ray and Gurtner, 2010). As with the SP3 files the ability to read multiple concatenated files was implemented to enable processing periods of more than one day.

Within *pppncl* the different navigation formats are abstracted behind a common navigation data interface. The underlying navigation data may be a broadcast ephemeris in RINEX navigation format or a precise ephemeris in SP3 format, possibly augmented with higher rate satellite clock corrections in RINEX clock format. Within the modelling functions the underlying navigation data source is hidden providing a simple "get satellite position at time t" subroutine.

For the mapping between GLONASS satellite number and GLONASS frequency number, the broadcast GLONASS navigation data is always required even when using precise orbits in SP3 format.

The standard format for distributing satellite and receiver antenna phase centre offsets and variations is the ANTEX format (Rothacher and Mader, 2003; Rothacher and Schmid, 2010). An ANTEX file parser was written to read ANTEX v1.4 format files which contain the required satellite and receiver PCO and PCV as discussed in Section 3.7.

DCBs are distributed in a tabular format for use by `CC2NONCC` (Romero, 2010). In order to avoid having to pre-process RINEX observation files from receivers that record C1 rather than P1, the ESOC updated version of the `CC2NONCC` software routines were integrated into *pppncl*.

5.5 Configuration file

Within *pppncl* there are some parameters that are needed in order to run and others for which there are a range of choices based on enabling specific functionality or a numerical value describing a particular property. For example, the location of the input and navigation files is required. The ability to enable optional functionality such as using GLONASS satellites and change state vector process noise, for example to correspond to the expected receiver dynamics, was also required.

The use of a configuration file allows for the input parameters to be adjusted easily. Compared to command line options this provides a documented record of the input options and allows for easily repeatable test runs. The syntax was kept simple to ease creation and parsing with a keyword on each line identifying the parameter that is being configured.

5.6 Output files

The output files and formats used were created to satisfy the needs of the analysis produced in the following chapters. They are all space separated tabular text files. Plain text output files do not require special tools for manipulation and provide the maximum compatibility for use with plotting tools.

5.7 Tools for setup and running

To aid setup and help with running repetitive tasks a number of Python scripts have been created. The Python programming language provides strong text manipulation functionality along with a comprehensive standard library, including the ability to easily download files from the Internet.

For every run of *pppncl* the following tasks must be performed: Acquiring and preparing all the required input files then creating a configuration file that specifies the prepared input files. To avoid having to do this manually when the desire is to run many sets of data that share a largely common set of configuration parameters, a set of Python scripts was created to facilitate the set up.

Scripts were written to address two common use cases of *pppncl*: estimate the position of a receiver using observations from a given RINEX file, and estimate the position of one or more named sites from the IGS network. The configuration parameters not relating to the input files can be specified as a template to the scripts. This facilitates estimating many sites using the same set of configuration parameters.

The data processing involved in generating the results presented in Chapters 6 and 7 required many runs of *pppncl*. The run time of *pppncl* is approximately 4 minutes for 24 hours of positioning at a 1Hz data rate on a 2.7 GHz Intel i5-2557M processor; performing this operation hundreds or thousands of times on a single computer takes a prohibitively long time.

The Condor software project describes itself as "a specialized workload management system for compute-intensive jobs. Condor provides a job queueing mechanism, scheduling policy, priority scheme, resource monitoring, and resource management." (Thain et al., 2005). As each run of *pppncl* is independent of any other, using Condor the required processing was distributed over multiple computers, thus greatly reducing the run time.

During use these scripts became the user facing interface to the program. Given that the software has become a composite of two languages each with different strengths, a more flexible way of constructing the program would be to create the split between Python and Fortran at a lower level. In this way the models and processing steps such as outlier detection, cycle slip detection and repair, and Kalman filtering would become composable units. This would simplify the "glue" code that sets the program up and calls each unit in turn. New ideas or approaches could be rapidly prototyped in the high level language, only being re-implemented in Fortran if successful and there was a need for reduced runtime.

5.8 Summary

This chapter has discussed the key areas that were considered in the creation of *pppncl* from a software design and implementation perspective. This includes the approach used to implement both a PPP software package and the extension to include GLONASS. Related sections have reflected on the high level software architecture, specifically the importance of code structuring.

A flexible structure is critical in a research context so that adaptations may be made to answer any further questions as they arise. By splitting conceptually related areas into modules with a small interface, the larger program is isolated from any changes required internal to that module. This also provides a secondary benefit for future use as an accessible research development platform. Careful consideration of the overall problem definition at the initial stage avoids design choices that require lengthy rewrites. The benefits of using high level scripting languages to automate repetitive tasks, and provide a more flexible interface to the low level computationally intensive parts are highlighted.

The needs for input and output data formats have been examined; the approach taken enabled full use of available datasets. Further, the practical implications of using *pppncl* to analyse large and varied datasets were addressed, with specific attention to the tools used to configure the program, process multi-day data, as well as the computer power required. The combination of all these factors has enabled the successful creation of *pppncl*, the use of which has produced the results required to answer the research questions investigated in this thesis within a practical time frame.

For reference the specific implementation details of *pppncl* are given in Appendix A.

Chapter 6 PPP validation

Before using the created program, *pppncl*, to quantify the impact of the addition of GLONASS observations on GPS PPP, it was necessary to verify the performance of the PPP implementation using only GPS observations. This verification included testing the performance of the program for both static and kinematic receivers.

The ideal characteristics of a PPP validation scheme to validate a PPP program against the performance metric described in Section 2.9 are described below. The key performance metrics against which *pppncl* is evaluated are convergence time and positioning accuracy.

In validation of both kinematic and static PPP implementation, the following characteristics are desirable. The coordinates of the receiver must be known, to provide the reference solution against which the estimated position is compared. In the ideal case, there is no error in the reference coordinates. The apparent accuracy of the position estimation is affected by the accuracy of the truth coordinates. This reduces the ability to determine the true accuracy of the estimated coordinates. For example any correlation in the errors in the estimated and truth coordinates, will appear to improve the accuracy of the estimated coordinates. A globally distributed set of sites is desirable to capture the range of the parameters which change with location; these include different satellite geometries, Earth tide and atmospheric variations. Additionally, analysis of multiple sites also ensures that any conclusions drawn are representative of the performance of the PPP implementation being validated.

It is preferable to cover the longest possible time period to account for temporal variation. Ideally, this would be one long continuous dataset (>1 year), or multiple shorter datasets dispersed throughout the year. There is a minimum useful time length for a specific dataset, as it needs to be long enough to capture the convergence period (order of hours). In the literature, static positioning accuracy is often considered over a 24 hour period, therefore this minimum length is useful for cross comparison of results. By contrast, in kinematic validation, the minimum useful time period is the period for the solution to converge, approximately 4 hours based on typical convergence times seen by Bisnath and Gao (2008). A longer period is preferable, providing more data to analyse the performance metrics in a converged state. In the ideal case, the validation scheme would cover a period of several years, to include a variety of stages in the solar cycle, a longer period temporal parameter.

Whilst the handling of multipath and cycle slips is important in terms of understanding the achievable accuracy and integrity of PPP, in terms of validating the

software, they complicate the assessment of best case accuracy and convergence time. It is known that multipath degrades the positioning accuracy but as no new techniques have been implemented in *pppncl* to mitigate it, this is not a focus area of the validation. Similarly, cycle slips, satellite obstructions or loss of lock will interrupt the filter convergence, and therefore reduce the utility of a dataset in assessing convergence time. Therefore, a "clean" environment is desirable, with low multipath and an uninterrupted sky view.

The other aspect of a validation scheme that should be considered is the statistical methodology used to compare the results of the PPP program to the reference solution, in particular accounting for uncertainties in the estimated parameters. For static positioning, the statistical measures that should be compared to validate the test solution versus reference solution are the mean, standard deviation, and the RMS. For kinematic datasets, in addition to these measures, the convergence time was also evaluated to show equivalent results to those published in literature. In this thesis, the static and kinematic PPP performance results were compared to the specific reference solution in each case, as well as in more general terms, to the performance metrics given in literature.

Whilst the above characteristics describe the ideal validation scheme, there are practical limitations to executing any validation scheme. In terms of the reference solution, exact coordinates do not exist. Any set of coordinates is measured with respect to some reference frame; both the definition of the reference frame, and the measurements introduce errors into the truth coordinates given. This complicates the analysis of the PPP estimation accuracy; with no error, any difference between the PPP and reference solution can be attributed to the PPP solution.

Availability of the datasets is another consideration, datasets must either be collected, a sometimes time consuming process, or available publicly. This impacts the time period for which datasets may be available. In particular, kinematic datasets are not widely available, particularly as a range of receiver dynamics is desirable. The availability of static sites in terms of global distribution is influenced by the location of available sites. Global distribution is also constrained by the geographical challenges of accessing and operating in some environments, in particular off-shore locations.

It is not possible to perfectly control the immediate environment of the receiver, in terms of multipath and potential for cycle slips. A further limitation is computational processing time of the datasets, this restricts how much data can be analysed

in a given time period with available computer resource. Finally, it is of course necessary that all supporting data, for example satellite orbit and clock data, are available corresponding to the datasets processed.

Throughout this thesis, orbit and clock products are used which have been obtained from IGS analysis centres and Veripos. Different products are used depending on the requirements of the test, and to provide comparison of available accuracy between different products. The advantages of using IGS analysis centre clocks are summarised by Kouba (2009a):

> "The users of the IGS products in fact take full advantage of the IGS AC global analyses, properly combined and quality checked, all in accordance with the current international conventions and standards."

Use of the publicly available IGS analysis center products makes the tests repeatable. Whilst the software has been formulated in a real-time mode, the majority of tests are performed using final orbit and clock products which are not available until one to two weeks after the date they relate to. In assessing static positioning, much of the published work, for example Leandro et al. (2011) and Bisnath and Gao (2008) make use of the combined IGS final orbit and clock products. In order to provide a comparison with other published results in assessing the implementation of *pppncl*, IGS final orbits were used in the static validation.

The individual orbits produced by the IGS analysis centers agree to within 1 cm to 2.5 cm 1D weighted RMS (Griffiths and Ray, 2009). The error budget derived in Section 3.16 can therefore be applied to position estimation using orbits and clocks from individual IGS analysis centres. For the GPS only kinematic validation, CODE orbits and clock products were used due to the availability of high-rate clocks tabulated at 5 seconds that capture the short term variability of the satellite clocks, reducing this error when performing 1 Hz positioning (Bock et al., 2009).

GPS/GLONASS PPP requires GPS and GLONASS orbit and clock products. Currently only ESA (Springer, 2010) and IAC (Oleynik et al., 2006) produce a GLONASS precise clocks product. The ESA products are used in this thesis as their formulation as a combined GNSS product removes the need for coordinate and time scale transformations. Published accuracies for the ESA GLONASS clock products are not available as with only one other analysis centre producing a clock product a robust combination against which to compare the ESA product is not available.

The results obtained using the Veripos orbit and clock products are indicative of the

potential performance of real time positioning as these are real time products; the other results, using the IGS analysis centre post processed final products, demonstrate the best available performance.

6.1 Static positioning

The initial stage was to assess the precision, accuracy and convergence time of the software for static receivers. Different locations around the Earth experience different satellite geometries, and variations in tropospheric and ionospheric effects. Therefore, a range of globally distributed sites was selected in order to give a complete picture of performance. The IGS is a voluntary collaboration of over 200 organisations that maintain a network of more than 300 globally distributed GNSS tracking stations (Kouba, 2009a). These sites are installed according to a set of best practices in order to minimise multipath and provide high quality data. Additionally relevant metadata for the sites is available including antenna offsets. All the sites for which 24 h of data was available were used to provide the fullest global coverage.

Coordinates for the receivers in the IGS network are estimated weekly and released by the IGS in SINEX format. The horizontal coordinate accuracy is 2 mm to 3 mm and the vertical accuracy is 7 mm (Ferland and Piraszewski, 2009). This provides a set of reference coordinates with which a PPP solution can be compared. The location of the 281 sites used in this study is represented graphically in Figure 6.1.

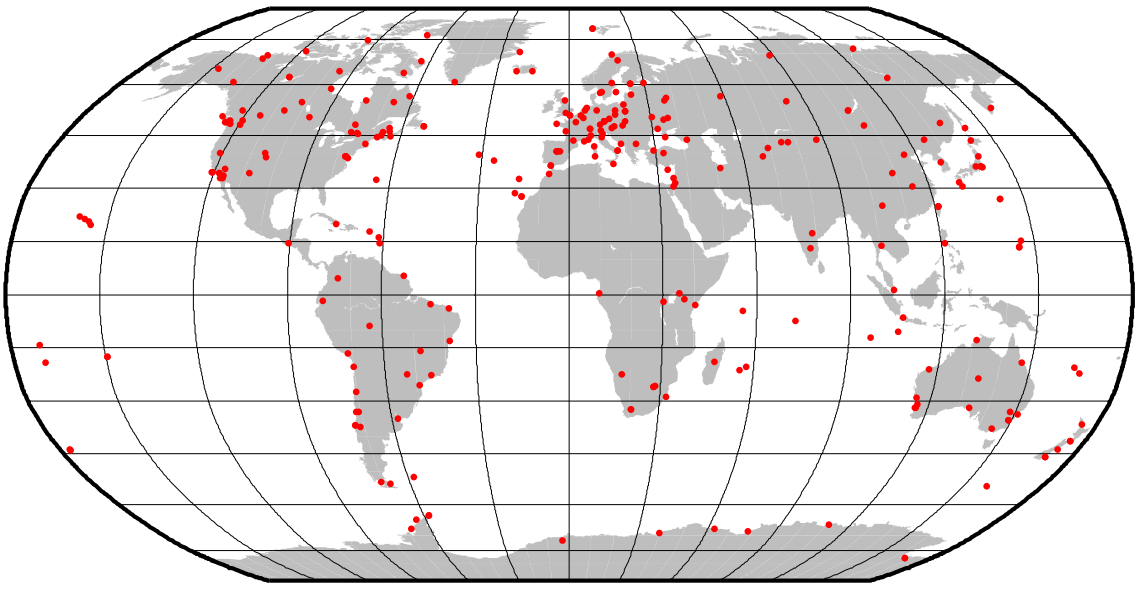

Figure 6.1: Map of the sites used in static PPP GPS verification, showing the global distribution

The concentration of sites in Europe and the absence of sites in North-Central Africa reflects the distribution of the underlying IGS network. The full list of station names and coordinates may be found in the Appendix.

The Crustal Dynamics Data Information System (CDDIS) archive stores daily observation files for sites in the IGS network (Noll and Dube, 2001). Dual frequency code and carrier phase observations are stored at 30 s observation intervals in compressed RINEX format files. The observation data described was downloaded for each of the stations for 10 October 2010 (GPS week 1605, day 0). Temporal changes are therefore not considered in this test but are covered in Section 6.1.3.

24 h of observation data was processed for each site in *pppncl* using the following options:

- The final satellite ephemerides from the IGS network solution in SP3 format were downloaded for the day of study and the preceding and following day from `ftp://cddis.nasa.gov/gps/products/` and concatenated into one file in order that orbit interpolation could be performed at the beginning and end of the studied day without being subject to boundary effects.
- Additional final IGS satellite clock offsets tabulated at the higher rate of 30 s were also downloaded in RINEX clock format from the same location. The clock products contain data from 00:00:00 to 23:59:30 so, due to the linear interpolation used for the clock offsets, only data for the processed day is needed. There is a small possibility of extrapolation for the final epoch of the day at 23:59:30 but as most receivers maintain their clock to within 1 ms of GPS time it would be a very small extrapolation.
- For receivers not recording the P1 code observation and only recording the C1 code observation the CODE P1C1 weekly bias solutions, available at `ftp://ftp.unibe.ch/aiub/CODE/p1c1bias.2000p`, were used to convert the C1 observation into a P1 equivalent observation.
- A 10° satellite elevation cutoff was used in the processing.
- To correct for antenna phase centre offsets and variations, the values from the IGS antex file available at `ftp://igscb.jpl.nasa.gov/igscb/station/general/igs05.atx` were used.
- Initial receiver coordinates were taken from the RINEX file header for each site.

- An initial position uncertainty of 200 m was used as the RINEX header coordinates are only approximate and to reflect the more general positioning scenario where precise initial coordinates are not known. This also ensures the PPP results reflect the accuracy of the method and are not simply the results of tightly constrained initial values.
- No epoch to epoch process noise was added to the position component of the covariance matrix in the Kalman filter time update step, as the receiver coordinates are modelled as stationary.

For each site the full 24 h of observation data was processed and the post fit state vector saved to a file at each 30 s observation epoch. The observation data was processed in a real-time mode reading and processing one epoch at a time, sequentially starting at midnight. At each epoch the following were estimated:

- three position components, modelled as a constant,
- the receiver clock offset, modelled as random walk,
- a correction to the wet tropospheric zenith delay, modelled as random walk,
- an ionosphere free carrier phase bias for each satellite, modelled as a constant.

Reference coordinates for each site were extracted from the SINEX file `ftp://cddis.nasa.gov/gps/products/1605/igs10P1605.ssc` containing the IGS combination solution for GPS week 1605. The final position estimate from the *pppncl* solution after processing the complete 24 h was compared to the reference coordinates from the IGS weekly solution. As no process noise is added to the coordinate covariance at each epoch, the values of the estimated coordinates at each epoch are the current estimate of the coordinates based on all the observation data incorporated up to that point. The final position estimate at 23:59:30 is therefore the single estimated set of coordinates based on the complete day's observations.

Figures 6.2, 6.3 and 6.4 show the distribution of the differences in the PPP coordinates with respect to the reference solution in the North, East and Height directions respectively, with the statistics summarised in Table 6.1. As would be expected the precision is highest in the North component and lowest in the Height. The Height component is always less accurate in GNSS due to all the satellites being above the receiver and the high correlation between the Height, receiver clock offset and zenith tropospheric delay. The reduced accuracy of the East component is a feature commonly seen in carrier phase GNSS positioning with floating ambiguities. This

is caused by the higher correlation of the phase biases with the East component, at mid and low latitudes, due to the North-South ground track of GPS satellites at the equator in the ECEF reference frame (Blewitt, 1989).

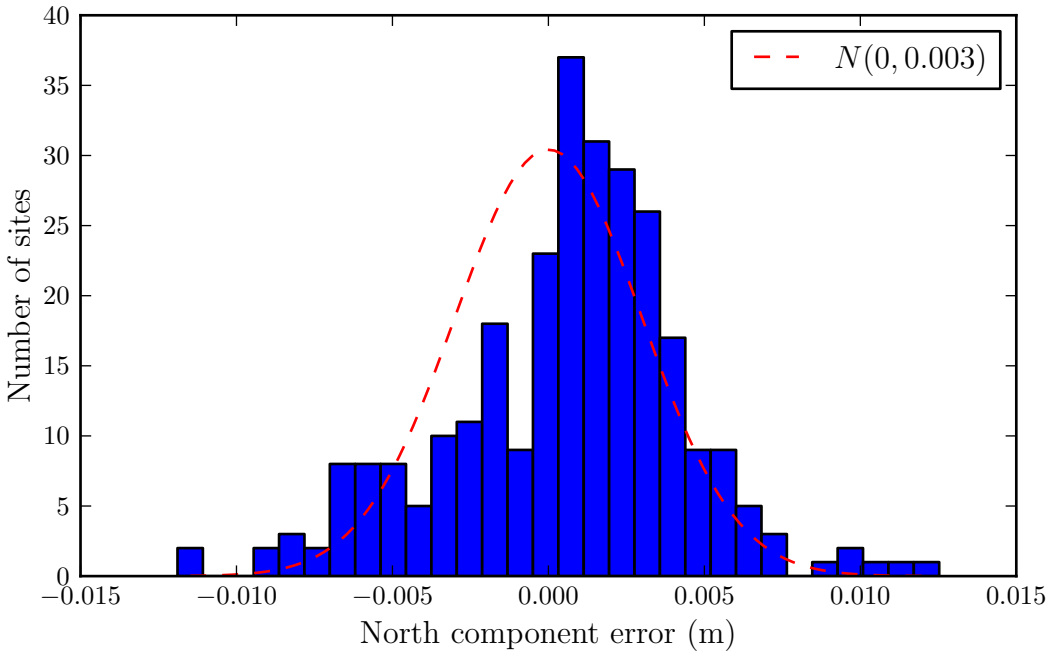

Figure 6.2: Static PPP error in the North component compared to the IGS weekly solution. A Normal distribution with standard deviation of the reference coordinates is overlaid.

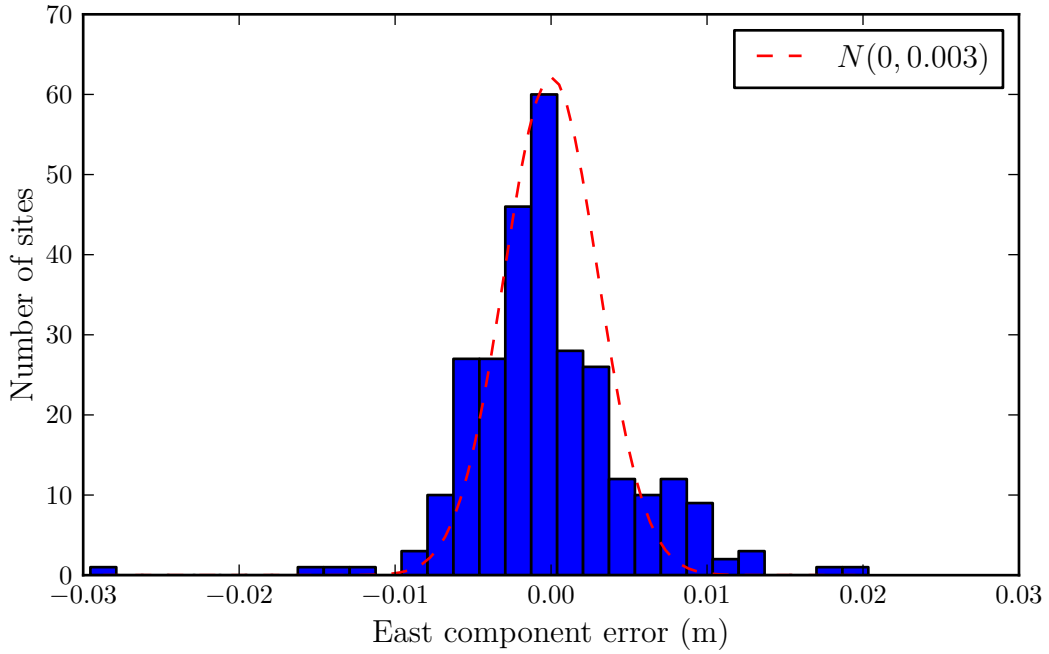

Figure 6.3: Static PPP error in the East component compared to the IGS weekly solution. A Normal distribution with standard deviation of the reference coordinates is overlaid.

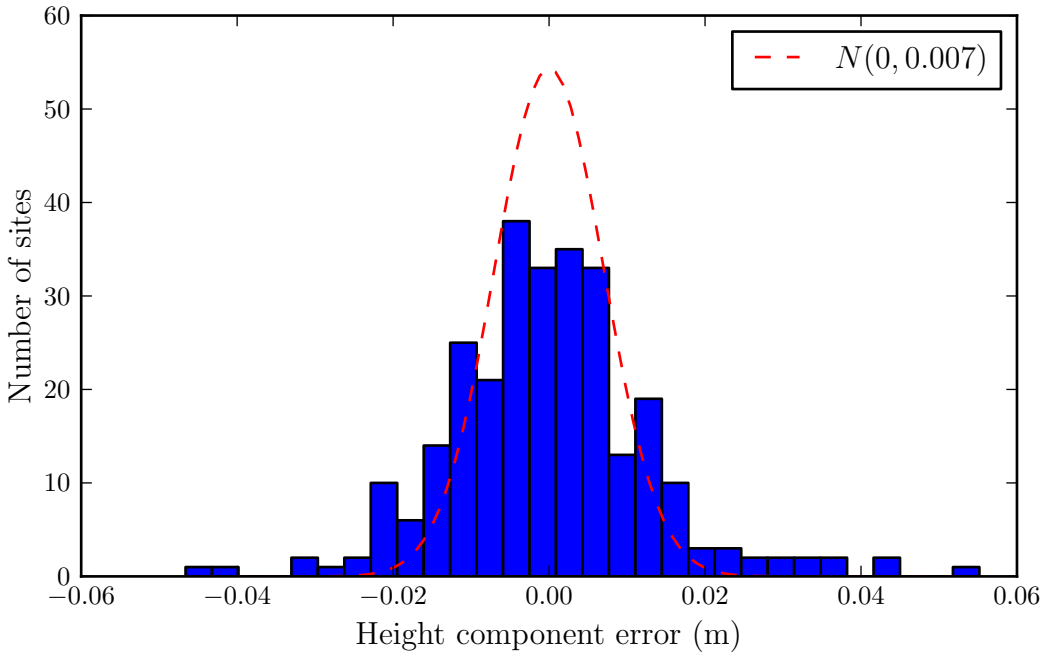

Figure 6.4: Static PPP error in the Height component compared to the IGS weekly solution. A Normal distribution with standard deviation of the reference coordinates is overlaid.

Direction	Mean (mm)	Standard deviation (mm)	RMS (mm)
North	0.6	3.8	3.8
East	−0.1	5.2	5.2
Height	−0.2	13.0	13.0

Table 6.1: Static PPP error compared to IGS weekly solution for 282 stations on 10 October 2010

The accuracy achieved in this test will represent the best static performance of *pppncl*. This is due to the use of IGS sites which are of very high quality. The use of high grade geodetic receivers minimises measurement noise; the common use of choke ring antennas and the careful location of sites reduces receiver multipath. Therefore two of the major contributions to the error budget are minimised in this data set.

Kouba (2009a) shows the coordinate RMS achieved at 36 IGS Reference frame stations during 24 h static positioning using GPS Pace PPP. For GPS week 1516 (January 25–31, 2009) using IGS Final orbit and clock products, RMS values of 3 mm, 5 mm and 14 mm in North, East and Height, respectively, were obtained. Thus it can be concluded there is not a considerable difference between the *pppncl* results and those from Pace PPP.

6.1.1 *Estimated tropospheric delay*

A further comparison may be made for the estimated tropospheric ZTD. The IGS generate a tropospheric product containing the total (hydrostatic + wet) ZTD at 5 min intervals (Byun and Bar-Sever, 2009). Using a post-processed PPP method, daily observation files are processed for each site in the IGS network. The key features of the processing approach are (Bar-Sever et al., 1998):

- Software: GIPSY
- Fixed orbits and clocks: IGS Final Combined
- Earth orientation: IGS Final Combined
- Transmitter antenna phase centre map: IGS Convention
- Receiver antenna phase centre map: IGS Convention
- Elevation angle cutoff: 7°
- Mapping function (hydrostatic and wet): Niell (1996)
- *A priori* hydrostatic delay based on altitude (2.3 m at sea level), and 0.1 m for the wet delay
- Data time span: 24 h
- Data rate: 5 min
- Estimated parameters: clock (white noise), station position (constant), wet zenith delay (random walk with variance of $3\,\mathrm{cm^2\,h^{-1}}$), atmospheric gradients (random walk with variance of $0.3\,\mathrm{cm^2\,h^{-1}}$), phase biases (white noise)
- Temporal resolution of zenith delay estimates: 5 min

Formal errors for the final tropospheric product are typically (one sigma) 1.5 mm to 5 mm (Byun and Bar-Sever, 2009). Actual errors are known to be higher, due to systematic errors in the GPS orbits and clock products. The difference between the IGS final tropospheric product and the ZTD product, from each IGS analysis centre, for all sites, has a daily bias of up to 5 mm. The standard deviation of this measure for each day is 3 mm to 10 mm (Byun and Bar-Sever, 2009).

Using the IGS final ZTD product as a reference, the *pppncl* estimated ZTD can be evaluated. The IGS final ZTD product was downloaded for all sites for 30 July 2010.

The two sites showing the largest and smallest daily variation in ZTD were chosen to highlight the performance at the two extremes. HNPT, located in North-East America, showed the largest variation in ZTD with a range of 194.3 mm. MAUI, located in Hawaii, had the smallest daily ZTD variation with a range of 6.9 mm.

The daily RINEX observation files for HNPT and MAUI were processed using *pppncl*. The same processing options as described in the generation of the IGS ZTD product were used, with the exception of the GMF in place of the Niell mapping function, and no estimation of atmospheric gradients. Observation data was processed at 30 s and the total ZTD extracted at 5 min intervals matching the IGS product.

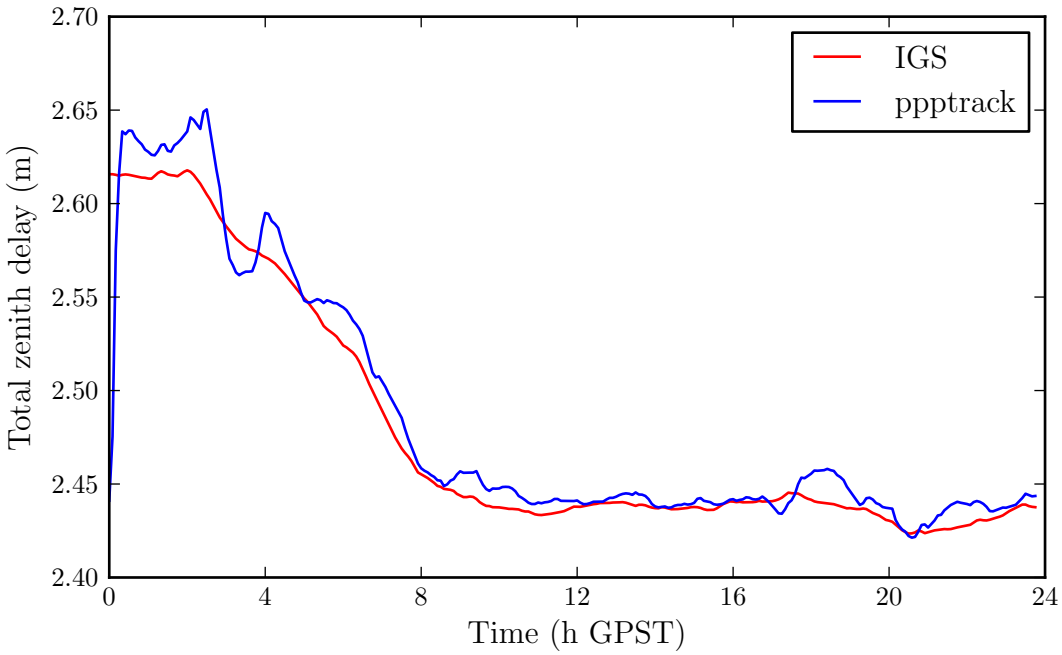

Figure 6.5: Total ZTD for IGS station HNPT, 30 July 2010

Figures 6.5 and 6.6 show the estimated total ZTD from *pppncl* and the IGS final product. The real-time mode nature of *pppncl* is seen during the first 30 min as the filter converges. For HNPT the *pppncl* estimate follows the rapid drop in the delay, although a slight lag can be seen. This is likely to be due to the forward only nature of the *pppncl* Kalman filter combined with the low weighting of satellites at low elevations.

The mean bias and standard deviation between the *pppncl* estimates and the IGS product are not far from those reported in Byun and Bar-Sever (2009). For MAUI with the low change in ZTD throughout the day, the difference between the PPP

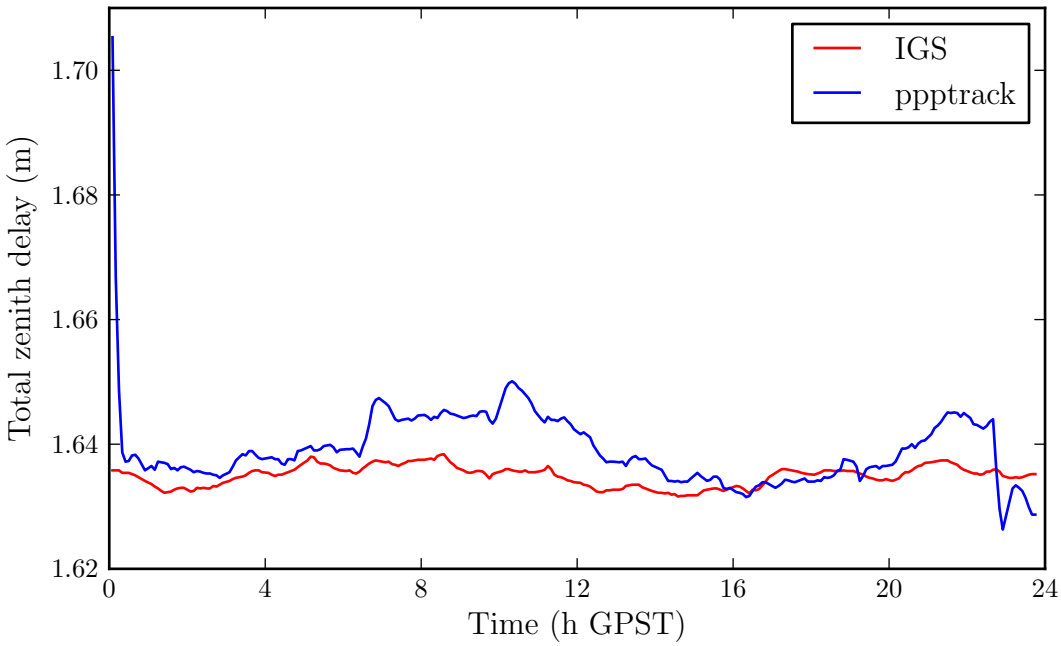

Figure 6.6: Total ZTD for IGS station MAUI, 30 July 2010

Site	Bias	Std
HNPT	7	9
MAUI	4	4

Table 6.2: The daily bias and standard deviation for *pppncl* estimated ZTD relative to the IGS ZTD product. The first hour of processing was not included to remove errors due to convergence. All units are in mm.

estimated ZTD is comparable to the variability seen amongst IGS analysis centres. HNPT, representing an extreme case, shows almost twice the bias seen at MAUI, however much of this can be attributed to the lag in response of the filter estimate, an artifact of real-time mode processing.

6.1.2 *Coordinate convergence*

The convergence time is an important aspect of PPP performance. To evaluate the convergence time of the Kalman filter within *pppncl* the following test was performed: Seven IGS stations were processed using the same methodology as described in the previous tests, using observation data from 24 October 2010 (GPS week 1607, day 0). The stations are globally distributed and vary in location from mid-ocean to continental (Figure 6.7).

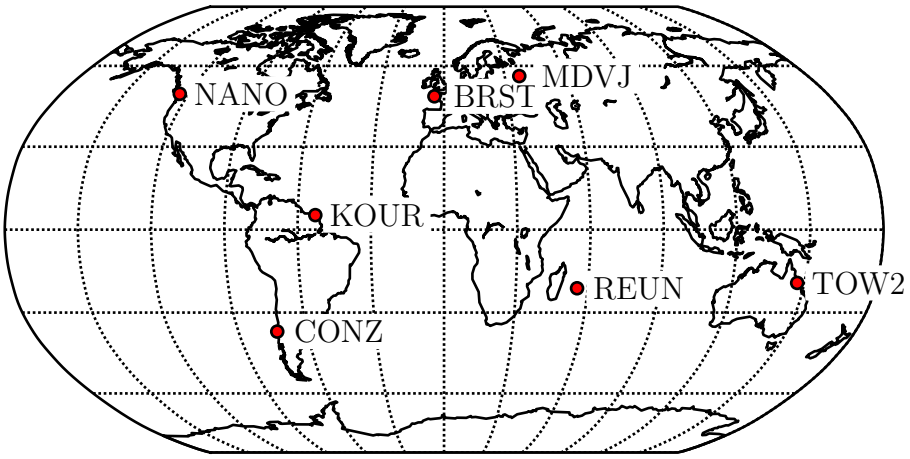

Figure 6.7: Map of the seven IGS stations used to characterise GPS PPP convergence behaviour

Figures 6.8, 6.9 and 6.10 show the evolution of the difference between the PPP solution and the IGS05 reference coordinates for each site on a log timescale. As in the previous test, the North component shows the smallest error and also the fastest convergence time. It should be noted that a larger scale has been used for the Height plot due to the larger errors present.

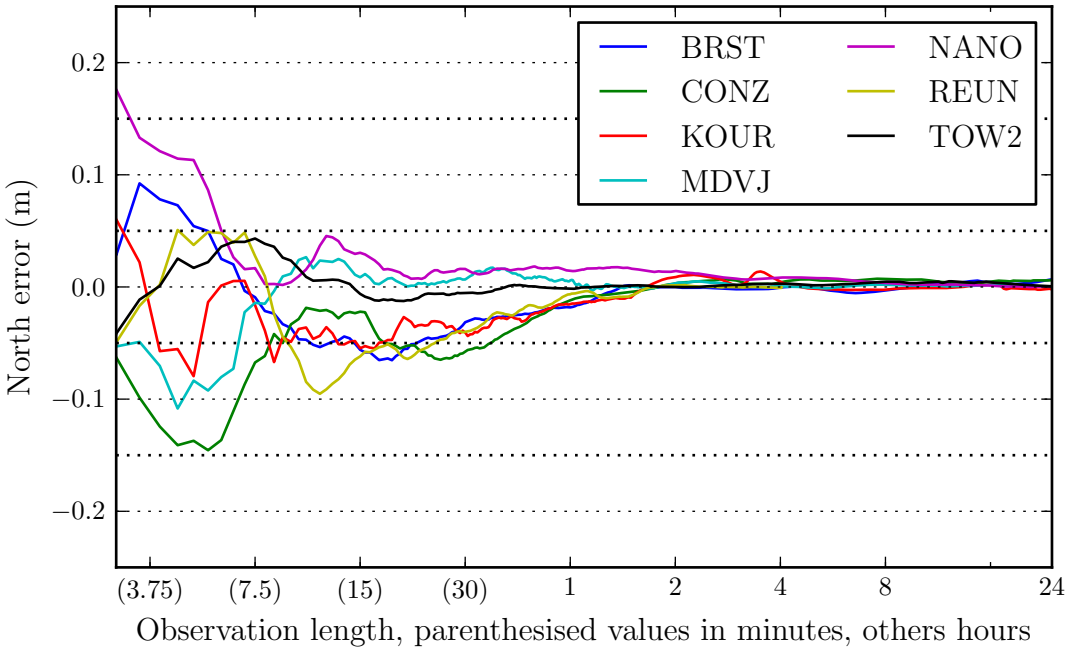

Figure 6.8: Position convergence in the North component for seven IGS stations on 24 October 2010

Table 6.3 shows the mean, minimum and maximum of the magnitude of the position errors after processing 1 h, 2 h, 3 h, 6 h, 12 h and 24 h of observation data. The improvement in positioning accuracy with time is seen clearly in both the graphs and

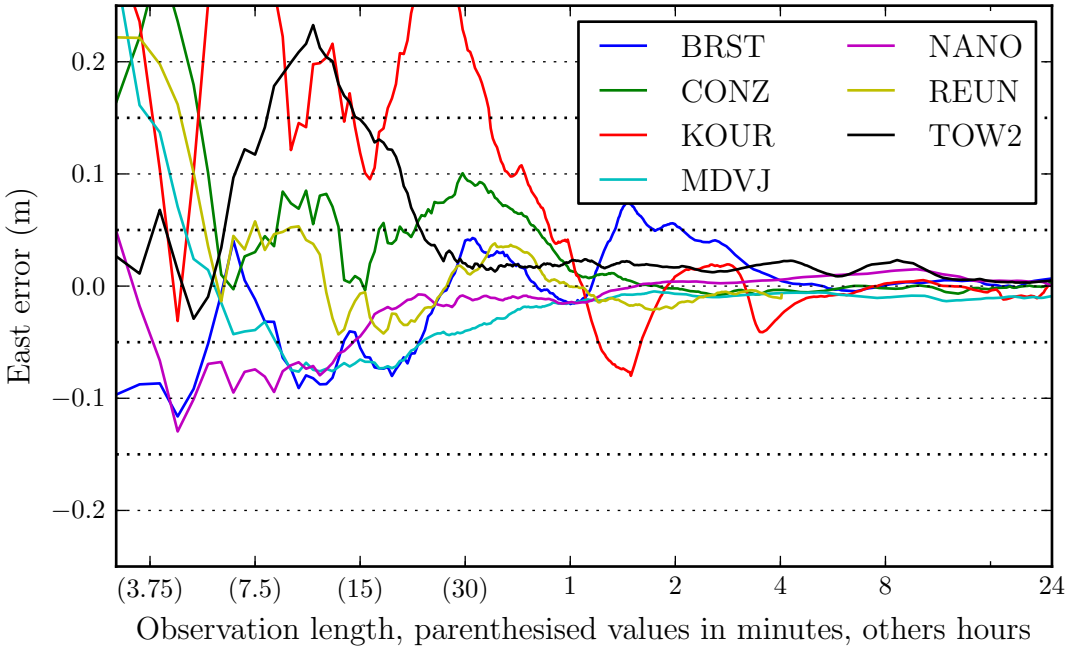

Figure 6.9: Position convergence in the East component for seven IGS stations on 24 October 2010

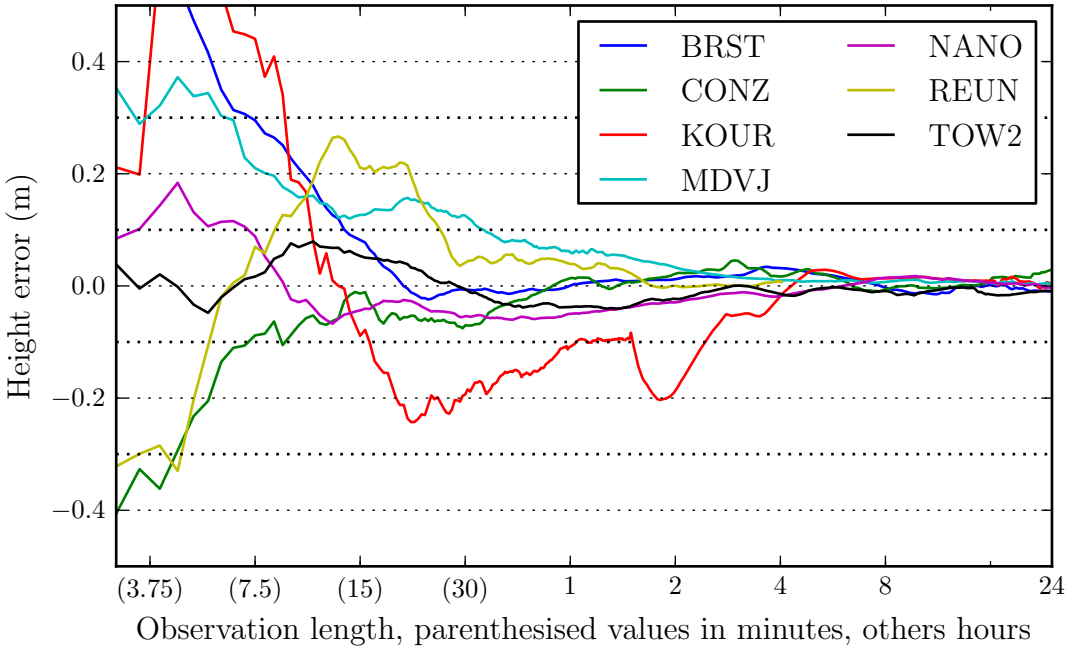

Figure 6.10: Position convergence in the Height component for seven IGS stations on 24 October 2010

the table. 10 mm level accuracy is reached after 1 h for the North component, 3 h for the East component and 6 h for the Height component. There is little improvement in the accuracy of North and Height after 12 h, whereas the East component accuracy does improve during the final 12 h.

Observation duration (h)	Mean			Min			Max		
	N	E	H	N	E	H	N	E	H
1	11	19	45	1	14	0	18	36	109
2	4	15	51	0	2	11	14	55	188
3	3	11	24	1	2	0	7	26	52
6	3	6	10	0	1	0	6	10	22
12	2	6	9	0	0	3	4	13	13
24	2	4	9	0	0	3	6	9	29

Table 6.3: Mean, minimum and maximum magnitude of position error in North (N), East (E) and Height (H) after six different observation durations for seven IGS stations on 24 October 2010. Units are mm

Using the same procedure as above, 154 days of observation data were processed using *pppncl* for the IGS station BRST. The days processed were in the period 30 July to 31 December 2010. The resulting coordinates estimated for every 30 s observation interval were compared to the IGS weekly coordinate estimates for the GPS week of that observation.

The resulting position errors in both horizontal and 3D were calculated. The horizontal error is given by the distance of the PPP coordinates from the reference coordinates in the horizontal plane defined by the North and East components. The 3D error is given by the total distance of the estimated coordinates from the reference coordinates. Given the North, East and Height errors dN, dE, and dH:

$$\text{2D horizontal error} = \sqrt{dN^2 + dE^2} \tag{6.1}$$

and

$$\text{3D error} = \sqrt{dN^2 + dE^2 + dH^2} \tag{6.2}$$

For each 30 s interval of the day this gave a set of 154 position errors, one from each of the days processed. As the processing started at midnight each day the coordinate error at any time during the day can be seen as the achievable accuracy after that length of PPP processing. By considering the 154 days as a whole,

the statistical properties of *pppncl* static GPS PPP can be examined. The errors for each epoch were sorted and the value corresponding to the 50^{th}, 68^{th} and 95^{th} percentile extracted. Figures 6.11 and 6.12 show how the value which bounds the given percentile in the 2D horizontal and 3D coordinate errors evolves with time. Horizontal accuracy of 10 cm is reached 95% of the time after 1 h, and 5 cm accuracy is achieved within 2 h. For 3D positioning, in 95% of cases 10 cm accuracy is reached within 2 h, and 5 cm within 5 h.

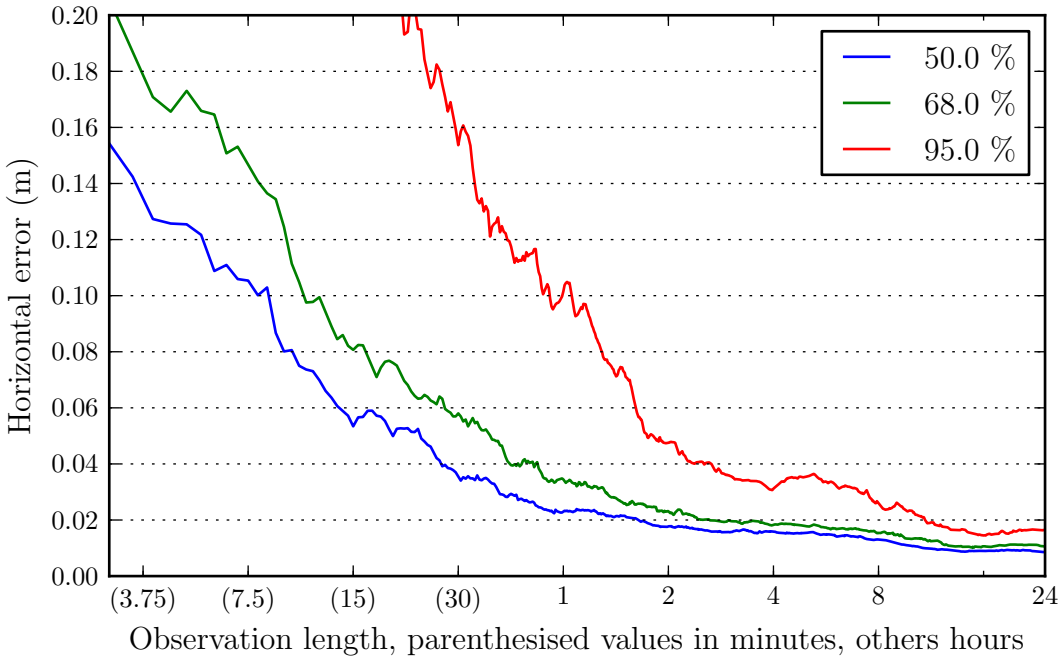

Figure 6.11: Horizontal coordinate convergence for 154 days at IGS station BRST

Héroux et al. (2004) looked at PPP convergence times using IGS precise orbits over a 7 day period. The convergence time showed a high degree of day-to-day variability, both within a single site and between sites (Bisnath and Gao, 2008). In their study, convergence to within 10 cm of the IGS solution took from 30 min to 4 h. The convergence times for *pppncl* are comparable to these values.

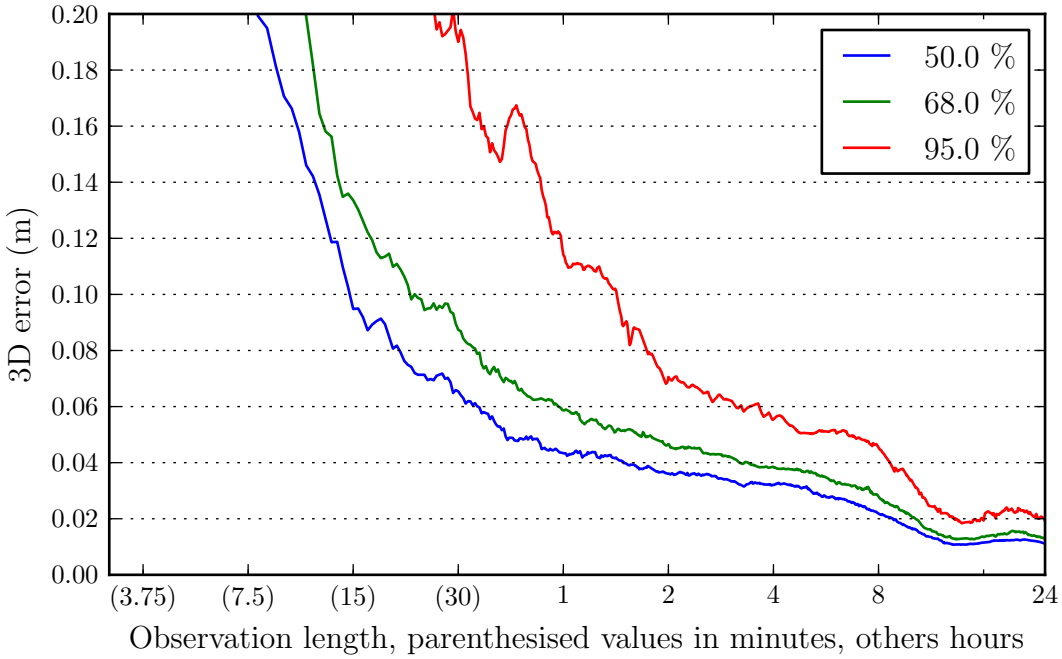

Figure 6.12: 3D coordinate convergence for 154 days at IGS station BRST

6.1.3 *Year time series*

Positioning a site for a whole year can reveal any errors that manifest as seasonal trends and allows repeatability to be assessed. Leandro et al. (2011) processed the observation data from the IGS station UNBJ for every day in 2008 using their GAPS PPP software. 24 h static positioning was performed each day to create a time series of coordinate errors. This test was repeated using *pppncl*.

For the site UNBJ the full year of 2008 was processed using the same configuration as described in Section 6.1. Each daily RINEX observation file was used to estimate a single static position for that day.

The continental plates making up the Earth's crust are drifting at different velocities with respect to the ITRF reference frame. This means that a "stationary site" is in fact moving at the plate's velocity in ITRF. The velocities for station UNB1 (which was replaced by UNBJ in 2006) in ITRF2005 are V_x: $-16.8\,\mathrm{mm\,year^{-1}}$, V_y: $-1.3\,\mathrm{mm\,year^{-1}}$ and V_z: $5.1\,\mathrm{mm\,year^{-1}}$ (from `http://itrf.ensg.ign.fr/ITRF_solutions/2005/doc/ITRF2005_GPS.SSC.txt`). The velocities given in ITRF2005 are linear so are unable to describe any seasonal variability in the coordinates due to, for example, atmospheric pressure loading effects.

To allow for this drift, PPP estimated coordinates were grouped by GPS week and compared to the IGS estimated coordinates for that week. Comparing to a weekly solution effectively ignores the tectonic change in position coordinates during a week. The maximum resulting error in considering reference coordinates at the weekly level can be determined by the station's ITRF2005 velocity. For UNBJ this is 0.3 mm, an order of magnitude lower than the uncertainty in the reference coordinates. Therefore ignoring the intraweek velocity will have negligible impact on the resulting PPP error estimate.

The difference between the *pppncl* daily position estimates and the IGS weekly reference coordinates is shown in Figures 6.13, 6.14 and 6.15. The coordinate errors show constant variability throughout the year. The error in the North component is consistently below 1 cm, with East and Height components at the 2 cm level. A linear fit to the North and East components gives low annual velocity errors of $-0.3\,\mathrm{mm\,year^{-1}}$ and $-1.3\,\mathrm{mm\,year^{-1}}$.

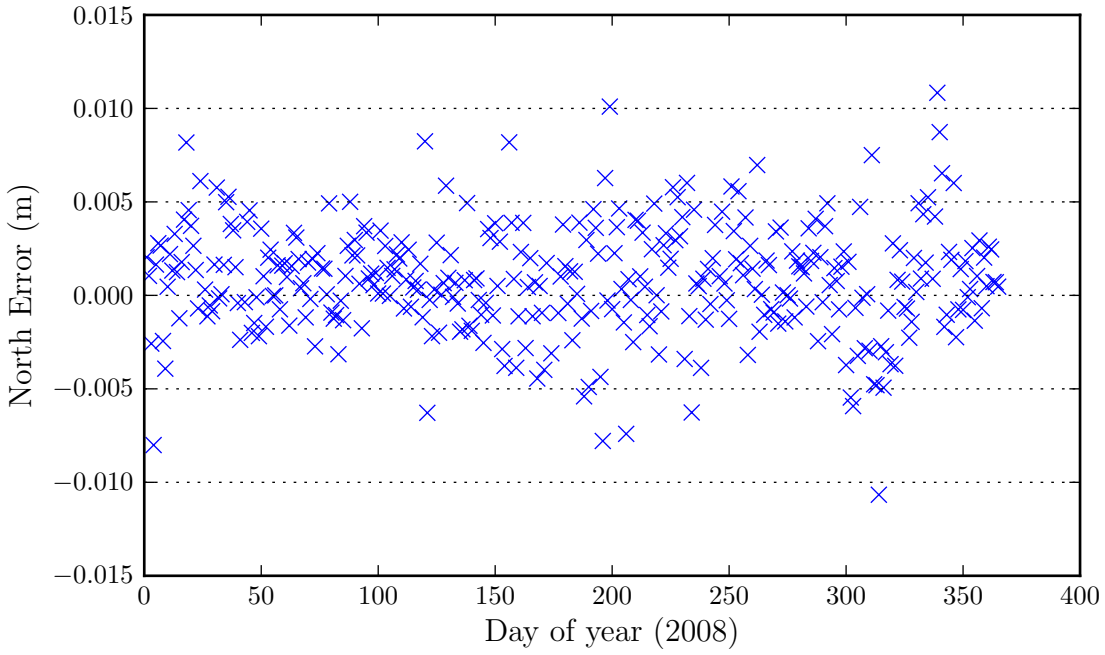

Figure 6.13: North 24 h *pppncl* position error for IGS station UNBJ

The horizontal ($\sqrt{dN^2 + dE^2}$) and 3D ($\sqrt{dN^2 + dE^2 + dH^2}$) error in the PPP solution is tabulated in Table 6.4 and graphed in Figures 6.16 and 6.17. There is no visible seasonal trend in the coordinate RMS. The horizontal coordinates agree with the IGS published coordinates to within 1 cm and the 3D coordinates to within 2 cm.

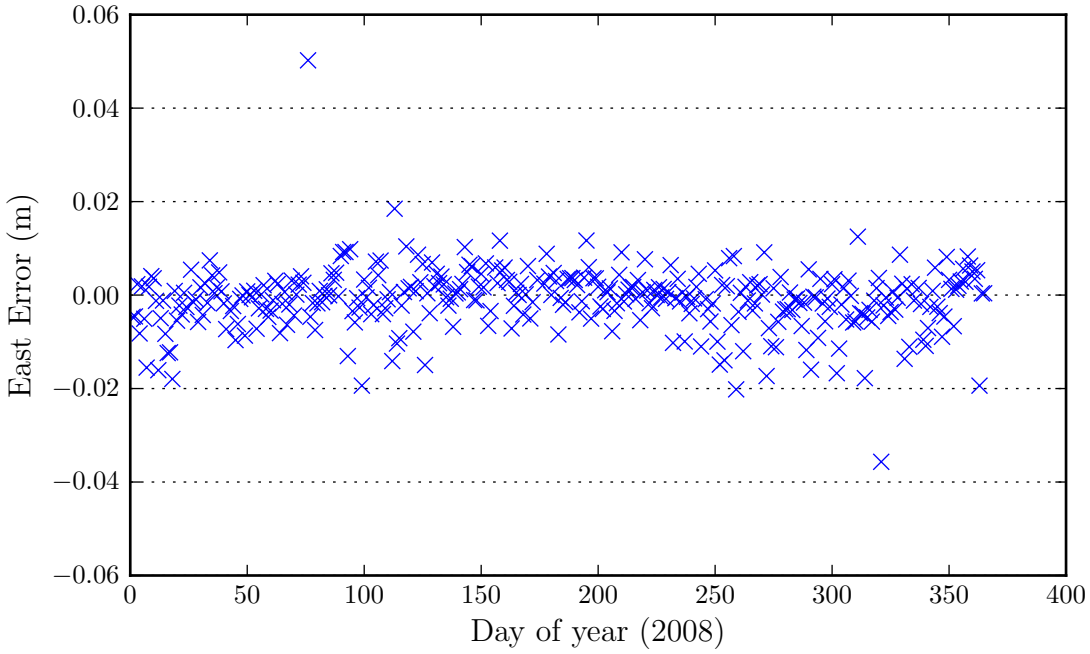

Figure 6.14: East 24 h *pppncl* position error for IGS station UNBJ

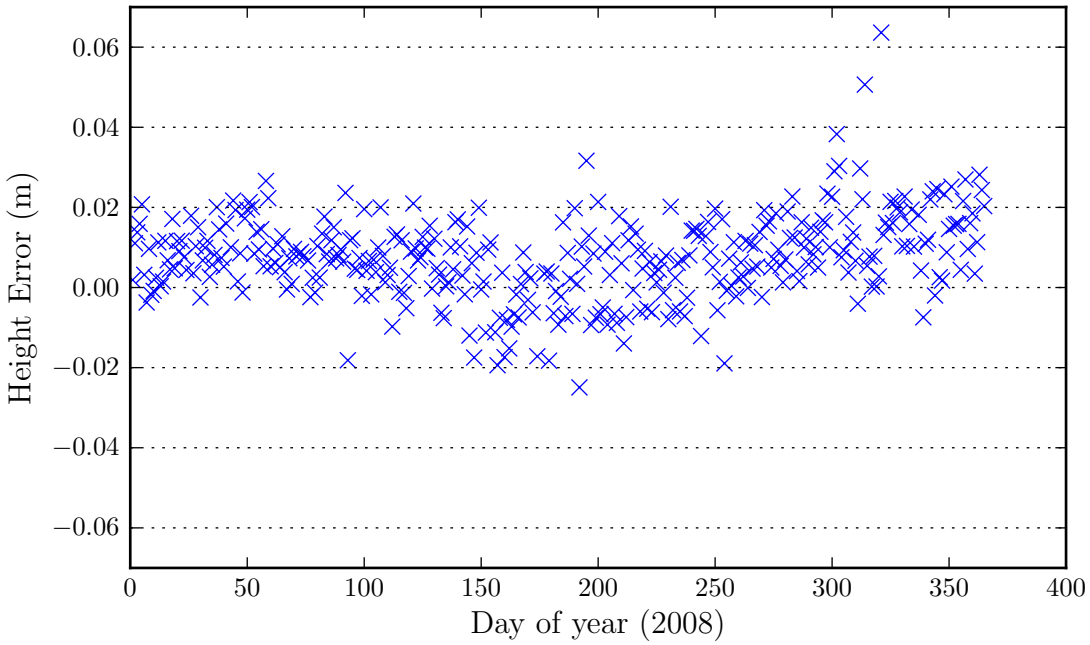

Figure 6.15: Height 24 h *pppncl* position error for IGS station UNBJ

	2D	3D
Mean Error (mm)	5.5	12.6

Table 6.4: Average 2D and 3D *pppncl* position error of IGS station UNBJ for 2008

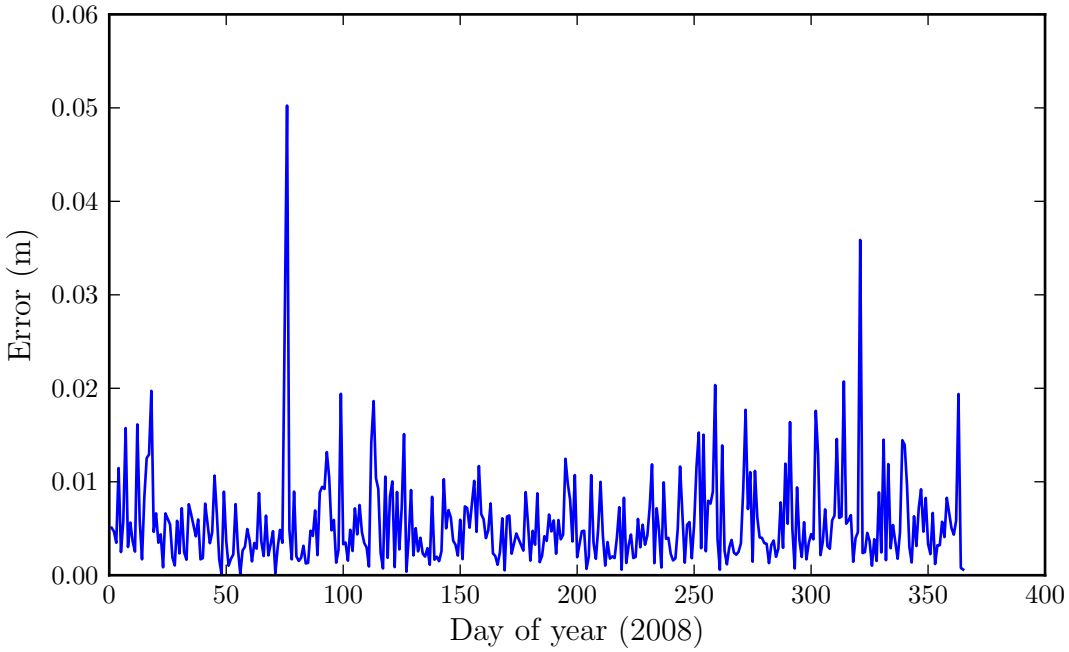

Figure 6.16: Horizontal position error for 24 h *pppncl* coordinates for IGS station UNBJ

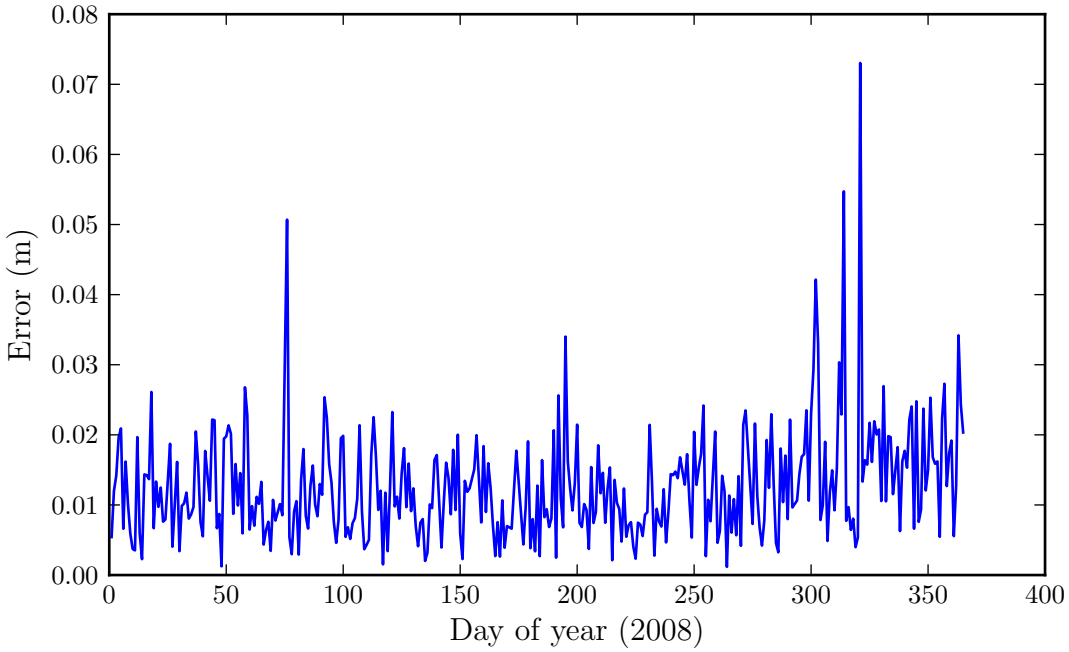

Figure 6.17: 3D position error for 24 h *pppncl* coordinates for IGS station UNBJ

Leandro et al. (2011) compared the coordinates estimated by GAPS PPP software with IGS solutions for the year 2008. The reported average 2D and 3D errors of 7.7 mm and 16.3 mm are slightly worse than those obtained using *pppncl* (Table 6.5).

	GAPS	*pppncl*
Mean horizontal error (mm)	7.7	5.5
Mean 3D error (mm)	16.3	12.6

Table 6.5: Mean horizontal and 3D position error of GAPS and *pppncl* compared to IGS weekly solutions for 2008

6.2 Kinematic positioning

To quantify the accuracy of the *pppncl* software in a kinematic environment, a dataset was collected at Albemarle Airfield, UK. This location was chosen due to its unobstructed sky view, providing an environment with minimal interference to observation signals. Being private land meant that it was possible to test a range of dynamics without being restricted to roads and constrained by traffic. This type of environment was chosen so that the kinematic functionality of the software could be quantified with a data set for which a high quality set of reference coordinates could be produced. It also meant that any excessive errors in the PPP solution could be directly attributable to the implementation and not to multipath and undetected cycle slips.

Due to the presence of trees around the perimeter of the airfield, the testing was completed in the runway area to ensure the vehicle remained well clear of any sky view obstructions. The runway used is 1.8 km long and approximately 0.1 km wide orientated in a SW to NE direction. The site, shown in Figure 6.18, is located at 55.02° N, 1.87° W.

Producing an accurate set of reference "truth" coordinates for a kinematic receiver is harder than for a static receiver. Whichever technique is used cannot benefit from the averaging of many measurements to reduce noise as for a static receiver. Some of the possible methods that can be used for generating a reference solution are:

- Laser target tracking
- Inertial navigation
- Relative carrier phase GNSS

Post processed relative carrier phase GPS positioning is often used to provide reference coordinates (Armatys et al., 2003). This is in part due to the simplicity, as it only requires a reference GNSS base station. Also, there are no issues with offsets between the GNSS antenna and the location of the receiver reference point. In other methods the relative position between the GNSS antenna reference point, and the reference point of that technique, must be determined and accounted for. In this thesis, relative carrier phase GPS positioning is used to provide truth coordinates due to equipment availability and *Track*, a carrier phase double differencing kinematic positioning software with ambiguity resolution (Chen, 1998).

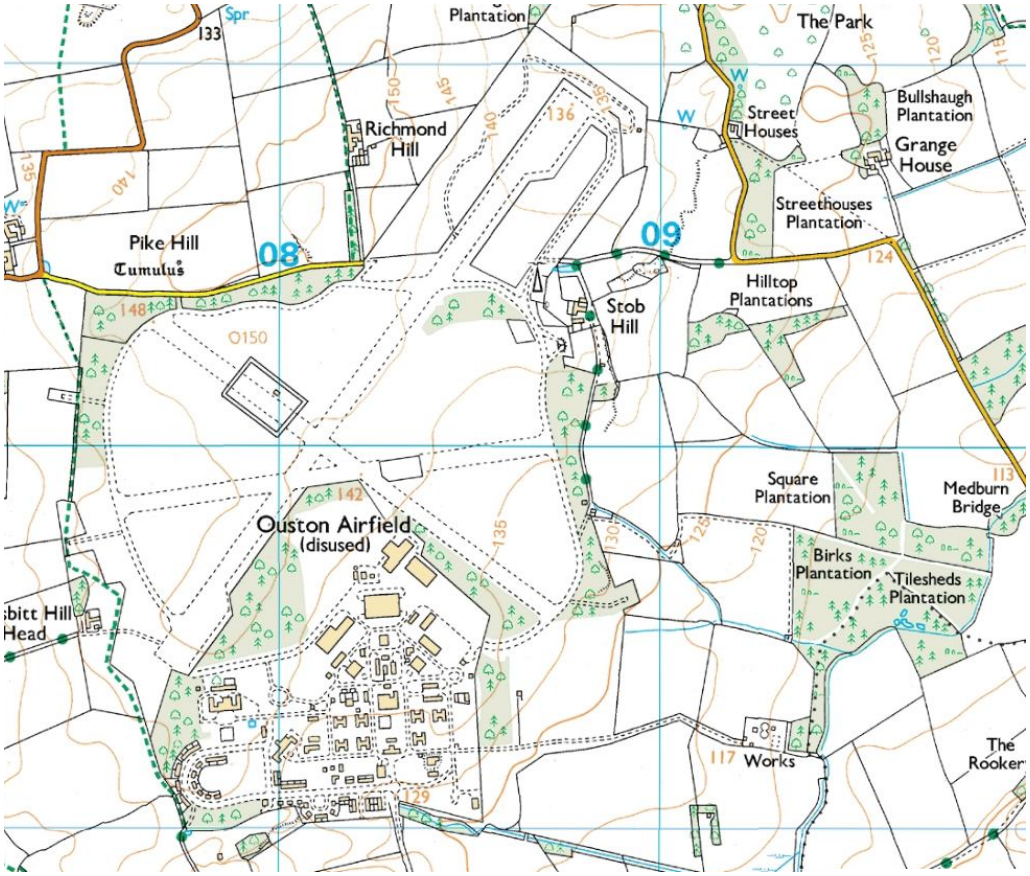

Figure 6.18: Ordnance Survey map of the airfield at Albemarle with 1 km grid lines

The test took place from 08:00 to 14:30 UTC on 22 August 2008. A Leica GX1230 receiver with external battery was placed in a Landrover vehicle. A Leica AX1202 antenna was mounted on the vehicle roof by means of a roof rack. The receiver was set to record code and carrier phase on both GPS frequencies at 1 Hz. The vehicle was driven around the airfield for six and a half hours, along various routes (Figure 6.19), and at a range of speeds from $2\,\mathrm{m\,s^{-1}}$ to $34\,\mathrm{m\,s^{-1}}$ (4.5 mph to 77 mph), (Figure 6.20). The vehicle was kept stationary for one hour at the start, to allow the

initial set of ambiguities to be found for the reference solution via static processing if required. Then the vehicle was driven at a slow speed of $2\,\mathrm{m\,s^{-1}}$ to $3\,\mathrm{m\,s^{-1}}$ (4.5 to 7 mph) for 2 hours back and forth along the length of the runway. Next followed a period of slow speed driving, with continual changes in direction. The final period involved driving up and down the runway at increasing speeds up to $34\,\mathrm{m\,s^{-1}}$ (77 mph).

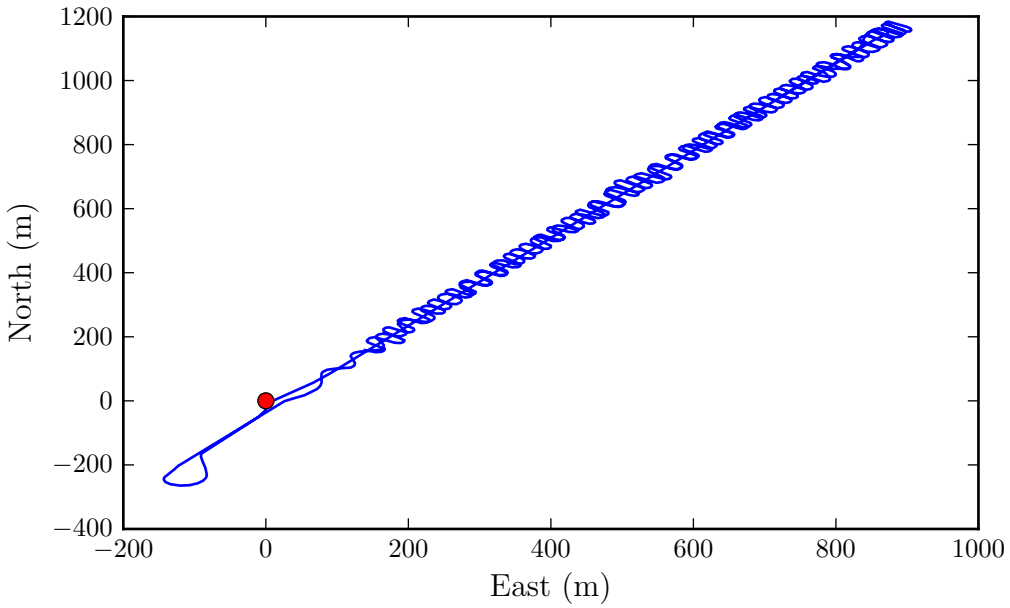

Figure 6.19: Kinematic route showing the distance of the vehicle from the base station, marked by a red dot

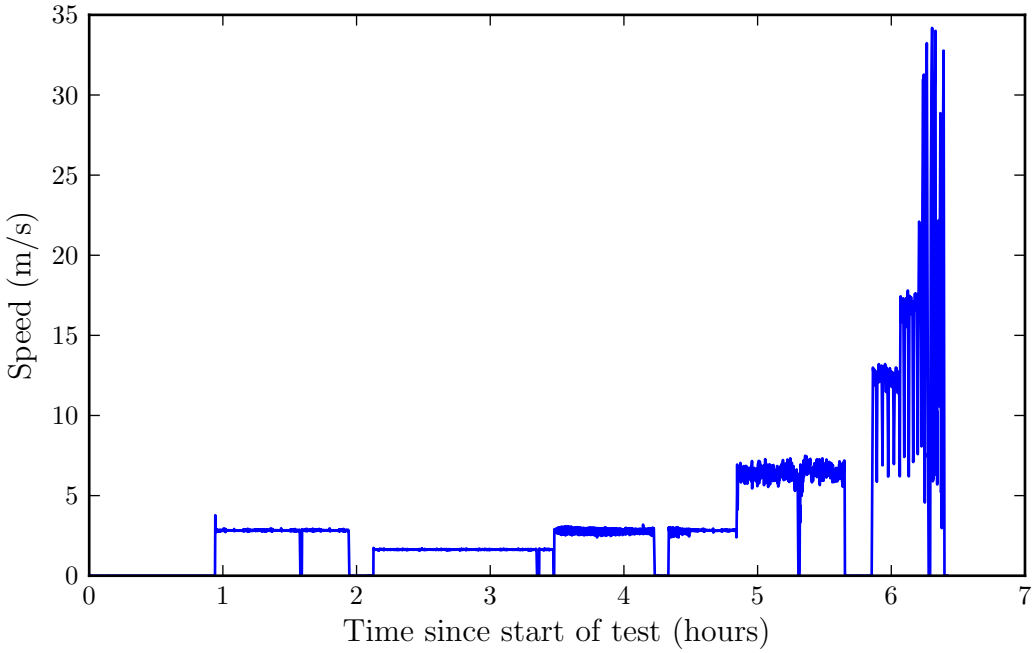

Figure 6.20: Speed of the vehicle during the kinematic airfield test

In this kinematic test the true coordinates of the rover were not known. A double difference solution was used to provide a reference solution. The double differencing solution requires a base station nearby, ideally as close as possible, and definitely less than 10 km, as described in Section 2.4.1. A second Leica GX1230 receiver with a Leica AX1202 antenna was therefore placed on a tripod at the side of the airstrip to act as a base station.

The coordinates of the base station were determined using a double difference carrier phase static baseline to the IGS station at MORP. The coordinates of MORP were held fixed to the values determined in the IGS weekly average coordinate solution of 3645667.799, -107277.178, 5215053.561 in metres X, Y, Z in the IGS05 reference frame. The coordinates of the airfield base station were then estimated relative to the MORP coordinates giving the base station coordinates in IGS05. This ensured the location of the base station placed on the airfield, and hence the reference solution coordinates, were in the same IGS05 frame as the orbits used in the kinematic PPP solution.

6.2.1 *Common processing elements*

To ensure the reference coordinates and the kinematic PPP estimated coordinates are in the same reference frame and both locating the same point, the following common elements were used for both sets of processing.

Final orbits from CODE (Dach et al., 2009) were used as they provide high rate clock products tabulated at 5 s intervals suitable for 1 Hz positioning. This is the highest rate available from any of the IGS analysis centres so therefore the best suited to 1 Hz PPP positioning. The orbits are in SP3 format. The orbit and clock products were downloaded from `ftp://cddis.nasa.gov/pub/gps/products/1493/` (orbit filename cod14935.sp3).

Absolute phase centre corrections consistent with the orbits were used in the ANTEX format. The offset file used is available from `ftp://igscb.jpl.nasa.gov/igscb/station/general/igs05.atx`

The Leica GX1230 records C1 and P2 observables. The C1 observable was corrected to P1 using the `CC2NONCC` program available from `ftp://ftp.unibe.ch/aiub/bcwg/cc2noncc/`. The P1–C1 bias values from the file p1c1bias.2000 were used which contains the monthly bias estimates generated by CODE as part of their global network analysis.

6.2.2 *Track double differencing solution*

To provide a reference truth solution with which to compare the PPP solution, post processed coordinates were estimated using MIT *Track* (Chen, 1998). *Track* is a post processing double difference GPS processing software package. It allows for static and kinematic positioning of an unknown site relative to a base station.

Track runs through the data several times as each step in the processing is performed. First an approximate position is determined at each epoch using the code observations. Then using the code solution as an *a priori* position estimate, a Kalman filter is used to estimate the position and floating ambiguities using carrier phase observations. The ambiguities are then resolved in one of two ways: either a search is performed in ambiguity space or those ambiguities that are sufficiently well defined by the Kalman filter are fixed to the closest integer. The Kalman filtering is then repeated with the removal of the fixed ambiguities from the state vector. This reduces the number of degrees of freedom and constrains the solution, potentially allowing further ambiguities to be well enough defined to be fixed.

The Kalman filter can be operated in forward, backward or smoothing mode. The forward and backward modes only use past or future data respectively to determine the current estimate. The smoothing mode uses both past and future observations, improving the quality of the solution at the expense of increased computation time.

The configuration used for *Track* is a combination of the short baseline static mode (SHORT) and the high rate aircraft mode (AIR). Due to the short baseline lengths involved, L1 and L2 observations were used separately. This reduces the observation noise versus using the ionosphere free combination L_c, whilst relying on the ionospheric delay being sufficiently similar for both receivers to cancel out in the double difference.

The following configuration file was used for *Track*:

```
obs_file
 base base.08o F
 rove rover.08o K

nav_file gps/products/1493/cod14935.sp3 SP3

site_pos
 base 3662715.9801 -120118.3281 5202960.6893
```

```
 rove 3662715.9495 -120118.3247 5202960.6551

mode short

site_stats
 base 4.7 4.7 4.7 4.7 4.7 4.7

ante_off
 base 0.0000 0.0000 0.0000 LEIAX1202
 rove 0.0000 0.0000 0.0000 LEIAX1202

cut_off 7

OUT_TYPE NEU

ANTMOD_FILE igs05.atx

USE_GPTGMF

BACK_TYPE SMOOTH
```

The smoothing mode of the filter was selected to avoid an initial period of reduced accuracy due to the initialisation of the Kalman filter in *Track*. A low elevation cutoff of 7° was used due to the open nature of the site allowing additional low elevation satellite observations to be included without being subject to high multipath and continual obstruction. The `LEIAX1202` antenna has been calibrated by robot at Geo++ GmbH so there are phase centre variation corrections available down to an elevation of 0° in the IGS05 ANTEX file `igs05.atx`.

As the baseline length was short, with a maximum length of just under 1.5 km (Figure 6.21) and all the ambiguities were resolved, the quality of the reference solution was deemed acceptable. Formal errors of the reference solution were in the range 2 mm to 12 mm as shown in Figure 6.22 and Table 6.6. The East component shows the lowest standard deviations. Both the horizontal and the vertical components follow a similar trend with two periods of increased standard deviation occurring together.

The PDOP is a measure of the strength of the satellite geometry when estimating the position. Figure 6.23 shows that there are no PDOP spikes and consistently six

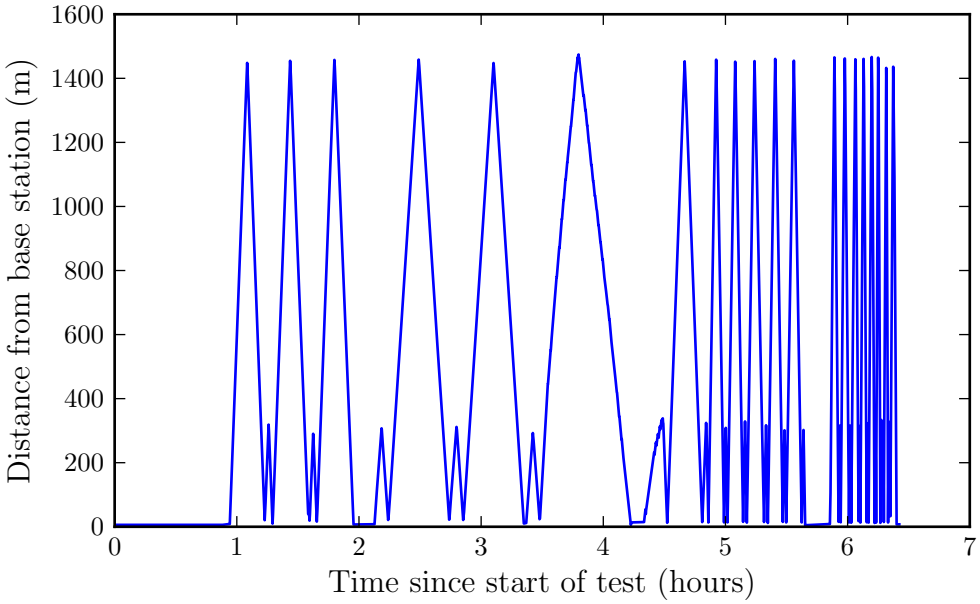

Figure 6.21: Baseline length during kinematic airfield test

Direction	Mean (mm)	Min (mm)	Max (mm)
North	5.0	3.8	7.6
East	3.3	2.6	4.7
Height	8.5	6.3	12.0

Table 6.6: Airfield reference solution formal errors from *Track*

or more satellites visible above the elevation cutoff. The periods of slightly higher standard deviations in the position solution correlate with the periods of reduced satellite availability and increased PDOP.

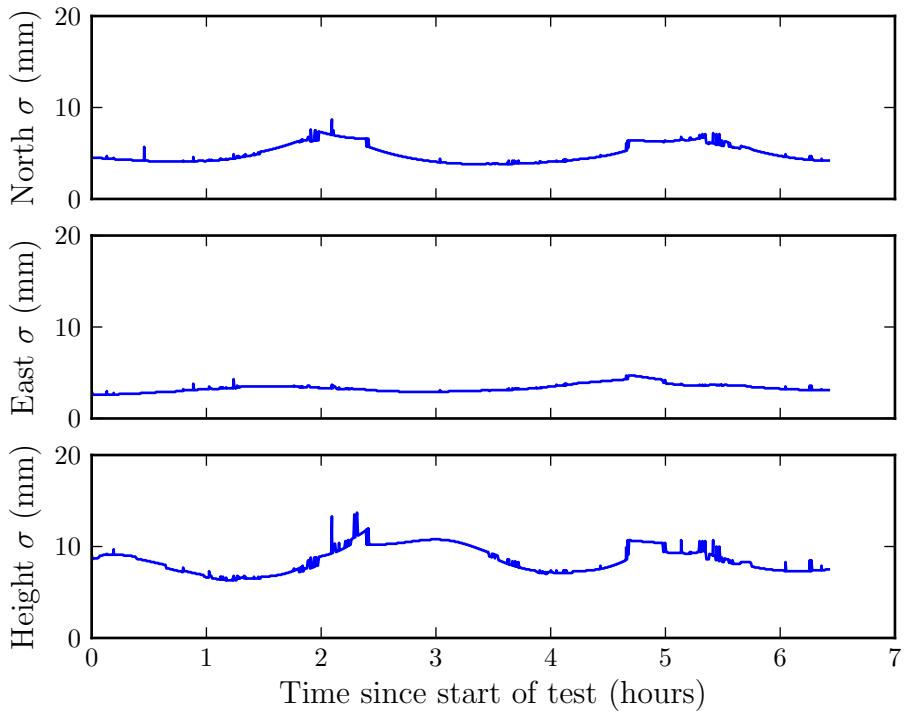

Figure 6.22: Formal errors of the *Track* reference solution at Albemarle

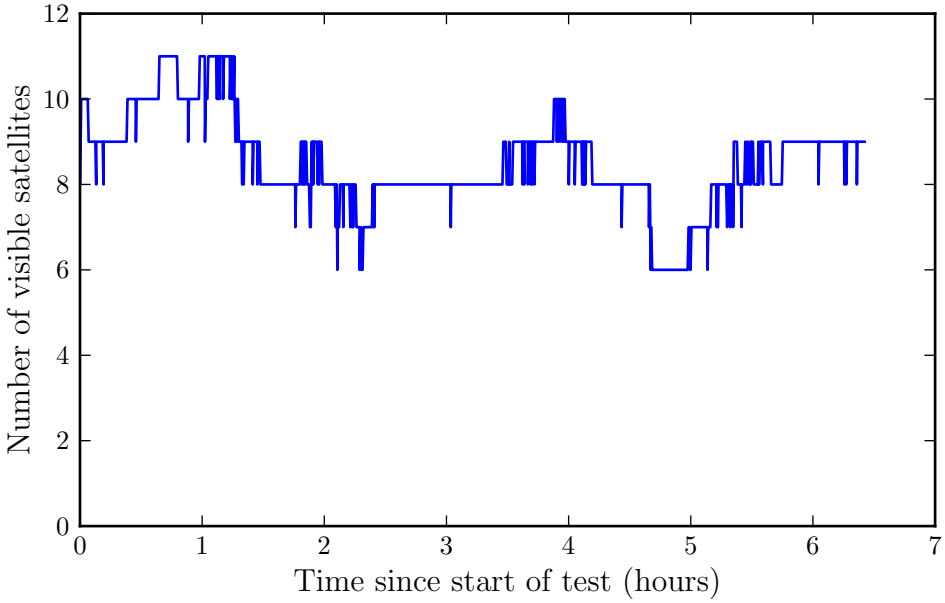

Figure 6.23: Satellites above the elevation cut-off used in the reference solution

6.2.3 *Kinematic PPP processing*

Details of the *pppncl* PPP solution parameters are as follows:

- The same 7° elevation cut off as used for the reference solution.
- Additional CODE final high rate clocks from `cod14935.clk_5` were used. These are tabulated at 5 s intervals in the RINEX clock format.
- The Niell tropospheric mapping function and Saastamoinen tropospheric zenith delay model were used for an *a priori* tropospheric delay model.
- The data was processed in a real-time mode, meaning that only data recorded up to and including the time of each estimated position epoch is used to produce that epoch.

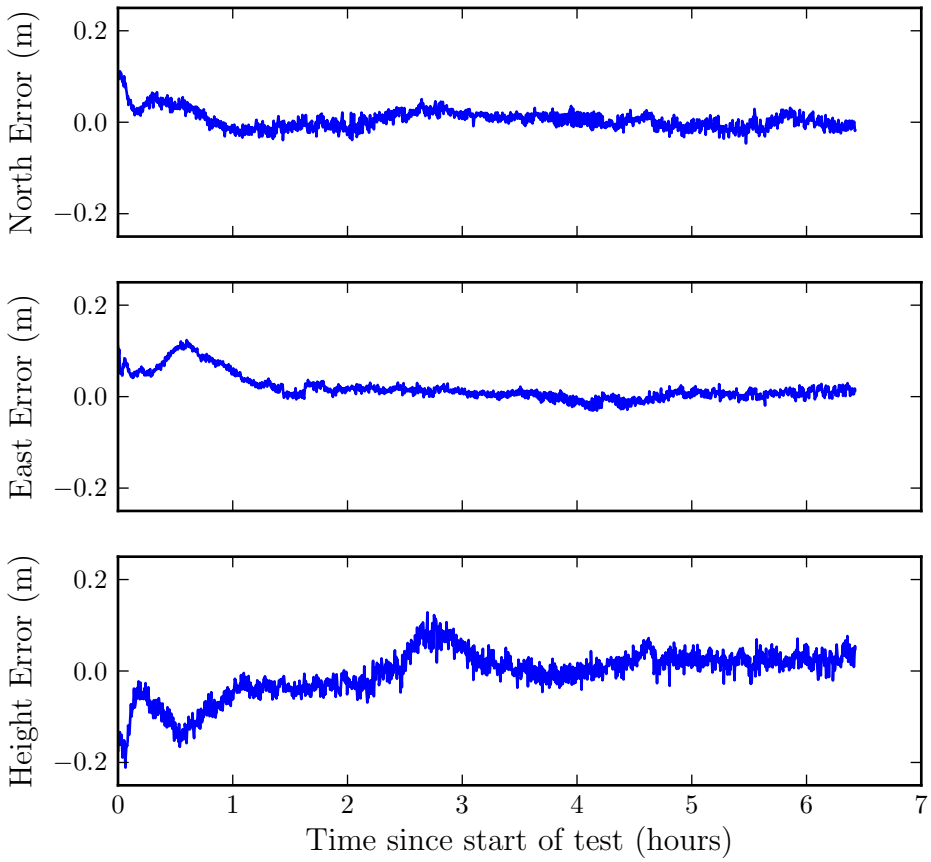

Figure 6.24: Error of *pppncl* coordinates with respect to the double difference *Track* solution at Albemarle Airfield

The graphs in Figures 6.24 and 6.25 show the North, East and Height error of the *pppncl* solution with respect to the reference coordinates. The initial convergence period can be seen in each component (approximately 1 h). In the North and East

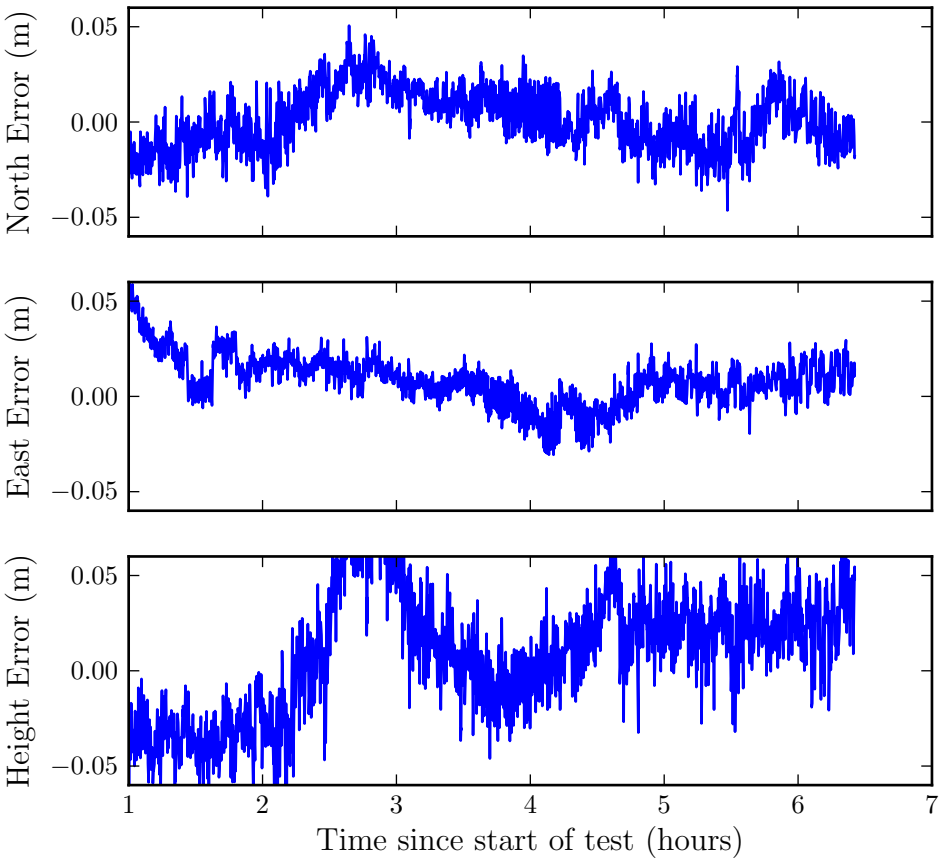

Figure 6.25: Zoomed in view of the error of the *pppncl* coordinates with respect to the double difference *Track* solution after 1 h at Albemarle Airfield

	Mean (mm)	Standard deviation (mm)	RMS (mm)
North	1.6	14.7	14.8
East	8.6	12.6	15.2
Height	9.7	32.8	34.1

Table 6.7: Mean, standard deviation and RMS of difference between the *pppncl* and reference coordinates at Albemarle Airfield

	Time (min)		
Absolute Error (m)	0.2	0.1	0.05
North	0	3	34
East	0	40	62
Height	5	167	382

Table 6.8: Time taken until kinematic *pppncl* coordinates are within a given difference from the reference coordinates, Albemarle Airfield

direction, after convergence there is consistent accuracy, with an RMS of 15 mm in each direction (Table 6.7); this is not affected by the different vehicle dynamics during the period. As expected, more variability is seen in the Height component, with an RMS of 35 mm. Whilst the error in the North and East solutions is contained within the epoch to epoch noise, the Height solution shows a variability in the average error between 2 h and 3 h after the start of the test. This coincides with the peak in the reference solution height uncertainty, shown in Figure 6.22. This is due to the geometry of the satellites at this time being sub-optimal, with regard to the estimation of height.

Table 6.8 lists the time taken until all subsequent coordinate estimates are within 0.2 m, 0.1 m and 0.05 m of the reference coordinates for North, East and Height respectively. Within 5 min, all coordinates converge to 20 cm accuracy, and 5 cm accuracy in the horizontal is obtained after 1 h. This is a very stringent definition of convergence with a 100% requirement on all subsequent coordinates to be within the limit, compared to one often used of two sigma RMS.

6.3 Conclusion

To conclude, Chapter 6 has described the validation of the performance of *pppncl* in both static and kinematic positioning. Static positioning was performed across a diverse range of global sites with coordinate RMS values of 4 mm, 5 mm and 13 mm in the North, East and Height components respectively, and with mean coordinate errors of less than 1 mm. These figures are comparable to published work (Kouba and Héroux, 2001).

The estimated zenith path delay due to tropospheric effects was compared to the IGS final product. Centimetre level agreement was seen for sites with both low and high variability in the zenith delay.

Convergence times for a subset of static sites were analysed. An horizontal accuracy of 10 cm was reached 95% of the time after one hour, and 5 cm was achieved within 2 h. For 3D convergence, 10 cm accuracy was reached 95% of the time in 1.5 h, and 5 cm accuracy was reached within 5 h. These figures are comparable to those in other published papers (Bisnath and Gao, 2008; Héroux et al., 2004).

The coordinate errors estimated using 24 h static PPP for IGS station UNBJ for each day in the year 2008 were compared to those obtained by Leandro et al. (2011) using GAPS PPP. The average coordinate errors obtained by *pppncl* of 5.5 mm in

the horizontal and 12.6 mm in 3D were slightly better than those obtained using GAPS PPP.

Based on the results obtained in comparison to other published work, *pppncl* has been seen to perform at a similar level to other PPP implementations. It can therefore be concluded that the PPP method has been successfully implemented and provides a useful platform from which to perform additional research.

Chapter 7 Combined GPS/GLONASS PPP

This Chapter examines the effect of including GLONASS in addition to GPS satellite observations into PPP. Tests were carried out to evaluate the impact on the chosen performance metrics (Section 2.9), specifically convergence time, positioning accuracy and continuity. Firstly, the relative magnitude of the GPS and GLONASS range error budgets are assessed, in order to complete the observation stochastic model used in the testing to assess the impact of GLONASS on positioning accuracy. The following performance metrics are evaluated: accuracy and convergence time for a range of static sites, and then accuracy, convergence time and continuity for a variety of kinematic positioning use cases; these were chosen to reflect some of the most likely applications and environments of PPP use.

For the assessment of the range error budget, it is desirable to remove as many of the estimated parameters as possible and replace them with accurate truth values; this is an attempt to measure the actual error budget, rather than the residual error after positioning estimation. Without this approach, the range error can bias the estimated parameters, reducing the observation range residuals, which could cause the error budget to be underestimated. On this basis, IGS static sites are used for the estimation of the error budget, as they have known coordinates with a high level of accuracy; these coordinates can be held fixed when calculating the residuals. The other benefit of the IGS static sites is that they operate in a clear sky environment, so can measure down to low elevations and at all azimuth angles, and therefore have a low level of cycle slips. This is important as any undetected cycle slip will bias the calculated residuals. This static site case would be expected to provide a lower bound on the error budget; for a kinematic receiver, one would expect to see increased multipath and higher receiver measurement noise, caused by increased receiver dynamics.

The ideal test design would cover a geographically diverse range of areas, in order to see all satellites with a range of elevation and azimuth angles, the corresponding range of satellite nadir angles. This also allows the range errors, due to spatially varying unmodelled error sources, to be sampled from a range of locations. In this Chapter, 87 static sites spread across the land areas of the Earth were investigated.

Ideally, the tests would be done over long periods, as some of the error sources are temporally variable, this also allows understanding of seasonal effects. At a minimum, datasets are required to cover a long enough period to show the convergence of the solution. The static datasets were evaluated for one week based on availability. To aid the statistical significance of any conclusions drawn, it is desirable to

have multiple datasets. There are constraints in collecting kinematic PPP datasets, and limited published data available; in this thesis three kinematic datasets were collected from a range of vehicles.

The first kinematic dataset was collected by a pickup truck driving on public roads in the UK. This dataset was designed to represent the challenges posed by buildings and other sky obstructions, which result in a lot of multipath, providing a stressed case on which to assess any improvement in continuity of the solution with the addition of GLONASS.

The next dataset considered was collected from an offshore survey vessel operating off the North coast of Norway. This dataset was chosen as it represents a real use case of PPP, in a commercial environment where there is a real desire to address the issues of convergence time and continuity (Veripos, personal communication July 2010). Additionally, the test was performed at a high latitude, where better geometry would be expected from the GLONASS satellites due to their higher orbital inclination angle. This dataset was the only dual frequency GPS/GLONASS data available from Veripos.

The investigation of these first two datasets suffered from the lack of an accurate reference solution. The final dataset chosen had a GNSS reference station within 2.5 km throughout. It was collected on board a small survey vessel operating in inshore waters on the East coast of England.

7.1 GLONASS observation noise

In order to combine heterogeneous observations in a Kalman filter, the relative noise needs to be known so that appropriate weights can be assigned to the respective measurements. Therefore to get the optimum contribution from GLONASS, the error in the measurements made, and the associated orbit and clock products, need to be quantified.

In order to quantify the relative accuracy of the GLONASS and GPS carrier phase observations, the observation residuals can be compared. Observation data for a range of static sites was downloaded for GPS week 1605 and run through *pppncl* with the position not estimated but held fixed at the value provided by the ESA weekly solutions. There were 87 sites in the IGS network recording GPS and GLONASS observations for week 1605.

Figure 7.1 shows the resulting ionosphere free LC carrier phase residuals for GPS and GLONASS respectively. The colouring indicates the logarithm of the proportion of residuals occurring at the given elevation angle for a residual of the corresponding size. The complete set of residuals from all 87 sites and all satellites observed during the week are included in the plots. For both GPS and GLONASS, the majority of all residuals fall in a narrow band centred about zero. Both satellite systems exhibit an increase in observation noise at lower elevation angles, with GLONASS showing a slightly more marked increase.

Figure 7.2 shows the RMS of LC residuals in 2 degree elevation bins.

The null hypothesis was stated as the mean of the difference between the RMS of the GPS and GLONASS ionosphere free carrier phase residuals being zero. Based on the apparent different behaviour of GLONASS at elevations below 40°, the RMS of the residuals is considered in two groups, those above 40°, and those below. A two tailed paired t-test was used to assess the null hypothesis. The p-value for elevation angles below 40° was 0.11, and the p-value for elevation angles above 40° was 0.42. Therefore the null hypothesis is accepted, indicating there is not a significant difference in the mean difference between the GPS and GLONASS ionosphere free carrier phase residuals, in either of the elevation groups considered.

An elevation dependent observation noise function was fitted to these RMS values. Two distinct functions were fitted to match the features seen at different elevation angles:

$$s(E) = \begin{cases} \dfrac{0.0063}{\sin E} & E < 25^\circ \\ 0.017 - 7.5 \times 10^{-5} \times E & E > 25^\circ \end{cases} \tag{7.1}$$

This observation noise function was then used to generate an elevation dependent weighting function:

$$w(E) = \frac{1}{s(E)^2} \tag{7.2}$$

In the following sets of PPP coordinate estimates generated using *pppncl*, the carrier phase observations were weighted using the elevation dependent function in Equation 7.2.

Using a similar methodology, Hesselbarth and Wanninger (2008) found no difference in the observation noise of GPS and GLONASS carrier phase measurements, and an almost identical noise level. This approach however suffers from requiring an initial observation weighting of the GPS and GLONASS observations. Even if site coor-

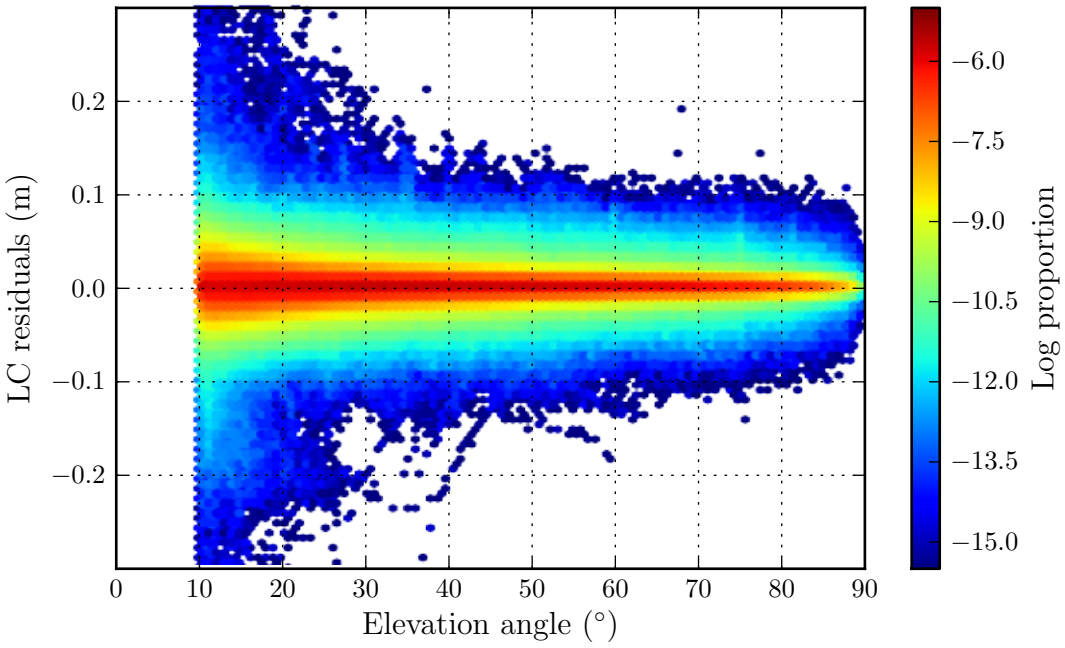

(a) GPS

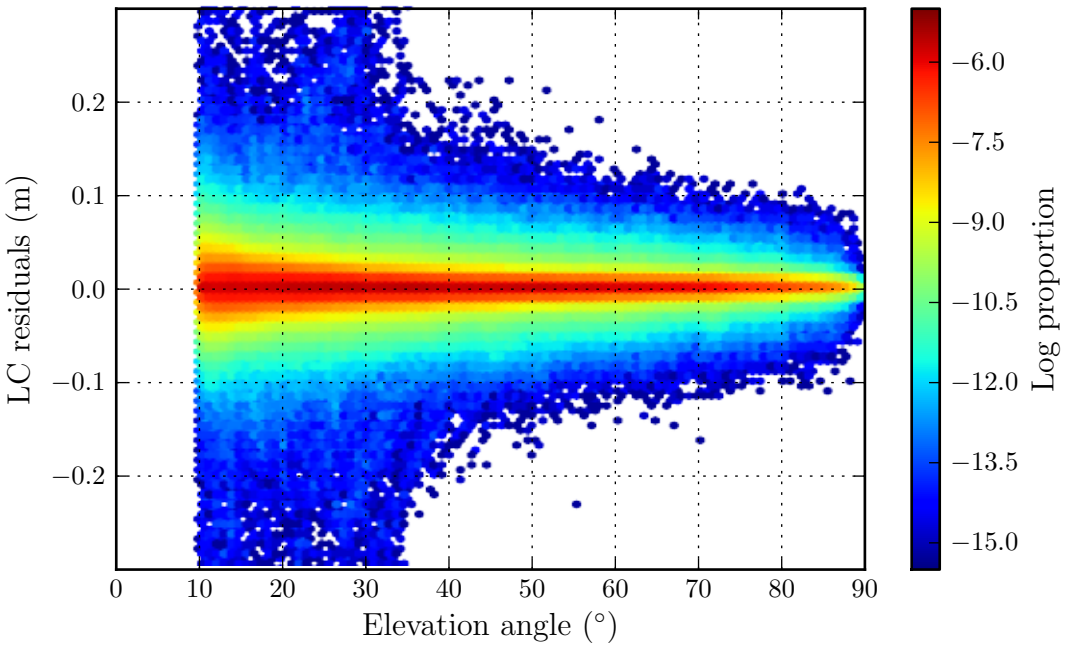

(b) GLONASS

Figure 7.1: Ionosphere free carrier phase residuals for 87 IGS stations over 5 days using ESA orbit and clock products. The colouring represents the normalised log frequency of residuals occurring at a given value.

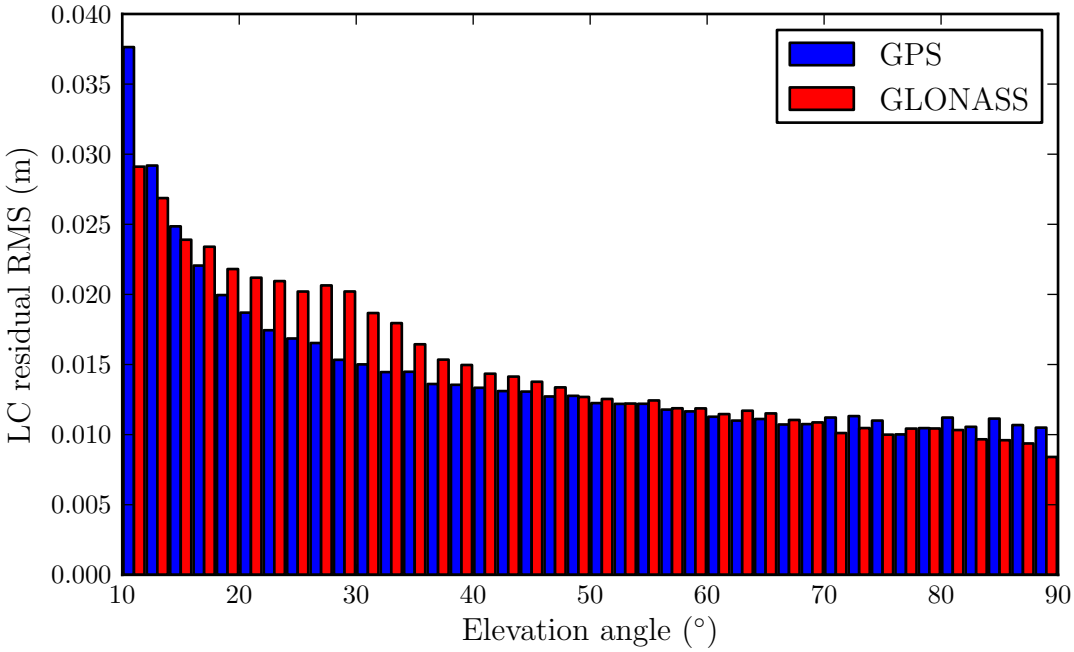

Figure 7.2: Comparison of GPS and GLONASS LC carrier phase residual RMS using 2 degree elevation bins with ESA final navigation products.

dinates are fixed whilst determining the observation noise using PPP, the receiver clock offset and the additional zenith tropospheric delay must still be estimated. How the observations are weighted in the PPP that generates the residuals will affect the values of those residuals. For example under-weighting the GLONASS observations will cause them to under-influence the estimated parameters. This then causes GPS observation noise, through incorrect estimation of the unknown parameters, to appear in the GLONASS residuals.

Despite its limitations this simple method provides a starting point from which to investigate the impact of GLONASS on PPP.

In comparison with the *a priori* error budget given in Section 3.16, the residuals determined in this test are considerably smaller. At higher elevation angles (greater than 50°) the *a priori* error budget of 8.3 cm overbounds all the observed residuals. This is likely to be due to the estimated parameters absorbing some of the range error. In particular, the high correlation between the troposphere delay, receiver clock and height component may contribute to this (Witchayangkoon, 2000). Constant biases are also absorbed in the estimated parameters as they are not observable and so cannot be separated from the carrier phase ambiguity.

7.2 GLONASS orbit and clock products

Veripos, a company providing offshore positioning solutions, are in the process of testing a new real-time GPS/GLONASS precise orbit and clock product called "Apex G2". Veripos provided eight days of orbit and clock products for the period 11 to 16 October 2010. Allowing for an extra day at the beginning and end of the period to account for polynomial fitting of the orbit products, this gives orbit and clock data for six days in GPS week 1605, from 10 to 15 October 2010. The requirement for the days to all be within the same GPS week allows for the use of the same IGS weekly coordinates to be used as reference coordinates for each day.

The Veripos orbit and clock products were provided in SP3 format tabulated at 5 s intervals. This is at a higher rate than the ESA and IGS orbit and clock products which are tabulated at 15 min intervals for the orbits, and 30 s intervals for the clock products.

7.3 GPS/GLONASS static convergence time

The convergence time has been identified as a limitation of current PPP, in both the float and ambiguity fixed methods (Section 2.5). The addition of GLONASS satellites to GPS PPP stands to improve the DOP and has therefore been proposed as a method to reduce the convergence time (Section 2.9).

To quantify any reduction in convergence time due to the addition of GLONASS observations, the following approach was used:

Perform static PPP using *pppncl* with as many GPS/GLONASS sites as possible for the 6 days over the period 10 to 15 October 2010, for which the Veripos Apex G2 orbits were available. The RMS of the PPP estimated coordinates, with respect to the weekly coordinate solutions, describes the repeatability of static PPP at that site. To compare the impact of the different orbital products, static PPP coordinate estimation was performed with IGS final, ESA final and Veripos Apex G2 real-time orbit and clock products. For the ESA and Veripos products two processing runs were performed, once using only the GPS satellites and once using both GPS and GLONASS. The IGS clock products do not contain GLONASS satellite clock offset corrections, so could only be used to perform GPS PPP, but were included to act as the "best currently available" GPS only PPP benchmark.

To assess the influence of GLONASS on the convergence time for each of the dif-

ferent orbit and clock products, the RMS of the coordinate errors was calculated at each of the 30 s observation intervals for each of the orbit and GPS/GLONASS combinations.

The observation data from all the IGS sites recording GPS and GLONASS observation data were downloaded from CDDIS (Noll, 2010). This gave a total of 87 sites with a global distribution for the 6 day period (Figure 7.3). Observation data was processed for 1 h, 2 h, 4 h, 8 h, 12 h and 24 h periods to quantify the improvement in repeatability with increasing observation length. GPS only solutions were produced using IGS, ESA and Veripos Apex G2 orbit and clock products.

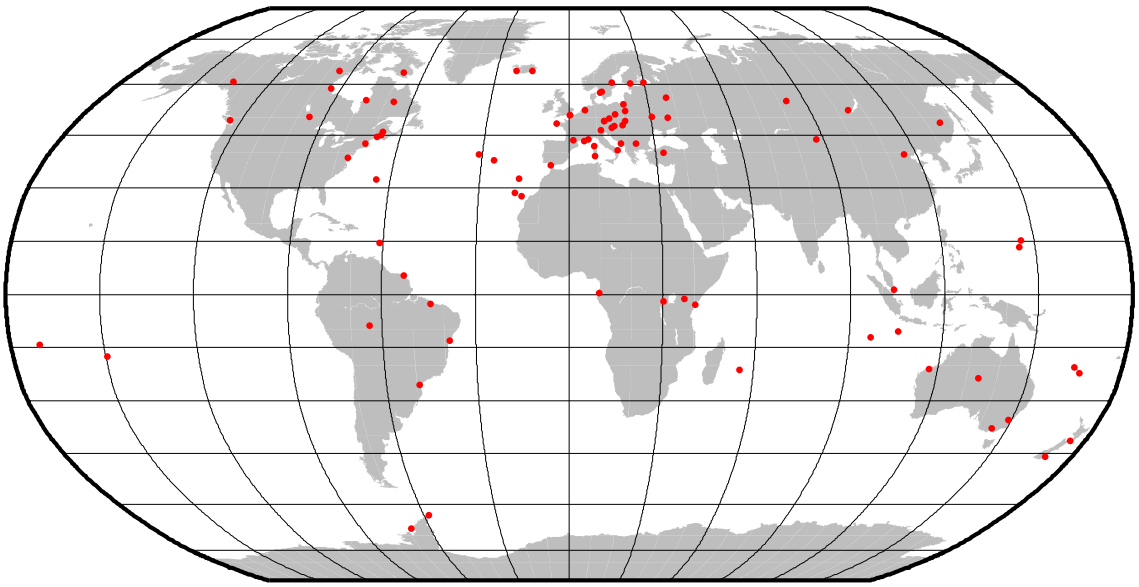

Figure 7.3: Distribution of the 87 sites used in the static GPS/-GLONASS PPP repeatability test

Using the same processing strategy as described in Section 6.1, coordinates were produced for all of the sites, for each orbit provider, and for all seven observation lengths. For the ESA and Veripos orbit and clock products a second set of processing was performed with GLONASS observations enabled. The GLONASS carrier phase observation noise was set equal to the GPS carrier phase observation noise using the values found in Section 7.1. All other parameters were kept the same as for the GPS only processing.

A total of 133,110 runs of *pppncl* were required to process all the combinations of orbit/clock provider, site and satellite system used. The resulting coordinates for each site were then compared to the IGS weekly solution and then a per site coordinate RMS was calculated for each 30 s position estimation interval. Figures 7.4, 7.5 and 7.6 show the mean RMS of the PPP estimated coordinates against time for

each of the five navigation products and GPS/GLONASS combinations considered. A lower RMS corresponds to increased accuracy and improved repeatability. All three coordinate components show a similar pattern of a decrease in mean RMS with increasing processing length for all five processing options.

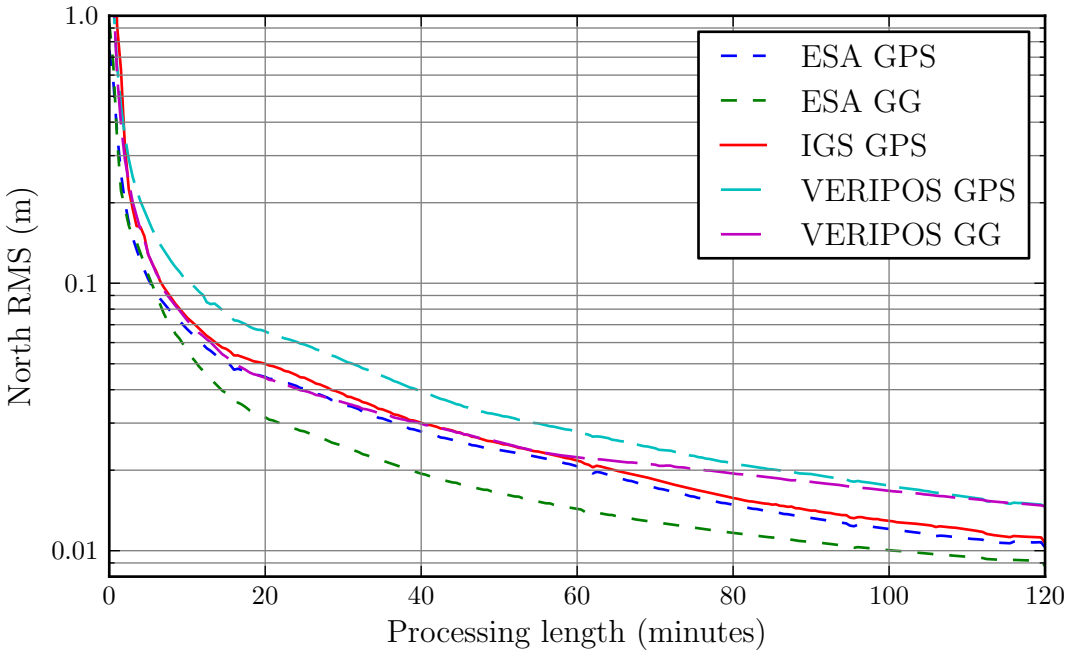

Figure 7.4: Mean RMS of static PPP estimated North coordinates with respect to IGS reference coordinates.

As would be expected from the reduced accuracy possible in real-time orbit and clock product generation, the accuracy obtained with the Veripos Apex G2 orbit and clock product is lower than that obtained with the corresponding ESA orbit and clock products.

For processing lengths of 2 h there is a clear improvement in accuracy with the addition of GLONASS observations (Figure 7.6). The accuracy of both of the GPS/GLONASS solutions is better than that of the respective GPS only solutions. Towards the end of the two hour period the accuracy of the Veripos GPS/GLONASS and the GPS/GLONASS solution converges.

Table 7.1 gives the mean and standard deviation for the time until the RMS of the site coordinate estimation error is less than 10 cm for the set of sites used in this test. This table shows the reduction in convergence time due to the addition of GLONASS was between 17% and 47%. A one-tailed paired t-test was performed on the null hypothesis that the mean RMS convergence time of the GPS and GPS/GLONASS

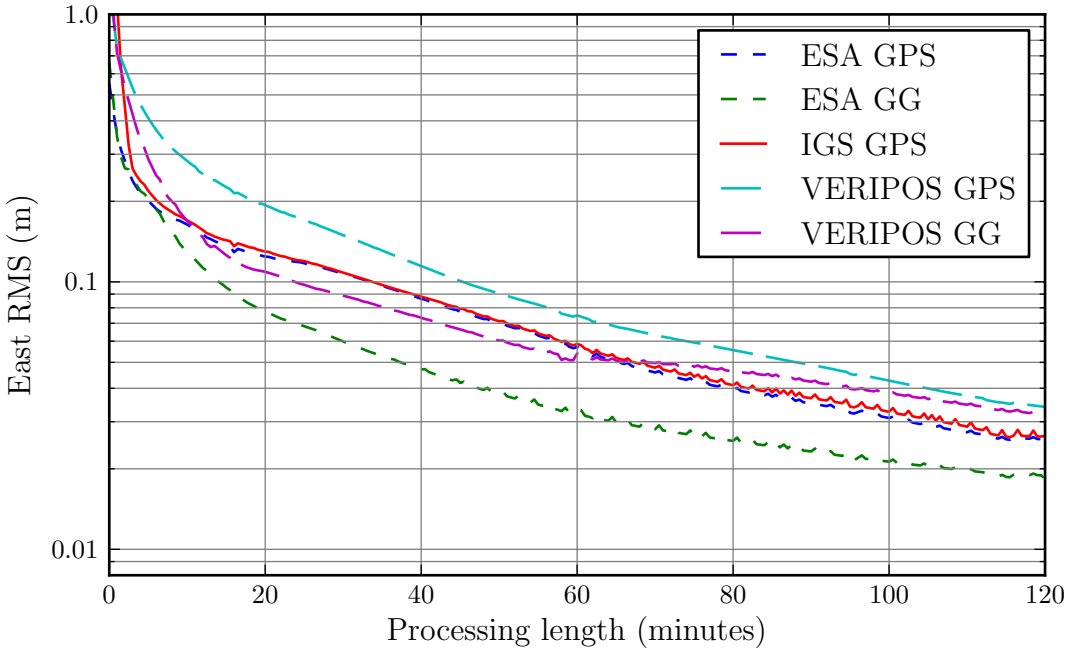

Figure 7.5: Mean RMS of static PPP estimated East coordinates with respect to IGS reference coordinates.

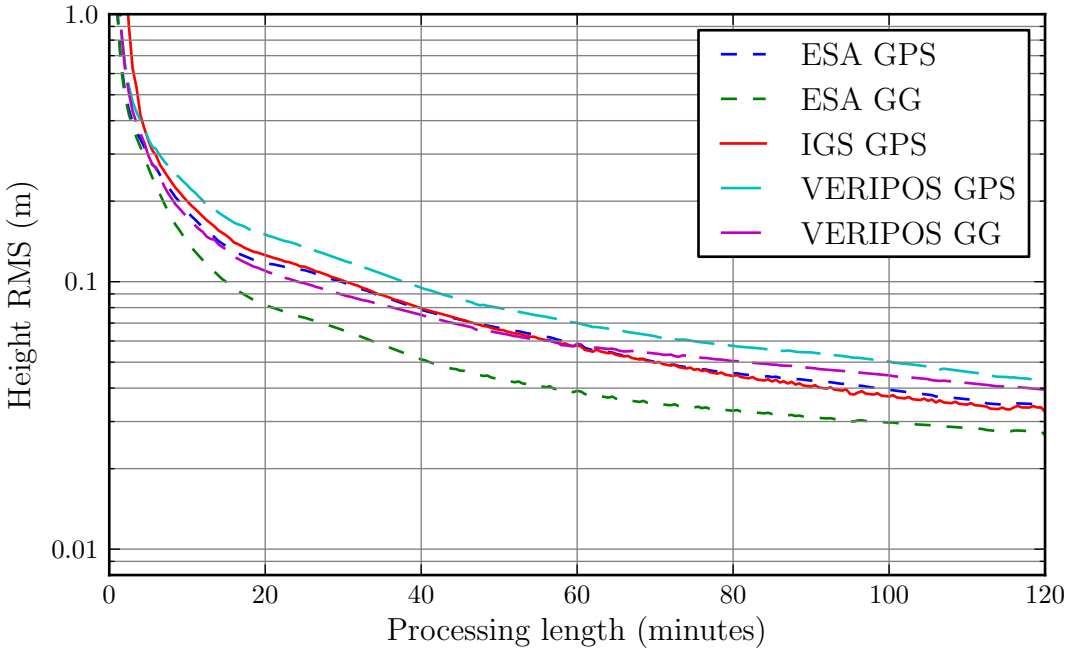

Figure 7.6: Mean RMS of static PPP estimated Height coordinates with respect to IGS reference coordinates.

Provider		GPS		GG		Improvement
		Mean (s)	σ (s)	Mean (s)	σ (s)	
ESA final	N	338	157	280	218	17%
	E	1521	1026	807	647	47%
	H	1575	1099	990	648	37%
Veripos	N	667	413	429	360	36%
	E	2465	786	1296	1296	47%
	H	2217	1326	1438	1438	35%

Table 7.1: Mean convergence time to 10 cm for GPS and GPS/-GLONASS (GG) static PPP.

Provider		p value
ESA final	N	9.5E-03
	E	3.2E-11
	H	4.4E-10
Veripos	N	2.2E-07
	E	2.5E-24
	H	8.9E-15

Table 7.2: GPS and GPS/GLONASS one tailed paired t-test p values for the comparison of PPP convergence time

PPP methods, for a given orbit and clock provider, were the same. Here the one tailed t-test was selected, as the alternative hypothesis is that the convergence time with GLONASS is lower than without. A paired t-test was used as both sets of data sample the same sites, with the measurement being the time until the RMS coordinate error was less than 10 cm. For both the ESA final orbits and the Veripos real-time orbits, in each of the coordinate components (North, East and Height), there was a statistically significant difference in the convergence time between GPS and GPS/GLONASS PPP (Table 7.2). These results suggest that the addition of GLONASS to PPP can reduce the convergence time to reach decimetre accuracy.

Martín et al. (2011) investigated the change in convergence time of eight sites when including GLONASS observations using MagicGNSS PPP (Píriz et al., 2008). For the day of 1 Jan 2010 they found no significant reduction in convergence time. Between 1 Jan 2010 and the start of the test performed here (10 Oct 2010), nine new GLONASS satellites were launched and two satellites were withdrawn from service. The results presented in this thesis show that using *pppncl* with the current GLONASS constellation, a clear reduction in convergence time is achieved with GPS/GLONASS PPP over a much larger set of sites, in contrast to the findings of

Provider	ESA	Veripos
GPS 3D coordinate RMS (mm)	10.5	11.8
GPS/GLONASS 3D coordinate RMS (mm)	11.0	13.7
W statistic	29952	26282
p value	0.82	0.03
Outcome	Accept H0	Reject H0

Table 7.3: Test statistics for the comparison of GPS and GPS/-GLONASS PPP 3D coordinate RMS after 24 h

Martín et al. (2011).

The accuracy of PPP estimated coordinates static coordinates after longer estimation periods of up to 24 h is show in Figures 7.7, 7.8 and 7.8. At longer processing lengths the difference between the RMS of the GPS and GPS/GLONASS (denoted as GG in the figures) PPP solutions reduces. Comparing the 3D coordinate RMS error between GPS only and GPS/GLONASS PPP, the null hypothesis that the coordinate RMS between for the two methods after 24 h for a given orbit and clock provider come from the same distribution. A Wilcoxon signed-rank test (Lowry, 2011) was performed for the comparison for both ESA and Veripos orbit and clock products. From the values given in Table 7.3, for $p<0.05$ we accept the null hypothesis for the ESA orbit and clock products and reject it for the Veripos products. We therefore conclude that for the ESA Final orbit and clock product GPS/GLONASS PPP does not produces statistically different coordinate RMS errors than GPS PPP. For the Veripos orbits we conclude that there is a statistically significant difference, with the median coordinate RMS error for GPS/GLONASS of 13.7 mm being larger than that measured with GPS PPP.

This would imply that once the Kalman filter has converged and the carrier phase ambiguities are accurately determined, the limiting factor in improved RMS is not the number and geometry of the visible satellites, but either the accuracy of the orbit and clock products or the models used in calculating the signal delay.

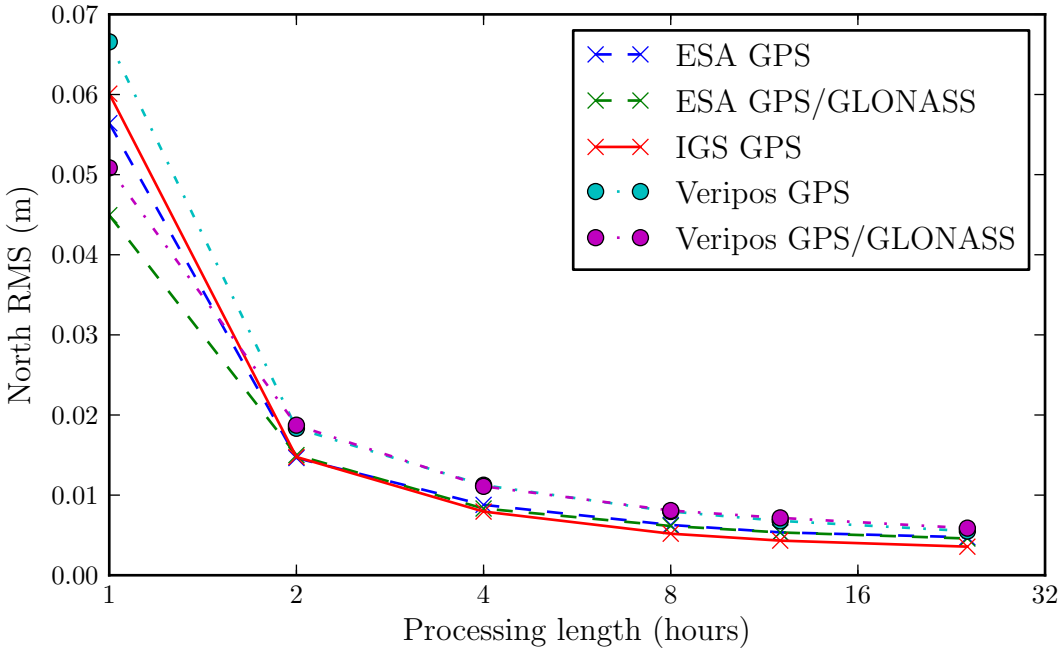

Figure 7.7: RMS of the static PPP estimated North coordinates with respect to IGS reference coordinates.

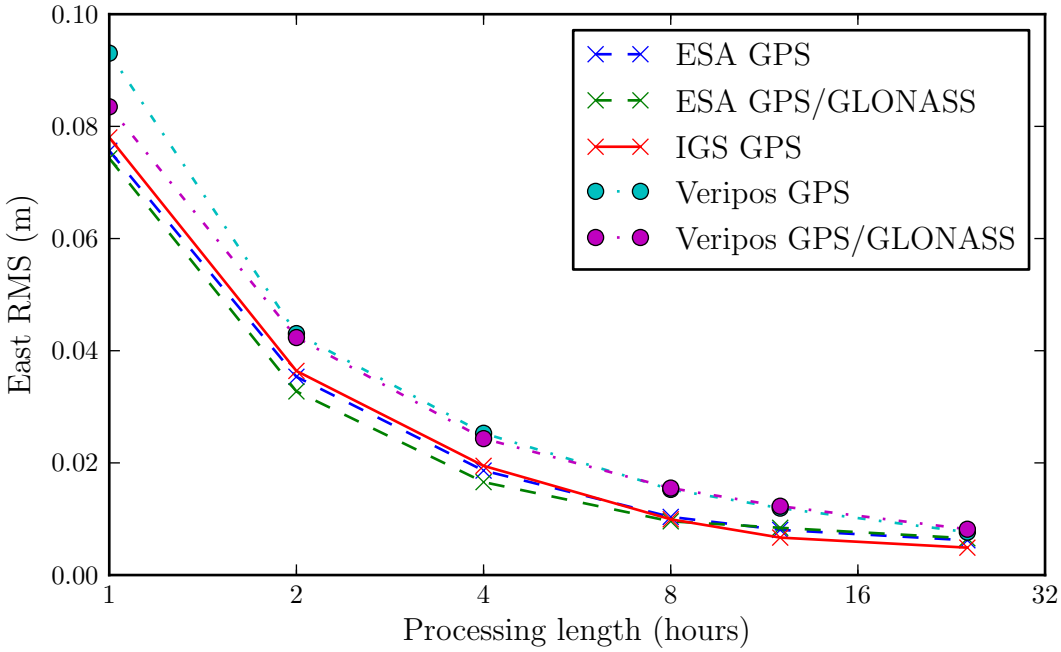

Figure 7.8: RMS of the static PPP estimated East coordinates with respect to IGS reference coordinates.

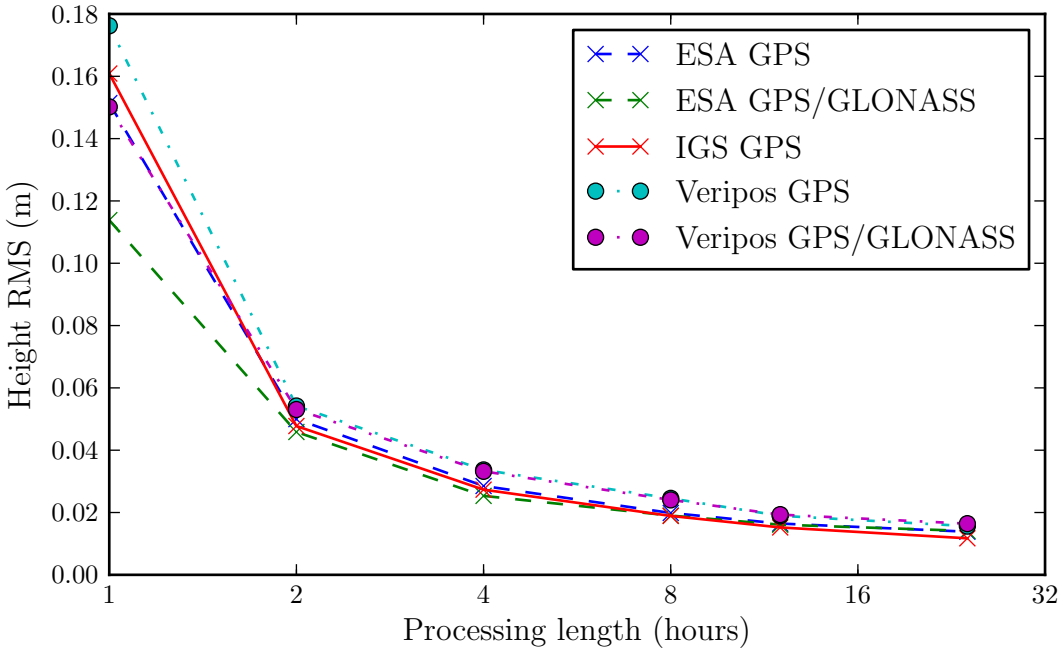

Figure 7.9: RMS of the static PPP estimated Height coordinates with respect to IGS reference coordinates.

7.4 Cycle slip and outlier detection

The method used for cycle slip detection (Section 4.8.2) for each satellite is independent of the other visible satellites as it only depends on linear combinations of observations from that satellite. Therefore the addition of GLONASS does not impact operation of the cycle slip detection step.

The fixing of cycle slips makes use of the carrier phase observations free from cycle slips to estimate the cycle slips prior to integer fixing using the LAMBDA method. The inclusion of GLONASS in addition to GPS provides more observations; if there are cycle slips on the carrier phase measurements for several satellites, then with more satellites, there are more likely to be sufficient unaffected satellites. This enables the cycle slips to be resolved and therefore corrected, providing continuity without requiring reinitialisation. An example of an extreme case of this where the receiver loses lock on all GPS satellites is described in the inshore survey vessel dataset in Section 7.5.3.

The method used for outlier detection is described in Section 4.8.1. The addition of GLONASS satellites affects the outliers in two different ways, the ability to detect outliers is impacted, as well the positioning accuracy in the case of undetected

outliers. The statistic used in the initial overall model test is derived from all of the observations made at a particular epoch.

Several examples were considered to demonstrate the impact of GLONASS on outlier detection. Four types of outlier were artificially introduced on GPS satellite ID 3 after 30 min of observation: step type in carrier phase, step type in code phase, ramp type in carrier phase, and ramp type in code phase. The step type change simulates a cycle-slip or period of code phase multipath. Ramp errors are the most difficult to detect early (Bhatti, 2007).

This test was completed by considering the IGS station, HERS, a dual frequency GPS/GLONASS receiver logging data at 1 Hz. The same processing strategy was used as described in Section 6.1, using the ESA orbit and clock products.

To test the addition of the step type to the carrier phase, a single cycle was added to the L1 and L2 carrier phase measurements of GPS satellite ID 3 for the period from 30 min after the start of the dataset until 60 min after the start. This combination of slips in L1 and L2 was chosen as the change is not measurable in the wide lane linear combination, making it harder to detect. Both the GPS and the GPS/GLONASS processes detected the cycle slips immediately, both at addition and subtraction of the step bias, and both were able to successfully identify the correct cycle slip. This step resulted in no impact to the positioning solution.

To test the addition of the step type in code phase, for the same time period as the above test, a 25 m bias was added to the C/A code phase measurement. In the GPS only solution this bias caused the overall model's test statistic to be larger than the threshold value. The ionosphere free code phase linear combination was identified as an outlier and removed from the estimation process for the entire period of the bias addition. The graph of the test statistic and the thresholds is shown in Figure 7.10, the effect on positioning performance is shown in Figure 7.11. For the GPS only solution, the 25 m bias was detected and removed for the entire period, it therefore did not impact the position apart from the effect of having one less code phase measurement in use. For the GPS/GLONASS PPP solution, this bias did not cause the overall model test statistic to exceed the threshold until 2887 s (approximately 16 min after the addition of the bias), the test statistic was not consistently above the threshold until 3189 s. After this time it was identified and removed from the estimation process. The late detection was due to the increased threshold value calculated in the outlier detection process.

Despite the failure of the GPS/GLONASS PPP to remove the step bias for the

majority of the addition period the 3D coordinate error remained lower than that of the GPS/GLONASS solution at all times. Also visible in Figure 7.10 is the large increase in the test statistic for both methods after the removal of the step bias at 3600 s. This is erroneously detected as a cycle slip using the Melbourne-Wübenna method, the slip resolution method then "successfully" fixes the apparent cycle slip to the wrong value. This is then detected by the outlier detection and the ambiguity is reset.

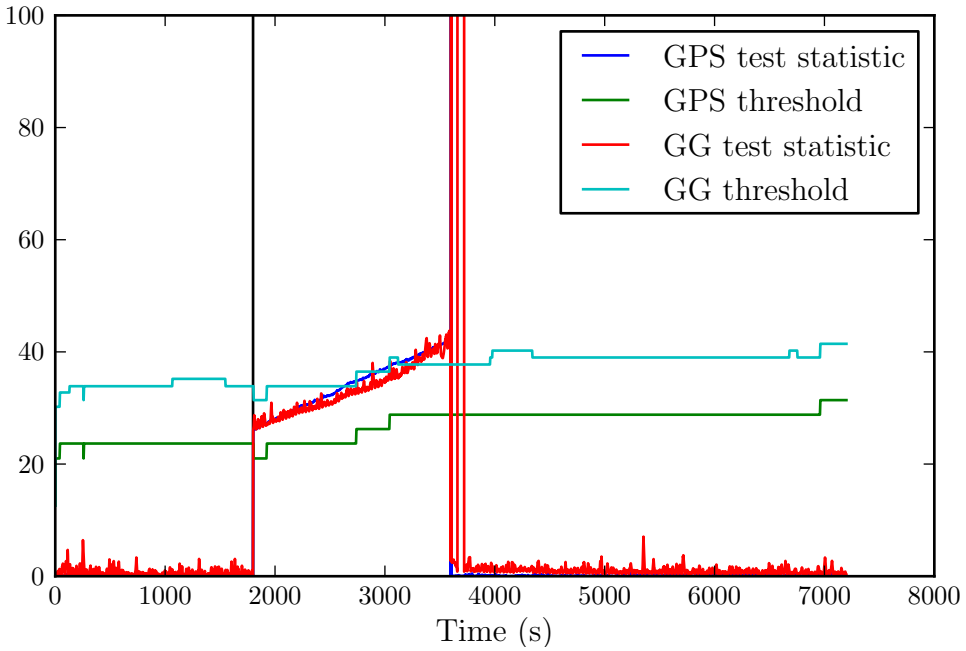

Figure 7.10: Overall model test statistics for GPS and GPS/-GLONASS PPP with code phase step bias, vertical black lines show start and end of bias addition at 1800 s and 3600 s respectively

To test the effect of a slowly increasing bias in the carrier phase, a ramp bias was added increasing at 1 cm every second. In the GPS only solution this bias was initially detected after 12 s, and in the GPS/GLONASS PPP solution, after 13 s (Figure 7.12). The carrier phase observation is then excluded from the solution, but not reset for up to 5 epochs. This approach to carrier phase outlier detection is an attempt to avoid unnecessarily resetting ambiguities due to any short term outliers. In both methods, the carrier phase ambiguity is reinitialised for this satellite, but as the bias continues to grow this triggers repeated outlier detections, causing the carrier phase bias to be repeatedly reset. The repeated outlier detections are shown in Figure 7.12 by the test statistic repeatedly crossing the threshold. The reset interval for GPS is lower, at an average of 21 s, than for GPS/GLONASS with an average of 28 s. The GPS only solution is able to detect the bias at a smaller

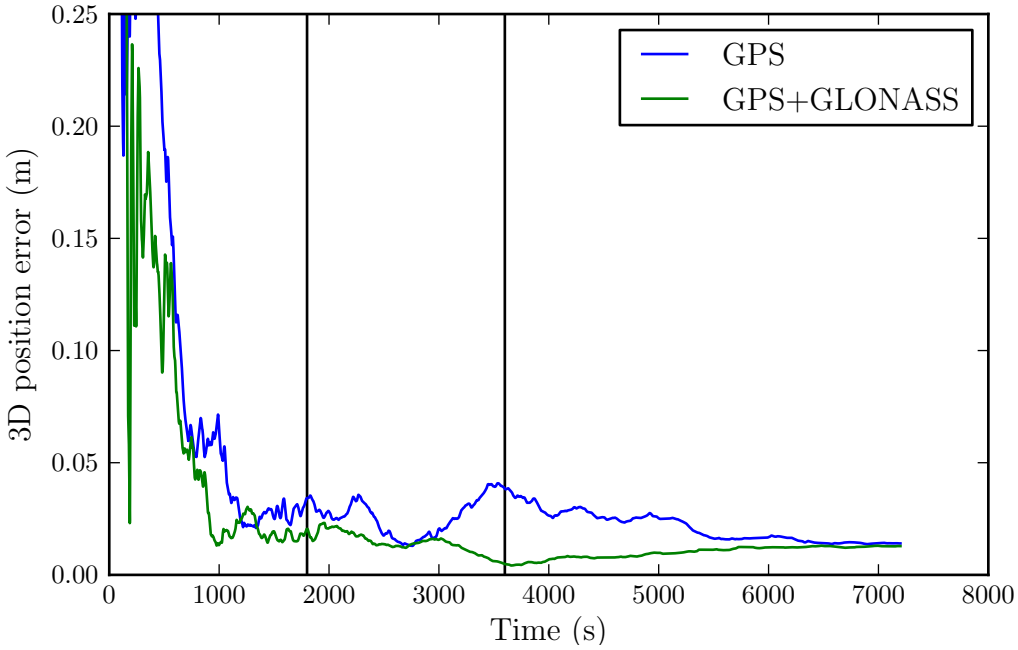

Figure 7.11: 3D RMS coordinate error for GPS and GPS/GLONASS PPP with code phase step bias, vertical black lines show start and end of bias addition

magnitude due to the lower threshold as for the code phase step bias detection.

Despite the earlier detection in GPS only PPP, there is a clear reduction in the position accuracy in the GPS only solution at the start of the bias introduction (Figure 7.13). With fewer observations the GPS only PPP solution is negatively influenced by the initial period when the bias is undetected, whereas the GPS/GLONASS solution does not suffer from an obvious discontinuity in coordinate accuracy.

To test the addition of the ramp bias to the code phase, a ramp bias was added at time 1800 s, increasing at 1 m every second. This causes the test statistic to slowly grow as the bias grows (Figure 7.14). In the GPS only solution this bias was detected after 23 s, and in the GPS/GLONASS PPP solution, after 28 s. Unlike in the case for the carrier phase ramp bias, once the bias grows above the detection threshold, it is then detected for the rest of the period it is added. The low weight of the code phase measurement, due to the expected multipath and receiver measurement noise contribution to the error budget, cause the effect of the undetected period of bias to be fairly small. Figure 7.15 shows the impact on 3D positioning accuracy with reference to the IGS weekly coordinates, there is no noticeable decrease in the GPS/GLONASS coordinate accuracy during the 28 s for which the bias is undetected.

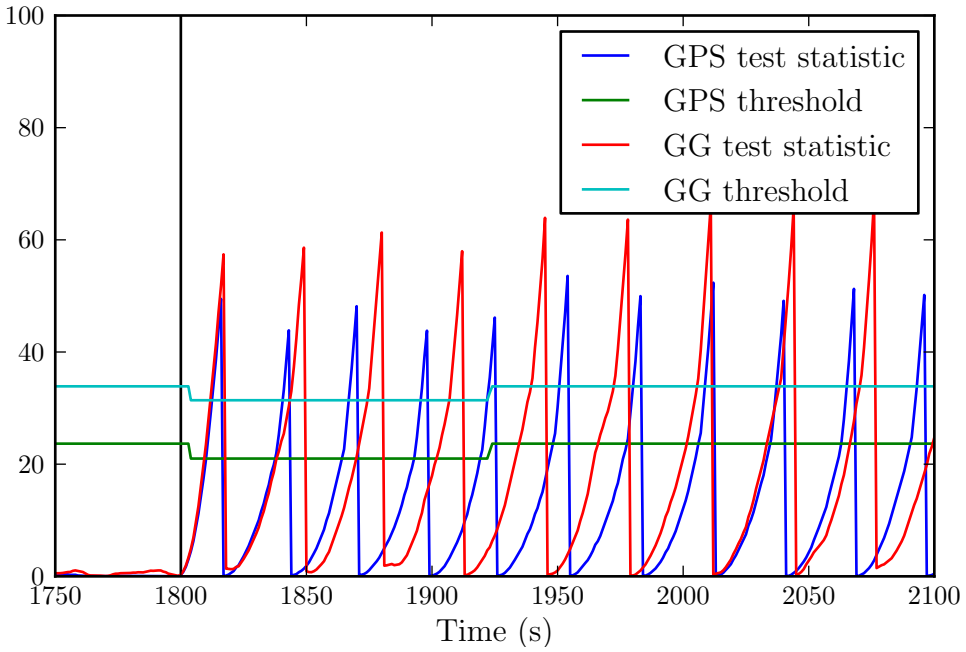

Figure 7.12: Overall model test statistics for GPS and GPS/-GLONASS PPP with a carrier ramp bias, vertical black lines show start and end of bias addition

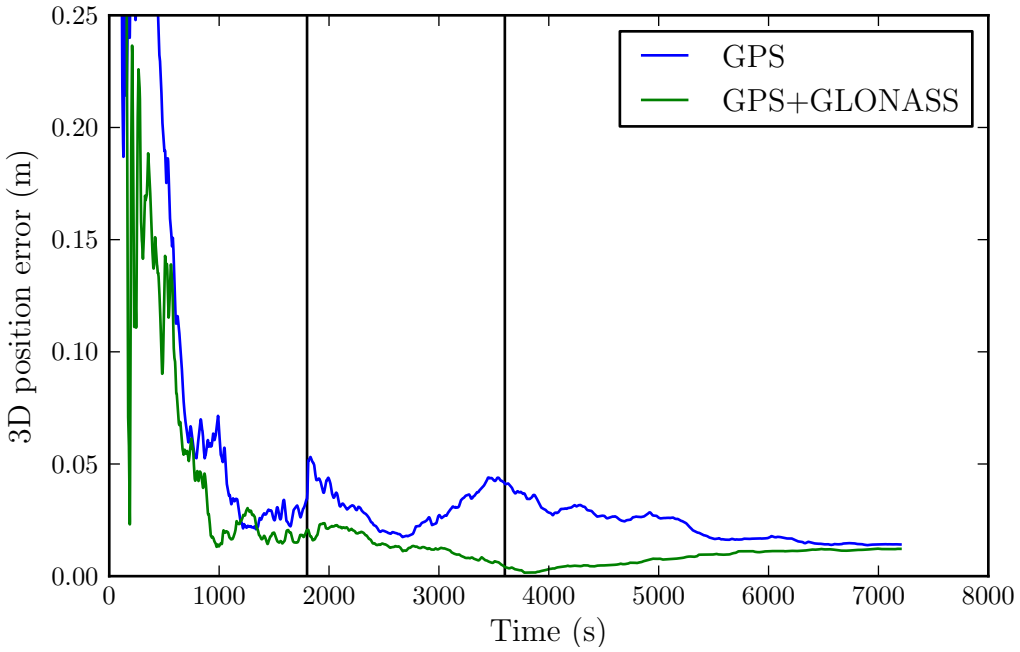

Figure 7.13: 3D RMS coordinate error for GPS and GPS/GLONASS PPP with a carrier ramp bias, vertical black lines show start and end of bias addition

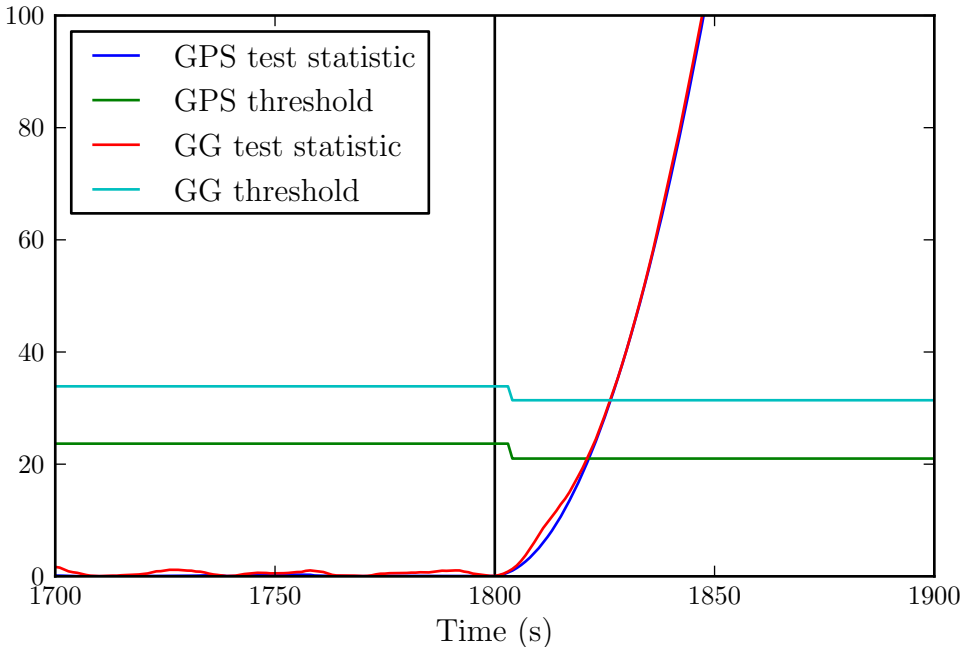

Figure 7.14: Overall model test statistics for GPS and GPS/-GLONASS PPP with a code phase ramp bias, vertical black lines show start and end of bias addition

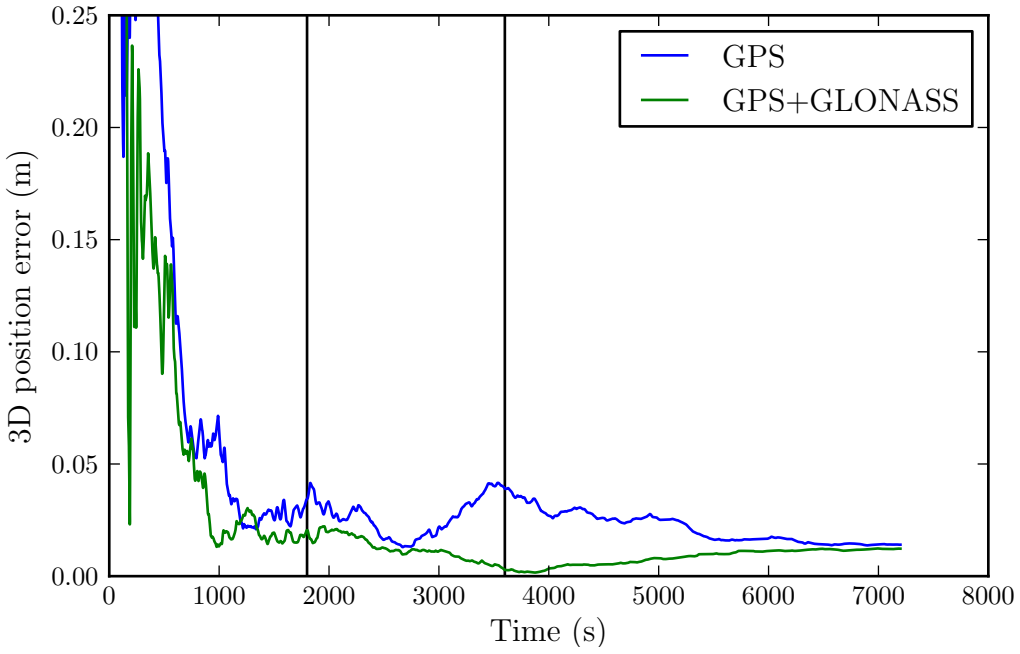

Figure 7.15: 3D RMS coordinate error for GPS and GPS/GLONASS PPP with a code phase ramp bias, vertical black lines show start and end of bias addition

To summarise this outlier detection test, the GPS only solution appears to be able to detect both smaller code phase biases and smaller carrier phase biases. In the GPS/GLONASS solution, the additional degrees of freedom, due to the additional observations on which outliers could occur, increases the threshold at a given significance, therefore increasing the minimal detectable bias.

However the robustness of the GPS/GLONASS solution in the presence of an outlier, due to the additional observations, appears to more than compensate in terms of the overall effect on positioning accuracy. This raises the question of the suitability of the overall model test in the presence of increased observations, in particular looking forward to the addition of future satellite systems. As more satellites are added, it seems the ability to detect outliers is reduced, and therefore to include an additional satellite system such as Galileo, the statistical approach to outlier detection may need to be adapted.

7.5 Kinematic positioning

To assess the impact of using GLONASS combined with GPS on kinematic PPP, a variety of kinematic datasets were collected using a range of transport modes as described below.

7.5.1 *Road vehicle in the United Kingdom*

This test involved driving a vehicle on public roads. A Leica GS10 receiver was mounted with an AS10 antenna on a pickup truck above the main cab to give the best clear sky view possible. The vehicle was driven for approximately 6 h on 20 Jan 2011 from Newcastle-upon-Tyne to Carlisle around the Lake District area and to Southwest Scotland, in the UK. The route passed through villages and hilly areas, representative of the UK countryside. As well as driving at a range of speeds, there were three periods during the journey when the vehicle was stationary. Data was collected at 1 Hz, recording all GPS/GLONASS satellites in view. Observation data from static sites along the vehicle's route that form part of the Leica Smartnet Network RTK service were downloaded via the Leica Smartnet website (Burbidge, 2006). For subscribed users of the Smartnet service it is possible to access the 1 Hz observation data from the reference network, with the past 30 days available for download. This provided a set of reference stations to use in estimating a set of "truth" coordinates using the double-differenced post-process carrier phase method.

MIT *Track* was used to produce a set of reference coordinates with which to compare the GPS and GPS/GLONASS PPP solutions. The route passed near three base stations: CARL, KIRK, DRUM, as shown in Figure 7.16. As these base stations are run by the Ordnance Survey (Cruddace, 2006), the known coordinates are given in ETRS89 and are therefore not compatible with the ESA GPS/GLONASS orbit and clock products which are given in ITRF2005. For each of the three base stations, Dr. Nigel Penna generated GIPSY PPP-based daily static coordinates using the ESA Final orbits. The weighted mean coordinates from each day of the surrounding week (composed of seven 24 h periods) were used as the reference locations. Table 7.4 shows the mean coordinates produced using GIPSY and the standard error of the mean. The sub-millimetre standard errors in all coordinate components are well below the achievable centimetre-level kinematic PPP accuracy, so are taken as truth in the following analysis.

Site	X (m)	Y (m)	Z (m)	σ_X	σ_Y	σ_Z
CARL	3671344.2932	-188441.0622	5194774.1971	0.6	0.5	0.7
DRUM	3601680.6339	-235186.8396	5241367.8543	0.5	0.6	0.7
KIRK	3672068.2812	-259826.9475	5191172.8759	0.6	0.5	0.7

Table 7.4: ITRF2005 coordinates of the reference stations used in the pickup test as produced using GIPSY PPP. Standard errors of the 7 day mean coordinate estimates, (σ), are in mm

All three reference stations were included in the *Track* coordinate estimation meaning multiple baselines can be formed. This means that the shortest baseline available is always included in generating the reference coordinates, to avoid having to process in multiple short discontinuous batches. The reference stations were held fixed at the calculated coordinates. All three of the reference stations used are equipped with the `LEIAR25 LEIT` Leica antenna for which phase centre corrections are available in the IGS ANTEX file (igs05.atx).

All the receivers observe C1 and P2 code observations so the monthly estimated P1-C1 biases from CODE were used to correct the C1 observable to a P1 equivalent observable.

Using the following configuration file, double difference coordinates for the receiver mounted on the pickup truck were produced using *Track*:

```
OBS_FILE
 carl data/carl020k00_p1.11o F
 kirk data/kirk020k00_p1.11o K
```

```
 drum data/drum020k00_p1.11o K
 rove data/leicapickup_p1.11o K

NAV_FILE data/gps/products/1619/esa16194.sp3 SP3

SITE_POS
 carl 3671344.2931 -188441.0622 5194774.1971
 drum 3601680.6339 -235186.8396 5241367.8543
 kirk 3672068.2812 -259826.9475 5191172.8759
 rove 3693831      -176914      5179434

MODE AIR

SITE_STATS
 all 0.005 0.006 0.007 0.0 0.0 0.0
 rove 200 200 200 4.7 4.7 4.7

ATM_STATS
 all 0.1 0.0001

ante_off
 all 0.0 0.0 0.0 LEIAR25         LEIT
 rove 0.0 0.0 0.0 LEIAS10         NONE

ANTMOD_FILE igs05.atx
CUT_OFF 10
OUT_TYPE GEOD+NEU+XYZ
INTERVAL 1
USE_GPTGMF
BACK_TYPE SMOOTH
```

The kinematic dataset was very challenging to process with regular complete loss of lock due to the vehicle passing under bridges and behind other obstructions such as forests. Due to periods with a low number of visible satellites, high dilution of precision and short continuous observation arcs, the reference solution has many holes and periods where confidence in the result is low due to *Track* being unable to fix the carrier phase ambiguities to integer values.

Figure 7.16 shows the sections of the route that *Track* was able to process are shown in relation to the base station locations. The gaps show periods for which the coordinate uncertainties produced by *Track* were greater than a threshold of 1 m for coordinate output. From Figure 7.17 it can be seen that the problematic periods occur whilst the vehicle is moving. If the formal errors for the estimated coordinates are taken into account, it can be seen that for all periods during which the vehicle is in motion, the estimated coordinates are only accurate to 20 cm (one sigma) at best.

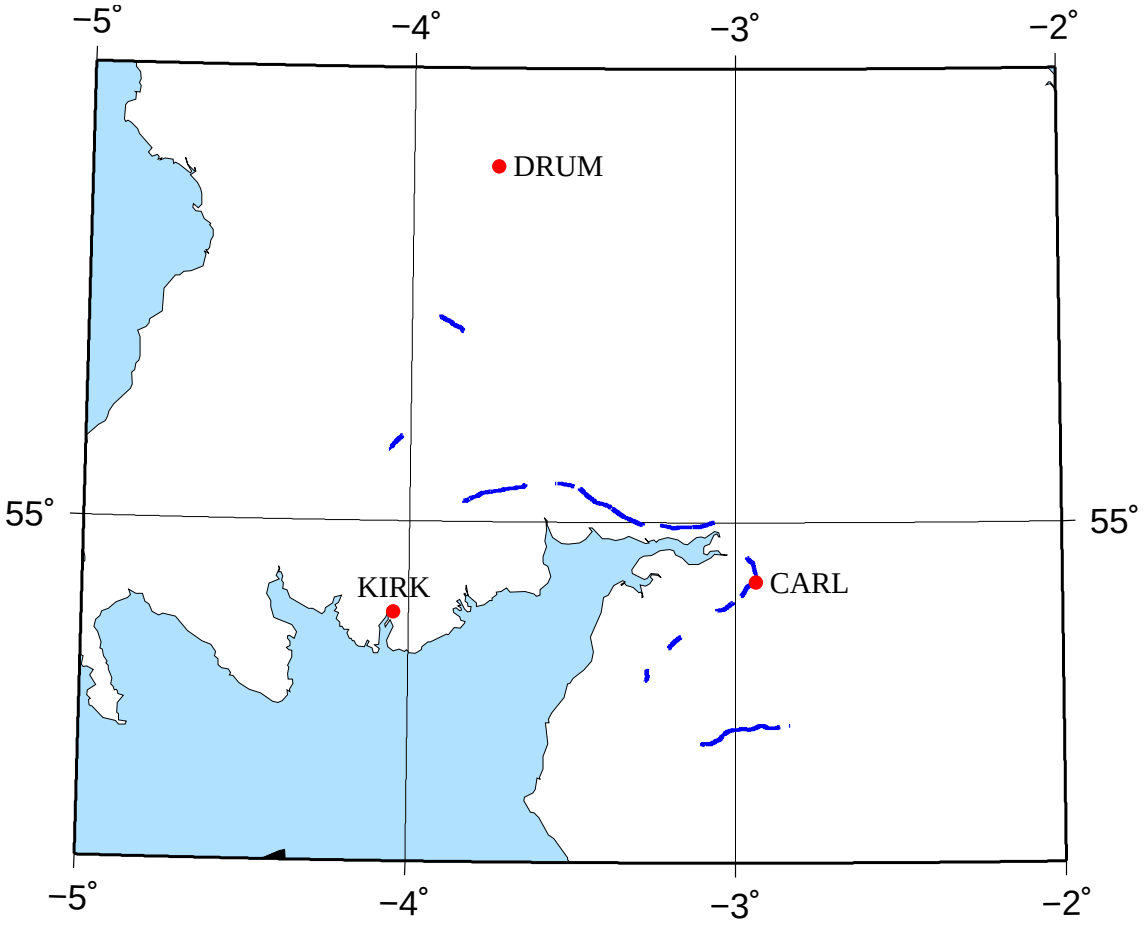

Figure 7.16: Sections of pickup truck route processed successfully using *Track*, and locations of the base stations used in generating the reference coordinates

This dataset demonstrates the challenges involved in gathering a kinematic dataset over a large land area in the densely populated United Kingdom. Where the route is not confined to private land, and road travel is required, there are inherently a large number of obstacles to the side and above the road, in particular where transport routes converge (major roads, minor roads and railways). Additionally, in Northwest England, trees and hedgerows are commonly found along the side of roads bordering

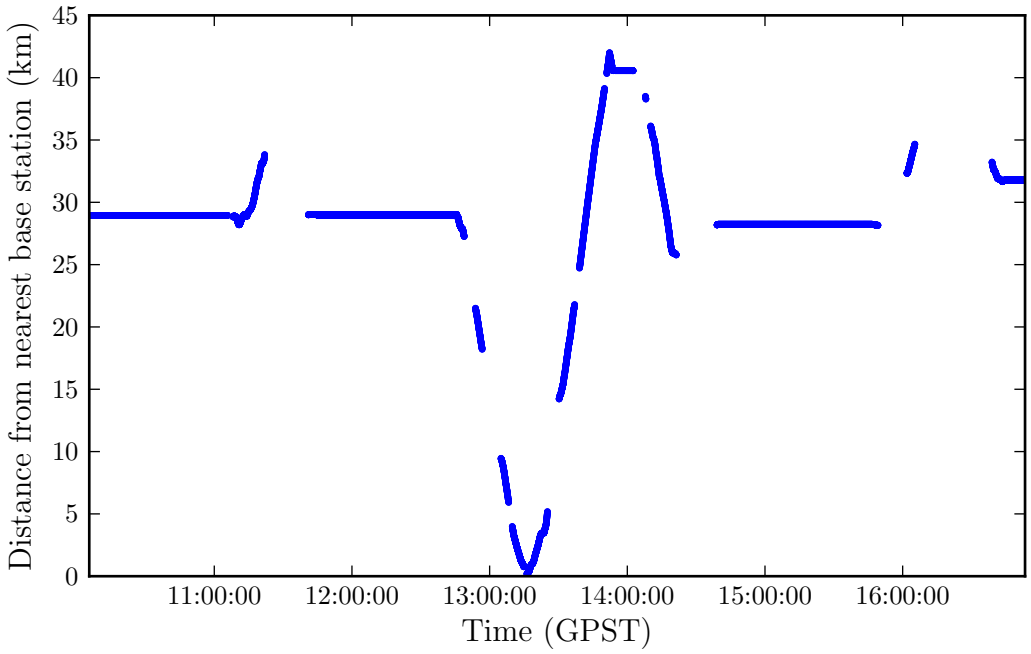

Figure 7.17: Distance of the pickup truck from the nearest base station

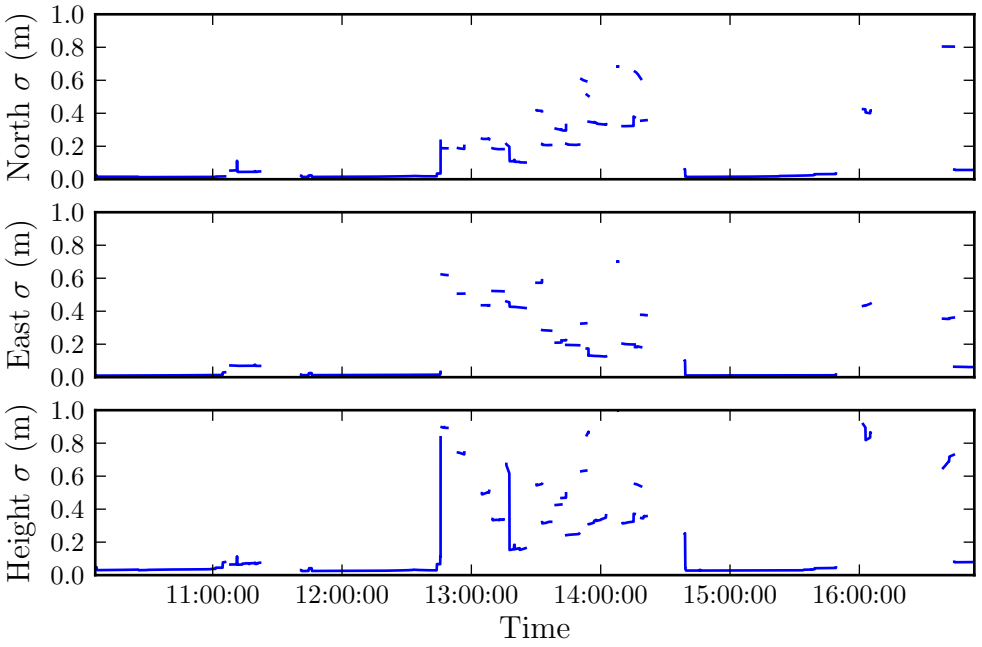

Figure 7.18: Pickup truck test *Track*-estimated reference coordinate uncertainty

fields.

The pickup truck data was processed with *pppncl* twice, once using only GPS observations, and once using both GPS and GLONASS observations. The following processing strategy was used:

- ESA final orbits tabulated at 15 min intervals,
- ESA high rate final clock corrections tabulated at 5 s intervals,
- 10° elevation cutoff,
- The following were estimated at each epoch:
  - three position components,
  - a correction to the wet zenith tropospheric delay,
  - a receiver clock offset,
  - a GLONASS specific receiver bias,
  - and the LC carrier phase ambiguities, one for each satellite.
- Observation data was processed in real-time mode.

The estimated position solutions were then differenced from the reference solution to produce a time series.

As for the reference solution, the PPP solution also struggled to converge (Figures 7.19 and 7.20) due to the repeated complete loss of lock which forced reinitialisation of the carrier phase ambiguity estimates. The only periods where continuous satellite tracking was possible coincided with periods when the vehicle was stationary.

As shown in Figure 7.19, during the three periods from 10:00–11:00, 11:45–12:40 and 14:30–15:45, when the vehicle was stationary, the PPP solution converges towards the reference solution. In the remaining periods, the receiver did not maintain lock on the satellites for long enough for the carrier phase ambiguities to be sufficiently well determined in the Kalman filter for accurate positioning. Figure 7.18 shows that the accuracy of the reference solution obtained in this period was worse than 40 cm, so is anyway not useful as truth coordinates.

After the receiver resumes tracking satellites after loss of lock, *pppncl* attempts to determine the introduced cycle slip in the carrier phase observations in order to avoid

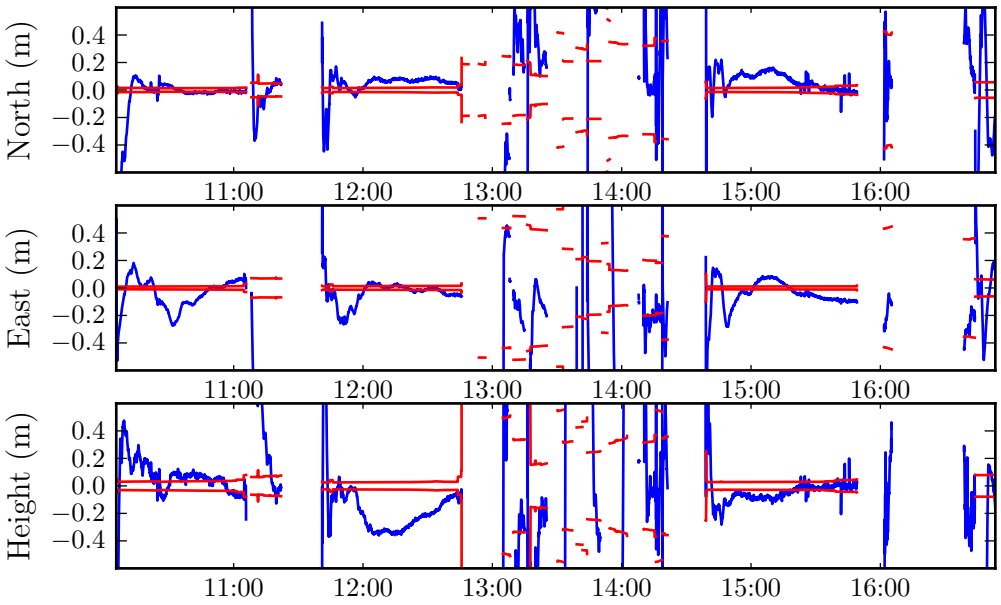

Figure 7.19: Difference between GPS PPP and reference coordinates during pickup test. The blue line shows the coordinate difference and the red lines mark the one sigma uncertainty of the reference solution.

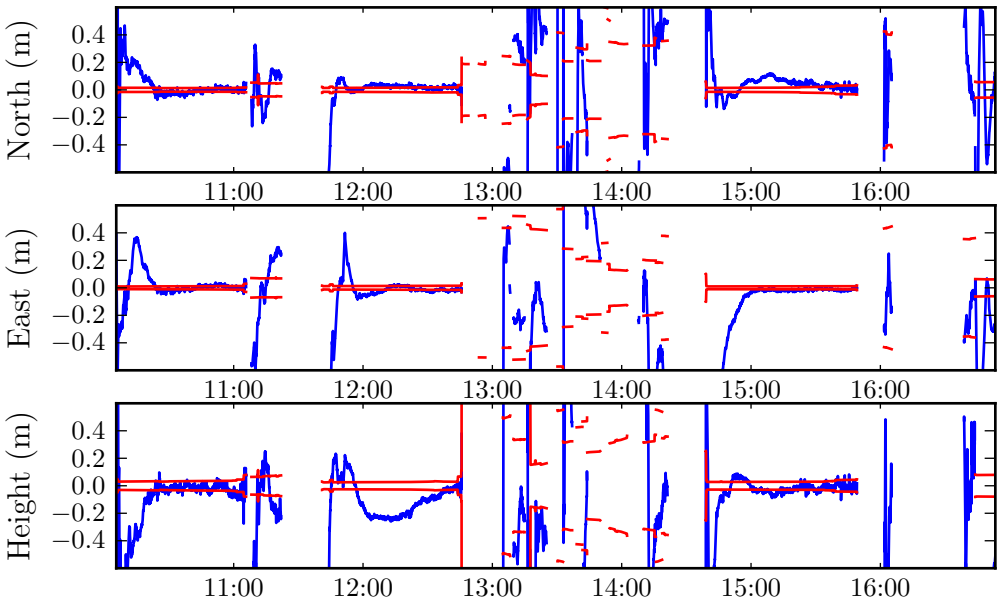

Figure 7.20: Difference between GPS/GLONASS PPP and reference coordinates during pickup test. The blue line shows the coordinate difference and the red lines mark the one sigma uncertainty of the reference solution.

reinitialising the estimates of the carrier phase ambiguities. If there has been total loss of lock, the cycle slip fixing method relies on the code observations to determine the discontinuity in the carrier phases. In many cases, cycle slip fixing is not possible after the complete loss of lock due to the low accuracy of the pseudorange during the initial period after the receiver resumes tracking of the satellites. This can be seen in the Melbourne-Wübbena combination of code and carrier phase (Equation 4.52) which, being invariant of the receiver satellite geometry, only contains the wide-lane carrier phase ambiguity and any measurement noise in the signals. Excluding the measurement noise, the Melbourne-Wübbena combination should be constant. The high variability seen during epochs 10–30 in Figure 7.21, with the nominally constant wide-lane bias changing by approximately 1.6 m, shows the poor accuracy of the code and carrier tracking. This is visible in the Melbourne-Wübbena combination for GPS satellite 2 after the receiver resumes tracking the satellite following total loss of lock.

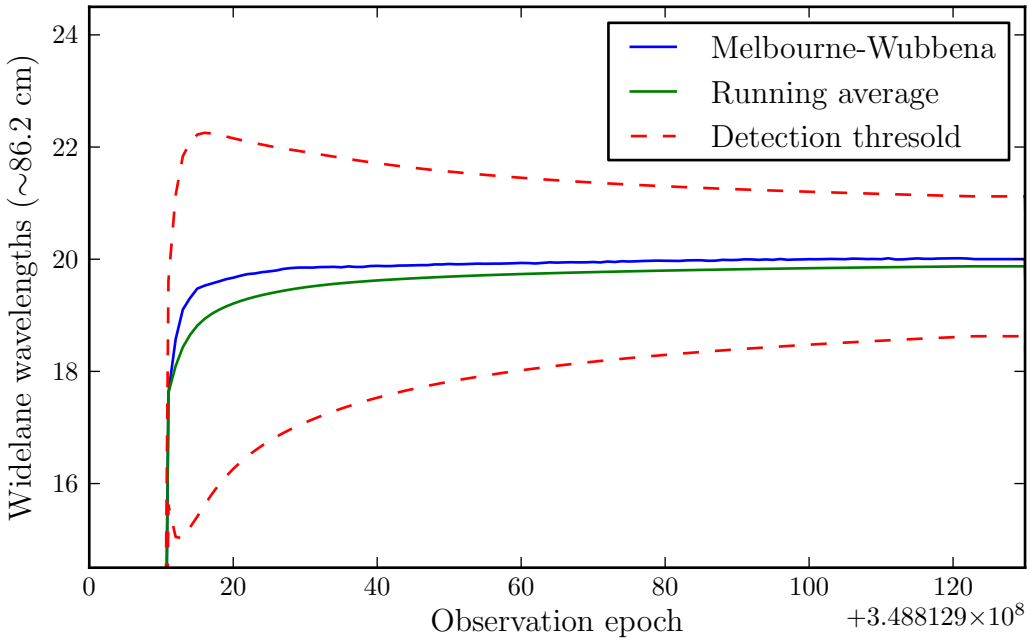

Figure 7.21: The Melbourne-Wübbena combination of code and carrier phase for GPS satellite 2 following a cycle slip. A two wavelength drift, corresponding to an approximate 1.6 m change, in the wide-lane bias is seen in the first 20 epochs after the cycle slip. The red dashed lines show the threshold outside which a cycle slip would be detected.

If the ambiguities have to be continuously reinitialised, the resulting positioning accuracy drops to that of code only positioning whilst they are re-estimated. This, combined with the poor quality of the reference solution, explains the low accuracy

of *pppncl* during the period 13:00-14:30. This dataset highlights the importance of a short convergence time in challenging environments where loss of lock is common.

A qualitative comparison of the GPS/GLONASS solution (Figure 7.20) with the GPS only solution (Figure 7.19) shows that although the position calculated is not very stable, whilst the vehicle is stationary, the GPS/GLONASS solution converges faster to the reference solution for the North and East components, than the GPS only solution. The improvement seen for the Height component with the GPS/GLONASS solution is less significant.

An attempt was made to process this dataset via alternative PPP programs using the PPP Software Centre (Banville et al., 2009). This was unsuccessful with none of the online PPP services returning a solution, reinforcing that the issue seen with this case study was the poor quality of data rather than the implementation of the PPP method in *pppncl*.

7.5.2 *Offshore survey vessel, Norway*

This test involved a comparison of GPS and GPS/GLONASS PPP methods to position in an offshore environment. Veripos provided observation data from a Topcon receiver onboard a commercial surveying ship during operations between Svalbard and North Norway, from 12 June 2010 to 17 June 2010, day of year 163 to 168. The route taken is shown in Figure 7.22. Unfortunately, normally Veripos only archive data which is reported as problematic by users, for use in improving their products. This means there is little choice in the datasets available and in this case the location is not ideal with regard to the long baseline lengths required in producing a reference coordinate solution.

The provided dataset contains observations recorded at 1 Hz. The only nearby reference station which archives data at a rate of 1 Hz or higher is NYA2 in Svalbard. There are no other stations in the region providing data at the required 1 Hz rate (NYA1 in Svalbard, TRO1 in Tromso, Norway and VAR2 in Northeast Norway all archive data at 30 s observation intervals).

NYA2 is a proposed IGS site, and therefore has high quality monumentation; it can thus be assumed that the receiver and installation are suitable for use as a reference station. However, as can be seen from Figure 7.23 the ship's route ranged from between 70 kilometres to over 1000 kilometres from the base station. This is a considerably larger distance than the ∼10 kilometres for which the single baseline

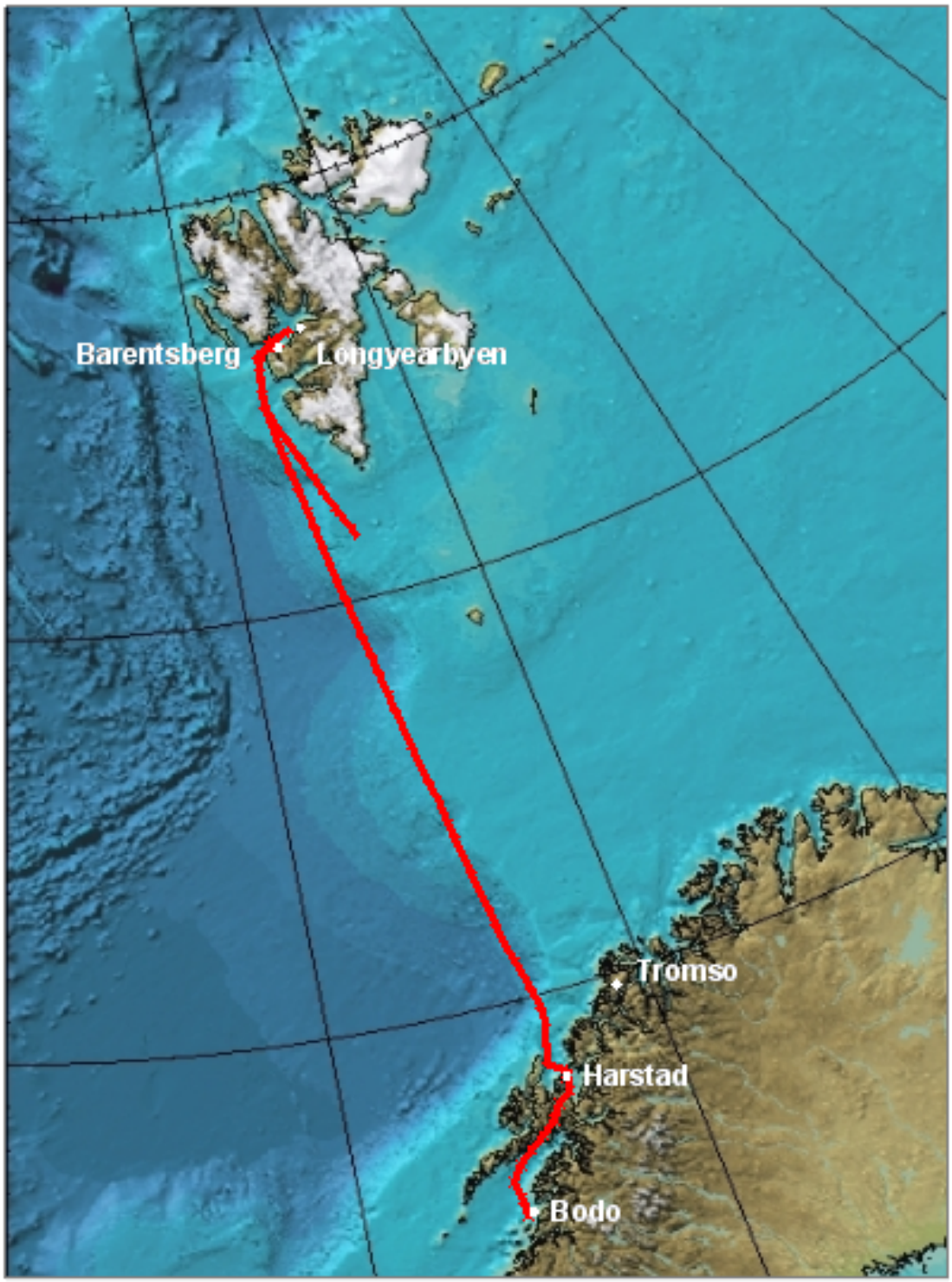

Figure 7.22: Route of the commercial survey vessel between Svalbard and North Norway

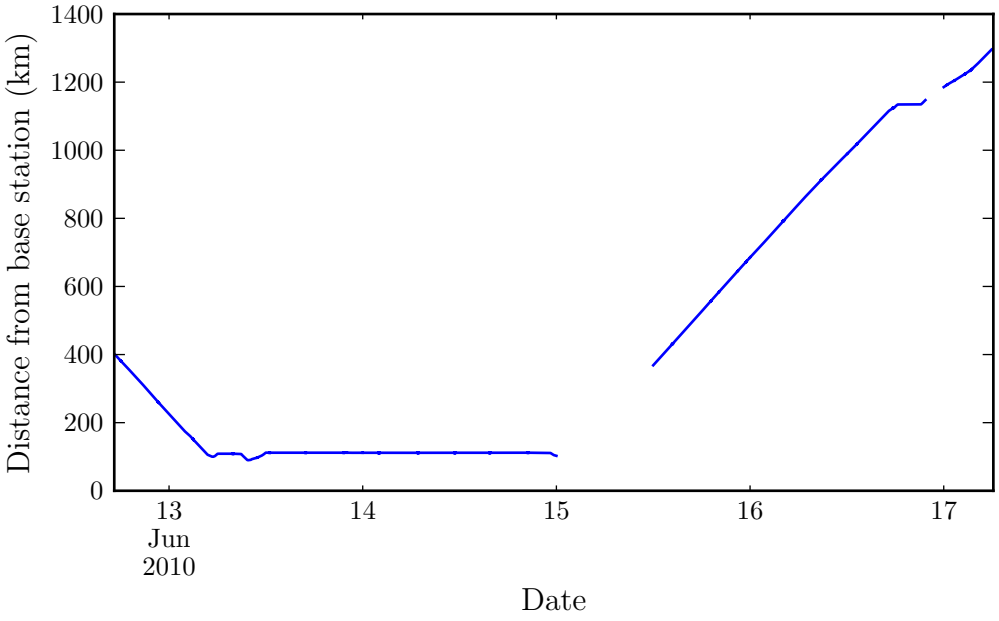

Figure 7.23: Distance of survey vessel from GPS reference station NYA2

relative carrier phase positioning would be expected to provide high quality results. However, given the remote location, and the limited sea based datasets available, this non ideal base station was used to generate the reference solution to allow some comparison to be made.

Precise coordinates for NYA2 are not available, however it is only 167 m North West of the IGS station NYA1. A precise weekly coordinate solution is available for NYA1 from ESA in the same, ITRF2005, reference frame as the ESA orbit and clock solutions to be used in the PPP positioning. Using *Track* in short baseline static mode, NYA2 was positioned relative to NYA1, providing coordinates for NYA2 given in Table 7.5. Due to the short base line, the L1 and L2 carrier phase observations could be used directly resulting in formal errors of less than a millimetre for the estimated NYA1-NYA2 baseline. The coordinate uncertainty for NYA2 was calculated using variance propagation of the combined uncertainty in the coordinates of NYA1 and the baseline uncertainty. The resulting estimated coordinates for NYA2 have 1 mm formal errors in the North and East directions.

A reference solution was created using *Track* with NYA2 as the reference station using the previously estimated coordinates. The achieved accuracy of the reference solution is shown in Figure 7.24. The average formal error of the reference solution

	NYA1		NYA2	
Coordinate	Position (m)	σ (mm)	Position (m)	σ (mm)
x	1202433.7652	1.2	1202379.4810	1.3
y	252632.3309	1.1	252474.5700	1.2
z	6237772.6440	5.2	6237786.3375	5.4

Table 7.5: Reference station coordinates used in Norway test. For NYA1 these are the ESA weekly coordinate solution for GPS week 1588. For NYA2 the coordinates are the result of a static baseline estimation relative to NYA1 using *Track*

is 2 cm to 3 cm in the North and East components, and 5 cm to 10 cm in the Height component. There are several clear spikes of reduced accuracy: these periods are not used in the comparison that follows. It was not possible to process the 12 h period starting at 00:00 on 15 June 2010 with *Track*. Either a problem with the data or a bug in *Track* caused the program to crash meaning there are no reference coordinates for this period.

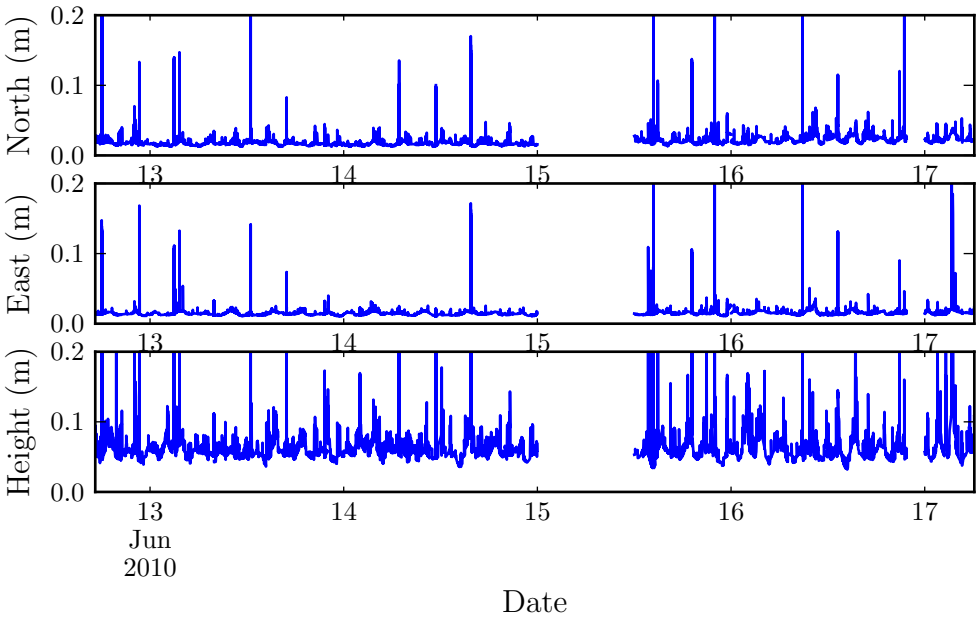

Figure 7.24: Formal errors of the *Track* estimated reference coordinates for the Norway survey vessel

The entire five day period was processed using *pppncl* in one continuous session. ESA final orbit and clock products were used due to the availability of precise GLONASS satellite clock corrections. The orbit and clock products for the observation period were concatenated to provide one file of continuous corrections. The

following processing strategy was used:

- Estimated parameters at each epoch were: three position components, a correction to the wet zenith tropospheric delay, a receiver clock offset, and the carrier phase ambiguities
- ESA final orbits tabulated at 15 min intervals
- ESA high rate final GNSS clock corrections tabulated at 30 s intervals
- 10° elevation cutoff
- Observation data was processed in real-time mode
- Processed once using only GPS and again with GPS and GLONASS

The resulting position solutions were then differenced from the reference solution coordinates to produce a time series for both GPS and GPS/GLONASS PPP.

Figures 7.25 and 7.26 show the coordinate errors in the North, East and Height components with respect to the reference solution for GPS PPP and GPS/GLONASS PPP solutions respectively. In both solutions, for GPS and GPS/GLONASS combined, the period from 16 June 2010 shows considerably worse accuracy with respect to the reference coordinates than the initial period from 13 to 15 June 2010.

Looking at the distance of the ship from the base station during the period considered (Figure 7.23), it is clear that the apparent period of poor accuracy from 16 June correlates with the period when the ship was a long distance from the base station. Despite the consistency of the formal errors for the reference coordinates reported by *Track* (Figure 7.24), it would seem that the true accuracy of the reference coordinates visibly deteriorates, as would be expected over such long base line lengths (greater than 500 kilometres). Therefore to ensure sufficient accuracy of the reference solution, the following analysis is restricted to the period during which the ship was less than 110 kilometres from the reference station. This resulted in approximately two days from the overall dataset, for which usable reference coordinates can be used to make a comparison of GPS versus GPS/GLONASS PPP positioning.

Figures 7.27 and 7.28 show the GPS PPP and GPS/GLONASS PPP solutions respectively by comparison with the reference solution, for the period 05:00 13 June to 24:00 14 June with reliable reference coordinates. Immediately obvious is the large discontinuity at 10:00 on 13 June 2010 in the GPS solution which is absent in the

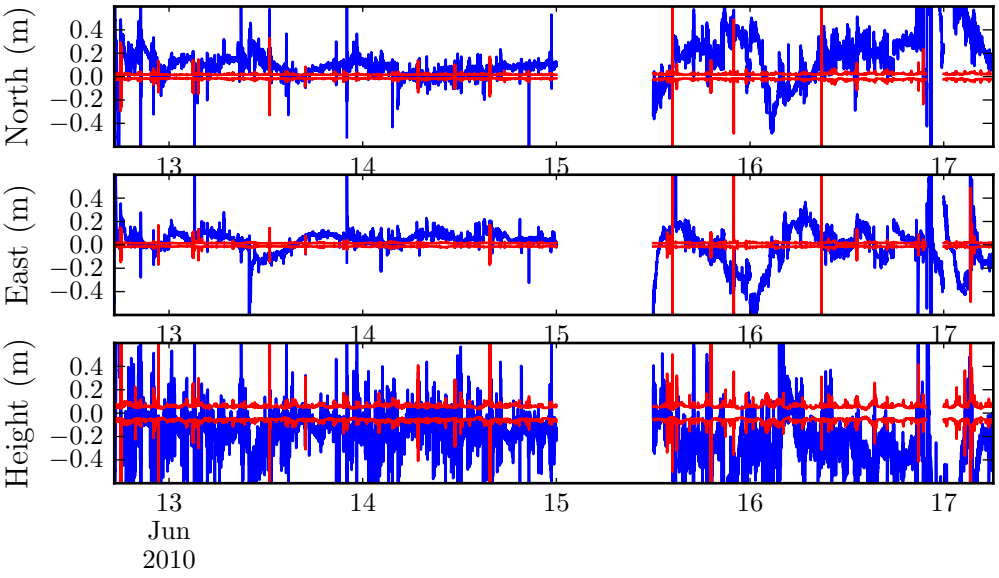

Figure 7.25: Difference between the GPS PPP coordinates and the reference coordinates, for the offshore survey vessel. Red lines show the one sigma uncertainty in the reference solution.

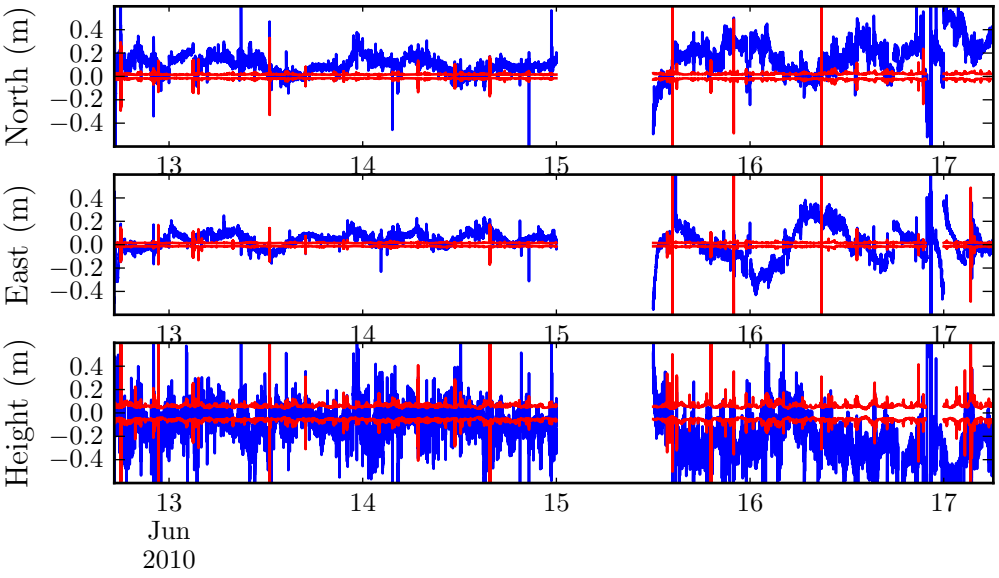

Figure 7.26: Difference between the GPS/GLONASS PPP coordinates and the reference coordinates, for the offshore survey vessel. Red lines show the one sigma uncertainty in the reference solution.

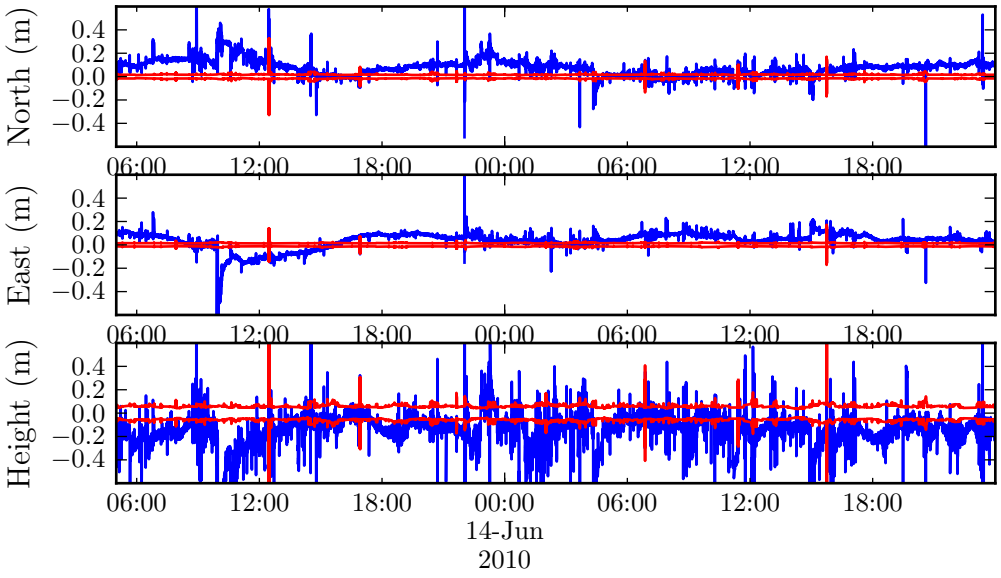

Figure 7.27: Difference between the GPS PPP coordinates and the reference coordinates, for the offshore survey vessel when less than 110 km from the base station.

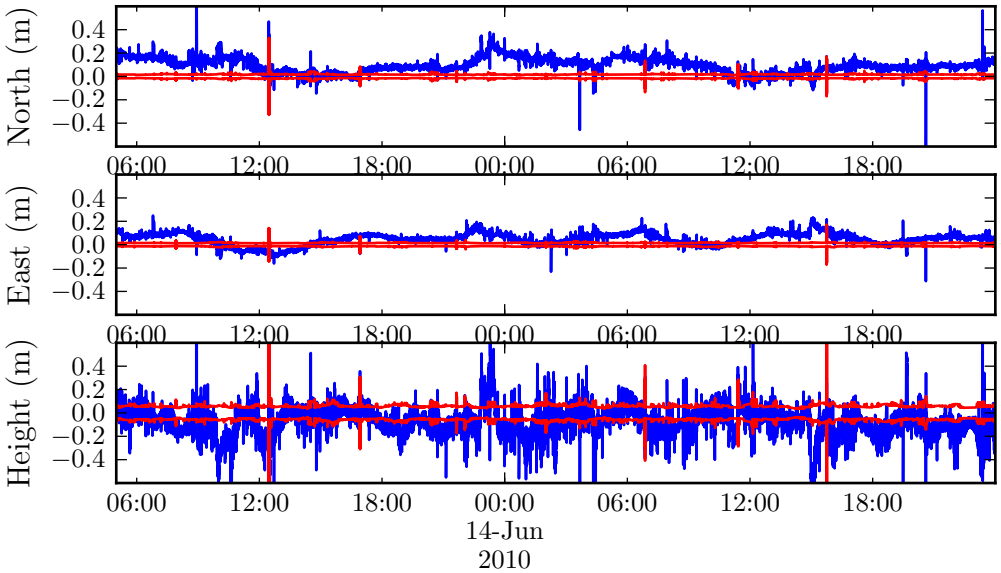

Figure 7.28: Difference between the GPS/GLONASS PPP coordinates and the reference coordinates, for the offshore survey vessel when less than 110 km from the base station.

	GPS	GPS/GLONASS
North	6.7	6.3
East	6.8	4.8
Height	18.1	12.9

Table 7.6: Standard deviations (cm) of the *pppncl* coordinate differences with respect to the *Track* reference coordinates whilst the survey vessel was less than 110 km from the base station.

GPS/GLONASS solution for the same period. This indicates that the additional GLONASS satellites help to make the positioning method more robust. Additionally, there are a number of jumps seen in the North and East GPS solutions which are not present in the more robust GPS/GLONASS solution. These events are very short (one to two epochs), and indicative of bad data below the MDB having a larger impact on the estimated position in the GPS solution.

The reported formal errors in the Height component of the reference coordinates are 5 cm to 15 cm (Figure 7.24). This leads to apparently noisy PPP Height solutions, and as such the difference between GPS and GPS/GLONASS PPP is less apparent. Table 7.6 shows the standard deviations of the coordinate differences with respect to the reference coordinates of the two solutions. There is a clear improvement with the addition of GLONASS in the East and Height components. One of the major factors in this reduction is the difference between the two solutions at 10:00 13 June. In the GPS only *pppncl* solution there is a clear discontinuity at this time, followed by a period of re-convergence that, in the case of the Height component, lasts approximately 1 h. The GPS/GLONASS solution maintains enough continuous observations over this period to avoid reinitialisation, highlighting the increased reliability of the dual system solution.

The accuracy of a kinematic double differencing solution is generally specified as 1–2 cm plus 1 part per million of baseline length (Wang et al., 2010). Therefore in this case, with a more realistic estimation of the reference solution uncertainty of 10 cm, it is not possible to confirm how much of this PPP noise is due to error in the PPP solution, and how much is due to the long baseline length affecting the reference coordinates.

Comparing the Height component of the GPS and GPS/GLONASS PPP solutions (Figure 7.29) shows the addition of the extra GLONASS observations has a measurable effect on the coordinates. The RMS of the difference over the whole period is 26 cm. Referring to the difference with respect to the base station (Figures 7.25

and 7.26) it appears that metre level difference between the two PPP solutions is down to errors in the GPS only solution. However as the accuracy of the reference coordinates is so low during this period this is not a conclusive finding.

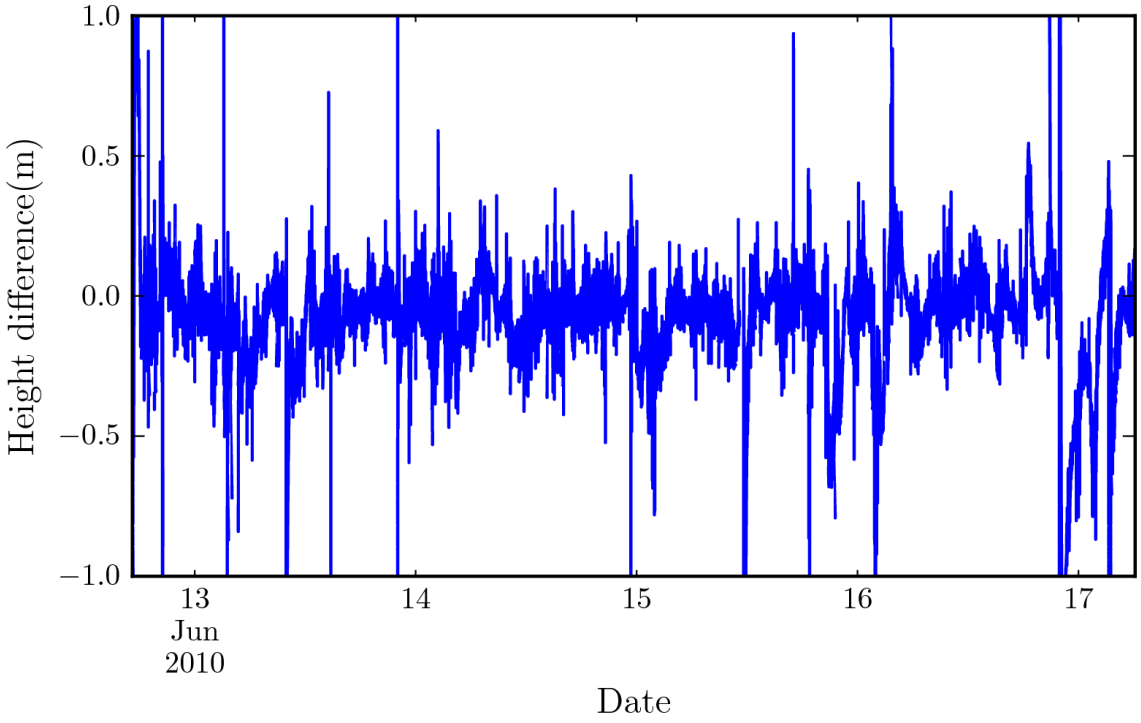

Figure 7.29: Difference between GPS and GPS/GLONASS PPP height solutions

As well as the assessment of the impact of GLONASS in addition to GPS using *pppncl*, a comparison of the *pppncl* solution was made with the solution provided by Veripos, produced using the commercially available Veripos Ultra GPS PPP service. Veripos Ultra is a real-time PPP service that uses real-time GPS only orbit and clock products transmitted via communications satellite. In contrast, the *pppncl* solution was generated using ESA Final orbit and clock products which are of higher accuracy, and therefore are expected to provide a more accurate set of coordinates as seen in Section 7.3.

Figure 7.30 shows the height of the GPS/GLONASS *pppncl* PPP solution compared with the Veripos Ultra solution. For much of the central part of the dataset, from approximately midday 13 June to midday 15 June, the Veripos solution is using broadcast orbit and clock corrections. This was due to the high latitude of the vessel which prevented the Veripos Ultra orbit and clock corrections being received from the communications satellite. Unfortunately this period, for which the Ultra orbit corrections were unavailable, coincides with the only usable part of the reference solution (05:00 13 June to 24:00 14 June as mentioned earlier). Therefore with

this dataset it is not possible to make a quantitative comparison of the *pppncl* and Veripos Ultra solutions, as the true coordinates are not known.

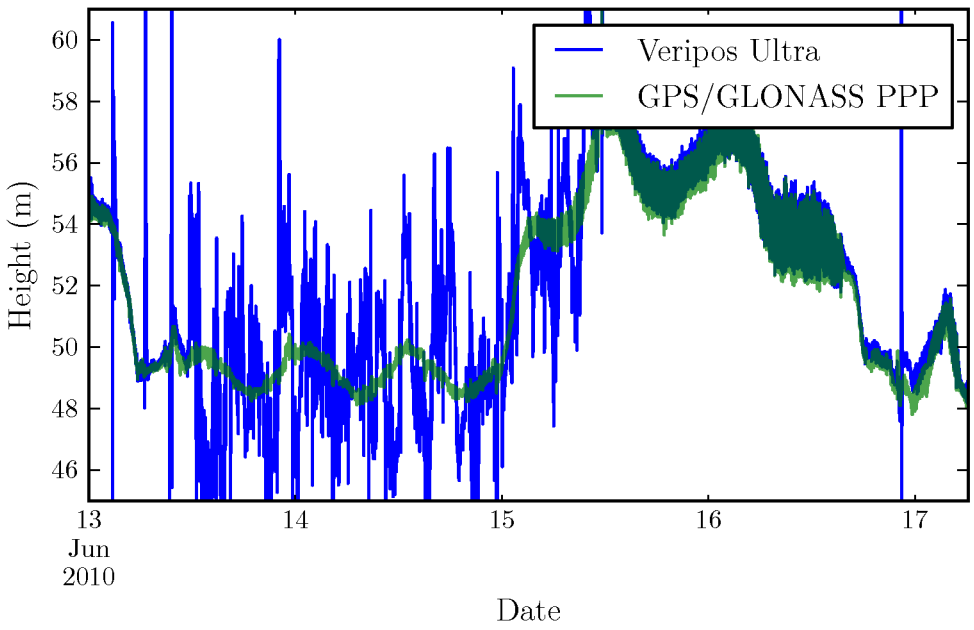

Figure 7.30: GPS/GLONASS PPP and Veripos Ultra real-time Height solutions compared

Looking at Figure 7.30 for the period 15 to 16 June, what appears as 2 m level noise reflects the real height change as the ship moves over the waves. Towards the end of 16 June there is a spike in the Veripos Ultra Height solution followed by a clear discontinuity. This feature is highly unlikely to be correct given the ship is floating on the sea. The *pppncl* GPS/GLONASS solution does not show this discontinuity, but the extent to which this is an improvement over the Veripos Ultra solution unfortunately cannot be determined. With the absence of a high quality reference solution there is little more that can be drawn from comparing these two datasets.

7.5.3 *Inshore survey vessel on the River Tyne*

This test involved comparison of GPS and GPS/GLONASS PPP methods to position a moving vessel in an inshore sea environment. A Leica GS10 receiver with an AS10 antenna was mounted on the foredeck of the Port of Tyne vessel, Lynceus, during underwater surveying operations in the mouth of the River Tyne, North East England. The River Tyne has high ground surrounding it, and is a working port with large ships and oil rigs moored in the river, or transiting through. The land

shape combined with other shipping can potentially lead to a noisy environment from a data collection point of view.

Data was collected during 24 March 2011, from 09:12 until 14:50 (GPS time), including a 10 min gap in data recording at 11:30 (GPS time) due to unplanned receiver shutdown. During this period the boat made several trips up and down the river and performed a detailed survey of the river entrance; the ground track followed is shown in Figure 7.31. The boat was always less than 2.5 km from the base station used (Figure 7.32); this is within the range over which a double differencing carrier phase solution using one base station would be expected to provide centimetre accurate coordinates.

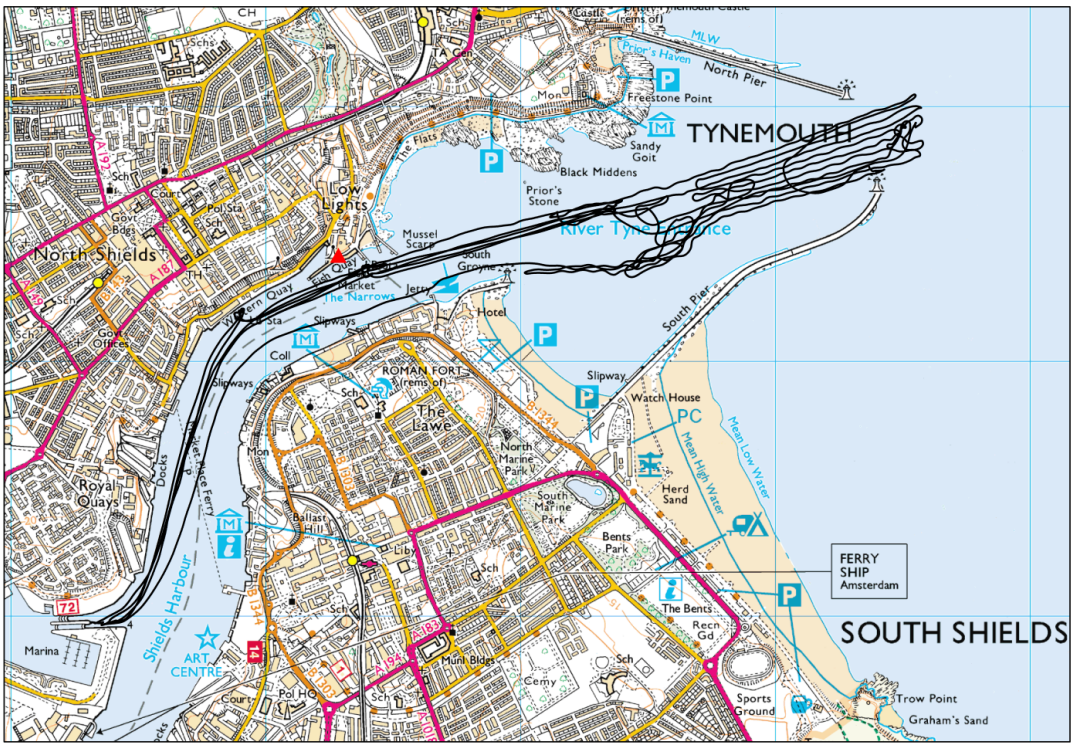

Contains Ordnance Survey data © Crown copyright and database right 2012.

Figure 7.31: Ground track of the survey vessel Lynceus. The red triangle marks the location of the GNSS site NSLG used as a base station

In order to generate a reference solution, double differencing with respect to the static GPS site NSLG was performed using *Track*. NSLG is a nearby base station installed as part of a tide gauge monitoring program.

The ITRF2005 coordinates of the reference station NSLG were estimated relative to the IGS station MORP. Using the IGS weekly coordinates for MORP to provide access to the ITRF2005 reference frame, a static baseline GPS solution performed with

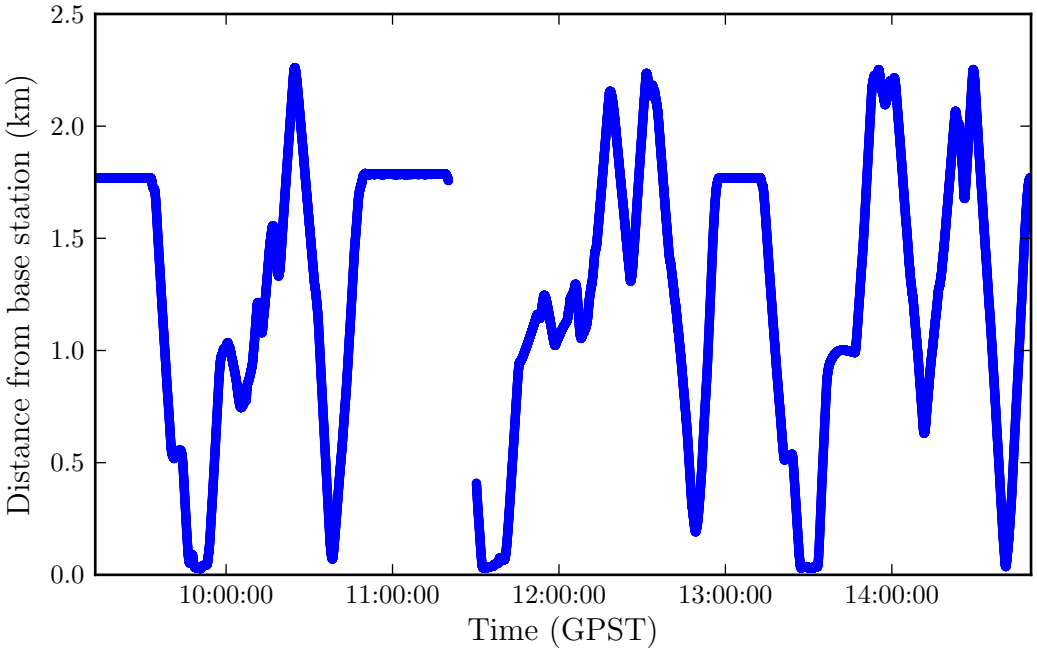

Figure 7.32: Distance of the survey vessel Lynceus from the base station NSLG

Track was used to estimate the coordinates of NSLG. Table 7.7 gives the coordinates used for MORP and the estimated coordinates of NSLG. The one sigma uncertainty for the NSLG coordinates was obtained by the method of variance propagation.

	MORP		NSLG	
Coordinate	Position (m)	σ (mm)	Position (m)	σ (mm)
x	3645667.762	4.1	3664667.331	4.2
y	-107277.138	1.5	-91646.772	1.6
z	5215053.596	4.8	5201998.175	4.9

Table 7.7: Coordinates and uncertainties of reference stations used for Tyne vessel reference solution

The reference solution was generated using:

- ESA final orbit and clock products,
- The LC linear combination of L1 and L2,
- 10° elevation cutoff,
- Absolute antenna phase centre offsets.

Apart from two short satellite arcs (one at the start and the other at the end, of

less than 40 s) all ambiguities were fixed to integer values. The formal errors of the coordinates produced by *Track* are shown in Figure 7.33. Both the North and East components have been estimated with reported formal errors of 1 cm to 2 cm, and the Height with 3 cm to 4 cm formal errors.

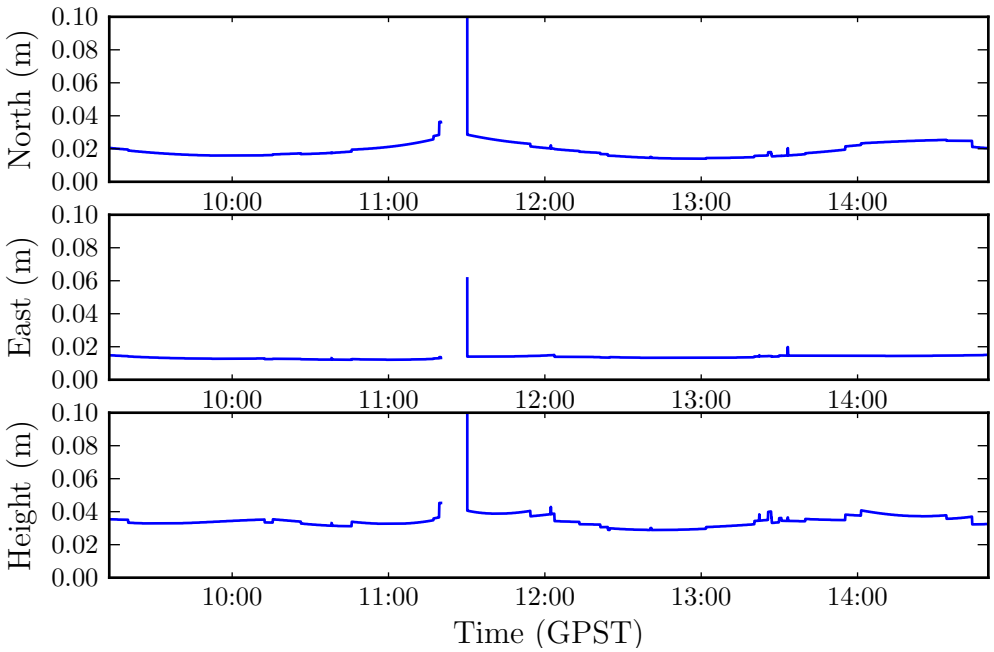

Figure 7.33: Tyne survey vessel *Track* reference coordinate formal errors

Again the data was processed using *pppncl*, once with only GPS observations and once with GPS/GLONASS observations combined. All other aspects of the PPP strategy for the two solutions were identical as follows:

- ESA final orbits tabulated at 15 min intervals,
- ESA high rate final clock corrections tabulated at 5 s intervals,
- 10° elevation cutoff,
- The following were estimated at each epoch:
  - three position components,
  - a correction to the wet zenith tropospheric delay,
  - a receiver clock offset,
  - an LC carrier phase ambiguity for each satellite.

- Observation data was processed in real-time mode.

The position solutions were then differenced from the reference solution to produce a time series of coordinate errors with respect to the reference solution.

Figure 7.34 shows the difference between the GPS only PPP estimated coordinates and the reference coordinates. It can be seen that although there is slow initial convergence, the GPS only PPP is capable of achieving coordinates accurate to within the uncertainty in the reference solution (1 cm to 2 cm in the North and East components, and 5 cm in the Height component). However, looking at both the initial period, and after the receiver reset at 11:30 (GPS time), the convergence time to the highest achieved accuracies is up to 90 min (Figure 7.36).

At 10:38 (GPS time) cycle slips are detected on 7 of the 10 visible GPS satellites due to the receiver losing lock on the GPS carrier phase for 10 s. After the receiver reestablished carrier phase tracking, the values of the cycle slips were not successfully identified and corrected for using the method described in Section 4.8.2. The affected satellites were GPS 17, 32, 31, 25, 13, 24 and 2.

After unsuccessful cycle slip fixing, the carrier phase ambiguities for these satellites are reset and then re-estimated in *pppncl*. This causes the reduction in accuracy visible in Figure 7.34 during the following 25 min period whilst the solution re-converges.

Figure 7.35 shows the difference between the GPS/GLONASS PPP estimated coordinates and the reference coordinates. Comparing Figures 7.34 and 7.35, it can be seen that there is a clear reduction in convergence time when GPS and GLONASS are combined. From Figures 7.36 and 7.37, it can be seen that the convergence time with GLONASS is reduced to approximately half an hour, one hour less than for the GPS only PPP. Here convergence is defined as the time until 2 cm RMS is achieved in the North and East components and 4 cm RMS is achieved in the Height component.

With the GPS/GLONASS combined observations, the issue seen in the GPS only observations at 10:38 due to cycle slips is not present, as there are no cycle slips on the GLONASS satellites at this time. This demonstrates the benefit of using GLONASS in addition to GPS to provide a more robust positioning solution.

The converged GPS/GLONASS coordinate estimation accuracy is comparable to the converged GPS only coordinate accuracy. This is consistent with the trend results presented in Section 7.3, that use of GLONASS combined with GPS does

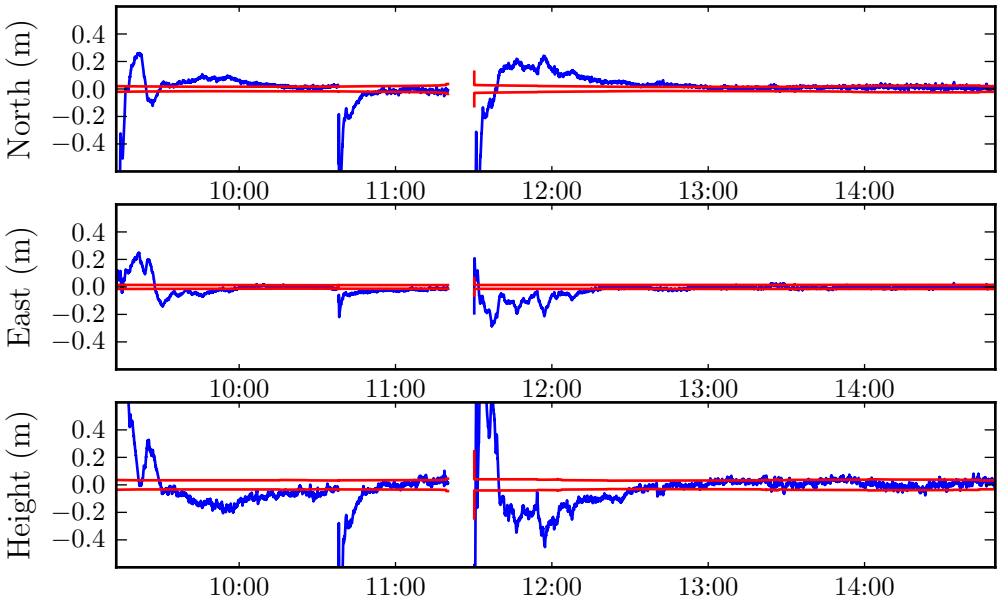

Figure 7.34: Difference between GPS PPP and reference coordinates for the Tyne survey vessel. Red lines mark the one sigma uncertainty in the reference solution.

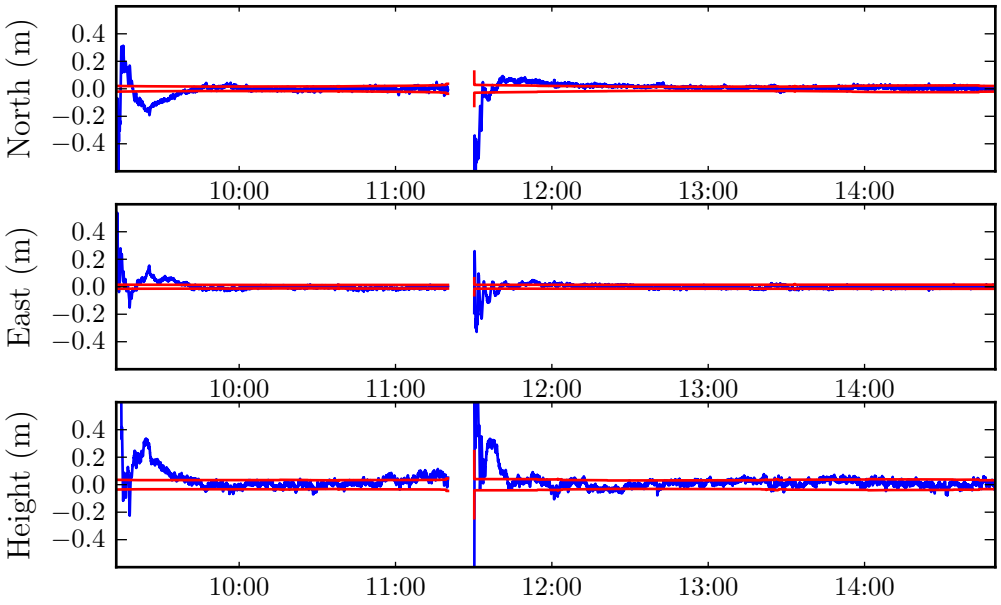

Figure 7.35: Difference between GPS/GLONASS PPP and reference coordinates for the Tyne survey vessel. Red lines mark the one sigma uncertainty in the reference solution.

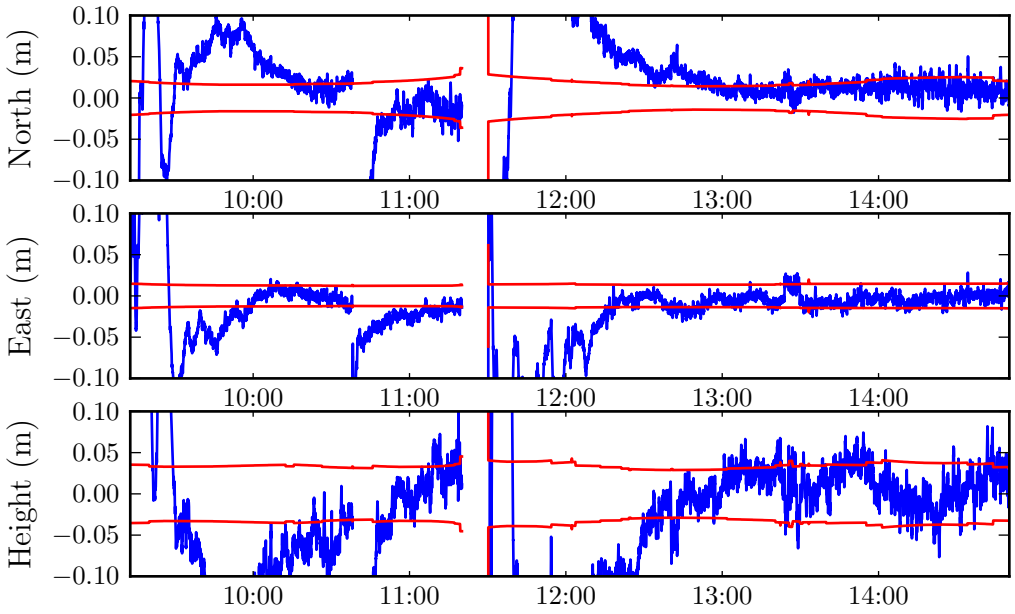

Figure 7.36: Large scale difference between GPS PPP and reference coordinates for the Tyne survey vessel. Red lines mark the one sigma uncertainty in the reference solution.

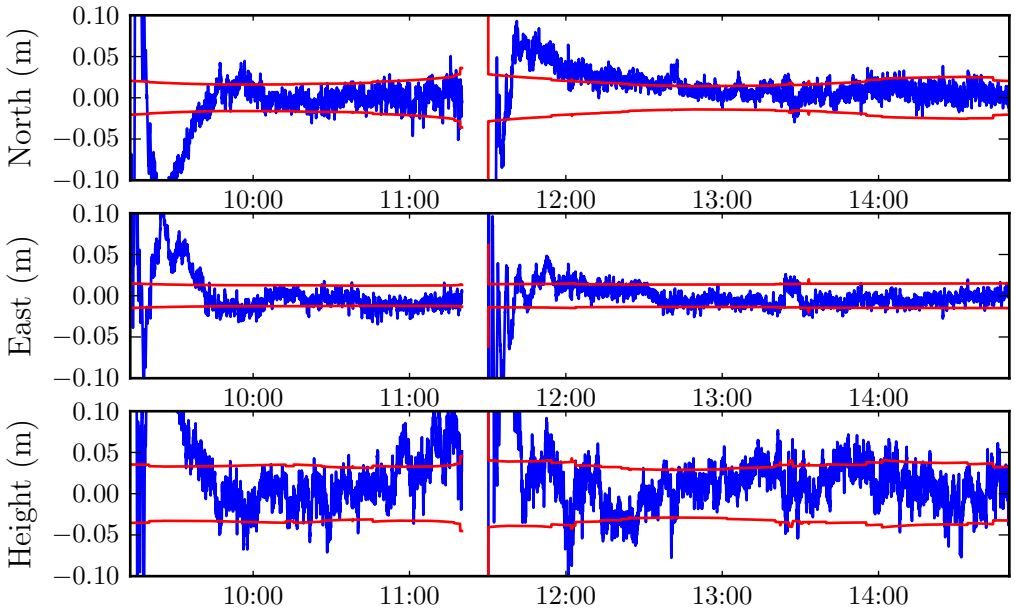

Figure 7.37: Large scale difference between GPS/GLONASS PPP and reference coordinates for the Tyne survey vessel. Red lines mark the one sigma uncertainty in the reference solution.

not bring higher ultimate accuracy than GPS only coordinate estimates, instead the benefit is faster convergence time and a more robust positioning solution.

Table 7.8 shows the overall RMS values for the full time period considered. The improvement in RMS seen is largely due to the improved convergence time of the GPS/GLONASS solution.

Method	North	East	Height	Horizontal	Total
GPS	14	6	32	15	35
GPS/GLONASS	8	3	25	9	26

Table 7.8: Tyne survey vessel PPP coordinate RMS with respect to the reference coordinates for the complete survey period. Units for all values are cm.

Considering the final 2 h period from 13:00 (GPS time) after both solutions have converged, there is little difference in the accuracy of the two solutions (Table 7.9).

The error in both the PPP solutions is comparable to the uncertainty in the double differencing reference coordinates so it is not possible to determine the underlying accuracy of the PPP solutions.

Method	North	East	Height	Horizontal	Total
GPS	1.4	0.8	2.6	1.7	3.0
GPS/GLONASS	1.1	0.9	2.6	1.4	2.9

Table 7.9: Tyne survey vessel converged PPP coordinate RMS with respect to the reference coordinates for the final 2 h. Units for all values are cm.

Figure 7.38 reinforces the above observations: the improvement brought about by the use of GLONASS in addition to GPS is seen primarily during the initial convergence period and in the case when there are problems with the cycle slips of GPS satellites. Secondly, after convergence, the accuracy achieved by GPS/GLONASS combined is comparable to that achieved by GPS only coordinate estimation.

To understand the difference in GPS/GLONASS combined and GPS only solutions, the cycle slip event at 10:38 (GPS time) was examined in more detail. After failure to repair the GPS carrier phase ambiguities, the carrier phase ambiguities are unknown, and so the carrier phase observations add no additional information to the coordinate estimate. In the GPS only estimate, the positioning immediately following such an event is dominated by the noise in the pseudoranges. This continues until sufficient observations have been made to estimate the carrier phase

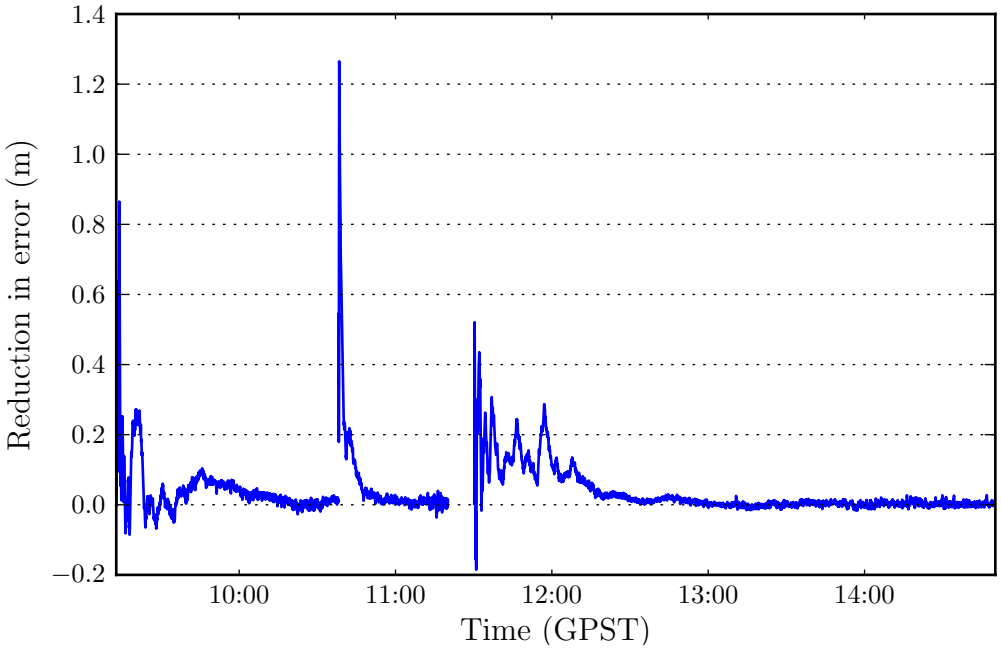

Figure 7.38: Reduction in horizontal error of the GPS/GLONASS PPP solution compared with the GPS only solution with respect to the reference coordinates

ambiguities with a high degree of confidence. Figure 7.39 shows the estimated value of carrier phase ambiguities varies by up to 2 m during this re-estimation period for the cycle slip event at 10:38 (GPS time). There is some curvature in the value of the estimated ambiguities; while this is happening the value of the carrier phase ambiguity is incorrect, leading to the reduced accuracy seen in Figure 7.36 and Figure 7.38.

With the eight additional GLONASS satellites visible in the GPS/GLONASS processing, the GLONASS carrier phase observations, with their well determined ambiguity estimates, provide precise observations allowing for accurate determination of the receiver coordinates. With the coordinates well defined, the initial estimates of the post cycle slip GPS carrier phase ambiguities in the Kalman filter are more accurate. This can be seen in the reduced variability in the GPS carrier phases after the cycle slip event (Figure 7.40). This is coupled with reduced *a posteriori* variance of the GPS carrier phase ambiguities. This causes the GPS carrier phase observations to carry more weight in the Kalman Gain matrix, thus contributing more to the following position estimates than in the GPS only case. These effects combined not only provide continuous high quality positioning solutions through such an event, but also create a system that rapidly returns to full accuracy.

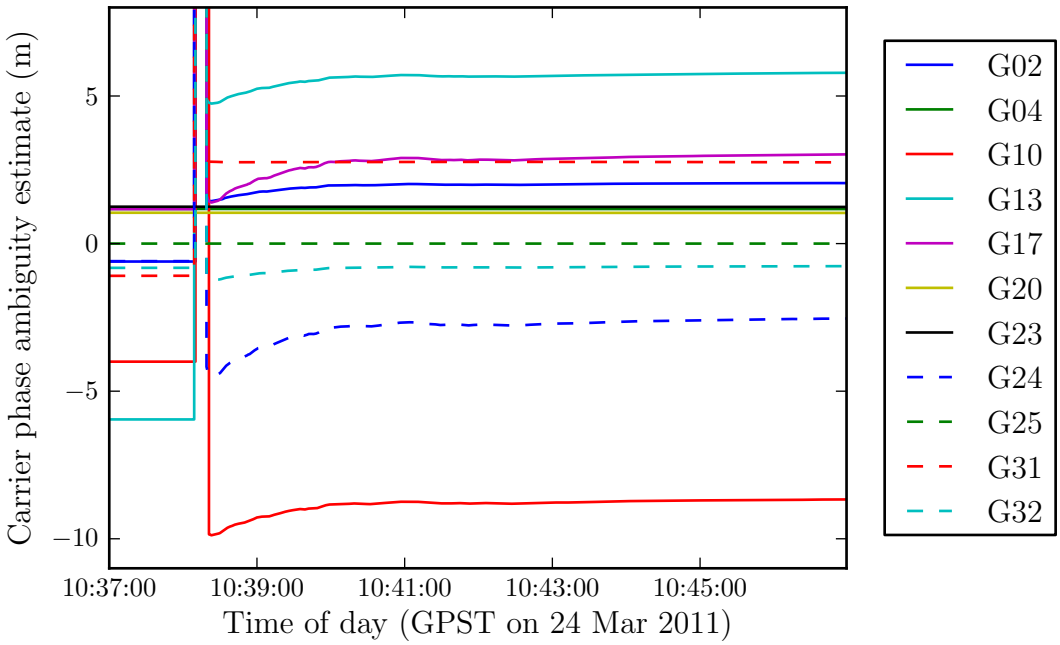

Figure 7.39: GPS carrier phase ambiguity estimates after a loss of lock event during GPS only PPP. The legend identifies the GPS satellites involved.

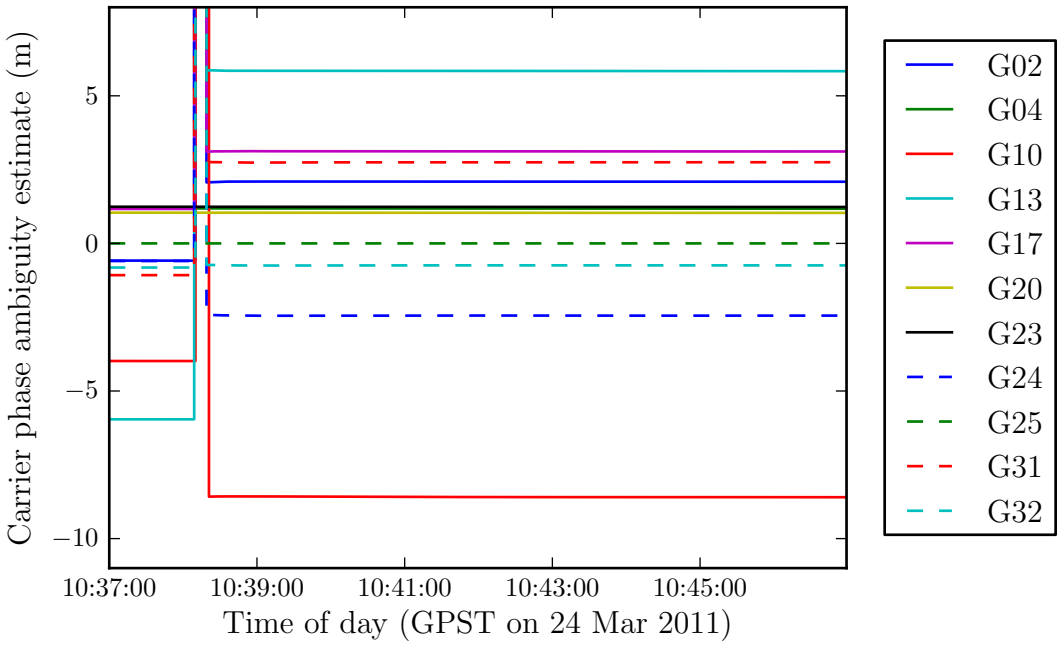

Figure 7.40: GPS carrier phase estimates after loss of lock event during combined GPS/GLONASS PPP. The legend identifies the GPS satellites involved.

A frequency analysis was made of the height component for the final 2 h converged period of this dataset as the GPS and GPS/GLONASS PPP solutions show quite different behaviour (Figures 7.36 and 7.37). The Lomb-Scargle periodogram (Scargle, 1982) in Figure 7.41 shows how the amplitude of the signal varies at different wavelengths. The peak at 600 s in the GPS solution is reduced in the GPS/GLONASS solution, however there is more power in the GPS/GLONASS solution at short wavelengths corresponding to high frequency noise. This high frequency noise is most likely due to either receiver measurement errors or high frequency noise in the GLONASS clocks.

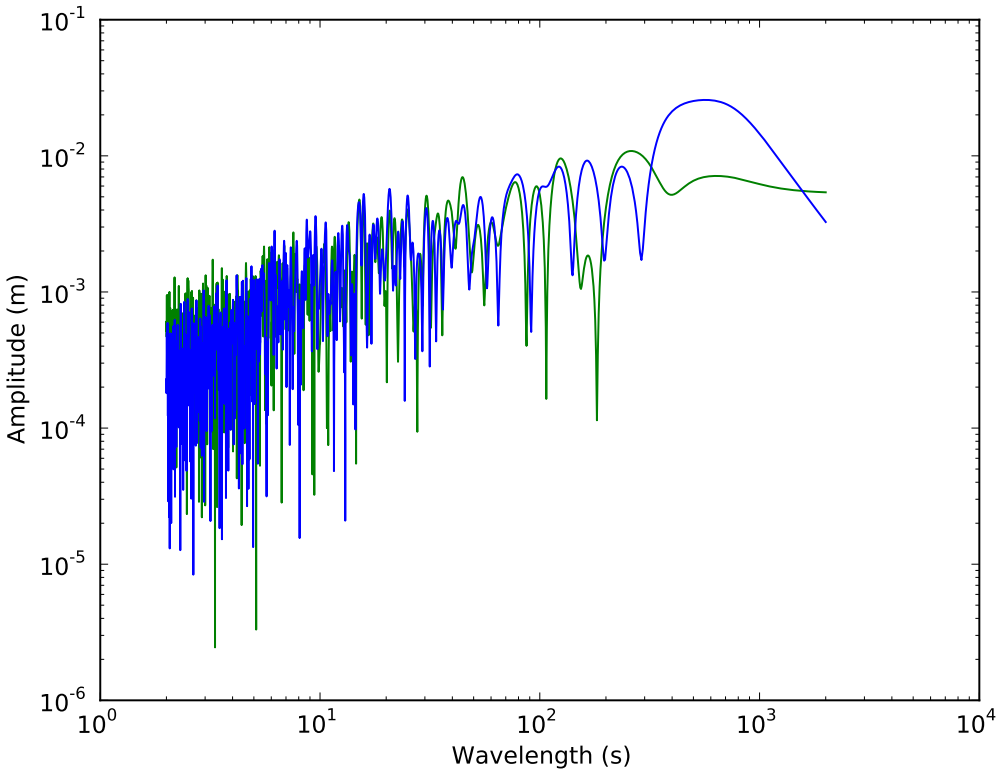

Figure 7.41: Frequency analysis of the height component timeseries for the final 2 h of the Tyne survey vessel dataset

7.6 Conclusion

The GLONASS measured carrier phase range residuals for GPS week 1605 were compared to the GPS carrier phase range residuals for the same period using static PPP at 87 IGS sites. Despite an apparent larger GLONASS RMS range residual at elevation angles lower than 40°, the mean difference in RMS range residuals

between GPS and GLONASS was not found to be statistically significantly ($p < 0.05$) different to zero. This is consistent with the results found by Hesselbarth and Wanninger (2008). A single elevation weighting function was fitted to the carrier phase range residuals and used in the subsequent comparison of GPS and GPS/GLONASS PPP. This result would benefit from a longer measurement time period, which would allow the seasonal effects of the residual unmodelled error sources to be evaluated.

Using a global distribution of sites, the convergence time to 10 cm RMS accuracy of GPS/GLONASS and GPS only PPP was compared at a range of observation lengths, and using three different orbit and clock products. Statistically significant ($p<0.05$) reductions in convergence time were measured due for GPS/GLONASS PPP compared to GPS only PPP using both the ESA Final orbits and clock products and the Veripos Apex products. The reduction in convergence time measured for GPS/GLONASS PPP compared with GPS only for static positioning with 30 s observation intervals was 17%, 47% and 37% for the North, East and Height components respectively using ESA Final orbit and clock products. When Veripos Apex G2 orbit and clock products were used, the improvement was 36%, 47% and 35% for the North, East and Height components respectively. This analysis confirms the potential of GLONASS observations in PPP in reducing the convergence time of PPP.

Previous studies have been inconclusive as to the benefit of the inclusion of GLONASS. Cai and Gao (2007) suggested that the lack of significant impact on positioning results found in their 2007 investigation was due to the incomplete GLONASS network of 12 satellites. Since then the GLONASS network has increased to 23 satellites; all the testing in this thesis has been done with this enlarged network. It would be possible to assess the impact of the number of satellites in combined networks on positioning accuracy. This could be done either by use of historical datasets gathered at stages during the development of the GLONASS network, or simulated by removal of specific satellites from the dataset. However, this simulated approach would not capture the effect of the improvement in the accuracy of the GLONASS orbit and clock products due to the enlarged network. In doing this investigation, an understanding may be gained as to what portion of a network needs to be included to see a significant improvement in positioning performance. This could predict when improved positioning would be obtained from the planned additional networks, for example, Galileo or BEIDOU.

In kinematic mode, the GPS/GLONASS PPP was shown to perform with the same

ultimate accuracy as GPS only PPP with a total position error RMS of 3 cm. A clear improvement is seen in the robustness of the GPS/GLONASS PPP coordinates resulting in reduced coordinate RMS errors over whole sessions. The additional GLONASS satellites can maintain centimetre accurate positioning in the presence of GPS only cycle slips. Whilst the inclusion of GLONASS satellites reduces the power of the outlier detection tests, the number and size of the jumps introduced by undetected outliers is reduced when GLONASS. Convergence time is seen to reduce with GLONASS by up to a factor of three, as in the case of the boat on the Tyne.

Analysis of the pickup truck showed the difficulty in obtaining a high quality dataset for a land based route in the United Kingdom. Although this may be representative of real world usage, with poor quality datasets, it was not possible to produce high quality reference coordinates and therefore it was hard to draw conclusions from the comparison made between any test solutions. An improvement in the convergence time was seen during the three periods whilst the pickup truck was stationary.

The testing in this chapter has reinforced how important it is to have a quality reference solution when comparing PPP performance. With hindsight, using carrier phase GPS as the reference solution limits the ability to perform the tests in remote locations, or in challenging environments such as obstructed sky-view or in the presence of high multi-path. In these situations, the GPS reference solution suffers from degraded accuracy due to reduced satellite numbers and multipath effects caused by the local environment that are not removed by the double differencing.

Positioning in the offshore environment is of commercial interest, however there can be problems with interference, as seen in the offshore survey vessel operating in Norwegian waters. Alternative methods could be used to provide a truth reference solution. One option is inertial navigation systems, however high accuracy units tend to be expensive. A low cost inertial navigation system integrated with a GPS receiver to control sensor drift would provide a potential solution for tests similar to the pickup truck test. This would fill in the gaps between the successful GPS fixes, providing continuity during GPS outages. Another option would be to perform the kinematic test on a guided route, for example a rail track, the location of which could be determined using traditional surveying techniques. A further option to determine the reference solution is laser ranging.

In assessing PPP, the advantage of using GPS is the shared antenna, avoiding any offset in sensors that would have to be accounted for in the other options proposed. A disadvantage of using relative carrier phase GPS as the reference solution is that it is

still influenced by multipath. This can produce both a biased GPS reference solution and biased PPP solution, as they can be biased by the same error; this potentially reduces the reported error. This potential correlation has not been accounted for in this thesis.

Chapter 8 Conclusion

8.1 Introduction

The research work contained in this thesis focused on investigating the impact of using GLONASS satellite observations in addition to GPS observations in PPP. In the offshore industry and work in other remote areas, there is a demand for shortened convergence times and improved robustness of positioning techniques. The investigation has been completed in several main parts:

1. Assessment of existing published knowledge relating to PPP techniques.
2. Creation of the program *pppncl*, using the starting point of *Track* to build a program to perform PPP, then validation in both static and kinematic modes.
3. Incorporation of GLONASS satellite data processing ability into *pppncl*, and comparison of coordinates obtained when GPS and GLONASS are used versus GPS only satellite data, across a range of static sites and transport modes (including inshore, offshore and land based routes).

Section 8.2 summarises the conclusions made from these investigations, and recommendations for further investigations are given in Section 8.3.

8.2 Conclusions

Based on the investigations described in the previous chapters, the following sections summarise the conclusions that can be drawn.

8.2.1 pppncl *software*

- A PPP software program, *pppncl*, has been created which in GPS only mode is capable of providing positioning comparable to other published software using this method.
- *pppncl* can read RINEX 2.11 observation data of unlimited length. Navigation data (satellite orbit and clock products) can be provided in either SP3 or RINEX 2 navigation format. Additional high rate clock products in RINEX clock format can be read and incorporated. Receivers providing C1 code observations instead of the P1 observations required for compatibility with IGS

clock products can be used with the addition of code P1C1 bias corrections provided in the `CC2NONCC` format.

- With the addition of the mappings from GLONASS satellite number to transmission frequency provided in RINEX 2 GLONASS navigation format, it is possible to include GLONASS carrier phase observations alongside GPS in the coordinate estimation.

8.2.2 *Static GPS PPP validation*

- In 24 h static positioning, daily coordinates are determined with an RMS of 3 mm, 5 mm and 14 mm in the North, East and Height respectively using IGS final navigation products. This has been shown across a global distribution of stations which experience a variety of atmospheric conditions and consist of various receiver models. The obtained RMS is almost identical to that shown in Kouba (2009a).
- *pppncl* produced zenith wet tropospheric delays show good agreement at the centimetre level with the IGS published troposphere product, even during periods of high variability.
- The convergence time in static mode was quantified, with 10 cm accuracy reached after 1 h in the Horizontal component, and 5 cm accuracy reached within 2 h. Full 3D positioning accuracy of 10 cm was reached within 2 h, and 5 cm accuracy within 5 h.
- For static positioning there is little improvement in coordinate accuracy after 12 h.

8.2.3 *Kinematic GPS PPP validation*

- *pppncl* was tested in kinematic mode using a vehicle on an open airfield, driving at a range of speeds, over a period of several hours, and found to be capable of producing coordinates with an accuracy of 1.5 cm RMS in the North and East components, and 3.4 cm in the Height component.
- The accuracy seen with *pppncl* was consistent throughout the test and not adversely affected by the increased velocity or varying dynamics of the vehicle.

8.2.4 *GLONASS carrier phase noise*

- The relative noise in the GPS and GLONASS carrier phase observations was quantified by analysis of the carrier phase residuals during static PPP. No significant difference between the GPS and GLONASS residuals was found.

8.2.5 *GPS/GLONASS static PPP repeatability*

- Using two different sets of GPS/GLONASS orbit products, the ESA Final product and the experimental Veripos Ultra real-time product, the effect of the addition of GLONASS on static PPP repeatability was assessed at a range of processing lengths. The improvement in repeatability seen for GPS/GLONASS PPP compared with GPS only after 1 h of static positioning with 30 s observation intervals was 20%, 2% and 24% for the North, East and Height components respectively using ESA Final orbit and clock products. When Veripos Apex G2 orbit and clock products were used, the improvement after the same time was 24%, 10% and 14% for the North, East and Height components respectively.
- After 1 h the accuracy obtained with real-time GPS/GLONASS orbital products was better than that obtained with Final GPS only products. This is clearly an indication of a reduced initialisation time seen with increased satellite number and distribution.

8.2.6 *GPS/GLONASS kinematic PPP*

Positioning quality was compared for several routes covering a range of transport modes to understand the impact of using GPS/GLONASS observations versus GPS only observations in kinematic PPP. In each case a reference solution was generated, using the dual frequency double differencing method as implemented in *Track*, and used as truth coordinates.

- The challenges facing PPP were clearly demonstrated in a test with a road vehicle on public roads, where a continual loss of lock on satellites was seen. The resulting short continuous phase connected arcs kept the PPP solution continuously returning to the initialisation phase. This also significantly reduced the accuracy of the double difference reference solution due to the short

time lengths without loss of lock, meaning the carrier phase ambiguities could not be well enough defined to be fixed at their integer values. With such a poor reference solution, no meaningful quantitative comparison between the GPS only and GPS/GLONASS PPP solutions could be made. Qualitatively, however, during the three 1 h periods for which a usable reference solution was available, the GPS/GLONASS solution showed faster convergence and hence more accurate positioning than the GPS only solution.

- With the data collected during the boat's route on the River Tyne, it can be seen that there is a clear reduction in convergence time when GPS and GLONASS are combined. The convergence time with GLONASS was reduced to approximately half an hour, three times less than for the GPS only PPP. Additionally, with the GPS/GLONASS combined observations, continuous high accuracy positioning was maintained during a period where the receiver lost lock on all GPS carrier phase observations. This demonstrated the benefit of using GLONASS in addition to GPS to provide a more robust positioning solution.

- The accuracy of the fully converged GPS and GPS/GLONASS PPP solutions was similar with 3 cm 3D RMS. However the session horizontal RMS was almost halved due to the increased robustness and faster convergence time of the GPS/GLONASS solution.

- In the Norway survey vessel offshore dataset the number of discontinuities due to cycle slips and unidentified outliers was reduced with the addition of GLONASS. Due to the long baseline lengths, it was not possible to compare the *pppncl* solution with the Veripos Ultra solution as there was no reference solution available.

- The total length of convergence time varies between the datasets, depending on the specific environment, although an overall improvement is seen with the addition of GLONASS across all the datasets studied. This applies not only to the time to the first usable measurements after powering up the receiver, but also to the time to recover after catastrophic events such as high levels of interference, accidental receiver reset, or total loss of lock due to obstructions such as bridges or dense tree cover.

- With ideal observations, when the receiver maintains lock for a long enough period (greater than 1 h) the RMS of GPS only PPP and GPS/GLONASS PPP are comparable. However, in the less than ideal case, often found in the

datasets considered, including GLONASS results in faster convergence time, improved solution continuity in the case of persistent cycle slip events and improved outlier removal. This causes a significant reduction in coordinate error RMS over the full length of the dataset.

- In several of the kinematic datasets considered, discontinuities in the coordinate solution with respect to the reference coordinates were seen, resulting in a period of above average error, whilst the estimate slowly drifts back to the correct value. Such discontinuities can be caused by multipath, undetected cycle slips or total receiver loss of lock. The survey vessel dataset on the River Tyne demonstrates a good example of this. The GPS/GLONASS solution maintains accurate positioning during a period where the total GPS loss of carrier phase tracking caused 20 min of degraded accuracy in the GPS only solution.

8.2.7 *Software architecture*

The following conclusions on software development can be made:

- The software *pppncl* consists of components written in two languages, Fortran, a low level compiled language, and Python, a high level interpreted language. Python allowed for rapid development and simple interaction with FTP archives for downloading data, whereas Fortran provides high performance for the linear algebra sections of the software. The Python code sets up the environment for the Fortran code. In hindsight the changeover point between Fortran and Python was too high, as the parsing of configuration files in Fortran is a laborious process, whereas in Python this process is part of the standard library. Increased use of Python code could have increased the ease of development and ability to make rapid modifications to the software.

- A more productive software development environment could be individual Fortran computation components tied together using Python or any other high level language. As part of the research process, the understanding of the problem and the requirements for software can change dramatically; this can be done more easily in a high level language which provides better abstractions and powerful built in data structures.

- The use of the Condor distributed computing platform allowed for rapid processing of the many discrete units of work such as when processing the 133,110

observation files analysed as part of the GPS/GLONASS repeatability testing analysis in Section 7.3.

8.3 Suggestions for further work

The following are suggestions for further research into this area:

- With the recent change to the IGS08 reference frame in April 2011, the IGS introduced GLONASS specific receiver antenna phase centre offsets and variations. The impact of this on PPP positioning could be investigated, with a possibility of increased accuracy.
- There is an opportunity for further work on the characterisation of the observation noise level for GLONASS, in particular one could assess the relative noise of the different satellite generations to include GLONASS-M. This would allow a more optimal combination of GPS and GLONASS observations in the same Kalman filter. Perhaps this would reduce the additional small amplitude of high frequency noise seen in the GPS/GLONASS PPP coordinate time series.
- One could investigate the use of auto correlation and adaptive Kalman filtering techniques for automatic quantification of the received observation noise.
- This research could be extended to look at the incorporation of GLONASS-M yaw attitude model (Dilssner et al., 2011), which as it becomes integrated into the orbit and clock products, will allow the use of GLONASS observations while the GLONASS-M satellites are in eclipse.
- In October 2011, the first launch of Galileo in-orbit validation satellites takes place. This presents an opportunity for further PPP positioning improvement with the addition of Galileo to GPS/GLONASS satellite observations. The inclusion of Galileo would bring improvements in satellite geometry due to increased number of satellites. The Galileo system uses CDMA, like GPS, so avoids the complication of each satellite transmitting on a separate frequency, and therefore there are no inter-frequency biases on the same signal. Galileo should also be less susceptible to multipath due to the code signal used.
- The inclusion of Galileo in a PPP implementation would be relatively straightforward. The methods used for GPS/GLONASS described in Chapter 4 could be largely reapplied to include the Galileo system. A receiver system clock offset would be required to account for any difference between the GPS and

Galileo time scales present in the precise clock products, and any biases introduced between Galileo and the other utilised GNSS in the receiver. Galileo will transmit on E1 and E5a frequency bands, in common with GPS to improve compatibility with GPS (Hofmann-Wellenhof et al., 2008). Therefore the same ionosphere free combination can be used for Galileo as for GPS.

- The error budget for Galileo is expected to be lower than that of GPS due to the more stable atomic clocks in the satellites and the more modern ranging codes that are less susceptible to multipath. Therefore, considering GPS combined with Galileo, it would be expected to provide improved performance in terms of the metrics described in Section 2.9, by comparison with GPS/-GLONASS.

- Additionally, when it becomes available, BEIDOU, the Chinese satellite system, could be incorporated, providing further benefit in terms of the number of satellites. Above a certain number of satellites, it is possible that more satellites will bring diminishing benefits. After a point, the improvements in geometry will be marginal, although extra satellites would help improve reliability and integrity, particularly in challenging environments such as urban canyons. There could also be a risk of interference if satellite numbers increase dramatically, as there is some overlap of the planned transmission frequencies used by the GNSS satellites.

- The addition of GLONASS satellites lead to a more even distribution of satellites in the sky and therefore reduced positional dilution. This may allow for better separation of the height, troposphere and clock estimated components within the Kalman filter, which could potentially make GPS/GLONASS PPP a valuable tool in precipitable water vapour estimation for use both in tropospheric model development, as a satellite based weather sensor, and as an observation source for numerical weather models.

- GLONASS and GPS systems are being modernised, with GLONASS adding CDMA encoding, the addition of the L5 frequency to GPS, and additional civilian signals such as L1C and L2C. Further work could be done to make best use of these new features in positioning accuracy and robustness.

- The addition of an RTCM decoder and NTRIP client functionality would enable true real-time PPP using data streams distributed over the internet via groups as part of the IGS Real-Time Pilot Project (Weber, 2006).

- One of the key benefits of combined GPS/GLONASS PPP is the reduced initialisation time. The recent developments in ambiguity fixed PPP still require an initial convergence period of up to 90 min until the integer valued biases are sufficiently well determined (Laurichesse et al., 2009). The addition of GLONASS observations to ambiguity fixed PPP could allow for a reduced initialisation time until the integer biases are identified.

- It would be beneficial to the GNSS user community to provide *pppncl* as a GPS/GLONASS PPP tool via an online PPP software service, including integration with the PPP software centre.

References

Abdel-Salam, M. A. (2005). *Precise Point Positioning using un-differenced code and carrier phase observations*. Ph.D. thesis, University of Calgary.

Anderson, B. D. O., and Moore, J. B. (1979). *Optimal Filtering*. Englewood Cliffs, NJ: Prentice-Hall.

Anderson, E., Bai, Z., Bischof, C., Blackford, S., Demmel, J., Dongarra, J., Du Croz, J., Greenbaum, A., Hammarling, S., McKenney, A., and Sorensen, D. (1999). *LAPACK Users' Guide*. Philadelphia, PA: Society for Industrial and Applied Mathematics, 3rd ed.

Armatys, M., Muellerschoen, R., Bar-Sever, Y., and Meyer, R. (2003). Demonstration of decimeter-level real-time positioning of an airborne platform. In *Proceedings of ION NTM*. Anaheim, CA, USA.

Arroyo-Suarez, E., Riley, J., Glang, G., and Mabey, D. (2005). Evaluating a global differential GPS system for hydrographic surveying. In *Proceedings of OCEANS 2005 MTS/IEEE*, vol. 3, (pp. 2557–2563). Institute of Electrical and Electronics Engineers. doi:10.1109/OCEANS.2005.1640155.

Ashby, N. (2003). Relativity in the Global Positioning System. *Living Reviews in Relativity*, *6*(1), 7–9. doi:10.12942/lrr-2003-1.

Bancroft, S. (1985). An algebraic solution of the GPS equations. *IEEE Transactions On Aerospace And Electronic Systems*, *AES-21*(1), 56–59. doi:10.1109/TAES.1985.310538.

Banville, S., and Langley, R. (2010). Instantaneous cycle-slip correction for real-time PPP applications. *Navigation, Journal of the Institute of Navigation*, *57*(4), 325–334.

Banville, S., Langley, R. B., and Santos, M. C. (2009). The Precise Point Positioning Software Centre: An Insight Into Online PPP Services. In *Poster presented at the IAG 2009 Meeting*. Buenos Aires, Argentina.

Bar-Sever, Y. E. (1996). A new model for GPS yaw attitude. *Journal of Geodesy*, *70*, 714–723. doi:10.1007/BF00867149.

Bar-Sever, Y. E., Kroger, P. M., and Borjesson, J. A. (1998). Estimating horizontal gradients of tropospheric path delay with a single GPS receiver. *Journal of Geophysical Research*, *103*(B3), 5019–5035. doi:10.1029/97JB03534.

Barker, R., Lapucha, D. D., and Wood, T. (2002). The impact of high performance GPS on the offshore marine survey, navigation and positioning industry. In *Proceedings of the Offshore Technology Conference, 6-9 May 2002, Houston, Texas*. doi:10.4043/14195-MS.

Beidou (2011). http://www.beidou.gov.cn/. Website.

Belehaki, A., Cander, L., Zolesi, B., Bremer, J., Juren, C., Stanislawska, I., Dialetis, D., and Hatzopoulos, M. (2006). Monitoring and forecasting the ionosphere over Europe: The DIAS project. *Space Weather*, *4*. doi:10.1029/2006SW000270.

Beutler, G., Davidson, D., Langley, R., Santerre, R., Vanicek, P., and Wells, D. (1984). Some theoretical and practical aspects of geodetic positioning using carrier phase difference observations of GPS satellites. Technical Report 109, University of New Brunswick, Canada.

Bhatti, U. I. (2007). *Improved integrity algorithms for integrated GPS/INS systems in the presence of slowly growing errors*. Ph.D. thesis, Department of Civil and Environmental Engineering, Imperial College London.

Bisnath, S. (2004). Precise orbit determination of low earth orbiters with a single GPS receiver based, geometric strategy. Tech. Rep. 220, University of New Brunswick.

Bisnath, S., and Gao, Y. (2008). Current state of precise point positioning and future prospects and limitations. In F. Sansò, and M. G. Sideris (Eds.) *Observing our Changing Earth*, vol. 133 of *International Association of Geodesy Symposia*, (pp. 615–623). Springer. doi:10.1007/978-3-540-85426-5_71.

Bisnath, S. B. (2000). Efficient, automated cycle-slip correction of dual-frequency kinematic GPS data. In *Proceedings of ION GPS*, (pp. 19–22).

Blewitt, G. (1989). Carrier phase ambiguity resolution for the global positioning system applied to geodetic baselines up to 2000 km. *Journal of Geophysical Research*, *94*(B8), 10187–10203. doi:10.1029/JB094iB08p10187.

Blewitt, G. (1990). An automatic editing algorithm for GPS data. *Geophysical Research Letters*, *17*(3), 199–202. doi:10.1029/GL017i003p00199.

Bock, H., Dach, R., Jäggi, A., and Beutler, G. (2009). High-rate GPS clock corrections from CODE: support of 1Hz applications. *Journal of Geodesy*, *83*, 1083–1094. doi:10.1007/s00190-009-0326-1.

Böhm, J., Heinkelmann, R., and Schuh, H. (2007). Short note: A global model of pressure and temperature for geodetic applications. *Journal of Geodesy*, *81*, 679–683. doi:10.1007/s00190-007-0135-3.

Böhm, J., Niell, A., Tregoning, P., and Schuh, H. (2006a). Global Mapping Function (GMF): A new empirical mapping function based on numerical weather model data. *Geophysical Research Letters*, *33*(7), L07304. doi:10.1029/2005GL025546.

Böhm, J., Werl, B., and Schuh, H. (2006b). Troposphere mapping functions for GPS and very long baseline interferometry from European Centre for Medium-Range Weather Forecasts operational analysis data. *J. Geophys. Res.*, *111:B02406*. doi:10.1029/2005JB003629.

Boucher, C., and Altamimi, Z. (2001). ITRS, PZ-90 and WGS 84: current realizations and the related transformation parameters. *Journal of Geodesy*, *75*(11), 613–619. doi:10.1007/s001900100208.

Braasch, M., and Van Dierendonck, A. J. (1999). GPS receiver architectures and measurements. In *Proceedings of the IEEE*, vol. 87, (pp. 48–64). doi:10.1109/5.736341.

Bucy, R. S., and Joseph, P. D. (1968). *Filtering for Stochastic Processes, with Applications to Guidance*. New York: Wiley.

Burbidge, M. (2006). Introducing SmartNet-UK, the first Leica Geosystems commercial network RTK correction service. In *XXIII FIG Congress, Munich, Germany*.

Byun, S., and Bar-Sever, Y. (2009). A new type of troposphere zenith path delay product of the International GNSS Service. *Journal of Geodesy*, *83*(3), 1–7. doi:10.1007/s00190-008-0288-8.

Cai, C., and Gao, Y. (2007). Precise point positioning using combined GPS and GLONASS observations. *Journal of Global Positioning Systems*, *6*(1), 13–22. doi:10.5081/jgps.6.1.13.

Chen, G. (1998). *GPS Kinematic Positioning for the Airborne Laser Altimetry at Long Valley, California*. Ph.D. thesis, Massachusetts Institute of Technology. Department of Earth, Atmospheric, and Planetary Sciences.

Collins, J., and Langley, R. (1999). Possible weighting schemes for GPS carrier phase observations in the presence of multipath. *Final contract report for the US*

Army Corps of Engineers Topographic Engineering Center, No. DAAH04-96-C-0086/TCN, *98151*.

Collins, P. (2008). Isolating and estimating undifferenced GPS integer ambiguities. In *Proceedings of ION National Technical Meeting*, (pp. 28–30). San Diego, CA.

Colombo, O., Sutter, A. W., and Evans, A. G. (2004). Evaluation of precise, kinematic GPS point positioning. In *Proceedings of the ION GPS GNSS 2004 Meeting*, (pp. 21–24).

Cruddace, P. (2006). OS Net: Positioning accuracy at the heart of Great Britain. *Geomatics World*, *15*, 22–27.

Dach, R., Böhm, J., Lutz, S., Steigenberger, P., and Beutler, G. (2011a). Evaluation of the impact of atmospheric pressure loading modeling on GNSS data analysis. *Journal of Geodesy*, *85*(2), 75–91. doi:10.1007/s00190-010-0417-z.

Dach, R., Brockmann, E., Schaer, S., Beutler, G., Meindl, M., Prange, L., Bock, H., Jäggi, A., and Ostini, L. (2009). GNSS processing at CODE: status report. *Journal of Geodesy*, *83*, 353–365. doi:10.1007/s00190-008-0281-2.

Dach, R., Schmid, R., Schmitz, M., Thaller, D., Schaer, S., Lutz, S., Steigenberger, P., Wübbena, G., and Beutler, G. (2011b). Improved antenna phase center models for GLONASS. *GPS Solutions*, *15*, 49–65. doi:10.1007/s10291-010-0169-5.

Dahlquist, G., and Björck, A. (2003). *Numerical methods*. Dover Publications Inc.

Daum, F. (2005). Nonlinear filters: beyond the Kalman filter. *IEEE Aerospace and Electronic Systems Magazine*, *20*(8), 57–69. doi:10.1109/MAES.2005.1499276.

Davis, J., Herring, T., Shapiro, I., Rogers, A., and Elgered, G. (1985). Geodesy by radio interferometry: Effects of atmospheric modeling errors on estimates of baseline length. *Radio Science*, *20*(6), 1593–1607. doi:10.1029/RS020i006p01593.

Decyk, V. K., Norton, C. D., and Szymanski, B. K. (1997). Expressing object-oriented concepts in Fortran 90. In *ACM SIGPLAN Fortran Forum*, vol. 16, (pp. 13–18). ACM. doi:10.1145/263877.263880.

Dilssner, F., Springer, T., Gienger, G., and Dow, J. (2011). The GLONASS-M satellite yaw-attitude model. *Advances in Space Research*, *47*(1), 160–171. doi:10.1016/j.asr.2010.09.007.

Dixon, K. (2006). StarFire TM: A global SBAS for sub-decimetre precise point positioning. In *Proceedings of ION GNSS*, (pp. 2286–2296). Fort Worth, Texas.

Dodd, D. (2007). *Utility of Ionosphere and Troposphere Models for Extending the Range of High-accuracy GPS.*. Ph.D. thesis, The University of Southern Mississippi.

Doherty, P. H., Klobuchar, J. A., and Kunches, J. M. (2000). Eye on the ionosphere: The correlation between solar 10.7 cm radio flux and ionospheric range delay. *GPS Solutions*, *3*, 75–79. doi:10.1007/PL00012820.

Dong, D.-N., and Bock, Y. (1989). Global Positioning System Network analysis with phase ambiguity resolution applied to crustal deformation studies in California. *Journal of Geophysical Research*, *94*(B4), 3949. doi:10.1029/JB094iB04p03949.

Dow, J., Neilan, R. E., and Rizos, C. (2009). The International GNSS Service in a changing landscape of Global Navigation Satellite Systems. *Journal of Geodesy*, *83*, 191–198. doi:10.1007/s00190-008-0300-3.

Edwards, S., Clarke, P., Penna, N., and Goebell, S. (2010). An examination of Network RTK GPS services in Great Britain. *Survey Review*, *42*(316), 107–121. doi:10.1179/003962610X12572516251529.

El-Mowafy, A. (2010). Local statistical testing in quality control of GNSS observations. *Journal of Global Positioning Systems*, *9*(1), 12–21. doi:10.5081/jgps.9.1.1.

El-Mowafy, A. (2011). Precise point positioning in the airborne mode. *Artificial Satellites*, *46*(2). doi:10.2478/v10018-011-0010-6.

ESA (2011). http://www.esa.int/Our_Activities/Navigation/The_future_-_Galileo/What_is_Galileo. Website.

Estey, L. H., and Meertens, C. M. (1999). TEQC: The multi-purpose toolkit for GPS/GLONASS data. *GPS Solutions*, *3*, 42–49. doi:10.1007/PL00012778.

Euler, H., Zebhauser, B., Townsend, B., and Wübbena, G. (2002). Comparison of different proposals for reference station network information distribution formats. In *Proceedings of ION GPS*, (pp. 2349–2358). Portland, OR.

Feng, S., Ochieng, W., Moore, T., Hill, C., and Hide, C. (2009). Carrier phase-based integrity monitoring for high-accuracy positioning. *GPS Solutions*, *13*(1), 13–22. doi:10.1007/s10291-008-0093-0.

Ferland, R., and Piraszewski, M. (2009). The IGS-combined station coordinates, Earth rotation parameters and apparent geocenter. *Journal of Geodesy*, *83*, 385–392. doi:10.1007/s00190-008-0295-9.

Ferreira, L. D. D., and de Moraes, R. V. (2009). GPS Satellites Orbits: Resonance. *Mathematical Problems in Engineering*, *2009*, Article ID 347835, 12 pages. doi:10.1155/2009/347835.

Gabor, M. (1999). *GPS Carrier Phase Ambiguity Resolution Using Satellite-Satellite Single Differences*. Ph.D. Thesis, University of Texas at Austin, Texas.

Gao, Y., Lahaye, F., Héroux, P., Liao, X., Beck, N., and Olynik, M. (2001). Modeling and estimation of C1–P1 bias in GPS receivers. *Journal of Geodesy*, *74*(9), 621–626. doi:10.1007/s001900000117.

Gao, Y., and Shen, X. (2002). A new method for carrier-phase-based precise point positioning. *Navigation*, *49*(2), 109–116.

Gao, Y., and Wang, M. (2008). Real-time kinematic OTF positioning using a single GPS receiver. In M. G. Sideris (Ed.) *Observing our Changing Earth*, vol. 133 of *International Association of Geodesy Symposia*, (pp. 655–668). Berlin, Heidelberg: Springer. doi:10.1007/978-3-540-85426-5_76.

Gao, Y., Wojciechowski, A., and Chen, K. (2005). Airborne kinematic positioning using precise point positioning methodology. *Geomatica*, *59*(1), 275–282.

Ge, M., Gendt, G., Rothacher, M., Shi, C., and Liu, J. (2008). Resolution of GPS carrier-phase ambiguities in precise point positioning (PPP) with daily observations. *Journal of Geodesy*, *82*(7), 401–401. doi:10.1007/s00190-007-0208-3.

Geng, J., Meng, X., Dodson, A., Ge, M., and Teferle, F. (2010a). Rapid re-convergences to ambiguity-fixed solutions in precise point positioning. *Journal of Geodesy*, *84*(12), 705–714. doi:10.1007/s00190-010-0404-4.

Geng, J., Meng, X., Dodson, A., and Teferle, F. (2010b). Integer ambiguity resolution in precise point positioning: method comparison. *Journal of Geodesy*, (pp. 1–13). doi:10.1007/s00190-010-0399-x.

Geng, J., Meng, X., Teferle, F., and Dodson, A. (2010c). Performance of precise point positioning with ambiguity resolution for 1 to 4 hour observation periods. *Survey Review*, *42*(316), 155–165. doi:10.1179/003962610X12572516251682.

Görres, B., Campbell, J., Becker, M., and Siemes, M. (2006). Absolute calibration of GPS antennas: laboratory results and comparison with field and robot techniques. *GPS Solutions*, *10*(2), 136–145. doi:10.1007/s10291-005-0015-3.

Grewal, M. S., and Andrews, A. P. (2001). *Kalman Filtering: Theory and Practice Using MATLAB*. John Wiley & Sons, Inc., 2nd ed.

Griffiths, J., and Ray, J. R. (2009). On the precision and accuracy of IGS orbits. *Journal of Geodesy*, *83*(3-4), 277–287. doi:10.1007/s00190-008-0237-6.

Grinter, T., and Roberts, C. (2011). Precise point positioning: where are we now. In *Proceedings of IGNSS Symp.*. Sydney, Australia.

Groves, P. D. (2008). *Principles of GNSS, Inertial, and Multi-Sensor Integrated Navigation Systems (GNSS Technology and Applications)*. Artech Print on Demand.

Gurtner, W., and Estey, L. (2007a). RINEX – the receiver independent exchange format-version 3.00. http://igscb.jpl.nasa.gov/igscb/data/format/rinex300.pdf.

Gurtner, W., and Estey, L. (2007b). RINEX: The receiver independent exchange format version 2.10. ftp://igscb.jpl.nasa.gov/igscb/data/format/rinex210.txt.

Hatanaka, Y. (2008). A compression format and tools for GNSS observation data. *Bulletin of the Geographical Survey Institute*, *55*, 21–30.

Hegarty, C., and Chatre, E. (2008). Evolution of the global navigation satellite system (GNSS). *Proceedings of the IEEE*, *96*(12), 1902–1917. doi:10.1109/JPROC.2008.2006090.

Héroux, P., Y. Gao, J. K., Lahaye, F., Mireault, Y., Collins, P., Macleod, K., Tétreault, P., and Chen, K. (2004). Products and applications for precise point positioning - moving towards real-time. In *Proceedings of ION GNSS 2004*, (pp. 1832–1843). Long Beach, CA.

Herring, T., King, R., and McClusky, S. (2006). GPS analysis at MIT, GAMIT reference manual, release 10.3. *Massachusetts Institute of Technology*.

Hesselbarth, A., and Wanninger, L. (2008). Short-term stability of GNSS satellite clocks and its effect on Precise Point Positioning. In *Proceedings of ION GNSS 2008*, (pp. 1855–1863). Savannah. GA.

Hilla, S. (2002). Extending the standard product 3 (SP3) orbit format. In *Proceedings of the International GPS Service Network, Data, and Analysis Center Workshop*. Ottawa, Canada.

Hofmann-Wellenhof, B., Lichtenegger, H., and Wasle, E. (2008). *GNSS — Global Navigation Satellite Systems: GPS, GLONASS, Galileo, and more*. Wien: Springer.

Hopfield, H. (1969). Two-quartic tropospheric refractivity profile for correcting satellite data. *Journal of Geophysical Research*, *74*(18), 4487–4499. doi:10.1029/JC074i018p04487.

ICAO (2005). *Global Navigation Satellite System (GNSS) Manual*. International Civil Aviation Organization, first edition ed. Doc 9849 AN/457.

ICD GLONASS (2008). Global navigation satellite system GLONASS interface control document, version 5.1. http://facility.unavco.org/data/docs/ICD_GLONASS_5.1_(2008)_en.pdf.

IGS (2011). IGS products. http://www.igs.org/components/prods.html.

IS-GPS-200E (2010). Navstar GPS space segment/navigation user interfaces. IS-GPS-200, Revision E.

Keshin, M., Le, A., and van der Marel, H. (2006). Single and dual-frequency precise point positioning: approaches and performances. In *NAVITEC 2006*. Noordwijk, The Netherlands.

Kouba, J. (2009a). A guide to using International GNSS Service (IGS) products. http://igscb.jpl.nasa.gov/components/usage.html.

Kouba, J. (2009b). A simplified yaw-attitude model for eclipsing GPS satellites. *GPS Solutions*, *13*(1), 1–12. doi:10.1007/s10291-008-0092-1.

Kouba, J., and Héroux, P. (2001). Precise point positioning using IGS orbit and clock products. *GPS solutions*, *5*(2), 12–28. doi:10.1007/PL00012883.

Lachapelle, G. (1991). GPS observables and error sources for kinematic positioning. In *Proceedings of IAG International Symposium*, vol. 107, (pp. 17–26). New York: Springer Verlag. doi:10.1007/978-1-4612-3102-8_2.

Lau, L., and Cross, P. (2006). A new signal-to-noise-ratio based stochastic model for GNSS high-precision carrier phase data processing algorithms in the presence of multipath errors. In *Institute of Navigation - 19th International Technical Meeting of the Satellite Division, ION GNSS 2006*, vol. 1, (pp. 276–285). Fort Worth, TX.

Lau, L., and Cross, P. (2007). Development and testing of a new ray-tracing approach to GNSS carrier-phase multipath modelling. *Journal of Geodesy*, *81*(11), 713–732. doi:10.1007/s00190-007-0139-z.

Laurichesse, D. (2011). The CNES real-time PPP with undifferenced integer ambiguity resolution demonstrator. In *Proceedings of the ION GNSS 2011*. Portland, Oregon.

Laurichesse, D., Mercier, F., Berthias, J. P., Broca, P., and Cerri, L. (2009). Integer ambiguity resolution on undifferenced GPS phase measurements and its application to PPP and satellite precise orbit determination. *Navigation*, *56*(2), 135–149.

Le, A., and Teunissen, P. (2008). *Optimal Recursive Least-Squares Filtering of GPS Pseudorange Measurements*. Springer-Verlag. doi:10.1007/978-3-540-74584-6_26.

Leandro, R., Santos, M., and Langley, R. (2011). Analyzing GNSS data in precise point positioning software. *GPS Solutions*, *15*, 1–13. doi:10.1007/s10291-010-0173-9.

Leick, A. (2004). *GPS satellite surveying*. John Wiley & Sons, 3 ed.

Li, X., Zhang, X., and Ge, M. (2011). Regional reference network augmented precise point positioning for instantaneous ambiguity resolution. *Journal of Geodesy*, *85*(3), 151–158. doi:10.1007/s00190-010-0424-0.

Lowry, R. (2011). Concepts and applications of inferential statistics. Available online at http://vassarstats.net/textbook.

Martín, A., Anquela, A. B., Capilla, R., and Berné, J. L. (2011). PPP technique analysis based on time convergence, repeatability, IGS products, different software processing and GPS+Glonass constellation. *Journal of Surveying Engineering*, *137*(3), 99–108. doi:10.1061/(ASCE)SU.1943-5428.0000047.

McCarthy, D. D., Boucher, C., Eanes, R., Fukushima, T., Herring, T., Lieske, J., Ma, C., Montag, H., Pâquet, P., Reigber, C., et al. (1989). IERS Standards

(1989). IERS Technical Note 3, Central Bureau of IERS - Observatoire de Paris, Paris.

McCarthy, D. D., and Petit, G. (2003). IERS Conventions (2003). IERS Technical Note 32, Verlag des Bundesamts für Kartographie und Geodäsie, Frankfurt am Main.

Melbourne, W. G. (1985). The case for ranging in GPS-based geodetic systems. In *Proc. 1st Int. Symp. on Precise Positioning with GPS, Rockville, Maryland*, (pp. 373–386).

Mendes, V., and Langley, R. (1998). Tropospheric zenith delay prediction accuracy for airborne GPS high-precision positioning. In *Proceedings of The Institute of Navigation 54th Annual Meeting*, (pp. 337–347).

Metcalf, M., and Reid, J. K. (1999). *Fortran 90/95 Explained*. Oxford University Press.

Monteiro, L. S., Moore, T., and Hill, C. (1999). What is the accuracy of DGPS? *Journal of Navigation*, *58*(2), 207–225. doi:10.1017/S037346330500322X.

Muellerschoen, R. J., Reichert, A., Kuang, D., Heflin, M., Bertiger, W. I., and Bar-Sever, Y. E. (2001). Orbit determination with NASA's high accuracy real-time global differential GPS system. In *Proceedings of ION GPS-2001*. Salt Lake City, UT.

Newcomb, S. (1895). Tables of the motion of the Earth on its axis and around the Sun. *Astronomical papers prepared for the use of the American ephemeris and nautical almanac , [Washington, Bureau of Equipment, Navy Dept., 1895]*, *6*(6), 169.

Niell, A. E. (1996). Global mapping functions for the atmosphere delay at radio wavelengths. *Journal of Geophysical Research*, *101*(B2), 3227–3246. doi:10.1029/95JB03048.

Noll, C. (2010). The Crustal Dynamics Data Information System: A resource to support scientific analysis using space geodesy. In *Advances in Space Research*, vol. 45, (pp. 1421–1440). doi:10.1016/j.asr.2010.01.018.

Noll, C., and Dube, M. (2001). The IGS global data center at the CDDIS — an update. *Physics and Chemistry of the Earth, Part A: Solid Earth and Geodesy*, *26*(6-8), 603–604. Proceedings of the First COST Action 716 Workshop Towards

Operational GPS Meteorology and the Second Network Workshop of the International GPS Service (IGS). doi:10.1016/S1464-1895(01)00108-9.

Ochieng, W. Y., Sauer, K., Walsh, D., Brodin, G., Griffin, S., and Denney, M. (2003). GPS integrity and potential impact on aviation safety. *Journal of Navigation*, *56*(1), 51–65. doi:10.1017/S0373463302002096.

Oleynik, E., Mitrikas, V., Revnivykh, S., Serdukov, A., Dutov, E., and Shiriaev, V. (2006). High-accurate GLONASS Orbit and Clock Determination for the Assessment of System Performance. In *ION GNSS*, (pp. 2065–2079).

Petrie, E., Hernández-Pajares, M., Spalla, P., Moore, P., and King, M. (2011). A review of higher order ionospheric refraction effects on dual frequency GPS. *Surveys in Geophysics*, *32*, 197–253. doi:10.1007/s10712-010-9105-z.

Petrov, L. (2004). Study of the atmospheric pressure loading signal in very long baseline interferometry observations. *Journal of Geophysical Research*, *109*, B03405. doi:10.1029/2003JB002500.

Píriz, R., Calle, D., Mozo, A., Navarro, P., Rodríguez, D., and Tobías, G. (2009). Orbits and clocks for GLONASS precise-point-positioning. In *Proceedings of the 22nd International Technical Meeting of The Satellite Division of the Institute of Navigation (ION GNSS 2009)*, (pp. 2415–2424).

Píriz, R., Mozo, A., Navarro, P., and Rodriguez, D. (2008). magicGNSS: Precise GNSS products out of the box. In *Proceedings of the 21st International Technical Meeting of the Satellite Division of The Institute of Navigation (ION GNSS 2008)*, (pp. 1242–1251).

Press, W., Teukolsky, S., Vetterling, W., Flannery, B., and Metcalf, M. (1996). *Numerical recipes in Fortran 90: the art of parallel scientific computing. Volume 2 of Fortran numerical recipes*. Cambridge University Press.

Ragheb, A., Clarke, P., and Edwards, S. (2007). GPS sidereal filtering: coordinate- and carrier-phase-level strategies. *Journal of Geodesy*, *81*(5), 325–335. doi:10.1007/s00190-006-0113-1.

Ray, J. (1999). Use of multiple antennas to mitigate carrier phase multipath in reference stations. In *Proceedings of ION GPS*, vol. 99, (pp. 269–279).

Ray, J., and Gurtner, W. (2010). RINEX extensions to handle clock information. http://igscb.jpl.nasa.gov/igscb/data/format/rinex_clock302.txt.

Reussner, N., and Wanninger, L. (2011). GLONASS inter-frequency biases and their effects on RTK and PPP carrier-phase ambiguity resolution. In *Proceedings of ION GNSS 2011*, (pp. 712–716). Portland, OR.

Revnivykh, S. G. (2007). GLONASS status, development, and application. In *Proc. 2nd Meeting United Nations Int. Committee Global Navig. Satellite Syst. (ICG)*. Bangalore, India.

Rocken, C. (2005). Atmospheric water vapor and geoid measurements in the open ocean with GPS. *Geophysical Research Letters*, *32*, L12813. doi:10.1029/2005GL022573.

Rocken, C., Mervart, L., Johnson, J., Lukes, Z., Springer, T., Iwabuchi, T., and Cummins, S. (2011). New real-time global GPS and GLONASS precise positioning correction service: Apex. In *Proceedings of the 24th International Technical Meeting of The Satellite Division of the Institute of Navigation (ION GNSS 2011)*, (pp. 1825–1838). Portland, OR.

Romero, N. (2010). CC2NONCC important software update. IGSMAIL-6398.

Rost, C., and Wanninger, L. (2009). Carrier phase multipath mitigation based on GNSS signal quality measurements. *Journal of Applied Geodesy*, *3*(2), 81–87. doi:10.1515/JAG.2009.009.

Rothacher, M., and Mader, G. (2003). Receiver and satellite antenna phase center offsets and variations. In P. Tétreault, R. Neilan, and K. Gowey (Eds.) *Proceedings of the Network, Data and Analysis Centre 2002 Workshop*, (pp. 141–152). Ottawa. http://igs.org/igscb/resource/pubs/02_ott/session_8.pdf.

Rothacher, M., and Schmid, R. (2010). ANTEX: The antenna exchange format, version 1.4. http://igscb.jpl.nasa.gov/igscb/station/general/antex14.txt.

Russell-Cargill, B. (2010). Vessel based solutions for the acquisition of geotechnical data in subsea site investigations. *Preview*, *2010*(148), 38–40.

Saastamoinen, J. (1973). Contributions to the theory of atmospheric refraction. *Bulletin Géodésique*, *107*(1), 13–34. doi:10.1007/BF02522083.

Scargle, J. D. (1982). Studies in astronomical time series analysis. II - statistical aspects of spectral analysis of unevenly spaced data. *The Astrophysical Journal*, *263*, 835. doi:10.1086/160554.

Schaer, S., and Steigenberger, P. (2006). Determination and use of GPS differential code bias values. In *IGS workshop in Darmstadt*.

Schenewerk, M. (2003). A brief review of basic GPS orbit interpolation strategies. *GPS Solutions*, *6*(4), 265–267. doi:10.1007/s10291-002-0036-0.

Schmidt, G. T. (1976). Practical aspects of Kalman filtering implementation. Tech. Rep. AGARD-LS-82, NATO Advisory Group for Aerospace Research and Development, London.

Springer, T. A. (2009). NAPEOS mathematical models and algorithms. Technical note DOPS-SYS-TN-0100-OPS-GN, ESOC.

Springer, T. A. (2010). ESA/ESOC ultra-rapid and rapid GNSS solutions. IGSMAIL-6107.

Sturza, M. A., and Brown, A. K. (1990). Integrated GPS/GLONASS for reliable receiver autonomous integrity monitoring (RAIM). In *Institute of Navigation, Annual Meeting*, 46, (pp. 9–13). Washington, DC.

Teunissen, P. (1990). Quality control in integrated navigation systems. In *IEEE Symposium on Position Location and Navigation. A Decade of Excellence in the Navigation Sciences*, (pp. 158–165). Institute of Electrical and Electronics Engineers. doi:10.1109/PLANS.1990.66172.

Teunissen, P. (1995). The least-squares ambiguity decorrelation adjustment: a method for fast GPS integer ambiguity estimation. *Journal of Geodesy*, *70*(1), 65–82. doi:10.1007/BF00863419.

Thain, D., Tannenbaum, T., and Livny, M. (2005). Distributed computing in practice: the condor experience. *Concurrency - Practice and Experience*, *17*(2-4), 323–356. doi:10.1002/cpe.938.

Thomas, I. D., King, M. A., Bentley, M. J., Whitehouse, P. L., Penna, N. T., Williams, S. D. P., Riva, R. E. M., Lavallee, D. A., Clarke, P. J., and King, E. C. (2011). Widespread low rates of Antarctic glacial isostatic adjustment revealed by GPS observations. *Geophysical Research Letters*, *38*, L22302. doi:10.1029/2011GL049277.

Urquhart, L. (2009). Atmospheric pressure loading and its effects on precise point positioning. In *Proceedings of the 22nd International Technical Meeting of The*

Satellite Division of the Institute of Navigation (ION GNSS 2009), (pp. 658–667). Savannah, GA.

Urschl, C., Dach, R., Hugentobler, U., Schaer, S., and Beutler, G. (2005). Validating ocean tide loading models using GPS. *Journal of Geodesy*, *78*(10), 616–625. doi:10.1007/s00190-004-0427-9.

Vermeer, M. (1997). The precision of geodetic GPS and one way of improving it. *Journal of Geodesy*, *71*(4), 240–245. doi:10.1007/s001900050091.

Wahr, J. (1981). The forced nutation of an elliptical, rotating, elastic, and ocean less Earth. *Geophys. J. Roy. Astron. Soc.*, *64*, 705–727. doi:10.1111/j.1365-246X.1981.tb02691.x.

Wan, E., and Van Der Merwe, R. (2000). The unscented Kalman filter for nonlinear estimation. In *Proceedings of the IEEE 2000 Adaptive Systems for Signal Processing, Communications, and Control Symposium*, (pp. 153–158). Institute of Electrical and Electronics Engineers. doi:10.1109/ASSPCC.2000.882463.

Wang, C., Feng, Y., Higgins, M., and Cowie, B. (2010). Assessment of commercial network RTK user positioning performance over long inter-station distances. *Journal of Global Positioning Systems*, *9*(1), 78–89. doi:10.5081/jgps.9.1.78.

Wanninger, L. (2011). Carrier-phase inter-frequency biases of GLONASS receivers. *Journal of Geodesy*, *86*(2), 139–148. doi:10.1007/s00190-011-0502-y.

Wanninger, L., and May, M. (2001). Carrier-phase multipath calibration of GPS reference stations. *Proceedings of ION GPS 2000*, *48*(2), 113–124.

Weber, G. (2006). Streaming real-time IGS data and products using NTRIP. In *Proceedings of the IGS2006 Workshop*. ESOC Darmstadt, Germany.

Weber, G., Mervart, L., Lukes, Z., Rocken, C., and Dousa, J. (2007). Real-time clock and orbit corrections for improved point positioning via NTRIP. In *Proceedings of ION GNSS 2007*, (pp. 1992–1998). Fort Worth, Texas: the 20th International Technical Meeting of the Satellite Division of The Institute of Navigation.

Welch, G., and Bishop, G. (1995). An introduction to the Kalman filter. TR 95-041, University of North Carolina at Chapel Hill, Chapel Hill, NC 27599-3175. URL: http://www.cs.unc.edu/~welch/kalman/kalmanIntro.html.

Witchayangkoon, B. (2000). *Elements of GPS precise point positioning*. Ph.D. thesis, University of New Brunswick.

Wu, J., Wu, S., Hajj, G., Bertiger, W., and Lichten, S. (1993). Effects of antenna orientation on GPS carrier phase. *Manuscripta Geodaetica*, *18*, 91–98.

Wübbena, G. (1985). Software developments for geodetic positioning with GPS using TI-4100 code and carrier measurements. In *Proceedings of the First International Symposium on Precise Positioning with the Global Positioning System*, vol. 19, (pp. 403–412).

Wulf, W., and Shaw, M. (1973). Global variable considered harmful. *ACM SIGPLAN Notices*, *8*, 28–34. doi:10.1145/953353.953355.

Yousif, H., and El-Rabbany, A. (2007). Assessment of several interpolation methods for precise GPS orbit. *The Journal of Navigation*, *60*(03), 443–455. doi:10.1017/S0373463307004250.

Zumberge, J., Heflin, M., Jefferson, D., Watkins, M., and Webb, F. (1997). Precise point positioning for the efficient and robust analysis of GPS data from large networks. *Journal of Geophysical Research*, *102*(B3), 5005–5017. doi:10.1029/96JB03860.

Appendix A Software reference

This appendix provides reference information on the software created as part of this thesis. The *pppncl* configuration file format is described in A.2. Output formats are described. Utility scripts functionality and command line options are given. Overview of the key functions and data types used in the *pppncl* source code.

A.1 Input formats

This section describes the types of input file that are needed by *pppncl* when performing PPP. The different formats that can be used for each type of input data are explained.

A.1.1 *Observation data*

Observation data can be read in RINEX 2.1 format (Gurtner and Estey, 2007b). As the file is read sequentially epoch by epoch, there is no limit to the length of the observation file that can be used. Files containing up to 14 observation types at each epoch can be read. The software places no restriction on the observation type identifiers in the RINEX file. The limit of 14 observations allows reading of files containing the currently complete following set of observations:

- Carrier phase: `L1`, `L2`, `L5`
- C code: `C1`, `C2`, `C5`
- P code: `P1`, `P2`
- Signal to noise ratio: `S1`, `S2`, `S5`
- Doppler: `D1`, `D2`, `D5`

Legacy GPS only files with no satellite system identifier or mixed GNSS system files can be read.

RINEX 2 was designed with only GPS in mind, and later adapted to allow mixed data from GPS and GLONASS satellites in the same file. It has become apparent that it has shortcomings as a reciever observation exchange format for files containing observation data of more than one satellite system, each one with different observation types. To address this Gurtner and Estey (2007a) proposed the RINEX 3 standard. Whilst it seems logical that RINEX 3 will replace RINEX 2 as the

standard data exchange format the not inconsiderable effort required to update all the tools used by the wider GNSS community has meant that RINEX 3 adoption has been very slow. For that reason only a RINEX 2 reader has been implemented in *pppncl* at this time.

A.1.2 *Navigation data*

pppncl can use broadcast orbits in RINEX format or precise orbits in SP3 format, with optional high rate clocks in RINEX clock format. For the RINEX GPS navigation format and the SP3 format, the routines from *Track* were used as a starting point. The SP3 routines were enhanced to allow reading of files containing multiple GNSS systems so that GLONASS data could be used.

The RINEX format contains a specification for the file format containing the broadcast ephemeris data; this can be read by *pppncl*.

Precise orbits and clocks can be read in SP3 format (Hilla, 2002). Repeated header blocks are ignored so for observation periods of longer than a day, or to avoid interpolation errors at the beginning and the end of the day, multiple SP3 files may be concatenated into a single file. Subsequent header blocks will be ignored.

High rate clock data, essential to high rate PPP can be read in RINEX 2.00 or 3.00 clock format (Ray and Gurtner, 2010). Only the satellite clock offset records (lines beginning `AS`) are read in by *pppncl*, other lines are skipped.

For the mapping between GLONASS satellite number and GLONASS frequency number, GLONASS navigation data is required. This can be read in RINEX 2.10 GLONASS navigation format. The CDDIS produce a merged navigation file containing the union of all broadcast navigation information received across all sites stored in the CDDIS archive.

A.1.3 *Phase centre offsets and variations*

The IGS maintain a list of satellite and receiver antenna phase centre offsets and variations in ANTEX format. An ANTEX file parser was written to read ANTEX v1.4 format files (Rothacher and Mader, 2003; Rothacher and Schmid, 2010). The list of receiver antennas that are contained in the IGS list can be found at `http://www.igs.org/igscb/station/general/rcvr_ant.tab`.

For positioning using older orbit and clock products that were generated using relative phase centre offsets, the GAMIT (Herring et al., 2006) GPS satellite information format `svnav.dat` may be used. Note this only provides block mean satellite phase centre offsets and no phase centre variations so accuracy will be limited. This file can either be obtained from a GAMIT installation in `~/gg/tables/svnav.dat` or online at `http://chandler.mit.edu/~simon/gtgk/svnav.txt`

A.1.4 *Differential code biases*

pppncl integrates the ESOC updated version of the `CC2NONCC` software routines (Romero, 2010) for correcting C1 observables to P1 like observables as described in Section 3.13. This allows reading `CC2NONCC` correction format P1C1 biases. Historical monthly average values are available from CODE at `ftp://ftp.unibe.ch/aiub/CODE/p1c1bias.2000` in one file. This is only updated periodically, so for the latest values or if values are only needed for a particular month they may be obtained from `ftp://ftp.unibe.ch/aiub/CODE/YYYY/P1C1YYMM.F.Z`, where `YYYY` denotes the four digit year, `YY` the two digit year and `MM` the two digit month. E.g. `ftp://ftp.unibe.ch/aiub/CODE/2011/P1C11107.F.Z` for P1C1 biases from July 2011.

A.2 Configuration file

The *pppncl* processing options are specified in a configuration file, largely based on the configuration file format for *Track*. All lines that do not start with a space are ignored as comment lines. The commands are case insensitive. Here follows a list of keywords used in the file, with an explanation of their effects and the format of any data they expect.

In the following descriptions of the configuration options, values that are required by a given command are enclosed in angled brackets (`< >`), optional values are enclosed in square brackets (`[ ]`). These should be replaced including the brackets with the required value or in the case of optional items ommited. For clarity, required spaces are shown using the character ␣ and newlines with the ¶ character.

Where a filename is required as an option the value should be either the relative path and filename or an absolute path and filename of the input file that should be used. Relative paths are interpreted relative to the directory *pppncl* is invoked

from, not relative to the configuration file.

List of commands:

␣obs_file¶
␣␣<site name>␣<RINEX observation file>¶

This required command defines the RINEX observation file that is used as input data. <site name> is a four letter identifier describing the name of the site and may be chosen freely. <RINEX observation file> is the path and filename of the observation file to be used, there is a limit of 256 characters.

␣nav_file␣<navigation file>␣[SP3]¶

This required command defines the navigation file used for orbits and clock data. <navigation file> is the filename of the navigation file, and may be a maximum length of 256 characters. By default, this is assumed to be a RINEX GPS broadcast navigation file. If SP3 format navigation data is to be used, the optional SP3 marker should follow the name of the navigation file. This is done rather than explicitly auto detecting the format as some providers use an alternative file extension to .sp3.

␣gnav_file␣<GLONASS RINEX navigation file>¶

This command is required for use of GLONASS observations. It specifies the filename of the GLONASS broadcast navigation file used to map the GLONASS satellite number to transmitting frequency. The maximum length of the filename is 256 characters.

␣clk_file␣<clock file>¶

This optional command is used to specify that high rate clock corrections in RINEX clock format should be used. <clock file> is the filename of the clock data to be used, with a limit of 256 characters. If this command is supplied, the navigation file must be in SP3 format.

␣site_pos¶
␣␣<site name>␣<X>␣<Y>␣<Z>¶

This command is used to specify the initial coordinates of the receiver in Earth centred Earth fixed coordinates, in the reference frame of the provided navigation data. The site name must match the site name given in the obs_file command. The units for <X>, <Y> and <Z> are metres. These values are also used as the

coordinates to which the North, East and Height relative coordinate output file, `neu.out` is referenced.

```
␣site_stats¶
␣␣<site name>␣<APR X>␣<APR Y>␣<APR Z>␣<noise X>␣<noise Y>␣<noise Z>¶
```

This required command specifies the initial coordinate uncertainty and the epoch to epoch process noise. `<site name>` must match the name given in the `obs_file` command. `<APR X>`, `<APR Y>` and `<APR Z>` are the X, Y and Z initial coordinate standard deviations, units are in metres. `<noise X>`, `<noise Y>` and `<noise Z>` are the X, Y and Z process noise added at each epoch, units are in metres per second. As the coordinates are modelled as random walk, the variance added at each epoch is $dt \times \text{noise}^2$, where dt is the observation step interval.

For static positioning, the `<noise>` values should be set to zero. For kinematic positioning the `<noise>` values should match the expected dynamics of the receiver. Specifying a large process noise will allow the solution to respond faster to high dynamic situations but will also increase the effect of observation noise on the estimated coordinates.

```
␣atm_stats¶
␣␣all␣<APR ATM>␣<noise ATM>¶
```

This required command specifies the initial uncertainty and noise in the estimated correction to the wet zenith tropospheric delay. `<APR ATM>` is the initial zenith tropospheric delay correction standard deviation, units are in metres. `<noise ATM>` is the process noise added at each epoch, units are in metres per second. As the wet zenith tropospheric delay correction is modelled as random walk, the variance added at each epoch is $dt \times \text{noise}^2$. Setting both values to zero will disable the wet tropospheric correction estimation.

```
␣clk_stats¶
␣␣all␣<initial std dev>␣<per epoch process noise>¶
```

This required command specifies the initial uncertainty and noise in the estimated receiver clock offset. `<initial std dev>` is the initial estimated receiver clock offset standard deviation, units are in metres. `<per epoch process noise>` is the process noise added at each epoch, units are in metres per second. As the receiver clock offset is modelled as random walk, the variance added at each epoch is $dt \times \text{noise}^2$.

␣ante_off¶
␣␣<station>␣<ARP offset>␣[L1 PCO]␣[L2 PCO]¶

This optional command is used in two cases:

If absolute antenna offsets are being used with a provided ANTEX file, then this command is not required unless the ARP offset provided in the RINEX file needs to be overridden, in which case the North, East and Up offsets should be given in units of metres.

If relative phase centre offsets are being used then additionally, the L1 and L2 PCOs may be given as North, East and Height offsets in units of metres.

␣data_noise␣<L1>␣<L2>␣<P1>␣<P2>¶

This optional command is used to specify the standard deviation of the zenith observation process noise for each of the GPS L1, L2, P1 and P2 observables, with units in metres. If the C1 observable is being used in place of P1, then the process noise specified for P1 will be used for the C1 observable.

␣data_type␣<data type>¶

This optional command selects the combination of observations to use in coordinate estimation. The following options are available:

- P1
- P2
- PC ionosphere free code
- KH ionosphere free code and phase (the standard PPP model)
- UC alternative ionosphere free code and phase Gao and Shen (2002)

If this command is not given then the default option is KH.

␣cut_off␣<Elevation cutoff angle>¶

This optional command specifies an elevation cutoff angle in degrees below which observations are not used. If this command is not given, the default value of 10° is used.

␣gnss_type␣<GNSS types>¶

This optional command specifies the GNSS types to be used, with the same letters

as in the RINEX file. The usable options are "G" for GPS only positioning, and "GR" for combined GPS and GLONASS positioning. If this option is not specified, the default is GPS only. Note, for the GR option to work, a GLONASS navigation file must be specified with the `g_nav_file` command.

`␣block_file␣<block file>¶`

This optional command specifies the GAMIT style satellite information file. It is only required when using relative phase centre offsets. This command is used to determine which block of GPS satellites (for example GPS 2a or 2b) each GPS satellite is from. This allows the block specific satellite phase centre offset to be applied.

`␣absolute_antenna␣<true | false>¶`

This command is used to enable absolute antenna offsets if it is set to `true`. If absolute antenna offsets are to be used, an ANTEX format file containing the required antenna offsets must be specified using the `antex_file` command. The receiver antenna is read from the header of the RINEX observation file.

`␣antex_file␣<path to ANTEX file>¶`

This command specifies the filename of the ANTEX file containing antenna phase centre offset variation data. For consistency, the same set of antenna offsets should be used as those used in the generation of the orbit and clock data.

`␣p1c1bias_file␣<path to p1c1bias file>¶`

This optional command specifies the filename of the `CC2NONCC` format, P1C1 bias file. This file is only required if the RINEX observation file does not include P1 observations, or if the RINEX file contains both P1 and C1 observations and it is desired to use the C1 observation as a fall back for missing P1 observations.

`␣code_type␣<C1 | P1>¶`

This optional command is used to specify if P1 or C1 observations should be used. If C1 observations are selected, then no P1C1 biases are applied to the C1 observations, even if a P1 C1 bias file is provided. However, if the P1 option is selected and the RINEX file only contains C1 observations then they will be corrected by the P1C1 biases provided in the file specified in the `p1c1bias_file` command. If the RINEX file header contains the comment that is added by `CC2NONCC` when C1 is corrected to P1 within the RINEX file, then P1C1 biases are not applied a second time.

␣slip_reset␣<noise | reset | none>¶

This optional command specifies what should be done when a cycle slip is detected but is not able to be fixed. The options are described here:

- If the option `none` is chosen then no action is taken,
- If the option `noise` is chosen, then a large amount of process noise will be added to the diagonal element of the *a priori* covariance matrix corresponding to the ambiguity for that satellite,
- If the `reset` option is chosen ambiguity is reinitialised from scratch using the same method as if the satellite had just appeared above the horizon. All correlations in the state vector covariance matrix are zeroed.

If this command is not given, then the `reset` option is used by default.

␣start_time␣<YYYY>␣<MM>␣<DD>␣<HH>␣<mm>␣<SS.S>¶

This command specifies the start time for processing observations. Observations in the RINEX file before this point will be skipped. `<YYYY>` is the four digit year, `<MM>` is the two digit month, `<DD>` is the two digit day of month, `<HH>` is the two digit hours, `<mm>` is the two digit minutes, and `<SS.S>` is a floating point value for seconds.

␣stop_time␣<YYYY>␣<MM>␣<DD>␣<HH>␣<mm>␣<SS.S>¶

This command specifies the end time for processing observations. Observations in the RINEX file after this point will not be used. `<YYYY>` is the four digit year, `<MM>` is the two digit month, `<DD>` is the two digit day of month, `<HH>` is the two digit hours, `<mm>` is the two digit minutes, and `<SS.S>` is a floating point value for seconds.

A.3 Output files

A.3.1 *atm.out*

This file contains the modelled and estimated zenith tropospheric delay. The format is as follows:

`<seconds of day>␣<Est ZWD>␣<Mod ZHD>␣<Mod ZWD>␣<Sigma Est ZWD>¶`

where:

Est ZWD is the estimated correction to the zenith wet delay in metres.

Mod ZHD is the modelled zenith hydrostatic delay in metres.

Mod ZWD is the modelled zenith wet delay in metres.

Sigma Est ZWD is the formal error of the estimated correction to the zenith wet delay, one sigma.

An example is shown here:

`53405.00␣0.0519␣2.2908␣0.0761␣0.0073¶`

A.3.2 *mw.out*

This set of files contain the state of the Melbourne-Wübenna cycle slip detector (Section 4.8.2). One file is generated for each satellite with the format `mw_SXX.out` with `SXX` replaced by the satellite number (eg G23) . The file format is as follows:

`<seconds since J2000>`$\,\sqcup b_\delta \sqcup \langle b_\delta \rangle \sqcup \sigma_{\langle b_\delta \rangle}$`¶`

where:

b_δ is the current value of the wide-lane bias (Equation 4.52),

$\langle b_\delta \rangle$ is the running average estimate of the wide-lane bias (Equation 4.53),

$\sigma_{\langle b_\delta \rangle}$ is the approximate standard deviation of the running average (Equation 4.54).

The units for all 3 values are wide-lane cycles.

An example is shown here:

`354229978.0␣-24.47839984␣-24.45920839␣0.6682412131¶`

A.3.3 *blunder.out*

This file records outlying observations detected using the method described in Section 4.8.1. It specifies the observation count at which an outlier was detected, the satellite number and GNSS constellation, and the number of consecutive times the observation from that satellite has been detected as an outlier.

An example line is shown here:

```
1750 Sat R23 LC failed blunder test 2 times
```

A.3.4 *cs.out*

This file contains a record of all the cycle slips detected by the two different methods as described in Section 4.8.2. An example is given below, with a Melbourne-Wübenna cycle slip detected for GPS satellite 24 at time 33,170 seconds since start of the day.

```
G24 MW slip @ 33170.0
```

If a cycle slip is detected on the ionospheric combination, MW is replaced with ION:

```
G24 ION slip @ 33170.0
```

A.3.5 *lc_residuals.out*

This file contains the LC carrier phase residuals at each epoch. Column 1 contains the time in seconds since the start of the day, columns 2 to 33 give the GPS LC residuals in metres for satellites 1 to 32 in order. If a satellite is not visible at that epoch, NaN is printed instead of a number. Columns 34 to 65 contain the GLONASS LC residuals in a similar manner.

A.3.6 *pc_residuals.out*

In a similar manner to the lc_residuals file, this file contains the pseudorange ionosphere free residuals. The format is the same as that described for the lc_residuals file.

A.3.7 *neu.out*

This file contains the North, East and Up difference (in metres) between the estimated PPP coordinates at each epoch and the initial coordinates for the site given in the command file. This is useful in static positioning when it contains the error in the PPP solution with respect to the known coordinates. The format of the file is as follows:

`<seconds of day>␣<North offset>␣<East offset>␣<Up offset>¶`

An example is shown here:

`33179.0␣-1433.0455␣-1039.5154␣1.2711¶`

A.3.8 *dop.out*

This file contains the dilution of precision given the used observations at each epoch. Satellites below the elevation cutoff or observations detected as outliers are not included in the calculation of dilution of precision. The entries are as follows:

`<PDOP>␣<HDOP>␣<VDOP>¶`

where `PDOP` is the positional dilution of precision, `HDOP` is the horizontal dilution of precision and `VDOP` the vertical dilution of precision.

A.3.9 *residuals_by_pos.out*

This file contains the carrier phase residuals for each satellite visible at every epoch, including the elevation and azimuth angles of the satellite at that epoch.

The format is as follows:

`<YY>␣<DD>␣<MM>␣<HH>␣<mm>␣<SS.S>␣<Sat>␣<Az>␣<Elev>␣<LC residual>¶`

The `<YY>` is the two digit year, `<MM>` is the two digit month, `<DD>` is the two digit day of month, `<HH>` is the two digit hour, `<mm>` is the two digit minute, and `<SS.S>` is a floating point value for seconds. `<Sat>` is of the format: one character specifying the network (G for GPS, R for GLONASS), followed by two digit satellite ID number. `<Az>` and `<Elev>` are given in degrees, and `<Az>` is counted clockwise from North with a range 0 to 360 degrees. `<LC residual>` is given in metres.

An example is shown here:

```
11␣3␣24␣9␣12␣51.0␣R02␣242.15␣77.20␣2.37224480947872962E-003¶
```

A.3.10 *slip_count.out*

This file contains information about the cycle slips detected and how many could be repaired.

The format is as follows:

```
<epoch>␣<#WL>␣<#NL>␣<#Sats>␣<#WL_fix>␣<#NL_fix>␣<#Sats_fix>¶
```

where `<epoch>` is simply the integer tally of observation epochs processed so far, `<#WL>` is the number of wide-lane cycle slips detected, `<#NL>` is the number of narrow-lane cycle slips detected, `<#Sats>` is the number of satellites with cycle slips, `<#WL_fix>` is the number of wide-lane cycle slips that could be fixed, `<#NL_fix>` is the number of narrow lane cycle slips that could be fixed and `<#Sats_fix>` is the number of satellites for which both the wide-lane and narrow-lane cycle slips could be fixed.

An example is shown here:

```
353␣1␣1␣1␣0␣0␣0¶
```

A.3.11 *sol.out*

This file contains the entire estimated state vector at every epoch. Column 1 is the seconds since the start of the day. The order of the subsequent columns is the same as that specified in the state vector in Section 4.3 . The final column contains the number of observations used to produce the estimate at that epoch. The units of all the estimated states are in metres.

A.3.12 *xyz.out*

This file contains the ECEF estimated coordinates of the receiver at each epoch in the reference frame defined by the orbit and clock products provided. The format of the file is as follows:

```
<seconds of day>␣<X>␣<Y>␣<Z>␣<Est ZWD>␣<dt>␣<GLONASS dt>¶
```

where `<Est ZWD>` is the estimated correction to the zenith wet delay, `<dt>` is the receiver clock offset and `<GLONASS dt>` is the receiver GPS-GLONASS hardware bias. The units of all values apart from the `<seconds of day>` are in metres.

An example is shown here:

```
179.0␣3665815.4628␣-92718.0128␣5201177.2662␣-1.783E-003␣-13.0870␣0.0¶
```

A.4 Running *pppncl*

pppncl is run with

```
pppncl -f <command file>
```

where `<command file>` is the path and name of a command file. The command file format is described in Section A.2. Any relative paths in the command file are evaluated as relative to the current working directory not the location of the command file. All output is created in the current working directory.

A.5 Scripts

To aid setup and help with running repetitive tasks a number of Python scripts have been created. Some of the scripts require `teqc` (Estey and Meertens, 1999) for RINEX file concatenation and `crz2rnx` for compressed RINEX file decompression (Hatanaka, 2008).

A.5.1 *datadownload.py*

This script can be used to download files from the CDDIS archive. The script downloads the given file type for a chosen year and day of year, decompresses it if necessary and then prints the location of the downloaded file to stdout. For all options the placeholder `<year>` should be replaced with the 4 digit year and `<doy>` replaced with the day of year for which the data is required. The types of file that can be downloaded and the command line format for that file type are:

`brdc [gn] <year> <doy>`

Download the merged broadcast navigation file in RINEX 2 format. Option `n` gets the GPS navigation file and `g` downloads the GLONASS navigation file.

`rinex <site> <year> <doy>`
: Download a RINEX 2 format observation file for a given site and date.

`sp3 <year> <doy>`
: Download satellite ephemeris data in SP3 format for a given date.

`ssc <year> <doy>`
: Download the IGS summary file in SINEX format for a given date.

A.5.2 *condor.py*

As described on the project website — "Condor is a specialized workload management system for compute-intensive jobs. Condor provides a job queueing mechanism, scheduling policy, priority scheme, resource monitoring, and resource management." (Thain et al., 2005). This allows many distinct runs of a program to be executed in parallel across many machines, greatly reducing the time taken to perform the required work.

This script, `condor.py` provides a set of functionality to simplify submitting *pppncl* jobs to a Condor cluster. The Python class `CondorRun` is used to submit a set of jobs to Condor. It is initialised with the path to a *pppncl* executable and then each command file that should be run is added using `add_site()`. The jobs may be submitted all at once using `submit()` or in batches of a chosen size using `submit_batched()`.

The scripts `run_files.py` and `run_directories.py` uses the `condor` module in this script to reduce running a set of command files using *pppncl* to simple to use command line programs.

A.5.3 *run_directories.py*

This script is designed to run every *pppncl* command file in a directory tree using a Condor cluster to parallelise the execution of multiple command files. A command file is taken to be any file with extension "`.cmd`". It is called as:

```
run_directories.py [options] [directories]
```

where `[directories]` is a list of directories in which to search for command files. If no directory is given the search will be performed in the current directory. For each

command file found the given executable will be run with the command file passed as a command line argument to the executable. The executable will be invoked in the directory containing the command file. For running on Condor the command file and all input files mentioned in the command file must be visible to the cluster.

The following options affect the program behaviour

`-e <exe>, --exe <exe>`
: Use `<exe>` as the program with which to run the command files. Usually this would be *pppncl* or MIT *Track*.

`-l, --local`
: Run the executable on the local machine rather than using Condor.

`-b, --batch`
: Submit to Condor in batches of 3000. This is useful if the number of jobs submitted overwhelms the Condor dispatcher.

A.5.4 *run_files.py*

This script runs an executable multiple times, once for each command file specified. The syntax is:

```
run_files.py EXE FILES
```

where `EXE` is the path to a copy of *pppncl* and `FILES` is a space separated list of one or more command files. The output for each command file is placed in the directory containing the command file so each command file should be in a separate directory.

A.5.5 *setup_rinex.py*

This program creates a basic *pppncl* command file given a RINEX observation file. It also downloads all the necessary navigation data. This includes an SP3 orbit file, high rate clock corrections, antenna phase centre offsets in ANTEX format, P1C1 bias data and GLONASS broadcast navigation data if required. It is called using:

```
setup_rinex.py [options] rinexfile
```

where `rinexfile` is the GNSS observation file for which the *pppncl* configuration file is to be generated.

The following options affect the program's behaviour:

`--data=<archive>`
: The location into which to download the navigation data. If the required files are already present in the archive they will not be re-downloaded.

`--center=<provider>`
: The navigation products provider to use, options are:

  igs The IGS combined product

  esa ESA products which include GLONASS orbit and clock corrections

  jpl JPL products

  cod CODE products which offer clock corrections tabulated every 5 seconds

The initial coordinates of the site are set to the values in the header of the RINEX observation file.

A.5.6 *setup_site.py*

This program creates a basic *pppncl* command file for static positioning for any station in the IGS network. It includes downloading and decompressing the observation data and all navigation data required. The script looks in three places for a set of initial coordinates for the site. The first two use the given station name to look up the coordinates within the given file. In priority order the locations are: the `.ssc` SINEX summary file for the chosen navigation data provider, the RINEX clock file header from the chosen navigation data provider and finally the coordinates in the RINEX header file.

The following options affect the program's behaviour:

`-s <site>, --station <site>`
: Station name to setup. This must be one of the stations for which data is stored on the CDDIS archive.

`-y <year>, --year=<year>`
: The year to use.

`-d <doy>, --doy=<doy>`
: The day of year to use.

`--highrate`

Download and use 1 Hz observation data. The individual hourly high rate files are downloaded and concatenated using `teqc` (Estey and Meertens, 1999).

`--data=<archive>`

The location into which to download the navigation data. If the required files are already present in the archive they will not be re-downloaded.

`--center=<provider>`

The navigation products provider to use, options are:

igs The IGS combined product

esa ESA products which include GLONASS orbit and clock corrections

jpl JPL products

cod CODE products which offer clock corrections tabulated every 5 seconds

A.5.7 *multi_position.py*

This program creates a set of *pppncl* command files for a list of IGS stations over a list of days. With the default settings it:

- downloads and decompresses all the required observation and navigation data, 30 s observation data is used;
- creates a three day SP3 file spanning the requested day to avoid orbit interpolation boundary effects at the start and end of the 24 h period;
- creates a directory named after the current time stamp in which all the output is placed;
- creates a *pppncl* command file for each site and day with settings for a 24 h static PPP solution;
- takes initial coordinates for each site from, in order of preference:
  - the IGS weekly SINEX file
  - the IGS RINEX clock file
  - the RINEX observation file header

- runs all of the command files using the *pppncl* executable version found in the path using the Condor compute cluster if it is not very busy, otherwise run *pppncl* locally;
- generates a set of plots and statistics on the coordinate accuracy and carrier phase residuals.

The following options affect the program's behaviour:

`--site-file=<sitefile>`

A file containing a list of four character site names, one per line. Lines starting with '#' are skipped as comment lines.

`-y <year>, --year=<year>`

The year to use

`-d <doy>, --doy=<doy>`

The day of year to use. This may consist of a comma separated list of values to specify multiple days. Each day listed is setup as a separate PPP run. If a range of days is wanted, this may be specified using the format `begin-end`. The following example shows how to process days 1, 3 through 10 inclusive and 27 as individual 24 hour sessions:

```
--doy=1,3-10,27
```

`--data=<archive>`

The location into which to download the navigation data. If the required files are already present in the archive they will not be re-downloaded.

`--center=<provider>`

The navigation products provider to use, options are:

igs The IGS combined product

esa ESA products which include GLONASS orbit and clock corrections

jpl JPL products

cod CODE products which offer clock corrections tabulated every 5 seconds

`-o <dir>, --o=<dir>`

Directory in which to place the output. Use in conjunction with `--no-datedir` to place the output directly in `<dir>`. Note this directory should be visible from the Condor cluster.

`--ppp <exe>`
: The location of the *pppncl* executable to use. Note this should be a path that is accessible from the Condor cluster.

`--continue-on-error`
: Continue running even if it was not possible to setup one of the requested sites.

`--single-sp3`
: Do not create a three day spanning SP3 file, use only the SP3 file for the relevant day.

`--setup-only`
: Stop after creating the command files and downloading all the required data.

`--no-datedir`
: Do not create an extra sub directory with the current date containing the output, place the output directly in the current directory or the location specified in `--output`.

`--highrate`
: Download and use 1 Hz observation data. Creates a single file for each day using `teqc`.

`--template=<template>` Specifies the location of a file to be used as a command file template (see Section A.5.7).

Command file template

The command file template is a command file with certain values set as placeholders. The placeholders are then replaced with the relevant value by the `multi_position.py` program. The format is based on the Python `string.Template` functionality.

The following placeholders will be replaced by the values specific to each site and day. The values that can be substituted are:

`$station`
: The name of the GNSS station.

`$rinex_file`
: The full filename of the RINEX observation file.

$combined_sp3
: The full filename of the SP3 navigation file.

$clk
: The full filename of the high rate RINEX clock file.

$x, $y, $z
: The receiver coordinates from the relevant IGS analysis centre weekly SINEX file.

$absolute
: The correct value for the `ABSOLUTE_ANTENNA` command based on the selected analysis centre and date.

$antex_file
: The full filename of the latest available ANTEX antenna phase centre file.

$block_file
: The full filename of the latest available GAMIT satellite information file `svnav.dat`.

$p1c1bias_file
: The full filename of the latest available P1C1 bias file.

$gnav_file
: The full filename of the GLONASS navigation file.

As many or as few as desired of the above placeholders may be placed in the template file. If a placeholder appears multiple time all copies of it will be substituted.

An example kinematic template file that explicitly uses C1 observations instead of P1:

```
␣obs_file¶
␣␣$station␣$rinex_file¶
¶
␣nav_file␣$combined_sp3␣SP3¶
¶
␣clk_file␣$clk¶
¶
␣site_pos¶
␣␣$station␣$x␣$y␣$z¶
¶
␣site_stats¶
␣␣$station␣20.0␣20.0␣20.0␣20.0␣20.0␣20.0¶
¶
␣clk_stats¶
␣␣all␣60000␣1000¶
¶
␣data_type␣KH¶
¶
␣cut_off␣5¶
¶
␣gnss_type␣G¶
¶
␣absolute_antenna␣true¶
¶
␣antex_file␣$antex_file¶
¶
␣code_type␣C1¶
```

A.6 Source code

The software program *pppncl* developed as part of this thesis is written largely in Fortran 90, with certain reused components in Fortran 77. Each set of functionality is packed in a Fortran module. Other modules or functions that make use of a particular module must explicitly state this with the `use` statement. This allows inter-module dependencies to be easily discovered when reading the source code. The structure of the program and the major modules and key functions are described below. Except where stated these modules and functions consist of new code written

explicitly for *pppncl*.

The structure of the main program is as follows:

- Read in command file
- Read navigation data
- Read observation file header
- Read in antenna phase centre offsets and variations
- If required read P1C1 bias file
- Start main loop

A.6.1 *Command file reading*

The command strings for the command file are specified in `batch_file_cmd.txt`. This file is converted into a Fortran 90 source file `batch_file_cmd.f90` by the Perl script `create_batch_cmds.pl`.

`batch_file.f90` actually performs the reading of the command file, matching commands in the command file to those given in `batch_file_cmd.txt`. It then reads the data associated with that command and sets the relevant variables in the module `batch_file_data`.

A.6.2 *Main loop*

The module `driver` contains the main loop which forms the core of the software. The subroutine loops over all the epochs in an observation file performing the following operation for each observation:

- Read next observation
- Perform Kalman filter time update step
- Get satellite frequencies
- Apply P1C1 biases if required
- Using `calc_model_data`:

  - Model observations
  - Form partial derivatives
  - Form observed minus computed prefit residuals
  - Model observation stochastics
- Check for millisecond jumps in the receiver clock
- Perform cycle slip detection
- Attempt to repair any detected cycle slips
- Perform outlier detection and removal
- Estimate new state based on the current set of measurements
- Output estimated state and other output files

A.6.3 *Rinex file reading*

Rinex reading and writing functionality is contained within the Fortran module `rinexlib` in `libraries/rinex`.

Observation files

The following types and functions are used to open a RINEX observation file and read the information in the header:

Data types

`rinex_file_t`:
: Represents a RINEX observation file. Encapsulates the path and Fortran unit to a RINEX observation file as well as the RINEX header information for that file.

Functions

`open_obs_file()`:
: Opens a RINEX observation file for reading.

rinex_file_data_type_present():
Returns `.true.` if a given observation type is present (e.g. "L1") in the RINEX file.

rinex_cc2noncc_applied():
Returns `.true.` if P1C1 biases have already been applied to this RINEX observation file using `CC2NONCC`.

antenna_delta():
Returns the antenna offset from the RINEX observation header. Values are Height, East and North displacements of the base of the antenna relative to the monument in metres.

antenna_type():
Returns the antenna type from the RINEX observation header.

approx_pos():
Returns the approximate receiver coordinates from the RINEX observation header.

Once the file has been opened, the observations in the RINEX file are read in one at a time and queried using the following:

Data types

observation:
Represents a single epoch in a RINEX observation file.

Functions

zero():
Clears an observation.

obs_sats():
Returns an array of the satellites present in an observation.

get_next_obs():
Reads the next observation in a RINEX file. Returns `.true.` on success, `.false.` if there are no more observations to read. The satellite networks for which observations will be read in are selected by passing a string containing the RINEX format letter for each of the required networks. For example the string "GR" would read in GPS and GLONASS observations, other satellite networks present in the file would be skipped.

`read_data_1` and `read_data_2` perform the actual reading and parsing of the RINEX observation.

`get_data_type()`:
Fills a two dimensional array with the requested data type e.g. “L1”, “P2” for all satellites in an observation. The first dimension of the array is the satellite corresponding to the satellites in the observation returned by `obs_sats()`. The second dimension is the requested data types in the order they were passed.

`data_type_present()`:
Similar to `get_data_type()` but returns an array of logical values indicating if each of the observation types was present for each of the satellites in the given observation epoch.

GPS navigation file

Data types

`nav_record`:
A data structure containing all the values from a RINEX GPS navigation data entry.

Functions

`open_nav_file()`:
Opens a given RINEX GPS navigation file, reads the header and the data entries.

`read_header()`:
Reads header information from a RINEX GPS navigation file.

`read_data()`:
Reads the data records of a RINEX GPS navigation file.

`get_nav_for_prn()`:
Used by `get_sat_clk_offset` and `get_sat_pos` to find the broadcast ephemeris data for a given GPS satellite at a given time.

`get_sat_clk_offset()`:
Calculates the clock offset for a given GPS satellite at a given time using the broadcast ephemeris. Clock offset is relative to GPS time.

`get_sat_pos()`:

Calculates the coordinates for a given GPS satellite at a given time using the broadcast ephemeris. The coordinates are x, y, z in metres in the WGS84 Earth centred reference frame and may be Earth fixed or inertial depending on the chosen option.

GLONASS navigation file

Data types

`nav_g_t`:

Contains a set of GLONASS broadcast navigation records.

`g_nav_record_t`:

A GLONASS broadcast navigation record.

Functions

`open_nav_g_file()`:

Opens a given RINEX GLONASS navigation file, reads the header and data entries.

`get_sat_slot()`:

Looks up the slot number for a particular satellite number at a given time. The slot number can then be used to determine the transmitting frequencies of the satellite. The returned value corresponds to k in Equations 2.1 and 2.2.

Internal functions

`read_header()`:

Reads header information from a RINEX GLONASS navigation file.

`read_record()`:

Reads an individual data record of a RINEX GLONASS navigation file into a `g_nav_record_t`.

`store_record()`:

Stores a record in a `nav_g_t`.

A.6.4 *SP3 file reading*

The module `sp3` contains functions for parsing SP3 format (Hilla, 2002) files and interpolating the data to calculate satellite coordinates and clock offsets. The compile time constants `max_sat`, `max_systems` and `max_sp3` defined in the module `config` affect the size of the arrays used to store SP3 data.

When interpolating the tabulated SP3 values there must be at least two entries before and two entries after the required time, to avoid the interpolation errors that appear at the edge of the interpolation interval known as Runge's phenomenon (Dahlquist and Björck, 2003).

Data types

`sp3_header_t`:
Stores the information contained in an SP3 file header.

`sp3_data_t`:
Stores the tabulated satellite coordinates and clock offsets from an SP3 file.

Functions

`read_header()`:
Parses an SP3 file header.

`read_sp3()`:
Opens and parses an SP3 file, multiple satellite systems are supported.

`eph_to_xyz()`:
Calculates the coordinates for a given satellite in either an ECEF or Earth Centred Inertial (ECI) coordinate system at a given time. Lagrange interpolation is used to interpolate the tabulated values to the required time (Press et al., 1996).

`eph_to_xyz_v()`:
As `eph_to_xyz` but also returns the satellite velocity by evaluating the derivative of the interpolating Lagrange polynomial.

`comp_svs_clk()`:
Calculates receiver clock offset for a particular satellite at a given time.

Internal functions

`find_index()`:
Finds the index in the SP3 data of start and end points for an interpolation of a given order for a particular satellite at a particular time. If possible the returned range will evenly span the required time. Missing data or proximity to the start and end points of the parsed SP3 data will cause the returned range to not be centred on the required time. If the requested time is outside the data available or the found span would result in interpolation near the edge of the span (resulting in problems as described above), a start index of -1 is returned.

A.6.5 *RINEX clock file reading*

The Fortran module `clk` contains functions for reading and interpolating RINEX 3.0 clock files (Ray and Gurtner, 2010). The compile time constants `max_clk`, `max_sat` and `max_systems` from the module `config` affect the size of the arrays used for storing data read in from a RINEX clock file.

Data types

`clk_data_t`:
Stores the parsed clock offset data.

Functions

`read_clk()`:
Opens and reads a RINEX 3.0 clock format file.

`comp_svs_clk()`:
Linearly interpolates the clock offset for a given satellite at a particular time. The offset is given in seconds.

A.6.6 *Navigation data*

The module `navigation_data` provides an abstraction over the used satellite navigation type. The underlying navigation data may be a broadcast ephemeris in RINEX navigation format or a precise ephemeris in SP3 format, possibly augmented with higher rate satellite clock corrections in RINEX clock format.

Functions

`setup_navigation_data()`:
Reads in and parses the selected navigation files.

`load_glonass_nav()`:
Loads an additional RINEX GLONASS navigation file to obtain the mapping from satellite number to GLONASS frequency number.

`get_sat_pos()`:
Calculates the position (in metres X, Y, Z) of a given satellite at a particular time using the corresponding method for the underlying navigation type. The returned coordinates are in the reference frame of the provided navigation data.

`get_sat_pos_v()`:
Calculates the position (in metres X, Y, Z) and velocity (in $\mathrm{m\,s^{-1}}$) of a given satellite at a particular time using the corresponding method for the underlying navigation type.

`get_sat_clk_offset()`:
Calculates the clock offset in seconds of a given satellite at a particular time using the corresponding method from the underlying navigation type.

`get_sat_frequency()`:
Returns the two carrier frequencies of the given satellite.

A.6.7 *Differential code biases*

The module `cc2noncc` provides functions to read and apply differential code biases. The file parsing uses code from `CC2NONCC v6.3` provided by ESOC (Romero, 2010).

Data types

`cc2noncc_t`:
Stores a set of DCB.

Functions

`cc2noncc_new()`:
Reads in a set of DCB biases in the `CC2NONCC` format (Section A.1.4) for a given month.

`cc2noncc_applyc1p1()`:
Applies a set of C1-P1 biases to a set of C1 observations given the observations and the corresponding satellites (Equation 3.30).

A.6.8 *GLONASS frequency*

The module `glonass_f` implements Equations 2.1 and 2.2 to determine the GLONASS frequency for a given channel number.

Functions

`glonass_frequency_for()`:
Calculates the L1 and L2 carrier frequencies for a given GLONASS channel number.

A.6.9 *Antenna phase centre offsets*

The module `phase_center` provides a consistent interface to the two supported types of antenna phase centre for both satellites and receivers. Phase centre offsets may either be used from an ANTEX format or GAMIT block mean format as described in Section A.1.3.

Data types

`sat_phase_center_t`:
Used to store the satellite phase centre data.

`rcv_antenna_t`:
Used to store the receiver phase centre offsets and variations.

Functions

`phase_center_from_block_list()`:
Loads satellite phase centre offset block mean values in the GAMIT `svnav.dat` format into a `sat_phase_center_t`.

`phase_center_from_antex()`:
Loads satellite phase centre offset block mean values from an ANTEX file into a `sat_phase_center_t`.

`get_sat_phase_centre_offset()`:

Gets the phase centre offset for a particular satellite at a given time given the satellite coordinates. The satellite body frame offset is converted to ECEF coordinates at the given time (Section 3.7). The units of the offset are metres.

`phase_center_variation()`:

Returns the satellite phase centre variation given a satellite and the nadir angle it is viewed from. The returned value is in metres.

`rcv_antenna_new_manual()`:

Initialises a `rcv_antenna_t` using a given phase centre offset for L1 and L2 carrier frequencies.

`rcv_antenna_new_antex()`:

Initialises a `rcv_antenna_t` using antenna phase centre offset and variation values from an antenna in an ANTEX file. The antenna can be searched for in an antex file using `find_matching_rcv_antenna` from the module `antex`.

`rcv_antenna_offset()`:

Gets the receiver antenna offset in metres for the L1 and L2 carrier frequencies.

`rcv_antenna_variation()`:

Gets the receiver antenna variation at a given elevation angle in metres for the L1 and L2 carrier frequencies.

The modules `antex` and `svs` contain analogous functions to those given above that implement the loading, look-up and linear interpolation of the values for a particular format.

A.6.10 *Observation modelling*

The module `theory` contains functions to model the expected GNSS observations (Section 4.4), calculate the partial derivatives with respect to the state vector (Section 4.5), determine the observation stochastics (Section 4.6) and compute the prefit residual vector (Equation 4.40).

Data types

`theory_t`:

Contains modelling options such as the antenna phase centre model and the atmospheric model to use.

model_out_t:

Contains the output of the modelling including the prefit residuals, the observation partial derivatives and the observation stochastics for a given observation combination for a particular satellite.

Functions

calc_model_data():

Given a predicted state, a set of observations and the time of observation, models the requested observation combination filling a `model_out_t` for each satellite. These steps correspond to Equations 4.4 and 4.7 of the Kalman filter.

Internal functions

predict_ranges():

Computes the predicted code and carrier phase observations (Equations 4.15 and 4.16) on the L1 and L2 frequencies for a set of GPS and GLONASS satellites at a given time. A state vector (Section 4.3) of receiver coordinates, receiver clock offset, wet tropospheric delay correction and estimated ambiguities are needed as inputs.

get_transmit_time():

The transmit time from each satellite is found by iteration as described in Section 4.4 so the computation may be performed without requiring any real observations. The satellite coordinates and clock offset are found using the selected navigation data (Section A.6.6).

o_minus_c():

Calculates the observed minus computed measurements for the chosen set of observation combinations e.g. LC and PC. Also computes the partial derivatives of the computed combinations with respect to the state vector (Section 4.3) and the modelled variance of the observation combinations.

form_partials():

Calculates the partial derivatives of a range measurement to a satellite with respect to the receiver coordinates and the tropospheric correction (Equations 4.25 and 4.26).

fill_partials():

Fills in the partial derivatives array of a `model_out_t` data type.

`check_millisecond_jump()`:

Given a set of prefit residuals, determines if the receiver has inserted a millisecond jump in its clock. Certain receivers, for example the Leica GS10, compensate for internal clock drift by inserting millisecond jumps whenever the receiver clock is offset from GPS time by more than half a millisecond. Failure to detect this can lead to errors in calculating the satellite position and clock offset.

Tropospheric modelling

Data types

`atm_zenith_model_t`:

An atmospheric zenith model.

`atm_mapping_funtion_t`:

An atmospheric mapping function.

Functions

`model_zenith()`:

Models the tropospheric zenith path delay using the Saastamoinen zenith delay model at a given time, latitude and height (see Section 3.3, Equations 3.4 and 3.3).

`atm_zenith_model_hydrostatic_delay()`:

Gets the value of the modelled hydrostatic delay from an `atm_zenith_model_t` in metres.

`atm_zenith_model_wet_delay()`:

Gets the value of the modelled wet delay from an `atm_zenith_model_t` in metres.

`atm_mapping_init()`:

Initialises an `atm_mapping_funtion_t` to use either:

NIELL The Niell mapping function (Niell, 1996).

GMF The Global Mapping function (Böhm et al., 2006a).

The code for the Niell mapping functions was used from *Track*, the GMF mapping function uses the routine provided at `http://mars.hg.tuwien.ac.`

`at/~ecmwf1/gmf.f_hu`.

`atm_mapping_function_update()`:
Updates the mapping function state based on the time, receiver coordinates and satellite elevation.

`atm_mapping_function_hydrostatic()`:
Returns the value of the hydrostatic mapping function.

`atm_mapping_function_wet()`:
Returns the value of the wet mapping function.

`tropospheric_delay()`:
Calculates the total tropospheric path delay due to the modelled wet and dry zenith delays and the wet and dry mapping functions. A correction to the zenith wet delay may be passed in (see Equation 3.12).

Phase windup and satellite orientation

The module `svs` contains models for the nominal yaw attitude that allow phase windup determination and mapping satellite body frame antenna offsets to an ECEF frame.

Functions

`SUN20()`:
Calculates a unit vector and range to the Sun at a given time. The code from *Track* was used which is based on the tables of the Sun by Newcomb (1895).

`windup()`:
Calculates the phase windup in radians for a given satellite and receiver location and time (Section 3.8). Keeps track of complete rotations to avoid adding single cycle discontinuities.

Relativistic correction

The module `relativity` contains functions that calculate the relativistic corrections due to orbital eccentricity and gravitational bending.

Functions

`relativity_eccentricity_correction()`:
Calculates the relativistic correction due to satellite orbit eccentricity (Equation 3.18).

`relativity_gravitational_correction()`:
Calculates the propagation correction for a satellite signal due to space-time curvature induced by the Earth's gravitational field (Equation 3.19).

Earth body tide

The module `earth_tide` contains routines from *Track* for calculating the distortion at a given point and time due to solid Earth tides (Section 3.10).

Functions

`earth_tide_dXYZ()`:
Calculates the X, Y, Z coordinate shift in metres due to solid Earth tides at a given position and time.

A.6.11 *Cycle slip detection and repair*

The modules `csdetector_mw` and `csdetector_ion` are implementations of the ionospheric combination and Melbourne-Wübbena cycle slip detectors described in Section 4.8.2.

Data types

`mwdata_t`:
Stores the values of the running mean and variance from Equations 4.53 and 4.54 for a single satellite.

`mw_detector_t`:
Contains a set of `mwdata_t`, one for each satellite and the chosen number of standard deviations outside of which a cycle slip is detected.

`csdetector_ion_history_t`:
Contains $\Phi_I(t_{k-1})$ and t_{k-1} for use in Equation 4.56 at the next epoch.

csdetector_ion_t:

Contains a set of csdetector_ion_history_t, one for each satellite and the absolute ionosphere combination rate of change outside of which a cycle slip is detected.

Functions

csdetector_mw_new():

Initialises a mw_detector_t with a chosen cycle slip detection threshold in units of number of standard deviations.

csdetector_mw_detect():

Given a set of carrier phase observations, returns an array of logical values indicating if a cycle slip was detected for each satellite using the Melbourne-Wübbena combination method described in Section 4.8.2.

csdetector_mw_force_slip():

If a cycle slip has been detected using some other method which would influence the wide-lane bias, this function should be used to reset the running average used in the cycle slip detection.

csdetector_ion_new():

Initialises a csdetector_ion_t with a chosen detection threshold given in metres.

csdetector_ion_detect():

Given a set of carrier phase observations, returns an array of logical values indicating if a cycle slip was detected for each satellite using the ionosphere combination method described in Section 4.8.2.

The module slip_fix implements cycle slip fixing using the integer least squares time differenced method of Banville and Langley (2010) as described in Section 4.8.2.

Functions

fix_slips():

Attempts to fix the cycle slips previously identified.

ls():

A wrapper around the LAPACK least squares function DGELS that performs least squares estimation using QR factorisation (Anderson et al., 1999). Used by fix_slips to perform the initial cycle slip estimation.

The module `lambda` is a Fortran 90 interface wrapper to the LAMBDA integer least squares implementation available from Delft University of Technology. The function `lambda4` returns a set of integer valued estimates given a set of float estimates and their associated covariance matrix. All calculations are performed using the Delft code; `lambda4` makes the use of the method simpler by allocating the space required for work vectors.

A.6.12 *Outlier detection*

The module `blunder` implements the outlier detection method described in Section 4.8.1.

Functions

`LOM_test()`:
: Given a set of prefit residuals and the prefit residual covariances found using `residual_covariance`, first identifies if the set of prefit observation residuals are consistent with their given covariance and if so identifies the most likely outlier. If the most likely outlier does not fail the local test (Equation 4.46), -1 is returned as the index of the most likely outlier.

`log_failure()`:
: Used to add an entry to `blunder.out` when an observation is detected as an outlier.

A.6.13 *Kalman filtering*

The module `kalman` contains an implementation of the parts of an extended Kalman filter that are independent of the system being modelled. This is the "Update Step" from Section 4.1 and Equations 4.8, 4.9 and 4.10.

If they are available the LAPACK routines `dgetrf` and `dgetri` are used to perform matrix inversion using LU decomposition (Anderson et al., 1999).

Functions

`ekf()`:
: Implements the extended Kalman filter update step given the predicted state

$\hat{x}_k(-)$, prefit residuals $(z_k - \hat{z}_k)$, linearised system dynamic model $H_k^{[1]}$, observation covariance matrix R_k and *a priori* state covariance matrix $P_k(-)$.

Elements in the state vector for which the corresponding row in the *a priori* state covariance matrix $P_k(-)$ is zero will not be changed by the update step (Equations 4.8 and 4.9). To avoid performing multiple matrix multiplications and inversions on unnecessarily large matrices, the rows of $P_k(-)$ are checked at the start of this subroutine. Using Fortran 90 array indexing only those rows and columns of the input vectors and matrices are selected and passed to `ekf_` that actually performs the filtering.

`residual_covariance()`:

Calculates the expected uncertainties in the pre-fit observation residuals given the observation stochastic model, the design matrix and the predicted state vector covariance. Returns C_{v_k} from Equation 4.42.

Internal functions

`ekf_()`:

Called by `ekf` to perform the filtering once the active elements of the input matrices have been extracted.

`kalman_gain()`:

Calculates the Kalman gain matrix (Equation 4.9).

`condition_on_measurement()`:

Adjusts the predicted state based on the measured observations (Equation 4.8).

`a_posteriori_covariance()`:

Calculates the *a posteriori* covariance matrix (Equation 4.10).

`a_posteriori_covariance_joseph()`:

Calculates the *a posteriori* covariance matrix using the alternative Joseph form (Equation 4.14).

Appendix B IGS sites and reference coordinates

The below table lists the IGS sites and their coordinates, for GPS week 1605, used in static PPP accuracy assessment. Coordinates are given in ITRF2005 using the GRS80 ellipsoid.

Site name	Longitude (°)	Latitude (°)	Height (m)
abmf	298.472 46	16.262 30	−25.57
abpo	47.229 21	−19.018 30	1552.97
aira	130.599 59	31.824 06	314.65
ajac	8.762 61	41.927 45	98.77
albh	236.512 52	48.389 78	31.74
algo	281.928 63	45.955 80	200.93
alic	133.885 51	−23.670 11	603.25
amc2	255.475 40	38.803 12	1911.39
ankr	32.758 46	39.887 37	976.02
antc	288.467 93	−37.338 70	745.42
areq	288.507 20	−16.465 51	2488.93
artu	58.560 45	56.429 82	247.58
aspa	189.277 56	−14.326 09	53.55
auck	174.834 38	−36.602 84	132.69
bake	263.997 65	64.317 81	4.51
bako	106.848 91	−6.491 05	158.12
bamf	234.864 89	48.835 32	10.78
barh	291.778 30	44.395 04	6.74
bjfs	115.892 48	39.608 60	87.46
bogt	285.919 06	4.640 07	2576.47
bor1	17.073 45	52.276 95	124.36
braz	312.122 13	−15.947 47	1106.01
brew	240.317 36	48.131 52	238.61
brft	321.574 46	−3.877 44	21.68
brmu	295.303 72	32.370 39	−11.62
brst	355.503 40	48.380 49	65.83
brus	4.359 22	50.797 81	149.68
bshm	35.022 98	32.778 98	225.08
bzrg	11.336 79	46.499 02	329.13
cags	284.192 67	45.585 02	234.97
cagz	8.972 75	39.135 89	237.98

Site name	Longitude (°)	Latitude (°)	Height (m)
cas1	110.519 70	−66.283 35	22.46
ccj2	142.195 02	27.067 53	104.23
ccjm	142.184 57	27.095 58	208.83
cebr	355.632 14	40.453 42	775.81
cedu	133.809 83	−31.866 66	144.73
chan	125.444 20	43.790 68	273.26
chat	183.434 15	−43.955 78	57.98
chpi	315.014 84	−22.687 14	617.42
chti	183.382 88	−43.735 47	75.68
chum	74.751 10	42.998 50	716.34
chur	265.911 27	58.759 07	−19.28
cnmr	145.743 09	15.229 69	64.38
coco	96.833 97	−12.188 34	−35.29
cont	286.974 58	−36.842 84	173.40
conz	286.974 48	−36.843 76	180.64
copo	289.661 76	−27.384 52	479.10
crao	33.990 98	44.413 26	365.81
crar	166.668 24	−77.848 04	−19.85
cro1	295.415 68	17.756 89	−31.95
cusv	100.533 92	13.735 91	74.27
darw	131.132 74	−12.843 70	125.11
dav1	77.972 61	−68.577 32	44.40
dgar	72.370 24	−7.269 68	−64.93
drag	35.392 07	31.593 20	31.83
drao	240.375 01	49.322 61	541.88
dubo	264.133 81	50.258 80	245.28
dubr	18.110 43	42.649 98	454.28
dund	170.597 16	−45.883 66	386.93
eprt	293.007 86	44.908 71	30.35
escu	295.201 28	47.073 40	−16.00
fair	212.500 75	64.977 99	319.01
falk	302.125 93	−51.693 65	50.83
flin	258.021 96	54.725 58	311.53
flrs	328.873 61	39.453 83	80.21
frdn	293.340 11	45.933 50	94.84

Site name	Longitude (°)	Latitude (°)	Height (m)
func	343.092 38	32.647 94	78.42
ganp	20.322 93	49.034 71	746.01
glsv	30.496 73	50.364 18	226.32
gmas	344.365 73	27.764 78	195.42
gmsd	131.015 56	30.556 44	142.35
gode	283.173 16	39.021 72	14.50
gold	243.110 74	35.425 15	986.65
gope	14.785 62	49.913 70	592.60
gras	6.920 57	43.754 73	1319.31
graz	15.493 48	47.067 13	538.28
guam	144.868 36	13.589 32	201.92
guat	269.479 81	14.590 40	1519.85
guug	144.802 71	13.433 20	134.74
harb	27.707 24	−25.886 96	1558.09
harv	239.317 93	34.469 40	14.90
hers	0.336 27	50.867 31	76.47
hert	0.334 35	50.867 48	83.33
hil1	115.738 58	−31.825 52	−27.25
hlfx	296.388 71	44.683 54	3.10
hnlc	202.135 45	21.303 28	21.96
hnpt	283.869 62	38.588 81	−27.98
hofn	344.802 08	64.267 29	82.78
holb	231.865 00	50.640 35	559.59
holm	242.238 76	70.736 30	0.43
hrao	27.686 98	−25.890 10	1414.16
hrm1	358.716 11	51.453 74	163.02
hyde	78.550 87	17.417 25	441.68
ieng	7.639 40	45.015 13	316.62
iisc	77.570 37	13.021 16	843.69
invk	226.473 03	68.306 18	46.36
iqal	291.489 50	63.755 96	91.69
iqqe	289.868 28	−20.273 54	38.99
irkj	104.316 18	52.219 02	502.05
irkt	104.316 24	52.219 02	502.34
joz2	21.032 35	52.097 83	152.52

Site name	Longitude (°)	Latitude (°)	Height (m)
joze	21.031 54	52.097 27	141.44
jplm	241.826 77	34.204 82	423.98
jplv	241.825 70	34.201 58	372.71
karr	117.097 19	−20.981 42	109.15
khaj	135.046 15	48.521 45	130.48
khar	36.239 00	50.005 10	201.03
kiru	20.968 44	67.857 35	391.02
kit3	66.885 44	39.134 76	622.48
kokb	200.335 06	22.126 26	1167.35
kosg	5.809 64	52.178 42	96.85
kouc	164.287 33	−20.558 69	84.14
kour	307.194 04	5.252 18	−25.75
ksmv	140.657 67	35.955 37	57.86
kunm	102.797 19	25.029 53	1986.20
kuuj	282.254 56	55.278 36	−0.35
lama	20.669 94	53.892 40	187.03
lmmf	299.003 82	14.594 81	−27.10
lpal	342.106 17	28.763 87	2199.19
lpgs	302.067 70	−34.906 74	29.87
lroc	358.780 68	46.158 94	57.86
mac1	158.935 83	−54.499 52	−6.79
madr	355.750 34	40.429 16	829.45
mal2	40.194 14	−2.996 05	−20.90
mar6	17.258 52	60.595 14	75.49
mars	5.353 78	43.278 77	61.82
mas1	344.366 72	27.763 74	197.14
mat1	16.704 54	40.649 06	534.53
mate	16.704 46	40.649 13	535.65
maui	203.742 97	20.706 65	3062.10
maw1	62.870 71	−67.604 76	59.13
mcm4	166.669 33	−77.838 34	97.97
mdvj	37.214 50	56.021 49	257.13
medi	11.646 81	44.519 95	50.02
mets	24.395 32	60.217 47	94.62
metz	24.395 33	60.217 48	94.60

Site name	Longitude (°)	Latitude (°)	Height (m)
mikl	31.972 84	46.972 78	93.91
mizu	141.132 82	39.135 16	116.97
mkea	204.543 65	19.801 35	3754.66
mobn	36.569 52	55.114 87	182.67
mobs	144.975 33	−37.829 40	40.59
moiu	35.290 01	0.288 32	2201.52
monp	243.577 64	32.891 94	1842.54
morp	358.314 50	55.212 79	144.45
mqzg	172.654 69	−43.702 73	154.68
mtbg	16.404 25	47.737 87	293.82
nain	298.311 28	56.536 97	32.80
nano	235.913 52	49.294 81	6.58
nico	33.396 44	35.140 98	190.02
nist	254.737 39	39.995 06	1648.33
nium	190.072 93	−19.076 52	89.71
nklg	9.672 12	0.353 90	31.51
nnor	116.192 72	−31.048 73	234.82
not1	14.989 78	36.875 84	126.33
novm	82.909 48	55.030 50	149.95
nrc1	284.376 17	45.454 16	82.51
nril	88.359 78	69.361 83	47.92
nrmd	166.484 88	−22.228 32	160.34
ntus	103.679 95	1.345 80	75.38
nurk	30.089 68	−1.944 55	1483.82
nya1	11.865 31	78.929 55	84.27
nyal	11.865 08	78.929 58	78.55
obe3	11.279 80	48.086 18	642.34
ohi2	302.098 66	−63.321 08	32.48
ohi3	302.098 61	−63.321 09	32.63
onsa	11.925 51	57.395 29	45.60
opmt	2.334 94	48.835 92	122.59
ous2	170.510 93	−45.869 47	26.10
pado	11.896 06	45.411 15	64.70
palm	295.948 87	−64.775 08	31.09
parc	289.120 11	−53.136 95	22.28

Site name	Longitude (°)	Latitude (°)	Height (m)
park	148.264 61	−32.998 76	397.36
pdel	334.337 23	37.747 75	110.62
penc	19.281 53	47.789 60	291.73
pert	115.885 25	−31.801 96	12.69
pets	158.650 13	53.023 29	102.08
pgc5	236.548 87	48.648 53	3.58
pie1	251.881 07	34.301 50	2347.72
pimo	121.077 73	14.635 72	95.53
pin1	243.541 83	33.612 15	1256.16
polv	34.542 93	49.602 61	178.37
pove	296.103 67	−8.709 33	119.60
prds	245.706 50	50.871 35	1247.95
pre1	28.224 03	−25.746 34	1416.32
ptbb	10.459 74	52.296 19	130.24
qaq1	313.952 23	60.715 26	110.44
qiki	295.966 33	67.559 33	13.28
quin	239.055 57	39.974 55	1105.78
rabt	353.145 71	33.998 10	90.09
ramo	34.763 14	30.597 60	886.84
rbay	32.078 38	−28.795 54	31.76
rcmn	36.893 48	−1.220 82	1591.99
redu	5.144 88	50.001 50	369.92
reso	265.106 30	74.690 82	19.99
reun	55.571 72	−21.208 22	1558.36
reyk	338.044 51	64.138 78	93.03
riga	24.058 77	56.948 62	34.72
rio2	292.248 88	−53.785 47	32.03
riop	281.348 89	−1.650 59	2817.17
roap	353.793 73	36.464 26	73.67
rosa	307.047 91	−22.523 30	299.68
roth	291.874 22	−67.571 38	39.70
salu	315.787 52	−2.593 45	18.98
sant	289.331 44	−33.150 28	723.06
sask	253.601 64	52.196 25	578.87
savo	321.567 74	−12.939 24	76.31

Site name	Longitude (°)	Latitude (°)	Height (m)
sch2	293.167 38	54.832 09	498.31
scor	338.049 66	70.485 33	128.51
scub	284.237 68	20.012 06	20.91
sele	77.016 90	43.178 73	1342.00
sey1	55.479 40	−4.673 71	537.20
sfer	353.794 35	36.464 34	84.17
she2	295.447 98	46.220 69	−15.28
sio3	242.749 58	32.864 70	34.86
sofi	23.394 73	42.556 09	1119.54
spt0	12.891 35	57.714 95	219.99
stj2	307.321 69	47.595 23	152.55
stjo	307.322 24	47.595 24	152.84
stk2	141.844 81	43.528 64	118.56
str2	149.010 15	−35.316 15	802.48
suth	20.810 46	−32.380 20	1799.76
sutm	20.810 91	−32.381 43	1797.61
suwn	127.054 24	37.275 51	82.27
svtl	29.780 87	60.532 86	76.70
sydn	151.150 38	−33.780 87	85.59
syog	39.583 74	−69.006 95	50.00
tah1	210.393 80	−17.577 02	99.81
tash	69.295 56	41.328 04	439.77
tcms	120.987 39	24.797 98	77.25
tehn	51.334 09	35.697 28	1194.57
thti	210.393 54	−17.577 06	98.02
thu3	291.174 95	76.537 04	36.15
tidb	148.979 99	−35.399 20	665.33
tixi	128.866 42	71.634 47	47.07
tlse	1.480 89	43.560 69	207.19
tnml	120.987 34	24.797 95	75.87
tow2	147.055 68	−19.269 27	88.12
tro1	18.939 64	69.662 71	138.11
tsk2	140.087 11	36.105 57	69.94
tskb	140.087 49	36.105 67	67.26
tubi	29.450 68	40.786 72	220.34

Site name	Longitude (°)	Latitude (°)	Height (m)
tukt	227.005 64	69.438 23	−1.53
twtf	121.164 50	24.953 56	201.53
uclu	234.458 35	48.925 63	10.07
ufpr	310.769 04	−25.448 36	925.78
ulab	107.052 32	47.865 06	1575.53
urum	87.600 66	43.807 94	858.86
usn3	282.933 72	38.920 56	57.39
usno	282.933 77	38.918 96	48.86
usud	138.362 04	36.133 10	1508.60
vacs	57.497 03	−20.297 07	421.16
vald	282.435 83	48.097 05	312.84
valp	288.373 90	−33.027 24	31.21
vesl	357.158 21	−71.673 79	862.36
vill	356.048 02	40.443 59	647.34
vis0	18.367 31	57.653 87	79.84
vndp	239.383 54	34.556 31	−11.51
wab2	7.464 25	46.923 74	611.20
wes2	288.506 67	42.613 33	85.01
wgtn	174.805 89	−41.323 45	26.04
wgtt	174.781 59	−41.290 43	42.97
whit	224.777 88	60.750 51	1427.40
will	237.832 18	52.236 86	1095.69
wind	17.089 43	−22.574 91	1734.66
wroc	17.062 04	51.113 26	180.82
wsrt	6.604 50	52.914 61	82.28
wtza	12.878 90	49.144 22	665.92
wtzj	12.878 93	49.144 20	665.93
wtzr	12.878 91	49.144 19	666.02
wtzs	12.878 62	49.144 78	663.43
wtzz	12.878 90	49.144 21	665.89
wuhn	114.357 26	30.531 65	25.86
xian	109.221 49	34.368 67	463.94
xmis	105.688 50	−10.449 96	261.51
yakt	129.680 30	62.030 95	103.40
yar3	115.347 15	−29.046 49	242.45

Site name	Longitude (°)	Latitude (°)	Height (m)
yebe	356.911 37	40.524 90	972.76
yel2	245.519 15	62.481 32	181.00
yell	245.519 29	62.480 89	180.94
yssk	142.716 72	47.029 73	91.29
zeck	41.565 06	43.788 39	1166.29
zimj	7.465 10	46.877 14	954.31

Table B.1: List of sites and their coordinates, for GPS week 1605, used in static PPP validation. Coordinates are given in ITRF2005 using the GRS80 ellipsoid